ABSTRACT

Title of Document: BIOPHYSICAL ASPECTS OF LEUKOCYTE TRANSMIGRATION THROUGH THE VASCULAR ENDOTHELIUM

Kimberly Murley Stroka, Doctor of Philosophy, 2011

Directed By: Associate Professor Helim Aranda-Espinoza, Fischell Department of Bioengineering

Leukocyte transmigration through the vascular endothelium is a key step in the immune response, and also in progression of the cardiovascular disease atherosclerosis. Much work has previously focused on the biological aspects of leukocyte transmigration, such as cytokine exposure, junctional protein organization in the endothelium, and signaling pathways. However, in recent years, many studies have identified links between the mechanical properties of the cellular microenvironment and cell behavior. This is relevant to the cardiovascular system in two ways: (1) it is likely that the mechanical properties of vasculature depend on both vessel size (large vessels versus microvasculature) and tissue type (soft brain versus stiffer muscle or tumor), and (2) both large vessels and microvasculature stiffen in atherosclerosis. For the first time, this dissertation provides a quantitative evaluation of the biophysical effects of vasculature stiffening on endothelial cell (EC) biomechanical properties, as well as leukocyte migration and transmigration.

A novel *in vitro* model of the vascular endothelium was created. This model mimics physiological conditions more closely than previous models, by taking into account the flexibility of the subendothelial matrix; previous models have mostly utilized glass or plastic substrates that are much stiffer than physiological. EC monolayers were formed on extracellular matrix (ECM) protein-coated hydrogels and activated with tumor necrosis factor-α or oxidized low density lipoprotein to induce an inflammatory response. We determined that three important components of the *in vitro* model (cell-cell adhesion, cytokine exposure, and subendothelial matrix stiffness) have significant effects on EC biomechanical properties. Next, we showed that neutrophils are mechanosensitive, as their migration is biphasic with substrate stiffness and depends on an interplay between substrate stiffness and ECM protein amount; these results suggest that any biomechanical changes which occur in vasculature may also affect the immune response. Finally, we discovered that neutrophil transmigration increases with subendothelial matrix stiffness, and we demonstrated that this effect is due to substrate stiffness-dependent EC contractile forces. These results indicate, for the first time, that the biophysical states of the endothelium and subendothelial matrix, which likely vary depending on size, location, and health of vasculature, are important regulators of the immune response.

BIOPHYSICAL ASPECTS OF LEUKOCYTE TRANSMIGRATION THROUGH THE VASCULAR ENDOTHELIUM

By

Kimberly Murley Stroka

Dissertation submitted to the Faculty of the Graduate School of the
University of Maryland, College Park, in partial fulfillment
of the requirements for the degree of
Doctor of Philosophy
2011

Advisory Committee:
Associate Professor Helim Aranda-Espinoza, Chair
Professor Robert M. Briber
Associate Professor John P. Fisher
Assistant Professor Arpita Upadhayaya
Appointed Faculty Irena Levitan

Dedication

This work is dedicated to my husband Tom and also to my parents, for their continuous love and support, for their many sacrifices, and for always encouraging me to dream big.

Acknowledgements

First, I would like to thank my advisor, Dr. Helim Aranda-Espinoza for introducing me to the world of cell biophysics, welcoming me into his lab, and mentoring me (scientifically and career-wise) over the past five years. I am grateful to him for providing me with so many opportunities, for continuously challenging me to be a better scientist/engineer, for supporting me every step of the way, and for keeping things fun with many practical jokes!

I would also like to thank the many individuals with whom I have had productive and stimulating scientific discussions, including Dr. Peter Davies, Dr. Silvia Muro, and Dr. Martin Schwartz, as well as many others I have met at various conferences all over the world. I thank my committee members for their support and comments. I thank collaborator Dr. Irena Levitan for serving on my dissertation committee and for her input to the oxLDL project; I also thank Tzu-Pin Shentu and Myung Oh in Dr. Irena Levitan's lab for preparation of oxLDL. I also thank the editors and reviewers of my manuscripts and fellowship proposals for taking the time to critically evaluate my work and provide constructive feedback that I was able to use to further refine my work.

I acknowledge the generous funding I have received over the past five years: (1) my National Scientific Foundation (NSF) Graduate Research Fellowship, which funded me through my first three years, (2) my National Institutes of Health NRSA predoctoral fellowship from the National Institute of Neurological Disease and Stroke, which funded my final two years of graduate study, (3) Dr. Aranda-Espinoza's NSF and NIH funding, and (4) various travel grants which allowed me to travel to many national and international conferences.

I also thank all past and present members of the Cell Biophysics Lab for their comments, critiques, friendship, and support. I also give a special thank you to the many volunteers (and their neutrophils!) who so generously donated blood for my projects. Also, thanks to the many friends I have made along the way; I am grateful for all the fun times we have shared throughout the years.

My family also deserves a huge thank you for all of their love and support over the course of my long journey as an academic. Thank you to my fantastic parents, step-parents, in-laws, and grandparents, all of whom have been great motivators. In particular, I thank my mom, Gayle, my dad, Don, and my brother, Chris, for leading by example and encouraging me to pursue what I love, follow my dreams, and never give up. They are constant reminders to me that if you love your job, you never have to work a single day of your life.

Finally, I would like to thank my wonderful husband, Tom, for being my best friend over the past 10 years. I am grateful for his continuous love and support and for always helping me keep everything in perspective. He himself is one of my greatest inspirations as an engineer due to his incredible ingenuity and ability to think outside the box. Thank you, Thomas!

Table of Contents

† These chapters were taken or adapted from K.M. Stroka's previously published (or submitted) manuscripts, with permission from the publishers. Specific citations are included in footnotes at the beginning of each chapter.

List of Figures

List of Tables

1 Introduction

Cardiovascular disease (CVD) is the leading cause of death in the world, and blood vessel stiffening is a hallmark of one type of CVD, atherosclerosis. However, it remains unknown how vascular stiffening affects the endothelial cells (ECs) lining blood vessels or the immune response. Importantly, leukocyte transmigration through the vascular endothelium is a key step in the immune response, and also in CVD progression. In recent years, many studies have identified links between the mechanical properties of the cellular microenvironment and cell behavior. In particular, it is now well established that changes in tissue biomechanics often lead to or are caused by disease conditions, such as CVD and cancer. It is clear from clinical measurements that CVD leads to an overall blood vessel stiffening, both in large vessels and microvasculature, though until recently it was not clear which components of blood vessels were affected by this stiffening. An important motivator for this dissertation is recent experimental evidence that the subendothelial matrix stiffness increases locally with CVD.

In addition, it is likely that blood vessel stiffness varies, depending on tissue type and vessel size. It is known that tissue stiffness itself can vary drastically, depending on where it is in the body. For example, brain tissue is very soft, while muscle is much stiffer. It is probable that the mechanical properties of a blood vessel are influenced by the stiffness of the tissue in which it is located. Further evidence of this is that vasculature in the core of a tumor is stiffer than outside the tumor. Thus, vasculature stiffness is quite relevant; however, its effects on EC biomechanics and the immune response were unknown prior to our work.

Previous *in vitro* leukocyte transmigration assays have mostly utilized glass or

transwell inserts as the EC substrate. However, these substrates are about 10^7 times stiffer than the actual stiffness of the subendothelial matrix *in vivo* and therefore are not physiological. In addition, no *in vitro* study has systematically varied the subendothelial matrix stiffness to determine its effect on the immune response. **The overall objective of this dissertation was to use a novel *in vitro* model to quantitatively evaluate the biophysical effects of vascular stiffening on EC biomechanical properties, as well as on leukocyte migration and transmigration.**

In our novel *in vitro* model, EC monolayers were formed on extracellular matrix (ECM) protein-coated hydrogels and activated with the cytokine tumor necrosis factor-alpha (TNF-α) to induce an inflammatory response. The stiffness of the subendothelial matrix was varied in order to mimic biomechanical changes that occur physiologically in vasculature. The design of this *in vitro* model is summarized in Chapter 3. We found that three important components of the *in vitro* model – cell-cell adhesion (Chapter 4), cytokine exposure (Chapter 5), and substrate stiffness (Chapter 7) – have significant effects on EC biomechanical properties. Next, we showed that neutrophils are mechanosensitive, as their migration in the absence of ECs is biphasic with substrate stiffness and depends on an interplay between substrate stiffness and ECM protein amount (Chapter 6); these results suggest that any biomechanical changes which occur in vasculature may also affect the immune response. Indeed, we discovered that neutrophil transmigration increases with subendothelial matrix stiffness (Chapters 7 and 8), though this cannot be explained by neutrophil mechanosensing; thus, we hypothesized that the biophysical state of the endothelium is responsible for this behavior. We found that EC properties such as intercellular adhesion molecule-1 expression, stiffness, cytoskeletal

arrangement, morphology, and cell-substrate adhesion cannot account for the dependence of transmigration on EC substrate stiffness. Rather, we discovered that this effect is due to myosin light chain kinase-dependent EC contractile forces that promote intercellular gap formation. Interestingly, this behavior holds for ECs treated with TNF-α (Chapter 7) and oxidized low density lipoprotein (Chapter 8). An experimental research overview is provided in Figure 1.1. **These results indicate, for the first time, that the biophysical states of the endothelium and subendothelial matrix, which likely vary depending on size, location, and health of vasculature, are important regulators of the immune response.**

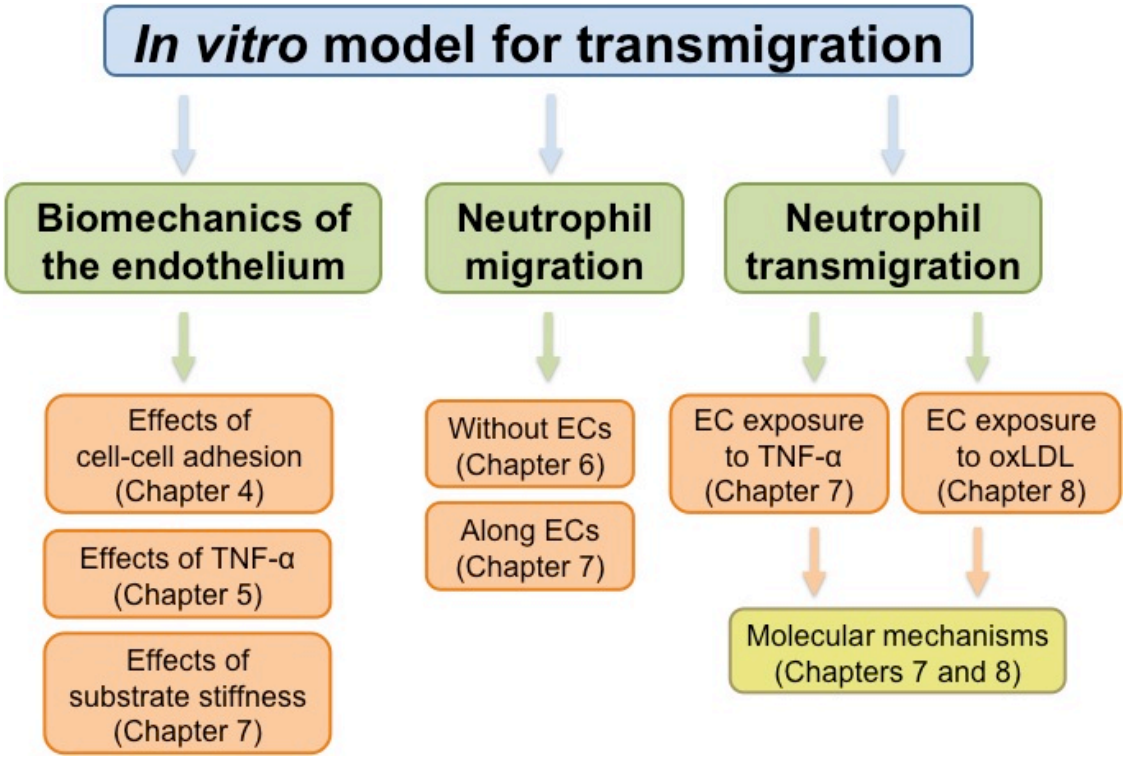

Figure 1.1. Experimental research overview. An *in vitro* model for transmigration was designed and used to determine the effects of subendothelial matrix stiffness on endothelial cell biomechanics, neutrophil migration, and neutrophil transmigration.

2 Background†

2.1 Leukocyte adhesion cascade

Polymorphonuclear neutrophils are the body's first line of defense against infection, arriving at the site of acute trauma within minutes. For these immune cells to exit the bloodstream and travel to infected tissues outside the blood vessel, they must first transmigrate through the endothelium lining the inside of the blood vessel. The sequence of events leading up to and including transmigration is referred to as the leukocyte adhesion cascade (Figure 3.1). This cascade is initiated by cytokines and inflammatory chemoattractants that are released from stromal cells as a result of the infection and induce endothelial cell (EC) signaling. This leads to upregulation of EC transmembrane glycoproteins called selectins and molecules of the immunoglobulin superfamily such as intercellular adhesion molecule-1 (ICAM-1) and vascular cell adhesion molecule-1 (VCAM-1).

In the first step of the leukocyte adhesion cascade, neutrophils (one type of leukocyte) **roll** along the endothelium, an event mediated by EC expression of selectins. Sialyl Lewis X protein (SLe^X) and P-selectin glycoprotein ligand-1 (PSGL-1) on neutrophils bind E-selectin and P-selectin, respectively, on the endothelium. Following rolling, neutrophils **firmly adhere** to the endothelium through binding of neutrophil lymphocyte function-associated antigen-1 (LFA-1) to ICAM-1 on the endothelium. Then, the neutrophil may **migrate** along the endothelium, and finally squeeze through the

---

† This chapter was adapted from Stroka, K.M. and H. Aranda-Espinoza (2010). A biophysical view of the interplay between mechanical forces and signaling in leukocyte transmigration. *FEBS Journal* 277, 1145-1158. Permission was obtained from the publisher to use this material in the current dissertation.

endothelium in a process known as **transmigration** (also called diapedesis or extravasation). This may occur via one of two methods, the paracellular route (between the EC junctions) or the transcellular route (through the middle of an EC), both which have been observed *in vivo* and *in vitro*. They may migrate for some time just below the ECs, before undergoing chemotaxis and continuing through the basement membrane, remaining layers of the blood vessel, and interstitial tissue toward the site of infection. **While there are important biophysical considerations at all stages of this process, this dissertation focuses on a quantitative understanding of transmigration.**

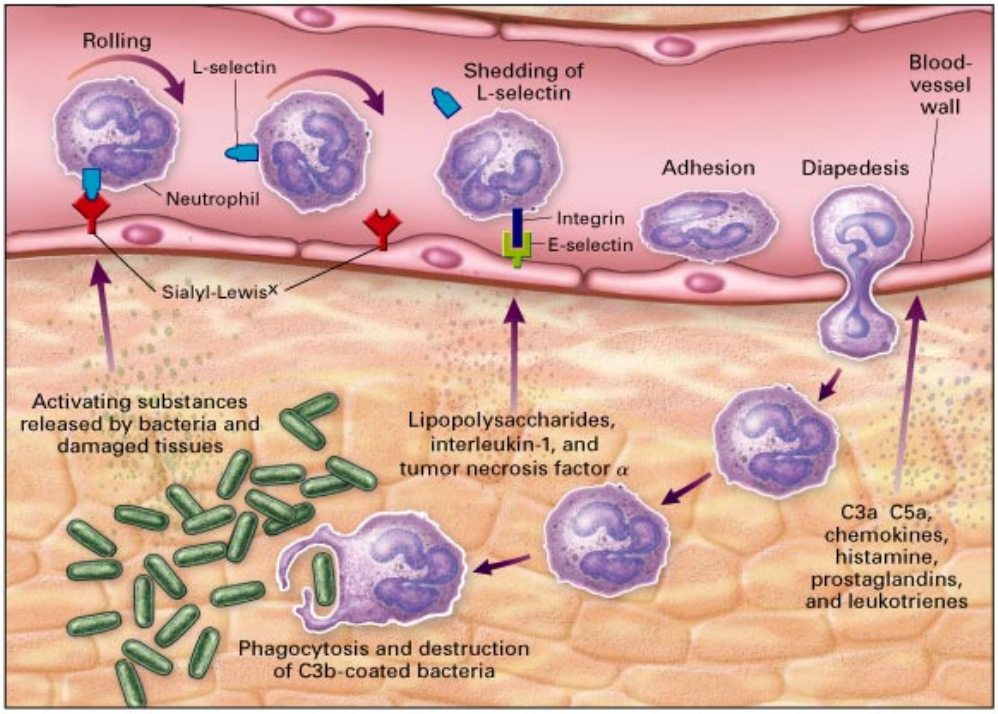

Figure 2.1. Schematic representation of the leukocyte adhesion cascade. To exit the blood stream, neutrophils (purple) roll along, firmly adhere to, migrate along, and finally transmigrate through (also called diapedesis) the endothelium. They may migrate under the endothelium for some time, or continue through the remaining layers of the blood vessel towards bacteria in a nearby tissue. Image was taken from [1].

2.2 Motivation

2.2.1 Transmigration and disease

Leukocyte transmigration plays a pivotal role both in the normal immune response and also in the development of cardiovascular disease, including atherosclerosis and stroke. Thus, inflammation is a normal response to foreign pathogens, but it may also lead to cardiovascular disease under certain conditions. For example, atherosclerosis initiates during increased levels of low-density lipoproteins that become oxidized by free radicals, come in contact with the arterial wall, and damage the endothelium. Leukocytes recruited by the immune system to the damaged vessel wall cannot process the oxidized low-density lipoproteins (oxLDL); this leads to recruitment of more leukocytes and begins a cycle that eventually leads to a pathological state (Figure 2.2). There are also numerous diseases of the immune system, such as asthma, rheumatoid arthritis, and psoriasis, which develop due to increased frequency of leukocyte transmigration. Cell transmigration is also involved in processes such as cancer cell metastasis and stem cell homing, and while the steps of cancer cell transmigration are believed to be similar to immune cells, the molecular players involved are different [2]. Further, blood/brain barrier (BBB) dysfunction is involved in pathological conditions, including multiple sclerosis and other neuroinflammatory processes or brain cancer [3, 4]. Interestingly, transmigration of immune cells across the BBB into the central nervous system is highly regulated and occurs limitedly in a process called ‘immune surveillance’ [5, 6]. However, in BBB dysfunction, there is an increase in immune cells or even cancer cells which cross the tight junctions of the BBB.

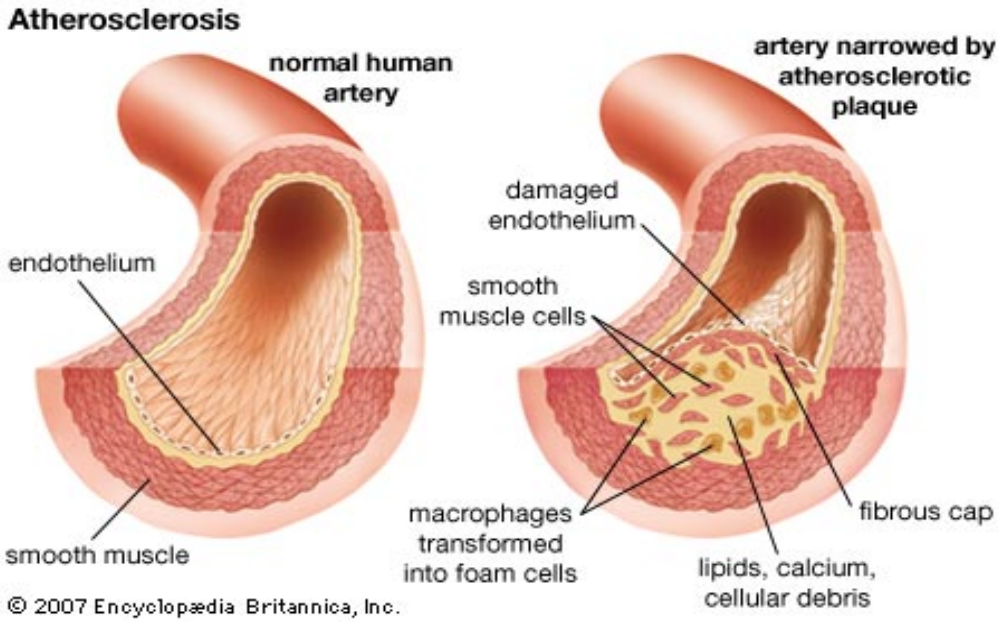

Figure 2.2. Schematic of a cross-section of an atherosclerotic artery. In the presence of increased risk factors, such as high amounts of lipids such as oxLDL, there is an increase in leukocyte transmigration and foam cell formation. A plaque forms beneath the endothelium, and this could block blood flow, leading to heart attack or stroke. Image was taken from [7].

2.2.2 Transmigration and biophysics

As leukocytes make their way through the endothelium, forces are exerted on the leukocytes, ECs, and basement membrane below the ECs. At the same time, they respond to various mechanical forces around them, including shear stress due to blood flow and effects from other neighboring cells and matrix. The biophysical aspects of the endothelium through which the leukocytes are transmigrating, in addition to the biophysical aspects of the leukocytes themselves, are linked to the biochemical pathways which govern transmigration. However, we are only beginning to understand how physical forces translate into biochemical signaling pathways during leukocyte transmigration. In this chapter we highlight work that has related the biophysical aspects of leukocyte transmigration with the biochemical pathways and molecular interactions

that take place during this process. We discuss the assortment of physical forces (including estimates of their magnitude) acting on ECs from all sides. This includes shear stress and adherent or migrating leukocytes at the luminal surface, neighboring ECs or transmigrating leukocytes at cell-cell junctions, transmigrating leukocytes through the body of the cell, and the substrate at the basal surface of the ECs. Interestingly, forces acting at one surface may be propagated internally or even to other surfaces of the cell, or they may initiate biochemical signaling cascades within the cell, leading to a cellular response. Figure 2.3 indicates the assortment of biophysical forces ECs feel and possible signaling molecules which could act as mechanotransducers in the cell.

Figure 2.3. Force transduction in ECs. Transduction of forces in ECs is a complex process involving signaling via many different molecules. This oversimplified schematic shows that at the luminal surface of ECs, forces due to leukocyte binding may be transmitted to the actin cytoskeleton via ICAM-1 receptors **(A)**, while forces due to shear stress may be transmitted via activation of stretch-activated ion channels or through displacement of the glycocalyx **(B)**. Forces due to junctional cell-cell contact, whether it is EC-EC contact or leukocyte-EC contact during transmigration, may be transmitted to the actin cytoskeleton via VE-cadherin at the cell borders **(C)**. EC mechanosensing of the underlying substrate is likely completed via integrin binding at focal adhesions, leading to stretching of talin and activation of vinculin to reinforce the focal adhesion **(D)**. The ECs respond to this interaction by forming stress fibers which contract, allowing for measurement of the traction forces on the EC substrate. Thus, an EC contains many mechanotransducing molecules on each of its surfaces that act to convert mechanical signals into biochemical signals within the cell. Many molecules which are known to be involved in mechanotransduction are also linked to the actin cytoskeleton, which is an important regulator of cell shape, alignment, and stiffness. Because ICAM-1 and VE-cadherin, two of the possible EC mechanotransducers, are also involved in leukocyte transmigration, it is likely that leukocyte transmigration affects force transmission within the ECs. In panel A the force acting on the EC (black arrow) has components both in the direction of shear stress and in the direction of pulling by leukocytes. In panel B the force on the EC is in the direction of shear stress. In panel C the force is in the direction of tension of actin filaments, maintained with the help of neighboring cells in contact. In panel D the force is in the direction of pulling at focal adhesions at the substrate. See text for more details on magnitudes of forces and specific molecules involved.

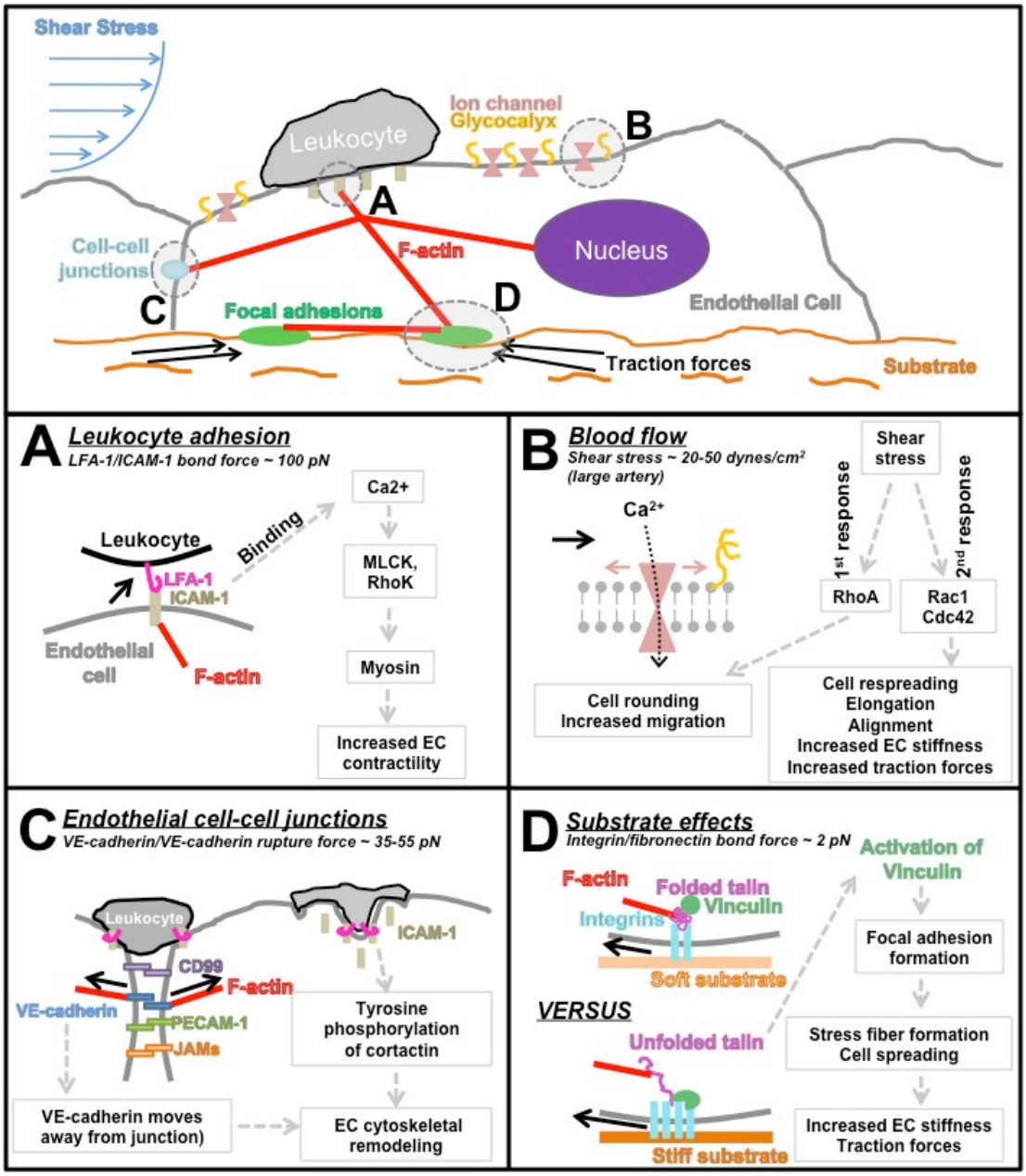

2.3 Endothelial cells respond to shear stress

A single sheet of ECs line the walls of the arteries and is responsible for transmitting shear stress due to blood flow to the underlying layers of tissue. These underlying layers include the basement membrane (composed mainly of laminin and collagen), the media (composed of smooth muscle cells, collagen, and elastin), and the adventitia (the stiffer outermost layer). Shear stress on ECs leads to mechano*transduction* (the conversion of physical forces into biochemical signals) and also mechano*transmission* (the physical propagation of forces to the underlying layers). In large arteries, mean shear stress along the wall is in the range of 20-40 dynes/cm^2 and is generally pulsatile rather than unidirectional [8]. However, most *in vitro* studies which apply shear stress to cells use values ranging from 0 to 100 dynes/cm^2, usually in unidirectional flow [8]. Shear stress affects EC cytoskeletal arrangement [9-11], cell morphology [10, 12-14], and gene expression [15-17]. While the method of EC mechanotransduction is still largely unknown, several molecular structures are believed to play a role in the mechanosensing process of converting shear stress into morphological changes and gene expression; these molecules include the glycocalyx, platelet endothelial cell adhesion molecule-1 (PECAM-1), stretch-activated ion channels, receptor Tyr kinases, vascular endothelial (VE)-cadherin, and vascular endothelial growth factor receptor (VEGFR).

ECs develop more stress fibers and less peripheral actin as larger shear stresses are applied [10]. F-actin stress fibers contract between cellular focal adhesions (FAs), adhesion structures which exert traction stresses on the underlying substrate (Figure 2.1). It has been shown that there exists a 2 pN bond between an integrin and fibronectin

molecule, and maintenance of this bond requires talin, which binds the integrin to an actin filament [18]. Stretching talin activates vinculin, a FA protein, leading to reinforcement of the FA [19] (See Figure 2.3). Therefore, a rearrangement of the F-actin cytoskeleton under shear stress would be expected also to influence FAs and cellular traction forces. Indeed, FAs realign parallel to flow [20], and shear stress increases RhoGTPase activation in single cells, leading to larger traction forces [21]. In addition, the vimentin intermediate filament permeates the actin network and has been shown to propagate shear stress [22, 23].

Bovine aortic ECs (BAECs) migrate faster under shear stress, as opposed to static conditions, and this is mediated by Rho, since inhibition of the Rho-associated kinase, p160ROCK, results in decreased traction forces and migration speed under both static and shear conditions [21]. Because cell-cell contacts are important regulators of cellular behavior, and these experiments were performed on sub-confluent cells, further work needs to explore whether shear stress affects EC monolayer migration in a similar manner. The magnitude of traction forces and stability of FAs both depend on the flexibility of the underlying substrate [24, 25], and thus in recent years researchers have placed focus on exploring the effects of substrate rigidity on cellular behavior. These effects are discussed later in Section 2.7.2 for the case of ECs.

Another study also shows involvement of small GTPases of the Rho family in EC response to shear stress [26]. RhoA, Rac, and Cdc42 are rapidly activated in response to shear stress, though the time course and effects (rounding, spreading, elongation, and alignment) of each molecule's activation differs. Within five minutes of application of shear stress, RhoA is activated, leading to cell rounding via Rho-kinase. Then, RhoA

activity returns to baseline, as Rac1 and Cdc42 reach peak activation, leading to cell re-spreading, elongation, and alignment in the direction of flow. Both Cdc42 and Rac1 are required for cell elongation, while Rho and Rac1 regulate cell alignment with the direction of flow [26].

EC morphology in the vertical plane (specifically, cell height) is carefully regulated by tension in the cytoskeleton, as indicated by recent experiments which combine cytoskeletal drug treatments with atomic force microscopy (AFM) indentation measurements [27]. Depolymerization of F-actin within subconfluent cells results in increased cellular height. Meanwhile, disruption of microtubules lowers cell height, and stabilization of microtubules elevates height [27]. Thus, the cytoskeleton is an important structure that contributes to cellular morphology, and so it makes sense that as shear stress affects the cytoskeletal arrangement, then cellular morphology is also affected. However, it is still not clear exactly what causes the cytoskeleton to rearrange under shear stress, but likely it is a combination of both mechanotransduction and mechanotransmission effects.

2.4 Mechanical properties of endothelial cells

It is believed that the mechanical state of the endothelium is extremely important in maintaining vascular homeostasis, and for that reason it is crucial to understand which factors affect EC stiffness. Table 2.1 summarizes the various treatments or conditions that affect the stiffness of the endothelium. For example, ECs stiffen under shear stress as a function of exposure time and magnitude of the shear stress [28-30]. Depleting cholesterol from untreated BAECs through methyl-β-cyclodextrin treatment increases

membrane stiffness, while enriching the cells with cholesterol does not affect the membrane stiffness [31]. Exposure to oxLDL has a similar effect in depleting cholesterol from the cell membrane, possibly through a disruption or redistribution of lipid rafts in the membrane [32]. There is evidence that treatment with oxLDL significantly increases membrane stiffness of human aortic ECs (HAECs), as measured by micropipette aspiration [32], and also of cell body stiffness of human umbilical vein ECs (HUVECs), as measured by AFM [33]. This increase in cell stiffness with oxLDL treatment is also accompanied by an increase in force generation and network formation in a three-dimensional collagen gel [32]. In addition, there is a significant increase in stiffness of aortic ECs isolated from hypercholesterolemic pigs, where oxLDL levels are higher in the blood plasma, as compared to cells isolated from healthy pigs [32]. These results suggest that risk factors for atherosclerosis and stroke, such as high cholesterol, lead not only to biological malfunction, but are perhaps accompanied by biophysical changes in the endothelium.

In addition to shear stress, cholesterol, and oxLDL, ECs are also exposed to varying levels of sodium in the bloodstream; this is another factor that regulates vascular tone. ECs significantly stiffen in a high sodium environment in the presence of aldosterone, which is a hormone that increases the reabsorption of sodium and is physiologically present in the bloodstream. Increases in cell stiffness range from about 10% to 50%, depending on extracellular sodium concentration (range of 135-160 mM) [34]. In addition, nitric oxide production is downregulated by aldosterone-exposed cells in a high sodium medium [34]. Meanwhile, increases in potassium soften ECs and boost nitric oxide production, though this effect is abrogated in the presence of high sodium

[35]. Thus, hyperpolarization or depolarization of the cell leads to changes in cell stiffness. Another recent study simultaneously measured the mechanical stiffness and electrical membrane potential of a vascular cell line derived from BAECs and correlated slow cell depolarizations with increases in cell membrane stiffness [36].

The inflammatory response also contributes to EC stiffness. For example, exposure of ECs to the cytokine tumor necrosis factor-α (TNF-α) leads to cell softening [37]. This effect is further explored in this dissertation (Chapters 5 and 7). Interestingly, neutrophil adherence to ECs also increases EC stiffness as measured by magnetic twisting cytometry [38, 39]. Meanwhile, monocyte adherence to ECs decreases EC stiffness, as measured by AFM, and at the same time also reduces the adhesiveness of ECs to the substrate, indicated by a decrease in electric cell-substrate impedance [40]. This suggests that leukocyte interactions with the endothelium affect mechanotransmission events, and that these effects are cell type-dependent.

Treatment	Effect on EC stiffness	Reference
Shear stress	increase	28, 29, 30
Cholesterol depletion	increase	31
Cholesterol enrichment	no change	31
oxidized LDL	increase	32, 33
Sodium	increase	34
Potassium	decrease	35
TNF-α	decrease	37
Neutrophil adhesion	increase	38, 39
Monocyte adhesion	decrease	40

Table 2.1. Effects of various physiological treatments or conditions on the mechanical properties (stiffness) of the endothelium.

The effects that leukocytes have on the endothelium indicate that stiffness may vary locally. Indeed, it has been shown that ECs have a heterogeneous mechanical surface. For example, AFM experiments have revealed that the Young's modulus of HUVECs ranges from 1.4 kPa near the edge of the cell to 6.8 kPa over the nucleus of the cell [41], while in bovine pulmonary aortic ECs (BPAECs) the Young's modulus ranges from 0.2 to 2 kPa [42]. In contrast, Sato *et al*. have found that BAECs are stiffer near the edge of the cell than at the nucleus, as measured by AFM [28]. The discrepancies of stiffness versus cell location in these studies may be due to differences in loading forces and indentation depths used when probing with the AFM cantilever [41], since cellular structures such as the cytoskeleton and nucleus are positioned at different heights within the cell. Using AFM, Engler *et al.* probed the smooth muscle cell-containing media layer of sectioned carotid arteries from six-month-old pigs and measured the Young's modulus to be in the range 5-8 kPa [43], which is of similar value to the single cultured cells discussed above. Therefore, it is obvious that the mechanical properties of ECs are very heterogeneous and location-dependent under normal conditions; but they are also influenced by biophysical factors such as shear stress, cholesterol distribution within the plasma membrane, exposure to increased sodium, cytokine exposure, and EC-leukocyte adhesion, all of which have been shown to be relevant in the onset and progression of disease. Further, in Section 3.1, we review the relationship between CVD and subendothelial matrix stiffening; this dissertation shows that subendothelial matrix stiffening also affects the mechanical properties of the vascular endothelium.

It is also possible to use AFM, in combination with total internal reflection fluorescence microscopy (TIRFM), to study the mechanotransmission of applied local

forces at the apical surface of an adherent cell to the basal surface of the cell. Using this technique, Mathur *et al*. observed that exerting a local force of 0.3-0.5 nN by an AFM probe over the nucleus of a HUVEC results in a global rearrangement of focal contacts at the substrate after the force is removed, including a significant increase in FA area [44]. Applying the same force over the edge of the cell does not result in any significant changes in FA contact area after the force is removed, suggesting that the nucleus is an important link in force transmission between the cytoskeleton and FAs [44]. Further, application of local force via an AFM probe also leads to mechanotransduction, as evidenced by increased intracellular calcium through activation of stretch-activated ion channels [45].

2.5 Endothelial cell-cell contacts as mechanosensors

Much biophysical characterization of cells has been done using single cells, where cell-substrate interactions are most important. However, in the case of the endothelium, the cells are packed in at high density, forming a monolayer where cell-cell interactions are as important, if not more important, than cell-substrate interactions. As discussed above, EC monolayers undergo global remodeling in response to mechanical stimuli such as shear stress; recent evidence also suggests that EC monolayers respond to local mechanical forces [46]. When a glass needle is used to apply local stretch to selective ECs and EC junctions, the ECs respond by aligning and elongating parallel to the direction of stretch, and this effect is accompanied by a reorganization of stress fibers. At the selective junctions where stretch is applied, Src homology-2-containing tyrosine

phosphatase-2 is recruited [46], and this molecule is known to bind to PECAM-1 [47]. These results suggest that cell-cell junctions both sense and transmit local forces.

Cell-cell contact has been shown to both inhibit and stimulate cell proliferation, in different experimental studies using different methods to regulate cell-cell contact. For example, a recent study by Gray *et al*. [48] has demonstrated that EC proliferation is biphasic with degree of cell-cell contact. In this study, cell-cell contact is controlled by cell micropatterning, so that a distinct number of cells can adhere in specific configurations. Cells with no neighbors and cells with more than three neighbors proliferate faster than cells with two or three neighbors. This relationship is mediated by RhoA, since expression of dominant-negative RhoA blocks the increase in proliferation. Higher proliferation can be simulated in single cells with no neighbors through contact with a VE-cadherin bead [48]. These results point to VE-cadherin as an important junctional signaling molecule capable of transmitting forces through cell-cell contacts (Figure 2.1). In this dissertation, Chapter 4 shows that cell-cell adhesion plays an important role in determining cellular mechanical properties in the endothelium.

2.6 Activation of the inflammatory response

Whether *in vivo* or *in vitro*, the immune response requires activation of the endothelium in order to allow leukocytes to adhere to and transmigrate through the EC barrier. Several known cytokines are known to induce the inflammatory response, including TNF-α and interleukin-1 (IL-1). The pathways activated by these cytokines result in drastic changes such as upregulation of adhesion molecule expression as well as junctional molecule reorganization, both which promote leukocyte transmigration.

TNF-α is produced mainly by innate immune cells, such as macrophages, as a response to infection or inflammation in the body. As a TNF-α molecule binds to the TNF receptor-1 on the extracellular side of the endothelial cell, the cytosolic tails of the receptors rearrange. A number of intracellular signaling proteins are recruited, resulting in the possible activation of three different pathways. These include NF-κB activation, a mitogen-activated protein kinase cascade, and proteolysis leading to apoptosis. Activation of the NF-κB pathway leads to recruitment and activation of IκB kinase kinase (IKKK); the phosphorylation and activation of IκB kinase (IKK) by IKKK; the phosphorylation of IκB; and the degradation of IκB, which releases the NF-κB. NF-κB then localizes to the nucleus, where it initiates transcription of many genes which contribute to the inflammatory response [49].

Following TNF-α stimulation, expression of both ICAM-1 and VCAM-1 are upregulated, while PECAM-1 (also known as CD31) expression is decreased in cultured HUVECs [50]. ICAM-1 and VCAM-1 are needed for leukocyte firm adhesion and transmigration through the ECs. In addition, activation of the NF-κB pathway results in a reorganization of EC F-actin cytoskeleton and junctional molecules, such as VE-cadherin [51, 52], as well as changes in cell shape [53] and a decrease in cell stiffness [37]. In particular, ECs activated by TNF-α become more elongated and arrange into whorls [53], while actin filaments thicken, leading to actomyosin-mediated cell retraction and intercellular gap formation [52]. Thus, even before leukocytes enter the picture, the ECs have undergone significant changes in response to activation of the inflammatory response. Although the response is controlled by signaling pathways, some of the pathways are inside-out signals that might occur through regulation of the interaction of

the cell with the extracellular matrix and through the response to shear stress. Thus, it is important to recognize the influence of these mechanical forces, not only as possible sources of outside-in signaling, but also as a form of feedback for the reorganization of the endothelium. In this dissertation, TNF-α is used to induce an inflammatory response in ECs, and therefore Chapters 5 and 7 explore how TNF-α regulates EC shape, cytoskeletal arrangement, mechanical properties, and migration.

2.7 Mechanosensitivity

2.7.1 Mechanical properties of the cellular microenvironment

In recent years, much attention has focused on the effects of substrate stiffness on cell adhesion and migration. Many cell types, including ECs [54-57], smooth muscle cells [58-60], fibroblasts [25, 56, 61], neurons [62, 63], stem cells [64], and macrophages [65] display behavior which changes as a function of underlying stiffness *in vitro*. While these cells are able to sense substrate stiffness, the mechanical properties of the cells also depend on many factors. These *in vitro* studies are quite relevant, because it is known that pathological conditions such as cancer and atherosclerosis are associated with changes in tissue and cell stiffness [66-68]. Effects of tissue stiffness are also important in the field of tissue engineering, where constructs are made to replace damaged or diseased tissues in the body. Obviously, these biological substitutes are most effective if they mimic the actual *in vivo* biochemical and mechanical conditions, but most experiments in the past have been done on glass, a very stiff substrate. Recently, however, polydimethylsiloxane with fibronectin micropatterning in FA-sized circular islands has been recognized as a substrate capable of achieving rapid EC confluence, cell densities similar to those *in vivo*,

and FA formation [69]. Furthermore, rigidity sensing is likely accomplished through integrin interactions with the extracellular matrix. It has been shown that substrate stiffness directs the mechanical activation of the $\alpha_5\beta_1$ integrin binding to fibronectin through myosin-II generated cytoskeletal force, leading to internal signaling via phosphorylation of focal adhesion kinase [70]. Unknown, however, is how the leukocyte adhesion cascade acts in response to any engineered endothelium.

Because there exists a complex interplay between the biochemical and mechanical conditions in the body, an understanding first must be made of how these conditions individually affect cells, and then how they act in concert. In the following sections we will review what is known about the effects of environmental stiffness on vascular ECs, as well as on immune cells. Substrate stiffness of ECs is relevant because changes of stiffness of basement membrane or underlying layers ("subendothelial matrix") may affect EC structure, organization, and gene expression. In addition, it may affect EC stiffness, and because immune cells migrate on and through ECs, it is important also to understand how immune cells respond to changes in substrate stiffness. In this dissertation, manipulation of the subendothelial matrix stiffness is a key component of our *in vitro* model, and we use it to understand how vasculature stiffening during CVD affects both the endothelium and the immune response.

2.7.2 Vascular ECs respond to substrate stiffness

Effects of environmental mechanical properties on EC behavior have been studied in both two dimensions (2D) and three dimensions (3D). Most of the previous work on 2D substrates has focused on individual cells or cells in networks. Meanwhile, this

dissertation mostly focuses on monolayers of ECs. Single BAECs show increased spreading areas and spreading rates on stiffer polyacrylamide gels in the range of Young's modulus 6 Pa to 165,000 Pa [56], while BAEC network assembly (before monolayer formation) depends on a balance between substrate compliance and extracellular matrix density [54]. In general, HUVEC morphology switches from a tube-like network to a monolayer with increasing substrate stiffness, both on polyacrylamide gels and on Matrigel [71]. It is also well-established that cellular cytoskeletal organization depends on the stiffness of the underlying substrate and controls the shape of the cell. For example, severing multiple F-actin stress fibers in bovine capillary ECs (BCECs) on stiff surfaces (glass) using a laser nanoscissor results in very little change in cellular shape. However, severing only one stress fiber in BCECs on compliant substrates (Young's modulus ~3,750 Pa) results in cytoskeletal remodeling, and, consequently, dramatic changes in cellular shape [72]. Further, HUVECs on soft Matrigel surfaces contain less actin and vinculin in comparison with the same cells on rigid Matrigel substrates [71].

Because the F-actin network contributes to the maintenance of prestress in the cell by regulating cellular tension, it would also be expected that the stiffness of the ECs depends on substrate stiffness. Indeed, single BAECs are two-fold more compliant on polyacrylamide gels of Young's modulus 1,700 Pa as compared with BAECs on 9,000 Pa substrates [73]. These results are consistent with the discovery that fibroblasts mimic the stiffness of their substrate, up to a threshold value, and that this response is dependent upon the organization of the F-actin cytoskeleton, where cells on stiff surfaces exerting larger traction forces have a more stretched and organized actin cytoskeleton than on a

softer surface [74, 75]. Recent work has also suggested that BAECs can communicate with each other through the compliance of their substrate [57]. Pairs of cells migrate less than single cells on polyacrylamide gels below 5,500 Pa, indicating that the traction forces exerted by one cell can be felt by another cell, resulting in altered behavior [57]. This behavior of ECs may be altered in a nonlinear strain-stiffening fibrin gel system, where recent studies have shown that fibroblasts and human mesenchymal stem cells are influenced by each other even when hundreds of microns away from each other [76].

ECs may also be capable of sensing the mechanical properties of their environment in 3D culture, as suggested by experiments utilizing collagen gels. This work is very promising for steps towards understanding the processes of vasculogenesis (formation of new blood vessels) and angiogenesis (formation of vascular trees), especially since one of the current hurdles in the field of tissue engineering is creating vascularized tissues. HUVECs spread more, have larger lumens, and exhibit less branching when suspended in stiffer collagen gels [55]. Similarly, bovine pulmonary microvascular ECs (BPMECs) cultured in flexible collagen gels form dense, thin networks and have small, intracellular vacuoles with few actin filaments localized along the cell membrane. Meanwhile, BPMECs in rigid collagen gels form thicker and deeper networks surrounded by intense actin filaments and with large lumens [77]. However, one must be careful in interpreting experimental results involving cells on or in collagen gels, since the strain exerted by cells on the collagen gel can modify the collagen fibers at the microscopic level [78], and cells can enzymatically cut collagen fibers. Vinculin expression is very low in BPMECs in soft gels, while large clumps of vinculin are seen in protruding regions at the tips of the branching networks in rigid gels [77]. Because EC

morphology, stiffness, organization, and gene expression are all regulated by substrate stiffness, manipulation of substrate mechanics is a possible mechanism to direct cell migration and wound repair. In this dissertation, subendothelial matrix stiffness is shown to influence neutrophil transmigration through EC monolayers via myosin light chain kinase-dependent EC contraction, in response to both TNF-α (Chapter 7) and oxLDL (Chapter 8).

2.7.3 Leukocytes respond to substrate stiffness

Interestingly, recent studies have shown that immune cell behavior also depends on substrate stiffness, though the rigidity-sensing mechanism is likely very different from endothelial cells, fibroblasts, and other tissue cells. Immune cells are highly motile cells which must move across and through ECs at high speeds in order to carry out normal physiological function. Our work (Chapter 6; published as [79]) was the first paper to show that neutrophils are sensitive to substrate stiffness. Since then, two other groups have confirmed these findings [80, 81]. Both neutrophils [79, 81] and alveolar macrophages [65] display increased spreading, from rounded to flattened morphology, with increasing substrate stiffness, though this spreading occurs without generation of F-actin stress fibers [65] or formation of FAs, which is a remarkable difference from tissue cells.

It has also been shown that neutrophil force generation during transmigration is dependent on substrate rigidity, with larger forces being exerted on micropillars with larger spring constants (39±6 nN versus 14±4 nN) [82]. Prior to our work (Chapter 7; published as [83]), this was the only study that took into account the flexibility of the EC

substrate while analyzing neutrophil transmigration. However, the use of the micropillar system for this application is questionable, since the micropillars force ECs to adhere only in specific locations, leading to possible differences in traction force exertion. Finally, alveolar macrophage stiffness is lower on softer substrates than on stiffer ones, though cytochalasin D treatment has negligible effects, suggesting that, unlike many tissue cells, alveolar macrophage stiffness is not regulated through tension of the F-actin cytoskeletal network [65].

2.8 Mechanotransduction during leukocyte transmigration

Transmigration is often considered the least-studied step of the leukocyte adhesion cascade. Some work has been completed on the role of adhesion molecules such as ICAM-1 [84-86], VCAM-1, PECAM-1 [87-89], and CD99 [90, 91] on leukocyte transmigration. However, while some of the important proteins are identified, there is still a lack of understanding of the overall process, especially its mechanics and how forces are propagated as leukocytes penetrate through the ECs. Rabodzey *et al.* [82] identified that the forces which ECs exert on a microfabricated pillar surface during transmigration increase when the rigidity of the pillars is increased, providing evidence that transmigration is a mechanosensitive process; further, ECs exert three times greater forces during leukocyte transmigration, in comparison with the case where leukocytes adhere but do not transmigrate [82]. Similar results were obtained for monocytes transmigrating through ECs using a micropillar system [92]. However, because the micropillar system likely affects EC adhesion and traction forces by constraining the ECs

to specific FA sites, much more work is needed to investigate exactly how leukocyte transmigration affects force propagation in ECs.

2.9 Mechanisms of transmigration

2.9.1 Paracellular transmigration

One method by which cells transmigrate through ECs is in a paracellular fashion, or by squeezing through the endothelial cell-cell junctions. Several junctional adhesion receptors of ECs are known to participate in leukocyte transmigration; these molecules include junction adhesion molecules (JAMs), PECAM-1, VE-cadherin, and endothelial cell-selective adhesion molecule. Non-junctional adhesion receptors involved in transmigration include ICAM-1, ICAM-2, and CD99. For a more complete understanding of these molecules see a review by Vestweber [93]. VE-cadherin is largely responsible for maintaining endothelial cell-cell contact in monolayers. Individual VE-cadherin to VE-cadherin bonds have been found to have an unbinding force of 35-55 pN, as measured by single molecule AFM [94]. VE-cadherin forms a molecular complex with alpha-, beta-, gamma-, and p120-catenins (p120). VE-cadherin is also known to link to the actin cytoskeleton of ECs, though the mechanism of this linkage has been under much debate [95]. This controversy has spurred since the discovery that alpha-catenin cannot bind simultaneously to beta-catenin and actin [96]. A recent study has suggested that epithelial protein lost in neoplasm (EPLIN; also known as Lima-1) links actin and alpha-catenin, and then alpha-catenin is simultaneously linked to beta-catenin and cadherin [97]. However, while this is true for epithelial cells, it is unknown whether a similar protein links VE-cadherin to actin in ECs. Somehow, though, VE-cadherin associates

with the actin cytoskeleton in ECs, maintaining tension within the cells via cell-cell contact.

Due to VE-cadherin's role in cell-cell contact, it obviously provides a physical barrier to leukocyte penetration at the junction. Thus, VE-cadherin rearranges away from the cell borders to form short-lived gaps in the junctions during leukocyte transmigration [98]. These gaps are necessary for transmigration to occur [99] and are induced by ICAM-1/LFA-1 interaction [100]. Because VE-cadherin associates with the F-actin cytoskeleton, a rearrangement of VE-cadherin during leukocyte transmigration would also be expected to affect the F-actin arrangement within the ECs, leading to changes in cellular prestress (Figure 2.3). The expression of VE-cadherin is mediated by p120, suggesting that p120 is an important intracellular mediator of VE-cadherin gap formation [99].

Also maintaining endothelial cell-cell junctions are homophilic interactions of JAM-A, and thus these molecules also create a physical barrier for leukocytes. Recently it has been shown that LFA-1 (on leukocytes) binding to JAM-A (at EC junctions) destabilizes JAM-A homophilic interactions [101]. AFM measurements indicate that interaction of JAM-A with LFA-1 is stronger than JAM-A hemophilic interactions; the unbinding force of JAM-A to JAM-A interactions increases from about 40 to 300 pN with increasing loading rate, while the unbinding force of JAM-A to LFA-1 increases from about 150 to 450 pN with similar range of loading rate [101]. Dufour *et al*. have also recently shown that CD99 is necessary for leukocyte transmigration *in vivo* [90] and *in vitro [91]*. Blocking CD99 on both leukocytes and on ECs inhibits transmigration,

suggesting that it is a homophilic interaction of CD99 which mediates transmigration [90].

2.9.2 Transcellular transmigration

In addition to leukocytes crossing through endothelial cell-cell junctions, they also may take a transcellular route through the body of the cell. See Carman and Springer [102] for a review on transcellular migration of cells. While both transmigration paths are available to leukocytes, it remains to be determined which is most energetically favorable.

It is believed that leukocyte transmigration via the transcellular route is initiated with the formation of a cup-like "docking structure" in which the adhesion proteins ICAM-1 and VCAM-1 localize in response to a leukocyte present on the EC surface. This docking structure, which may be 8-12 μm wide and 1 μm deep [103], forms as endothelial pseudopods embrace the leukocyte, engaging ICAM-1 on the EC surface with lymphocyte function-associated antigen-1 (LFA-1) on the leukocyte surface [104], leading to activation of RhoG downstream [105]. The interaction force between ICAM-1 and LFA-1 has been measured as 100 pN, with a 50 ms contact duration [106]. One study has shown that ICAM-1 and VCAM-1 are recruited independent of ligand engagement, actin cytoskeleton engagement, and heterodimer formation; instead, they are included within specialized preformed tetraspanin-enriched microdomains [107]. On the other hand, there is also evidence that ICAM-1 engagement upon leukocyte adhesion leads to EC cytoskeletal remodeling due to tyrosine phosphorylation of cortactin, linking ICAM-1 to the actin cytoskeleton and allowing ICAM-1 to form clusters which facilitates

transmigration [108] (Figure 2.1). Transmission electron microscopy images show that lymphocytes concurrently send protrusive podosomes into the ECs, and this occurs both *in vivo* and *in vitro*, possibly to probe the EC surface in order to find regions of low resistance [109]. Thus, initiation of leukocyte transmigration via the transcellular route involves active involvement from both the ECs and the leukocytes, but the molecular mechanisms are still not well understood.

2.10 Transmigration during atherogenesis: Role of oxLDL

The dynamics of leukocyte transmigration in atherogenesis should also be considered. That is, what is the mechanism for increased leukocyte extravasation through the endothelium, leading to formation of raised plaques under the endothelium during CVD? Treatments of HUVECs with oxLDL *in vitro* have recently been shown to promote monocyte invasion of the endothelium, presumably because oxLDL upregulates PECAM-1, leading to enhanced hemophilic interactions with monocyte PECAM-1, and downregulates VE-cadherin, leading to disrupted junctions and therefore increased endothelial permeability [110]. Monocyte adhesion to the apical surface of ECs and monocyte complete transmigration below the endothelium are not affected by oxLDL treatment [110], suggesting that initiation of transmigration is the critical step at which oxLDL level is important. In Chapter 8 of this dissertation, we show oxLDL also promotes neutrophil transmigration, an event which is relevant in microvasculature, through enhanced EC ICAM-1 expression and contractility.

2.11 Cytoskeletal involvement during transmigration

Leukocyte transmigration is facilitated by increased EC permeability. This can be accomplished through activation of the NF-κB pathway via stimulation with TNF-α, as discussed above. In addition, EC permeability can also be increased by treatments such as histamine, thrombin, vascular endothelial growth factor-A, or hydrogen peroxide. These agents are believed to increase tyrosine phosphorylation in the cadherin-catenin complex [93]. Recent work suggests that the spatial organization of the cytoskeleton, specifically F-actin, controls the permeability of ECs *in vitro* [111]. For example, treating ECs with junction-disrupting agents induces stress fiber formation, while treating ECs with junction-tightening agents (such as oxidized 1-palmitoyl-2-arachidonoyl-*sn*-glycero-3-phosphocholine, hepatocyte growth factor, and iloprost) enhances the peripheral actin cytoskeleton [111]. These treatments will also facilitate or hinder leukocyte transmigration, respectively, and therefore the spatial organization of the F-actin network as a physical barrier is a crucial regulator of leukocyte trafficking.

When neutrophils are removed from the endothelium during transmigration using AFM, they leave behind footprints 8-12 μm wide and 1 μm deep [103]. This work claims that these footprints are formed without net depolymerization of F-actin, since ECs do not soften at the site of adhesion [103]. However, other work has shown that both neutrophils and ECs stiffen during neutrophil-EC adhesion, and this process is cytoskeleton-dependent [38, 39]. Depolymerization of actin has also been recently observed during transmigration [112]. Obviously, the role of the EC cytoskeleton in leukocyte transmigration is still not understood, and further experiments are necessary to determine how it may transmit forces during leukocyte transmigration. In this dissertation, Section

10.1 provides an introduction to methods that can be used to more fully understand the role of the EC cytoskeleton during transmigration.

2.12 Conclusions

The mechanical state of the endothelium is influenced by many external factors, both chemical and mechanical. Because the mechanical state of the endothelium is likely an important regulator of vascular homeostasis and leukocyte transmigration, many biophysical tools, such as AFM, magnetic tweezers, traction force microscopy, and immunofluorescence are very relevant and useful. Leukocyte transmigration through endothelial cells is a complex process that is involved both in the healthy immune response and also in the development of disease. It is evident that the process involves a transmission of physical forces as the leukocytes pass through the endothelium. The propagation of these forces through ECs is likely affected by interactions with neighboring ECs, interactions with the basement membrane beneath the ECs, and shear stress. How these forces, individually or together, translate into biochemical signaling pathways is only beginning to be understood. In the future, it will become increasingly necessary to develop similar biophysical tools as those currently used *in vitro* in this dissertation, for more *in vivo* experiments, so that we can understand how force transmission in an actual blood vessel differs or is similar to that in an engineered endothelium. A prerequisite step, however, is developing a more complete understanding of how blood vessel biomechanics affects the immune response using closer-to-physiological *in vitro* models, as in this dissertation.

3 Overview of the *in vitro* Model for Transmigration

The purpose of this chapter is to provide a general overview of the *in vitro* model for transmigration that has been designed in this dissertation. Each component of the model is introduced and rationalized. Meanwhile, the experimental details of the model will be discussed in the Materials and Methods sections of the relevant chapters.

3.1 Physiological stiffness of polyacrylamide hydrogel substrates

Thin polyacrylamide gels are currently used extensively in *in vitro* experiments to evaluate the effects of substrate stiffness on cellular behaviors such as morphology, cytoskeletal arrangement, migration, and differentiation. Major advantages to utilizing these gels include the ability to (1) tailor the stiffness easily by changing the concentration of the cross-linker, (2) create gels in the kilopascal range of stiffness, which is physiologically relevant to the cardiovascular system, (3) control the stiffness of the gels independent of the extracellular matrix protein amount, and (4) use microscopy to visualize cells through the gels due to their optical transparence.

An important consideration is the range of gel stiffness to be used in the *in vitro* model. In this work we varied the stiffness of the EC substrate from 0.42 to 280 kPa in order to mimic changes which occur during cardiovascular disease [113] or cancer [114], and possibly throughout the body depending on tissue location. Clinically, pulse wave velocity measurements have been used to determine that diseased arteries are consistently stiffer in patients with atherosclerosis or hypertension versus healthy patients [115, 116]. Further, *in vivo* AFM measurements of aortic vessels in living rats show a significant increase in blood vessel stiffness with vasodilation, and softening with vasoconstriction

[117]. It is believed that the microcirculation also undergoes stiffening during hypertension, as pulse wave velocity waves reflect deep into microvasculature [118]. Thus, it is clear that cardiovascular disease leads to blood vessel stiffening, though further work has been necessary to demonstrate that the subendothelial matrix specifically varies in stiffness with disease.

AFM has been used to quantify *ex vivo* blood vessel mechanical properties. For example, physiological porcine aorta stiffness is 5-8 kPa [43]. Further, the arteries of ApoE-null mice, a model of atherosclerosis, are stiffer than wild-type mice; healthy arteries measure 5kPa, while ApoE knockout vessels measure 28 kPa [119]. These measurements were made after the endothelium was scraped away and thus represent the stiffness of the EC substrate in an actual artery. Interestingly, the subendothelial and endothelial layers of bovine carotid arteries are similar in stiffness, around 2.5 kPa [120]. In another study, injury to the femoral artery increased vessel stiffness from 3 kPa to 10 kPa, indicating that injury can also affect stiffness of the vasculature [121]. In our model, stiffnesses in the range 3-5 kPa represent the healthy physiological stiffness of the subendothelial matrix, while stiffnesses in the range 13-280 kPa represent diseased conditions (Figure 3.1).

It is also possible that the stiffness of blood vessels, specifically the microvasculature where neutrophils most often transmigrate, depends on the mechanical properties of the surrounding tissue. For example, the stiffness of brain (0.3-0.5 kPa) is much less than that of collagenous bone (~100 kPa) [64, 122]. Further, vasculature within the core of a tumor is stiffer than surrounding vasculature [114]. Thus, "healthy stiffness" likely depends on location within the body, as well as size of vessel, and our substrates

span a large range of physiological stiffnesses, from 0.42 kPa to 280 kPa. Our lower range of subendothelial matrix stiffness (0.42-0.87 kPa; Figure 3.1) could be relevant in brain microvasculature where the blood vessel microenvironment is very soft (0.3-0.5 kPa as discussed above) or in development of future cardiovascular disease-targeting drugs which return elasticity to blood vessels; it would be important to understand how these potential drugs affect EC biomechanics and the immune response.

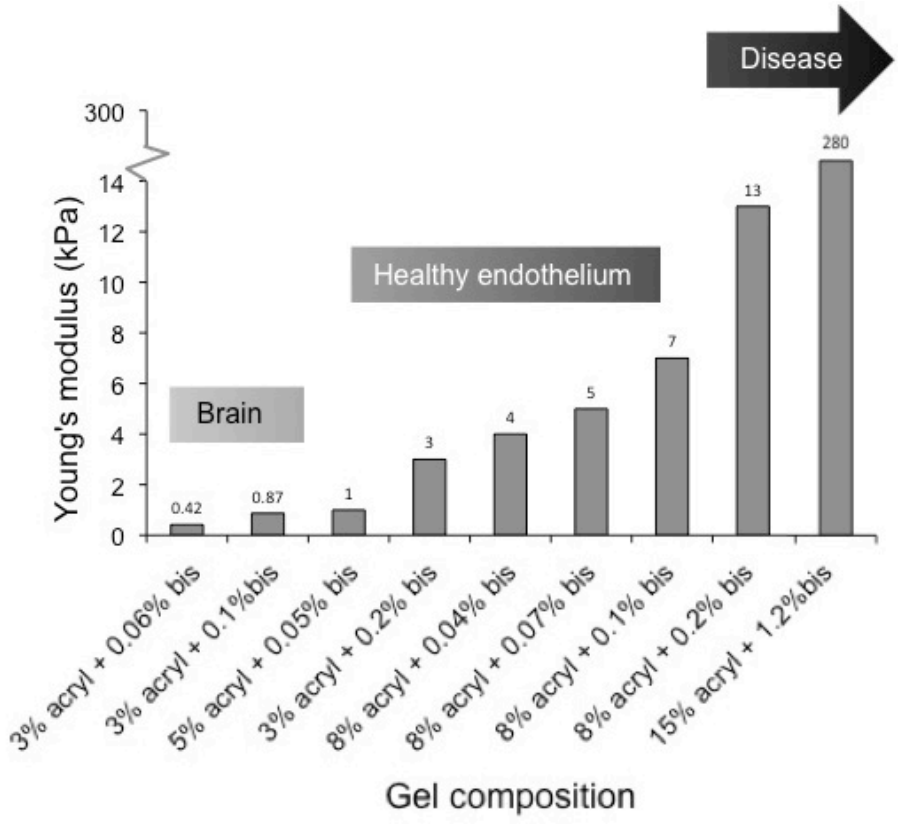

Figure 3.1. Summary of polyacrylamide gel compositions used for leukocyte migration and transmigration assays. Compositions are shown on the x-axis in percentage acrylamide (acryl) and bix acrylamide (bis). The Young's modulus of each gel was measured using either dynamic mechanical analysis or atomic force microscopy. Bars indicate the averages of at least 3 different samples; the average value is shown at the top of each bar. Also shown is the physiological relevance of each stiffness range.

3.2 Extracellular matrix protein coating

Without extracellular matrix (ECM) protein, the polyacrylamide gels are not suitable for long-term cell attachment. Therefore, the gels were coated with the ECM protein fibronectin using a photactivation procedure to covalently bind the fibronectin to the gels. Cellular integrins interact with the RGD binding site on fibronectin, resulting in strong cellular attachment on all stiffnesses. The amount of surface-bound fibronectin on the gels is independent of gel stiffness, as we and others have characterized. ECs also polymerize their own fibronectin matrix during growth, which likely enhances their ability to bind to the gel.

3.3 Endothelial cells

For transmigration experiments, human umbilical vein ECs (HUVECs; a model of large vessels) and human brain microvascular ECs (HBMECs; a model of microvasculature) were purchased and used to model the vascular endothelium. HUVECs or HBMECs were plated onto fibronectin-coated polyacrylamide gels, attached within an hour, and subsequently formed a monolayer within 2 days (Figure 3.2, top). When plated at low density (less than $2x10^5$ cells per 22x22mm substrate), ECs formed monolayers faster on stiffer substrates. When plated at high density ($4x10^5$ cells), however, all substrates supported monolayer formation with similar cell densities within 2 days. After complete monolayers formed, the endothelium was treated for 24 hours with the cytokine TNF-α (Chapter 7) or with oxLDL (Chapter 8) to induce an inflammatory response (Figure 3.2, bottom). In both cases, ICAM-1 expression was significantly increased after these treatments, allowing for leukocyte adhesion, migration, and transmigration.

Subsequent chapters will characterize the effects of cell-cell adhesion (Chapter 4), TNF-α (Chapters 5 and 7) or oxLDL (Chapter 8) treatment, and substrate stiffness (Chapters 7 and 8) on the morphological, cytoskeletal, and biomechanical properties of the ECs.

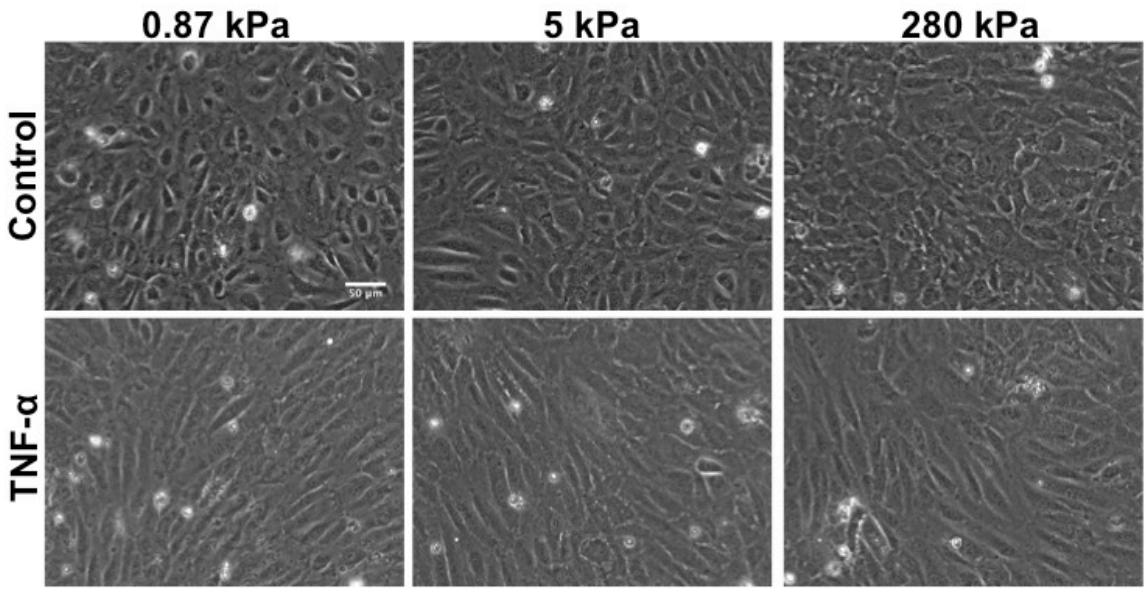

Figure 3.2. Phase contrast microscopy images of control and TNF-α-activated human umbilical vein endothelial cells (HUVECs) on fibronectin-coated polyacrylamide gels of varying stiffness. Stiffnesses are indicated at the top of each column of images. Scale bar for 0.87 kPa control is 50 μm and applies to all images.

3.4 Leukocytes

Polymorphonuclear neutrophils are the final component of the *in vitro* model. These white blood cells are the body's first line of defense against an infection and primarily transmigrate in the microvasculature, which, as described above, has also been shown to stiffen in CVD. Shear stresses in the microvasculature are significantly lower than those in larger vessels, and thus this work approximates physiological conditions by focusing on static conditions. Neutrophils were freshly isolated from human blood and subsequently plated on the TNF-α- or oxLDL-treated endothelium. Lymphocyte function-associated antigen-1 (LFA-1) on the surface of the neutrophils binds to ICAM-1 (increased expression due to TNF-α or oxLDL) on the surface of ECs, which allows for firm neutrophil adhesion to, migration along, and transmigration through the endothelium. Figure 3.3 displays a schematic of the *in vitro* assay for transmigration used in Chapters 7 and 8 of this dissertation.

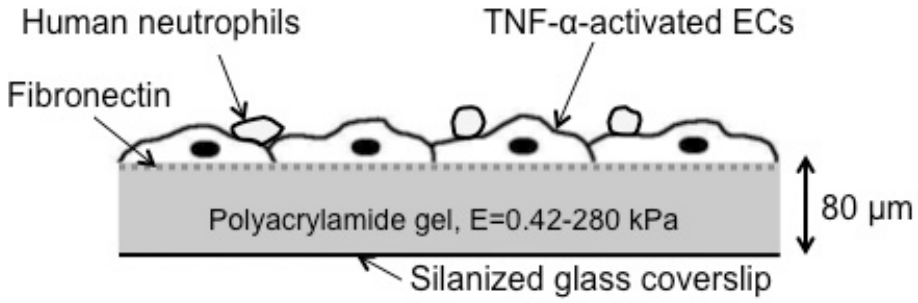

Figure 3.3. Schematic that summarizes the *in vitro* model for leukocyte transmigration through the vascular endothelium. Stiffness range of gels is given by the Young's modulus, E.

3.5 Summary

The novel assay described in this chapter (Figure 3.3) allows for a controlled analysis of the effects of subendothelial matrix stiffness on ECs and the immune response. A key feature of this *in vitro* model is the incorporation of soft, ECM protein-coated hydrogels in the kilopascal range of stiffness into the transmigration assay. Previously, most transmigration assays have used glass or transwell inserts as the EC substrate; however, because these substrates do not have physiological mechanical properties, we chose to improve upon these methods by taking into account the flexibility of the ECs' underlying substrate.

Before putting the entire model together in Chapters 7 and 8, we first explored the role of individual components of the model, including cell-cell adhesion and TNF-α treatment, on the morphological and biomechanical properties of the ECs. As cells form monolayers, they transition from individual cells with only cell-substrate adhesions, to groups of cells which form some contacts with each other, and finally to confluent monolayers where the cells experience both cell-substrate and cell-cell adhesions. In Chapter 4 we show that single cell morphology and biomechanics vary significantly from cells within a monolayer and relate these discrepancies to the role of cell-cell adhesion.

Another important aspect of the *in vitro* model is EC activation via TNF-α treatment. TNF-α is known to cause drastic reorganization of the endothelium, including changes in morphology and stiffness. In Chapter 5 we explore more fully these changes and also relate them to the migratory behavior of the ECs.

4 Effects of Morphology Versus Cell-Cell Interactions on Endothelial Cell Stiffness†

4.1 Introduction

The mechanical properties of cells are important contributors to the health of a tissue, and a pathological state can sometimes be determined by measuring the stiffness of cells or tissues [115, 116]. For example, arteries stiffen during the progression of atherosclerosis [68] and tissues stiffen in cancer [123]. In the case of arteries, the mechanical properties of endothelial cells (ECs) are affected by many factors, including substrate stiffness, substrate ligands, shear stress, and the presence of soluble molecules. In Section 2.4, we summarized various *in vitro* treatments and conditions that affect endothelial cell stiffness (Table 2.1). While it has been widely recognized that it is important to study the mechanical properties of cells, much of the published work regarding cell stiffness focuses on single cells. Though this simplifies the experimental system, it is not always physiological, since, for example, ECs exist as a monolayer at the luminal surface of blood vessels. In this state, the cells are exposed to many neighbors in close contact, and the junctions are lined with many different molecules which bind the cells together [124], one of which is vascular endothelial (VE)-cadherin. VE-cadherin is a homophilic proteinthat localizes to cellular junctions, physically links to F-actin, and plays an important role in both mechanical [125-128] and biochemical signaling [129-131] pathways. Due to their role as mechanosensors, cadherins have been suggested as

---

† This chapter was originally published as Stroka, K.M. and H. Aranda-Espinoza, Effects of morphology vs. cell-cell interactions on endothelial cell stiffness (2011). *Cellular and Molecular Bioengineering* 4(1), 9-27. Permission was obtained from the publisher to use this material in the current dissertation.

targets for cancer therapy [132]; further, interactions between cadherins, actin, and myosin can create the forces necessary for wound closure [133]. While there are many proteins that localize at cell-cell junctions, this manuscript focuses on VE-cadherin due to its linkage with the actin cytoskeleton, an interaction that seems to be very relevant to tension homeostasis and cell stiffness.

Cell-cell interactions play a critical role in angiogenesis and endothelial homeostasis. As cells gain neighbors during monolayer formation, their morphology changes drastically, and it is known that cell geometry plays a significant role in regulating homeostasis of a cell [134]. Despite the occurrence of contact inhibition [135-137] in a monolayer, ECs do have the ability to reorganize themselves, but it is likely a different process than what occurs in single cells. While single cells are able to move freely, with constraints only due to adhesion with the substrate and cytoskeletal remodeling, cells in a monolayer are constrained by cell-cell adhesions as well as cell-substrate adhesions [138].

Cell mechanical properties, specifically, traction force generation, have been shown to depend on the presence of neighbors. Cell traction forces increase when two cells come in contact [139]. Further, two cells are able to communicate mechanically with each other when grown on soft, flexible substrates [57]. There is also evidence that cells maintain tension through cell-cell junctions [46, 140] and are able to communicate mechanically during collective cell migration [141]. However, we do not know how cell-cell interactions affect cell stiffness, nor do we fully understand how cells communicate mechanically in a monolayer. As mentioned above, such changes in cell stiffness might

affect important physiological functions, such as immune cell transmigration, atherogenesis, and cancer cell metastasis.

Here we use atomic force microscopy (AFM) to measure the Young's modulus of live human umbilical vein endothelial cells (HUVECs). AFM is a useful tool for measuring the response of cells to an applied force, from which the Young's modulus can be calculated. Hoffman and Crocker provide an extensive review on the response of cells to applied forces and a summary of different tools for measuring those responses [142]. AFM imaging can further be used to obtain topographical information about a sample. Previously, AFM has been used to quantify the Young's modulus of many cell types. For example, for ECs specifically, AFM has been used to determine the effects of environmental conditions such as oxidized low density lipoprotein [33], potassium [35], plasma sodium [34], and substrate stiffness [73] on cell stiffness. For soft samples such as cells, the Hertz-Sneddon model has often been used to determine Young's modulus from AFM force-distance curves (for review see [143]), and AFM cantilevers with spherical probes have been used to minimize exerted traction on the cells. The Hertz-Sneddon model [144] represents cells as isotropic, linearly elastic half-spaces and holds when deformations are small. It assumes an infinitely hard tip that is much stiffer than the deformable sample, and it can also account for the geometry of the tip. These assumptions can be made under our experimental conditions, and thus the Hertz-Sneddon model is appropriate to use in our case. Further details on the theoretical basis for this model can be found in several references [144-146].

Here, we combine AFM imaging with force measurements on live cells to obtain a topographical map that contains local measurements of Young's modulus at specific

locations. We measure both Young's modulus and area of spreading cells and find that cell stiffness increases with spreading area. Then, we measure the area and stiffness of single cells, groups, and monolayers and find that morphology can roughly be used to predict cell stiffness, though monolayers are stiffer than expected based on cell area. However, when F-actin is significantly disrupted using a high dose of cytochalasin B (cytoB), we observe drastic cell rounding, as previously reported [147, 148], and the stiffness of the cells softens to the measured value based on spreading area. When cell-cell junctions in a monolayer are presumably weakened through a low dose of cytoB treatment or VE-cadherin antibody application, cell monolayer stiffness approaches that of single cells, and cell-substrate adhesion increases, suggesting the importance of cell-cell adhesions in signaling to the cell's mechanical machinery.

4.2 Materials and methods

4.2.1 Cell culture

HUVECs were obtained from Lifeline Cell Technology (Walkersville, MD) and grown in tissue culture polystyrene flasks (Fisher Scientific, Pittsburgh, PA) at 37˚C, 5% CO_2, and 55% humidity. HUVECs were cultured in VascuLife Basal Medium (Lifeline Cell Technology) supplemented with 2% fetal bovine serum (FBS), 10 mM L-glutamine, 0.2% EnGS, 5 ng/mL rh EGF, 1 µg/ml hydrocortisone hemisuccinate, 0.75 units/mL heparin sulfate (Lifeline Cell Technology), 10,000 units/mL penicillin, and 10,000 µg/mL streptomycin (Gibco, Carlsbad, CA) according to the manufacturer's specifications. HUVECs were split at 80-90% confluency, and passages 2-5 were used for experiments. Synchronization of cells was accomplished by (a) growing cells to

confluency and (b) using low serum media (2%), according to Reinhart-King, 2008 [149]. Glass coverslips (22x22 mm, No. 1.5, Fisher Scientific) were coated with 0.1 mg/mL fibronectin (Sigma, St. Louis, MO) for 2 hours at room temperature. Cells were plated onto fibronectin-coated glass coverslips at high density ($4x10^5$ cells) and grown for approximately 48 hours until monolayer formation. For single cell studies, HUVECs were plated at low density ($8x10^3$ cells), while for groups, HUVECs were plated at medium density ($2x10^4$ cells). Media was changed every 48-72 hours. To weaken cell-cell junctions, two treatments were used: (a) HUVECs were treated with 2 μg/mL, 100 ng/mL, or 10 ng/mL cytochalasin B (Sigma) for 1 hour at 37˚C, and (b) HUVECs were treated with 1:100 dilution (10 μg/mL) of anti-VE-cadherin (Sigma V1514) for 1 hour at 37˚C just prior to experiments.

4.2.2 Cell staining

HUVECs were fixed in 2% paraformaldehyde (MP Biomedicals, Solon, OH) for 20 minutes, permeabilized in 1% TRITON-X 100 (VWR International, West Chester, PA) for 5 minutes, and blocked for non-specific binding in 2% bovine serum albumin (BSA; Sigma) for one hour. For visualization of cellular borders, cells were incubated in primary antibody (rabbit polyclonal to β-catenin; Abcam ab2365, Cambridge, MA) at a 1:100 dilution (2 μg/mL) for 2 hours. For visualization of focal adhesions, cells were incubated in primary antibody (anti-vinculin antibody, produced in mouse; Sigma V9131) at a 1:200 dilution (48 μg/mL) for 1 hour. Non-specific binding was blocked again after primary antibody application in 2% BSA for one hour. For β-catenin primary antibody, cells were incubated in secondary antibody (Rabbit Ig, Fluoroscein-linked

Whole Ab; GE Healthcare N1034, Piscataway, NJ) at a 1:20 dilution (105 µg/mL) for one hour. For vinculin primary antibody, cells were incubated in secondary antibody (anti-mouse Alexa 488; Invitrogen A11001, Carlsbad, CA) at a 1:200 dilution (10 µg/mL) for one hour. Primary and secondary antibodies were diluted in 2% BSA with phosphate buffered saline (PBS). For visualization of F-actin, cells were incubated in 0.1 µM Phalloidin-TRITC (Sigma) for 30 minutes. For nuclear staining, cells were treated with 2 µg/mL Hoechst stain (Invitrogen) for 5 minutes. All treatments were completed at room temperature. Cells were washed with PBS between each step.

4.2.3 Atomic force microscopy

Young's moduli of live HUVEC monolayers were measured using an atomic force microscope (AFM; Agilent, Santa Clara, CA) with a silicon nitride cantilever (Novascan, Ames, IA) with a spherical glass SiO_2 probe of diameter 5 µm. The deflection sensitivity of the cantilever was measured using glass as a stiff surface. The cantilever spring constant was measured using Thermal K software (Molecular Imaging Corporation, San Diego, CA), where the cantilever was treated as a simple harmonic oscillator, according to the thermal fluctuation method [150, 151]. The power spectrum of the AC signal was used to determine the mean-square amplitude of the cantilever, which was then used to solve for the spring constant. The manufacturer's nominal value for the cantilever spring constant (k) was 0.01 N/m, and the values obtained with ThermalK were within a factor of 2 (generally 0.006-0.008 N/m). Glass substrates with HUVECs attached were positioned under the AFM tip and typical force curves (Figure

4.1A) were captured in different locations along the cells. All force curves and imaging were done at room temperature in FBS-free HUVEC media in an AFM liquid chamber.

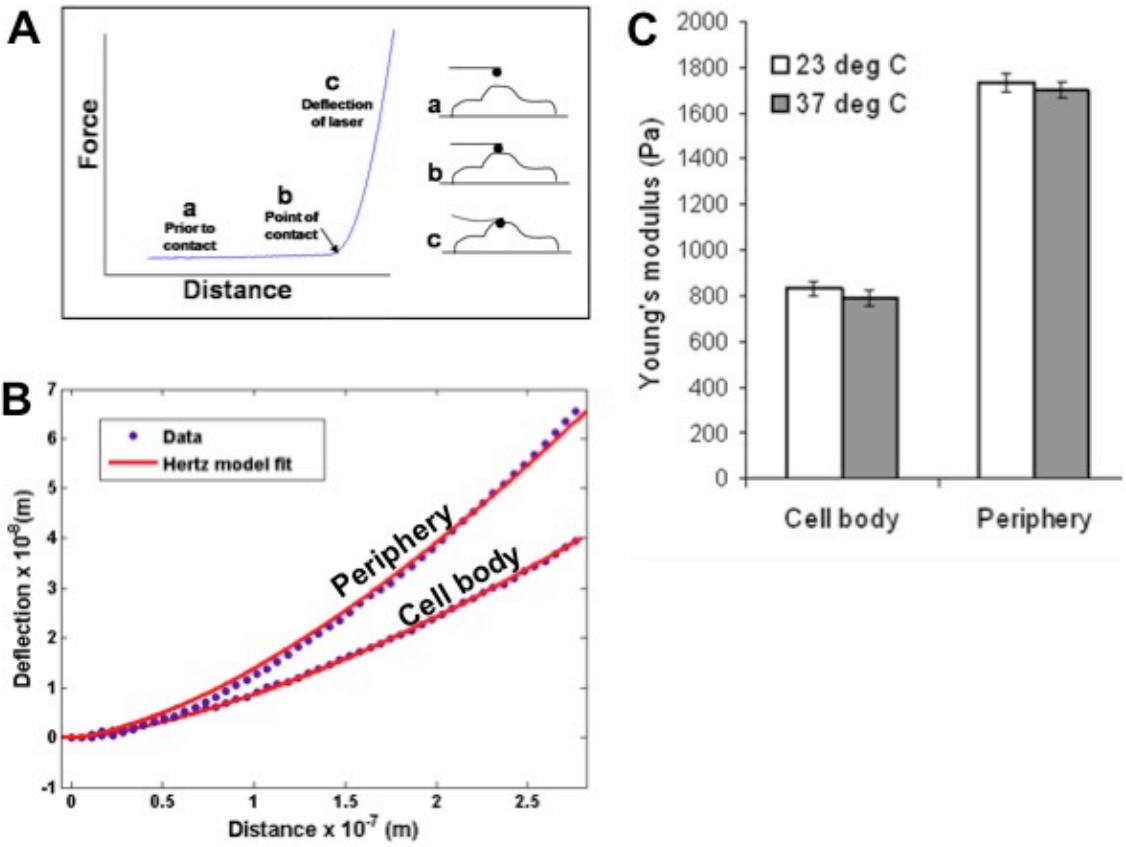

Figure 4.1. Atomic force microscopy methods. **(A)** Example of a force versus distance curve obtained by atomic force microscopy (AFM). Prior to contact between the AFM tip and the sample (a) there is no deflection of the laser. Once the tip has contacted the sample (b), the laser begins to deflect as the sample is indented (c). **(B)** Deflection versus distance data were fit using the Hertz-Sneddon model (see Materials and Methods). The point of contact was chosen when the slope became nonzero (approximately 50 pN/nm after converting to force versus distance), while the final indentation was chosen to be about 250 nm. In the case of a very stiff sample, the deflection (or force) rises sharply with distance. Curves are shown for a soft location (i.e. cell body) and a relatively stiff location (i.e. periphery). **(C)** Young's modulus of single cells at the cell body and periphery locations (See Figure 3-A for clarification) at both room temperature (23˚C) and 37˚C with 5% CO_2 and 55% humidity. No significant differences were measured between these conditions using our experimental set-up.

The AFM procedure was begun by first scanning a region of interest (90x90 μm) using contact mode. Then, in the AFM Picoscan software, specific locations (25 per scan) were selected by hand, both at the periphery and cell body. The region of interest was scanned again and this time force versus distance curves were taken at the chosen locations. Five to 20 images were obtained per sample, and 2-5 different samples were analyzed for each condition. The maximum size of the scan (90 μm by 90 μm) was large enough to capture most of one single cell per image and 3-6 cells within a monolayer per image. A force of approximately 2 nN was applied to the cells by the AFM cantilever, and this force was spread out over the large area of the 5 μm spherical probe attached to the cantilever, lessening the resulting applied traction. In performing AFM on living cells, AFM cantilevers containing spherical probes have an advantage over sharp tips, which can damage cells due to their tiny surface area (traction=force/area). AFM imaging and measurements were generally taken within one hour.

In a custom-written Matlab (The MathWorks, Natick, MA) program (Appendix A), data were fit to the Hertz-Sneddon model [144] for a paraboloid indenter [146]:

$$F_{paraboloid} = \frac{4}{3}\left(\frac{E}{1-\upsilon^2}\right)R^{1/2}\delta^{3/2},$$

where $F_{paraboloid}$ is the force exerted by the paraboloid indenter, E is the Young's modulus of the cell, R is the radius of curvature of the indenter, and δ is the distance of the indenter from the sample (Figure 4.1B). Note that R for a sphere is equal to the radius of the sphere, and therefore R=2.5 μm for the glass probe. The cells were assumed to be nearly incompressible [152] and therefore it was assumed that v = 0.45 is the Poisson's ratio of the elastic halfspace. Note that the force is also equal to the cantilever spring constant (k) times the change in position of the laser (as a measurement of the deflection

of the cantilever). The Young's modulus was found for each force curve using the fitting algorithm. A maximum indentation of about 250 nm was chosen for fitting, since at small indentations the Young's modulus depends greatly on indentation depth [153], while the Hertz-Sneddon model does not hold at large indentations. Two hundred fifty nanometers is sufficiently small compared to the height of the cell (several microns). The point of contact of the cantilever (Figure 4.1A) with the sample was chosen to be the point at which the derivative of the force-distance curve became nonzero, or about 50 pN/nm. Thus, data were fit from the point of contact to the maximum indentation value. Average Young's modulus was computed by averaging all force curves for a given condition. Statistical tests were done between pairs using a Student's t-test, or among groups using ANOVA, where $P<0.05$ indicated statistical significance. Multiple comparisons were done in ANOVA using Tukey's honestly significant difference criterion. All measurements reported in this article are in the format mean ± standard error.

4.2.4 Cell spreading combined with AFM

To determine the relationship between cell spreading and cell stiffness, HUVECs were trypsinized from tissue culture flasks, diluted with media, centrifuged, resuspended in FBS-free media, plated onto fibronectin-coated glass coverslips immediately, placed within the AFM liquid chamber, and allowed to attach to the substrate for 15-30 minutes before beginning AFM measurements. A low number of cells ($8x10^3$) were plated in order to ensure the presence of single cells on the surface of the coverslip. Cells that were relatively close to other cells were not analyzed, to avoid effects of cell-cell contact on the spreading process. The AFM tip was positioned over the cell. A minimal amount of

cell attachment was necessary to ensure the cell did not move out from between the cantilever and the substrate. This level of attachment was determined through observation of the cell morphology in brightfield microscopy, when lamellipodia formation began. When this occurred, the AFM tip was lowered to the raised spherical central region of the cell (not the flattened periphery). AFM force measurements were taken every 30 seconds or 2 minutes during spreading without moving the cantilever horizontally in between measurements, and brightfield images were captured simultaneously every 30 seconds during spreading. Young's modulus was determined from force-distance curves as described in the previous section. To compute area, cells were traced by hand in ImageJ. A sample size of N=8 spreading cells was used. A "morphology curve" was created using the spreading data, by plotting Young's modulus versus area, with each data point representing the average area and Young's modulus of N=8 spreading cells at the same time points. Because the stiffnesses of spreading cells were averaged for each time point, and these data points included both periphery and cell body regions, the average stiffness of the periphery and cell body regions was plotted for each of single cells, groups, and monolayers.

4.2.5 Phase contrast, confocal, and total internal reflection fluorescence microscopy

Brightfield and phase contrast microscopy of HUVECs was completed at 37°C, 5% CO_2 and 55% humidity using an inverted microscope (Olympus IX71, Center Valley, PA). Images were captured with a QImaging Retiga-SRV charge-coupled device (CCD) digital camera (QImaging Corporation, Surrey, British Columbia, Canada). Confocal microscopy was completed at room temperature on immunostained HUVECs using an

inverted scanning disk confocal microscope (Olympus IX81). Images were captured with 0.3 μm between planes on a Hamamatsu ORCA-ER CCD digital camera (Leeds Precision Instruments, Minneapolis, MN).

Total internal reflection fluorescence microscopy (TIRFM) was completed on samples (on n=1.5 glass coverslips) stained with vinculin antibody and FITC secondary antibody (as described above in Section 4.2.2) at room temperature using an inverted microscope (Olympus IX81) using a 60x oil immersion lens, as previously described [154]. Samples were illuminated with an ion laser of wavelength 488 nm (Melles Griot, Rochester, NY), and images were captured with a QImaging Rolera-MGi CCD digital camera (QImaging Corporation). The angle of laser incidence was adjusted once at the start of the experiment and was not adjusted between samples to ensure that the same plane was illuminated in each sample. In TIRFM, when the angle of incidence of light is greater than the critical angle for total internal reflection, an evanescent field is generated at the glass-sample interface. This evanescent field decays exponentially with distance normal to the interface, creating a thin layer of illumination (≤100 nm; [155]). TIRFM was chosen for imaging cell-substrate interactions over widefield fluorescence microscopy due to the thin layer of illumination that eliminates background fluorescence in TIRFM.

4.2.6 Morphological analysis

To aid with morphological analysis, HUVEC monolayers were fixed and immunostained for β-catenin in order to visualize cellular borders. For area analysis of single cells and cells within groups, individual HUVECs were traced by hand in ImageJ

(National Institutes of Health, Bethesda, MD). For analysis of focal adhesion size and density we used the method as previously described [154]. Briefly, cells were stained for vinculin and TIRFM images were obtained. Images were made binary and the particle analyzer was used in ImageJ to measure vinculin punctuate sizes larger than 0.5 μm^2 and counts per area. Statistical tests were done using a Student's t-test, where $P<0.05$ indicated statistical significance.

4.3 Results

4.3.1 Cell stiffness measurements are similar to those under culture conditions

Our AFM images and force curves on single cells, groups of cells, and monolayers were all performed at room temperature conditions. To evaluate the dependence of cell stiffness on temperature, CO_2, and humidity, we measured the stiffness of single cells at both room temperature (23˚C) and culture conditions (37˚C with 5% CO_2 and 55% humidity) using an enclosed chamber. In our experimental set-up, performing AFM at room temperature versus culture conditions does not make a difference (Figure 4.1C). There is no statistical difference between the Young's moduli at the cell body ($P=0.34$; N=326 force curves from 30 cells at 23˚C and N=181 force curves from 14 cells at 37˚C) or periphery ($P=0.56$; N=410 force curves from 30 cells at 23˚C and N=302 force curves from 14 cells at 37˚C), according to a Student's t-test. Distinction between cell body and periphery locations are later discussed in Figure 4.3.

These results may differ from experiments where the cells are placed in room temperature medium, allowed to equilibrate to room temperature, and kept at room temperature for long periods of time, much longer than one hour. In our experimental

procedure, we removed cells directly from the incubator (conditioned at 37˚C and 5% CO_2), washed them with PBS (warmed to 37˚C), and then added the media (also warmed to 37˚C) for AFM. Therefore, the cells began in a 37˚C environment. We imaged them and took force measurements for relatively short periods of time (under one hour, as stated in our methods), though we would expect the media to cool moderately over the course of the experiment. However, we did not observe stiffening or softening of the cells over the course of AFM, further indicating that the temperature or CO_2 conditions did not affect our measurements during our experimental time window.

4.3.2 Cell area depends on degree of cell-cell contact

HUVECs were plated at low, medium, or high density onto glass coverslips coated with fibronectin. At low density, single cells were observed. At medium density, cells were observed in groups of 3-13 cells where they formed isolated islands. At high density, cells formed confluent monolayers within 48 hours.

We found that single cells are larger in area (2045±65 μm^2; N=167 cells) than cells within a monolayer (1029±25 μm^2; N=192, $P<0.001$), consistent with previous reports [156]. Cells in groups are larger (3030±73 μm^2; N=249, $P<0.001$) than both single cells and cells in a monolayer (Figure 4.2A). Phase contrast images of single cells (Figure 4.2B), a group of 4 cells (Figure 4.2C), and a monolayer of cells (Figure 4.2D) show the differences in cell size as a function of degree of cell-cell contact.

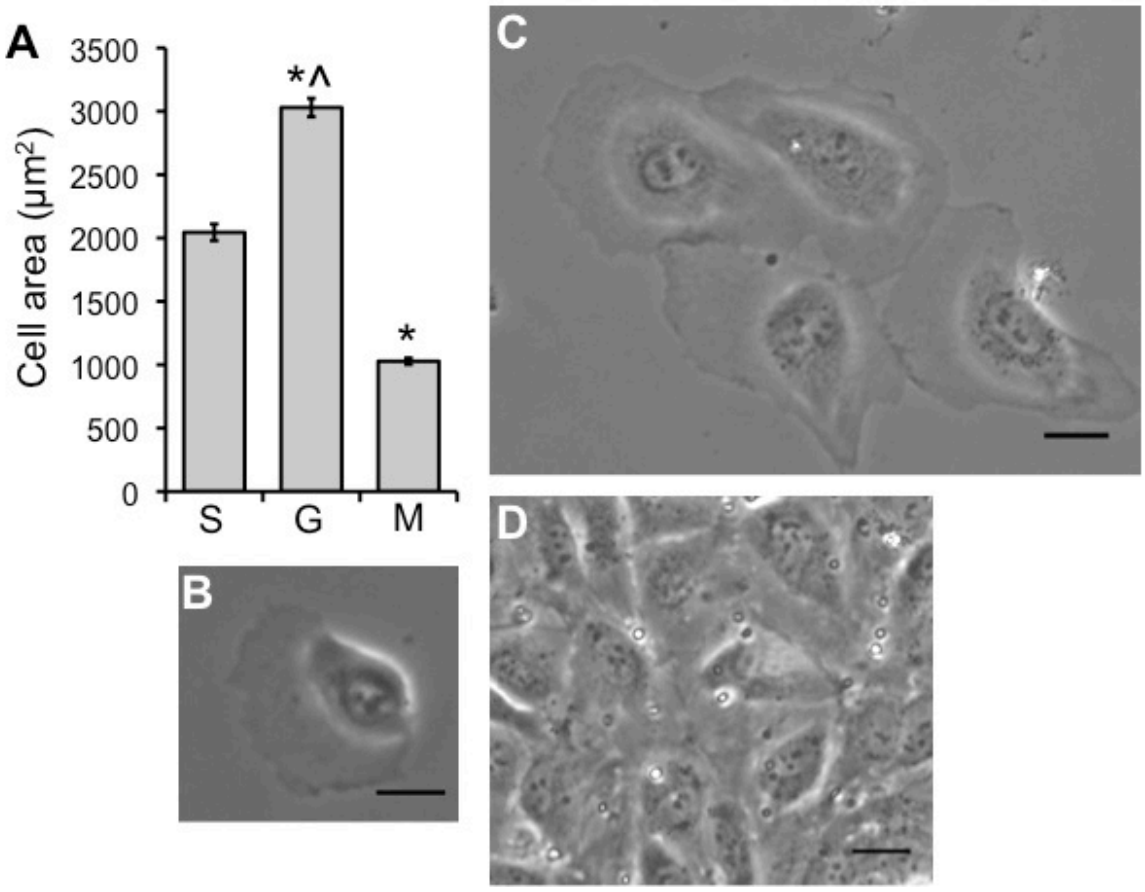

Figure 4.2. Effects of cell-cell adhesion on cell morphology. **(A)** Cellular area as a function of degree of cell-cell contact on fibronectin-coated glass substrates. Bars indicate mean of N cells, while error bars indicate standard error. N equals 167, 249, and 192 for single cells (S), groups (G), and monolayers (M), respectively. * indicates $p<0.05$ with single cells, while ^ indicates $p<0.05$ with monolayers using ANOVA. Also shown are phase contrast images of **(B)** a single cell, **(C)** four cells in contact, and **(D)** a monolayer of cells. Scale bars are 20 μm.

4.3.3 Single cells are stiffer than cells in a monolayer

AFM was performed on HUVECs at varying degrees of cell-cell contact on fibronectin-coated glass substrates. AFM deflection images demonstrate the topography of a single HUVEC (Figure 4.3A), group of three HUVECs (Figure 4.3B), and monolayer of HUVECs (Figure 4.3C). Each of these images indicates that the cell topography consists of both a raised portion, which likely contains the nucleus and other organelles and which we label the "cell body" (black arrows in Figures 4.3A through 4.3C), and also a more flattened region, which we label the "periphery" (white arrows in Figures 4.3A through 4.3C). We also compared the Young's moduli of single cells at room temperature and at 37˚C with 5% CO_2 and 55% humidity and verified that under our experimental conditions AFM gave similar results.

For all degrees of cell-cell contact, the Young's modulus of the periphery is larger than the Young's modulus at the cell body location (Figure 4.3D). We found that the Young's modulus of single cells is larger than that of monolayers, both at the cell body ($E=854\pm39$ Pa, $N=195$ for single cells and $E=757\pm16$ Pa, $N=246$ for monolayers, $P=0.013$) and periphery locations ($E=1558\pm46$ Pa, $N=284$ for single cells and $E=1042\pm14$ Pa, $N=457$ for monolayers, $P<0.001$) (Figure 4.3D). At the cell body ($E=886\pm72$ Pa, $N=44$ for groups of 3 cells; $E=880\pm76$, $N=67$ for 4-5 cells; and $E=786\pm130$, $N=16$ for groups of 6-13 cells), the Young's modulus of groups of 3-5 and groups of 6-13 cells is not different from that of single cells ($P>0.600$), while at the periphery ($E=1899\pm60$ Pa, $N=100$ for groups of 3 cells; $E=1742\pm70$, $N=98$ for 4-5 cells; and $E=1738\pm106$, $N=46$ for groups of 6-13 cells) the Young's modulus is larger than both single cells ($P<0.001$,

P=0.037, P=0.139, respectively with increasing group size) and monolayers (P<0.001 for all groups) (Figure 4.3D).

Further, the distributions of Young's moduli for single cells (Figure 4.3E), groups (Figure 4.3F), and monolayers (Figure 4.3G) indicate the large variation in stiffness among cells, even when looking at the same region (cell body or periphery). These distributions show that for single cells and groups, the distributions are fairly wide (Figures 4.3E and 4.3F), while for monolayers, the distributions are much tighter (Figure 4.3G). Thus, monolayers are more homogeneous in terms of stiffness than both groups and single cells.

Figure 4.3. Effects of cell-cell adhesion on endothelial cell stiffness. Atomic force microscopy contact deflection images of **(A)** a single control endothelial cell, **(B)** 3 cells in contact, and **(C)** a monolayer of cells. Image size is 90 μm by 90 μm. Black arrows point to examples of cell body locations, while white arrows point to examples of periphery locations. **(D)** Young's modulus of cells for the cell body and periphery locations as a function of cell-cell contact. Bars indicate mean of N force curves per condition, while bars indicate standard error. * indicates p<0.05 with single cells at the same location, while ^ indicates p<0.05 with groups of 3 cells at the same location using ANOVA. For all locations, the periphery region is stiffer than the cell body region (p<0.05 using t-test). N=195, 44, 67,16, 246 for single cells, groups of 3 cells, groups of 4-5 cells, groups of 6-13 cells, and monolayers, respectively, at the cell body location. N=284, 100, 98, 46, 457 for single cells, groups of 3 cells, groups of 4-5 cells, groups of 6-13 cells, and monolayers, respectively, at the periphery location. Also shown are distributions of Young's moduli for **(E)** single cells (N=195 for cell body and N=284 for periphery region), **(F)** all groups of cells (N=127 for cell body and N=244 for periphery region), and **(G)** monolayers (N=246 force curves for cell body and N=457 force curves for periphery region).

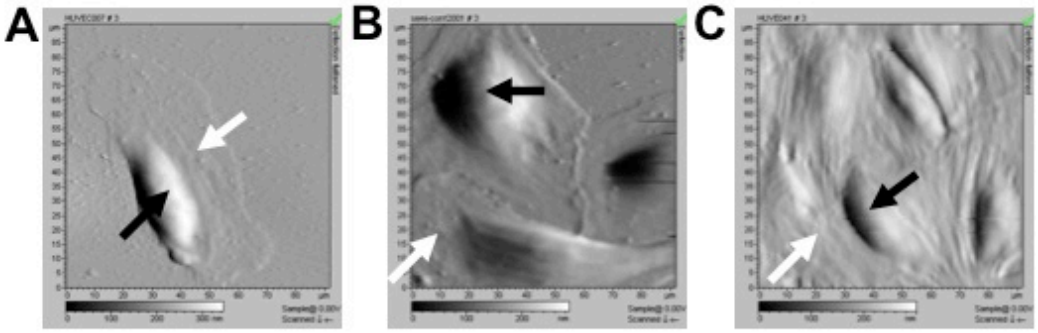

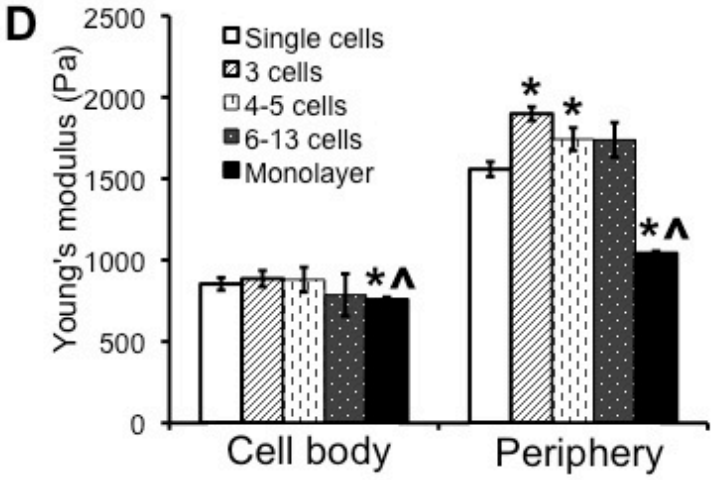

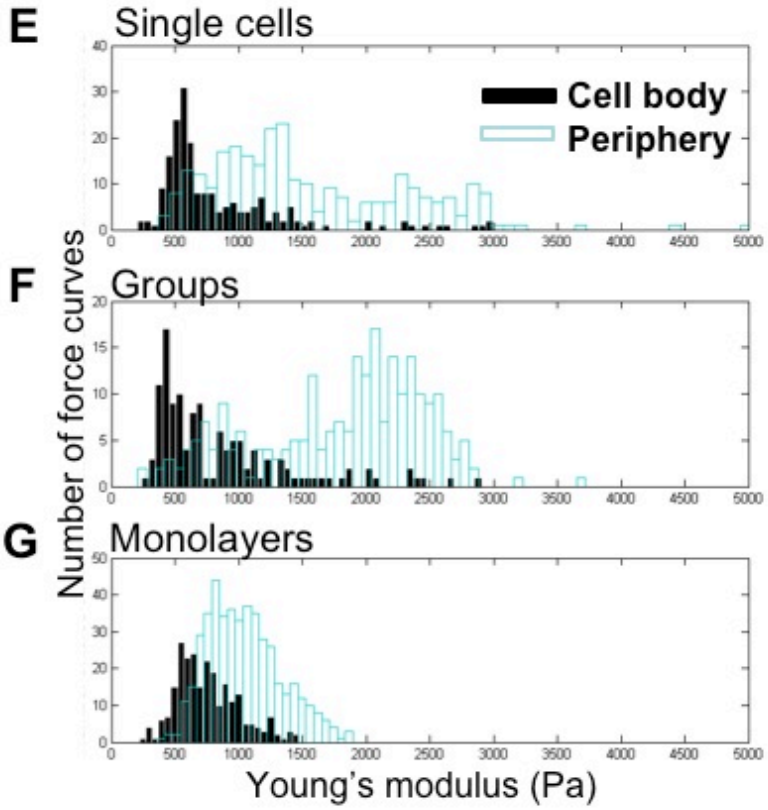

4.3.4 Cell stiffness increases during spreading

One approach to determine the relationship between cell morphology and stiffness is to measure the stiffness and area of a single cell simultaneously as it spreads (Figure 4.4). We performed this experiment by obtaining brightfield timelapse images while taking AFM force curves on a single spreading cell following trypsinization. Note that we did not scan the cell with AFM, but rather the cantilever remained stationary (in the horizontal plane) as the cell spread. Following the typical cell spreading process [157], the HUVECs began as spheres upon plating, presumably formed initial adhesions to the substrate upon lamellipodium formation (Figure 4.4D, T=0), and spread fairly isotropically onto the substrate over the course of one hour (Figures 4.4D and 4.4E). HUVECs flattened as they spread, as it was necessary to bring the sample closer to the AFM cantilever during spreading in order to avoid flat-lining the force-distance curves.

We found that for all cells probed (N=8 cells), the Young's modulus of the cell increased as spreading area increased (Fig 4.4). This behavior was independent of how often the cell was probed with the AFM cantilever (every 30 seconds in Figures 4.4A and 4.4B and every 2 minutes in Figure 4.4C). The Young's modulus at the initial timepoint (E~400 Pa) indicates a lower bound of cell stiffness, where the cell is (visibly) slightly attached to the substrate as determined by brightfield microscopy, but still is round in morphology. The Young's modulus at this point is very similar to that when cells have been treated with cytoB to disrupt F-actin (gray outlined dots at time=0 in Figure 4.4). See Section 4.3.6 and Figure 4.5A for more discussion on the effects of cytoB treatment.

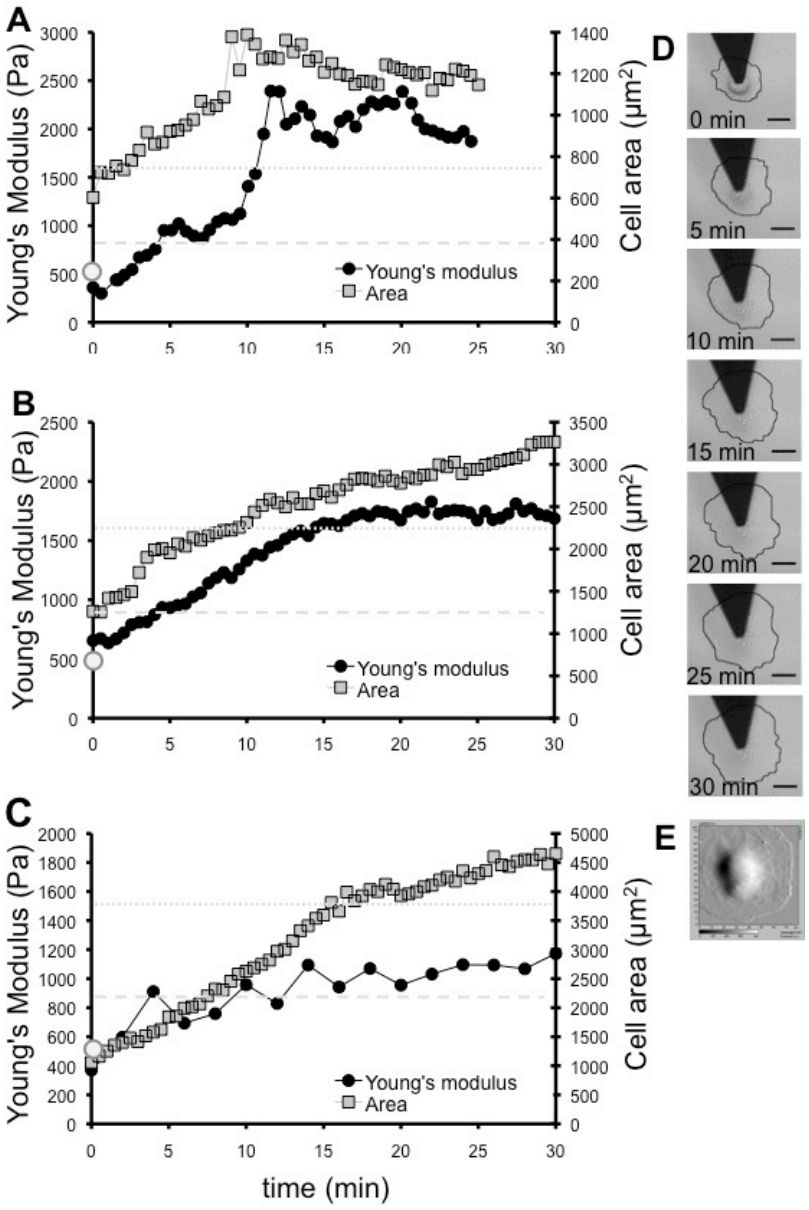

Figure 4.4. Young's modulus and cell area versus time for three representative spreading cells. A time of T=0 indicates the time at which measurements began; typically this was 15-30 minutes after plating. Shown are plots for three different representative cells, with AFM measurements taken every 30 seconds **(A and B)** or every 2 minutes **(C)**. Gray outlined dot at T=0 indicates typical Young's modulus of cytochalasin B-treated cells. Gray large dashed line and gray small dashed line indicate typical Young's modulus of control single cells at the cell body and periphery locations, respectively. **(D)** Time-course sequence of spreading cell from panel B. These images show the AFM cantilever positioned over the cell during spreading. The cantilever remained stationary during the course of spreading. In each image cells have been outlined in black by hand to help with cell visualization. Scale bar is 20 μm for all images. **(E)** AFM deflection image of cell from panel C after it has completely spread. Image size is 90 μm by 90 μm.

4.3.5 Cell stiffness and spreading area correlate for single cells and groups

Using the data obtained from performing AFM on spreading cells, we also plotted Young's modulus versus area, with each data point indicating the average Young's modulus and area of N=8 cells (Figure 4.5) at the same time point. We call this the "morphology curve." The white outlined circles in Figure 4.5 therefore represent the measured Young's modulus of a cell, given its area. We found that the (area, stiffness) of single cells and groups both lie on this curve, while monolayers are stiffer than expected (Figure 4.5). Furthermore, monolayers treated with 2 µg/mL cytoB do lie on the measured morphology curve, while monolayers treated with VE-cadherin antibody and 10 ng/mL cytoB lie above it.

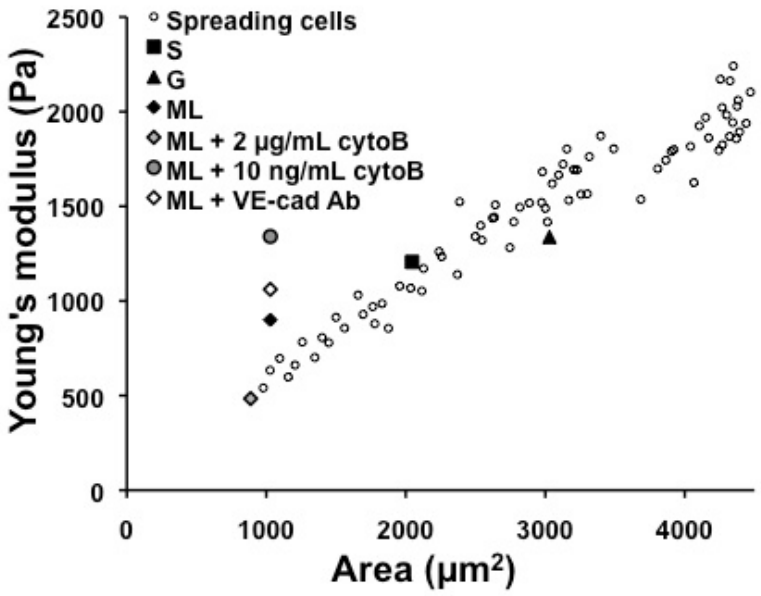

Figure 4.5. Young's modulus versus area for spreading cells. Also shown are the average (area, stiffness) of single cells (S), groups (G), monolayers (ML), and monolayers treated with VE-cadherin antibody (VE-cad Ab) or cytochalasin B (cytoB). In all cases, the stiffness plotted is the average stiffness of the cell body and periphery regions. N=8 spreading cells.

4.3.6 Cell stiffness is dependent on concentration of cytochalasin B

Cell-cell adhesions in a monolayer can be broken or weakened via several methods. In the extreme, they can be completely disrupted by interfering with the F-actin network, which is critical for maintaining cell-cell junctions and tensional homeostasis within the cells. We used the cytoB treatment to cap actin filaments, preventing further polymerization and leading to net depolymerization of the filaments. It has previously been reported that cells soften when treated with drugs of the cytochalasin family [147, 148].

We treated HUVECs with decreasing concentrations of cytoB to vary the amount of F-actin disruption. The mechanical response of the monolayer depended on the concentration of drug applied (Figure 4.6A). With the highest concentration of cytoB (2 μg/mL; "high"), the average Young's modulus is smaller than control cells, both at the cell body ($E=454\pm27$ Pa, $N=70$, $P<0.001$) and periphery locations ($E=583\pm29$ Pa, $N=22$, $P<0.001$). With this treatment, the monolayer is completely disrupted, as evidenced in the AFM deflection image (Figure 4.6B), where the HUVECs have undergone significant rounding due to the high degree of actin depolymerization. With a smaller concentration of cytoB (100 ng/mL; "intermediate"), the average Young's modulus is smaller than control cells at the cell body ($E=623\pm26$, $N=110$, $P<0.001$), but it is not different from control cells at the periphery ($E=986\pm30$, $N=198$, $P=0.051$). AFM deflection images indicate that with this amount of F-actin disruption, some cell-cell adhesions have remained intact; however, there are also large gaps in the monolayer where the cells have retracted and cell-cell adhesions are disrupted (Figure 4.6C). Finally, with the least harsh treatment of cytoB (10 ng/mL; "low"), the Young's modulus is surprisingly larger than

control cells, both at the cell body (E=1157±46, N=116, P<0.001) and periphery (E=1524±43, N=176, P=0.004). With this treatment, the cell monolayer is still mostly visibly intact, with some disruption indicated by the presence of tether-like structures between adjacent cells (Figure 4.6D; white arrowheads). These tether-like structures are present at many cell-cell adhesion sites. There is no statistical difference in area of the cells, compared with cells in control monolayers. The Young's modulus of cell monolayers treated with low cytoB is not different from control single cells at the periphery region, while it is different at the cell body region.

4.3.7 Monolayers stiffen when junctions are destabilized with VE-cadherin antibody

A second approach to destabilizing cell-cell adhesions in HUVEC monolayers is by applying a VE-cadherin antibody. We found that in HUVEC monolayers, treatment with a VE-cadherin antibody results in an increase in Young's modulus, both at the cell body (E=908±21, N=241, P<0.001) and periphery (E=1214±14, N=583, P<0.001) (Figure 4.6E). Meanwhile, there is no difference in cell area, compared with control monolayers.

To determine the baseline effect of the VE-cadherin antibody when no cell-cell adhesions are present, we performed the same experiment on single cells. Interestingly, single cells treated with a VE-cadherin antibody are softer than control cells, both at the cell body (E=623±28, N=84, P<0.001) and periphery (1387±61, N=160, P=0.025). Further, VE-cadherin antibody-treated cells follow the trend that single cells are stiffer than cells within a monolayer. AFM deflection images of single cells and monolayers

treated with VE-cadherin antibody do not look different from images of control cells (Figures 4.6F and 4.6G).

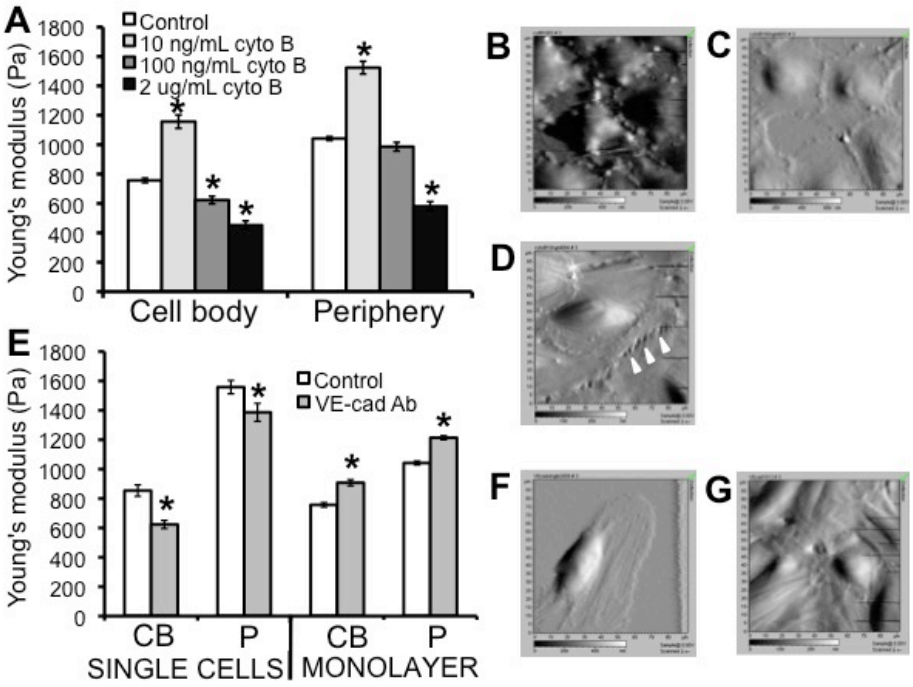

Figure 4.6. Effects of F-actin and cell-cell adhesion disruption on endothelial cell stiffness. Mean Young's modulus for **(A)** cytochalasin B (cytoB)-treated cells and **(E)** VE-cadherin antibody (VE-cad Ab)-treated cells at the cell body and periphery locations. Bars indicate mean of N force curves, while error bars indicate standard error. * indicates $p<0.05$ with control at same location using Student's t-test. N=246, 241, and 70 for control, VE-cadherin antibody-treated, and cytoB-treated cells, respectively, at the cell body (CB) location. N=457, 583, and 22 for control, VE-cadherin antibody-treated, and cytoB-treated cells, respectively, at the periphery (P) location. Also shown are AFM contact deflection images of HUVEC monolayers treated with **(B)** 2 µg/mL cytoB, **(C)** 100 ng/mL cytoB, and **(D)** 10 ng/mL cytoB. White arrowheads in panel D point to tether-like structures at cell-cell junctions. Also shown are **(F)** single cells and **(G)** monolayers, both treated with a VE-cadherin antibody. AFM image size is 90 µm by 90 µm.

4.3.8 Actin cytoskeleton architecture depends on degree of cell-cell contact

We used confocal imaging of phalloidin-actin-stained samples to evaluate the architecture of the F-actin network as a function of degree of cell-cell contact. We found that control single cells and groups have well-developed stress fibers arranged in parallel throughout the entire length and width of the cell, and most of these stress fibers within a given cell are oriented locally in the same direction (Figures 4.7A and 4.7B). Cells in monolayer also have well-developed stress fibers, yet they are oriented mostly around the cell borders, with only some extending along the length of the cell (Figure 4.7C). Cells treated with 2 μg/mL cytoB show complete disruption of F-actin, as expected (Figure 4.7D). Cells treated with 100 ng/mL show significant monolayer disruption, with several F-actin filaments or bundles tethering to neighboring cells (Figure 4.7E; white arrowheads). Meanwhile, in cells treated with a very low dose of cytoB (10 ng/mL), we do not observe differences in F-actin arrangement as compared to control monolayers (Figure 4.7F). Further, the F-actin structure of both single cells and monolayers treated with VE-cadherin antibody do not show differences as compared with the controls (Figures 4.7G and 4.7H).

4.3.9 Focal adhesion size and density depend on degree of cell-cell contact

To determine whether differences in cell stiffness could be partially explained by focal adhesion (FA) assembly [154, 158], we immunostained for vinculin, performed total internal reflection microscopy (TIRFM) on the samples (Figures 4.7I and 4.7J), and measured the size and density of FAs as a function of degree of cell-cell contact. We found that FAs in monolayers are the same size as in single cells (~1.4 μm^2, P=0.900;

Figure 4.7K), but there are less FAs per area in monolayers (P<0.001; Figure 4.7L). FAs in groups are larger than in single cells (~1.6 μm^2, P<0.001) but are present at the same density as in single cells (P=0.501; Figure 4.7L). FAs in single cells treated with VE-cadherin antibody are not different in size from FAs in control single cells (P=0.289; Figure 4.7K), but, interestingly, they are more densely arranged (P<0.001; Figure 4.7L). Finally, FAs in monolayers treated with VE-cadherin antibody or a low dose of cytoB are larger than FAs in control monolayers (P<0.001; Figure 4.7K), and FAs in both treatments are more dense (P<0.001; Figure 4.7L). FAs of cell monolayers treated with intermediate (100 ng/mL) and high (2 µg/mL) doses of cytoB were significantly dissolved and thus we did not measure their size or density.

Figure 4.7. Effects of cell-cell adhesion on F-actin and focal adhesion arrangement. Confocal images of control **(A)** single cell, **(B)** group of cells, and **(C)** monolayer of cells. Also shown are confocal images of monolayers treated with **(D)** 2 µg/mL, **(E)** 100 ng/mL, and **(F)** 10 ng/mL cytochalasin B to disrupt F-actin. White arrowheads in panel E indicate F-actin filaments or bundles tethering neighboring cells. Also shown are confocal images of **(G)** single cells and **(H)** monolayers treated with a VE-cadherin antibody. White scale bar in panel A is 20 µm and applies to all images. Phalloidin-actin is stained in red, vinculin (focal adhesion marker) in green, and DNA in blue. Total internal reflection fluorescence microscopy (TIRFM) images were also taken using a laser of wavelength of 488 nm to illuminate the FITC-labeled vinculin, resulting in images which we analyzed for focal adhesion (FA) size and density (number per area). We show a **(I)** raw TIRFM image of a single cell and **(J)** a processed TIRFM image made into binary, as described in the Section 4.2.6. White scale bars in panel I and (J) are 20 µm. Shown also are plots of **(K)** average FA size and **(L)** average FA density. Bars indicate average while error bars indicate standard error of measurements from a minimum of 20 images. * indicates p<0.05 with control of same degree of cell-cell contact (single cell or monolayer), while ^ indicates p<0.05 with single cell control using Student's t-test. S=single cells, G=groups, M=monolayers, VEcad=VE-cadherin antibody-treated, cytoB=cytochalasin B-treated.

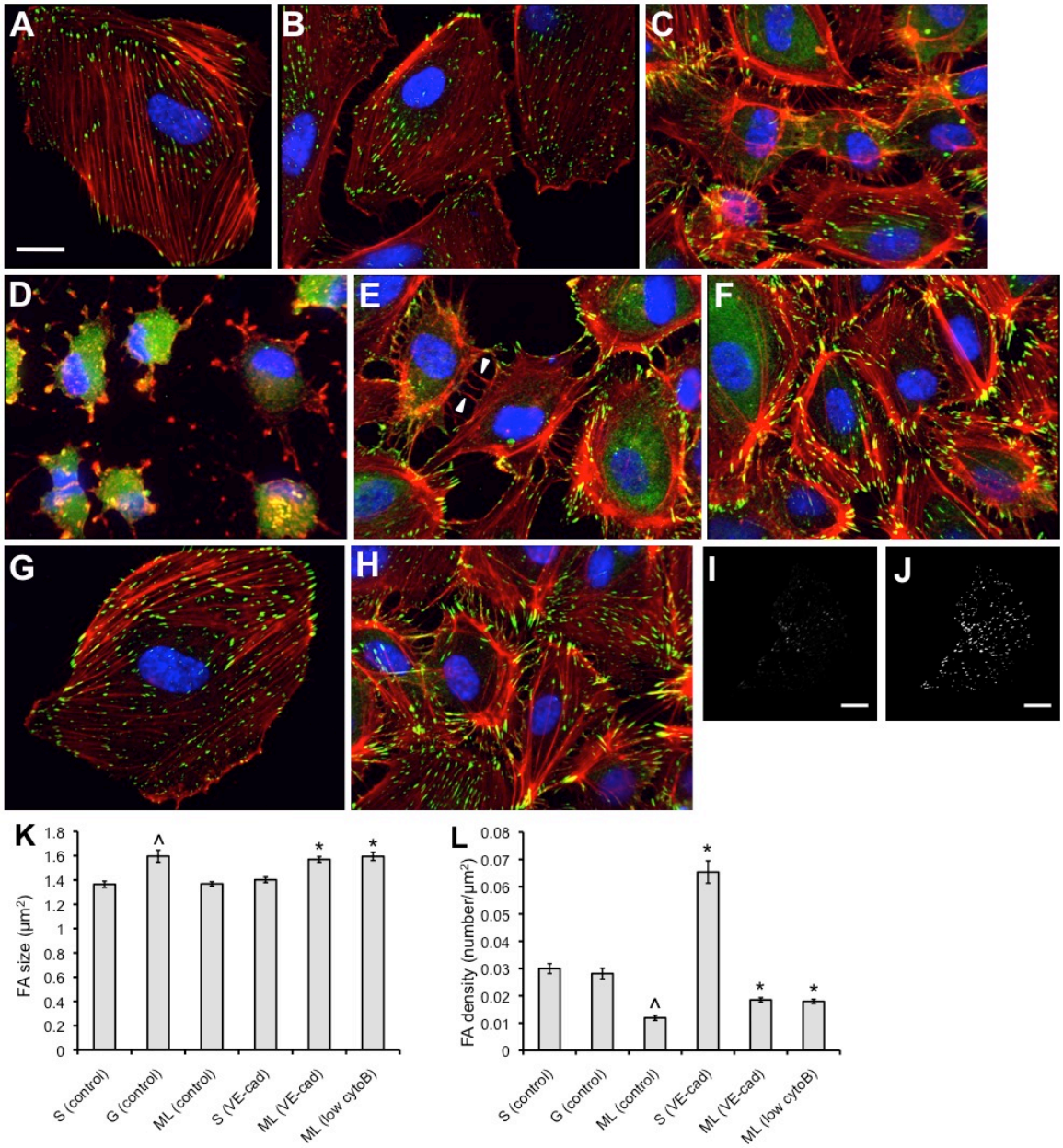

4.4 Discussion

Our data suggest that cell area correlates roughly with cell stiffness. However, in groups or in monolayers, cells have several neighbors, and cell-cell interactions likely play a role in determining cell stiffness. It was our goal to determine whether cell mechanics is necessarily governed by spreading area or whether cell-cell interactions play a significant role in determining the mechanical properties of cells within a monolayer.

Our rationale for evaluating the stiffness of groups of cells was to have a system in which the size of the cells was similar to that of single cells, yet cell-cell adhesions were also present. However, we observed that cells in groups of cells are actually larger (by a factor of ~1.5), and also stiffer, than single cells (Figures 4.2 and 4.3). One possibility is that the cells, after coming in contact with another cell or group of cells, are extending towards the free periphery, away from the group, to facilitate migration. This is reminiscent of the leading edge of an epithelial cell sheet, where microtubule plus ends are very dynamic near free non-contacted cell edges and suppressed at cell-cell contacts; further, the continuous polymerization and retrograde flow of actin which is necessary for cell motility is inhibited at cell-cell contacts [159]. Some degree of cell-cell adhesion has already formed at this point, and the cell's area may increase because it is attempting to move away from the group, as in EC sheet migration [160]. If this is true, it is possible that the larger cell contains an actin cytoskeleton-plasma membrane cortex which is under more tension than in smaller, single cells. Experimentally, we measure larger FAs in groups than in single cells (Figure 4.7K), and because traction forces and FA area are correlated [161] and also F-actin tension and cell stiffness are correlated [24], we believe

that stress fiber tension may be increased in groups, even though we do not observe differences in F-actin structure. This is in agreement with the reports of Califano and Reinhart-King (2010) where cell traction forces increase when two cells come in contact [139]. Further, cells in a monolayer are tightly packed and smaller (Figure 4.2), with less FAs per area (Figure 4.7L) and stress fibers oriented mainly around the cell borders (Figure 4.7C), possibly leading to decreased F-actin tension and decreased cell stiffness compared with single cells and groups. The decreased FA density and rearrangement of F-actin in monolayers suggests that the monolayer integrity is maintained more through cell-cell contacts than through cell-substrate contacts, while single cells must rely solely on cell-substrate adhesion for support.

Previously, it has been shown by Nelson *et al*. [156] that cell area and FA area both decrease with increasing cell density through activation of RhoA, which is in contrast to the increased cell area and FA size in our groups. However, in Nelson *et al*., when spreading area is confined using a micropatterned substrate, FA size is larger for two cells in contact, as compared with a single cell, which is in agreement with our results for groups. It could be possible that in our experiments, our cells had more free space around them during group formation, allowing for outward extension, while in Nelson *et al*. there was an increased cell density which restricted cell size. It would be interesting to investigate the effects of cell-cell contact length on FA size; using a micropatterned substrate, this could be achieved by increasing or decreasing the cell-cell contact region in Nelson *et al*.'s bowtie configuration.

To corroborate the notion that cell morphology affects cell stiffness, we simultaneously measured the stiffness and area of a spreading cell using AFM combined

with brightfield timelapse images. This experiment allowed us to observe changes in cell area without the presence of neighboring cells or cell-cell adhesions. Our measurements began when the cells were approximately 30-40% of their final spreading area. Our results show that HUVECs increase in stiffness as they spread (Figure 4.4), which might be expected since they transform from round spheres with a layer of cortical actin, to spread-out objects adhering to the substrate and containing a stiff network of cross-linked actin filaments and cortical actin under tension [162]. The value which the final Young's modulus approaches provides a rough indication of whether the cell body (compare with gray large dashed line in Figure 4.4) or periphery (compare with gray small dashed line in Figure 4.4) has been probed. For example, in Figures 4.4A and 4.4B the periphery is likely being probed, while in Figure 4.4C it is likely the cell body. We believe that the force exerted by the AFM cantilever had minimal effect on cell spreading, as we did not observe differences in spreading when we increased the time interval (30 seconds to 2 minutes) between "pokes" with the AFM cantilever. Further, HUVEC spreading in the presence of the AFM cantilever was similar to spreading in its absence, suggesting that the AFM tip itself had minimal impact on cell spreading. Further, using an AFM tip which contained a 5 μm bead was much gentler than using a sharp 10 nm-sized tip, which resulted in irregular spreading behavior.

Further, our results are consistent with the measurements that cell traction forces increase during spreading [157]. Interestingly, another previous study by Gauthier *et al*. (2009) showed that membrane tension decreases during cell spreading, as measured by optical tweezers [163]. However, this is not necessarily contradictory to our results. Because the thickness of the cell membrane is only on the order of 3-4 nm [164], and we

are probing approximately 250 nm into the cell, we are likely measuring the stiffness of the cortical actin rather than the cell membrane. Although the cell membrane and cortex are physically linked, the cortex likely provides more resistance to the AFM cantilever than the cell membrane itself, resulting in a stiffer measurement. Therefore, if it is true that the cell membrane softens during spreading, we would not be able to detect it.

The "morphology" curve represented by Figure 4.5 may be interpreted as the measured stiffness of a cell, given its area, and we can use it to roughly predict a cell's stiffness knowing its area. When we plot the average (area, stiffness; measured separately in different cells) of single cells and groups (data from Figures 4.2 and 4.3), the points lie on the morphology curve. Interestingly, the data point for single cells lies in the middle of the morphology curve, rather than at the upper end where it would be expected to lie for fully spread cells. To explain this, it could be possible that cells spread fully by 1 hour, but then detach slightly over the course of 16 hours; however, we also cannot fully rule out possible effects of the AFM cantilever, though for reasons discussed earlier in this section, we believe these to be minimal.

Meanwhile, the average (area, stiffness; measured separately in different cells) of monolayers (data from Figures 4.2 and 4.3) lies above the curve, indicating that its stiffness is higher than we would expect based on its area. Further, when we depolymerize actin filaments using a high dose of cytoB, the monolayer is completely disrupted, and the (area, stiffness; measured separately in different cells) of the cells returns to lie on the morphology curve. If we weaken junctions (e.g. through treatment with VE-cadherin antibody or a low dose of cytoB), the monolayer stiffness increases to

further from the morphology curve. Therefore, it seems possible that cell-cell contacts influence cell mechanical properties, but the form of this influence is currently unknown.

To further investigate the effects of cell-cell junction integrity on cell stiffness, we first used a titration of cytoB treatment to destabilize the cell-cell junctions to varying degrees. At the lowest dose of cytoB, the HUVEC monolayers show small disruption in cell-cell adhesions, indicated by tether-like structures at cell junctions in the AFM deflection image (white arrowheads in Figure 4.6D) while the F-actin does not appear to have changed (Figure 4.7F). Interestingly, the monolayer remains visibly intact, except for the tether-like structures, and there is an increase in cell stiffness (Figure 4.6A). This could in part be explained by the increased FA size and density with low cytoB treatment (Figure 4.7L), which may generate increased tension within the cells, even though we do not see differences in F-actin architecture. It could be possible that the low dose of cytoB is only affecting the cortical actin along the cell membrane, which might affect the overall tension balance in the cell. This may lead the stress fibers to take up some of the tension, resulting in increased cell-substrate adhesion and decreased cell-cell adhesion. In addition, cytoB is an actin filament capping protein rather than a direct depolymerization agent, and at low doses it could have other effects that lead to cell stiffening. Thus, with low cytoB treatment, it seems that we disrupt the cell-cell junctions minimally (according to AFM images) without completely breaking the cells apart and the stiffness of cells within the monolayer approaches that of single cells.

Our second approach to destabilize cell junctions was to apply a VE-cadherin antibody to the HUVEC monolayers. VE-cadherin is a homophilic protein which localizes to cellular junctions and binds to actin, leading to maintenance of tension

between cells [124, 165]. Further, VE-cadherin engagement has been demonstrated to activate RhoA [156], which would result in an increase in cell tension and stiffness. Treatment of EC monolayers with a VE-cadherin antibody decreases cell-cell adhesivity and increases monolayer permeability [166-168]. Thus, the treatment weakens cell-cell junctions without completely breaking them [168]. We expected that molecular engagement of homophilic VE-cadherin might be similar to the presence of leukocytes attempting to transmigrate at cell borders and therefore cause rearrangement of VE-cadherin away from the junction, an effect which has previously been validated [168]. We thought that the resulting effect would be similar to cytoB treatment, where the monolayers approach the stiffness of single cells. However, VE-cadherin is one of many proteins localized at cell-cell junctions, and how the antibody treatment affects the localization or bond strength of other homophilic junctional proteins remains unknown.

Despite the potential involvement of other junctional proteins, our results agree with the above hypothesis – HUVEC monolayers stiffen with VE-cadherin antibody treatment (Figure 4.6E). Though we do not observe changes in F-actin structure (Figure 4.7H), the increased size and density of FAs (Figures 4.7K and 4.7L) may cause the F-actin tension of cells within the monolayer to increase and approach that of single cells. It has been shown that development of cadherin adhesions causes an increase in integrin expression [169], as well as recruitment of vinculin to cell-cell adhesions, leading to a reduction in vinculin at FAs [170], so the opposite process may also be true, according to our results. Also in agreement with our data, de Rooij *et al*. [171] showed that epithelial cell scattering is induced by increased tension on cell-cell junctions (e.g. on stiffer surfaces or on extracellular matrices which promote larger FAs), suggesting that the F-

actin cytoskeleton mediates a cross-talk between cadherins in cell-cell junctions and integrins at the cell-substrate interface.

Further, we probed the stiffness of single cells treated with a VE-cadherin antibody in order to evaluate whether the antibody itself results in any changes in cell stiffness, possibly due to signaling events that are not associated with weakened cellular junctions. Neither the higher density of FAs (Figure 4.7L) nor the F-actin arrangement (Figure 4.7G) can account for the softening of the cells. We would expect the higher density of FAs to result in an overall increase in cell tension; however, the softening of the cells does not support this idea. While we do not know the specific reason for this softening, it seems obvious that VE-cadherin antibody treatment affects single cells differently than cells within a monolayer, further suggesting the importance of cell-cell adhesions in determining cell stiffness. Localization of VE-cadherin in single cells and monolayers is very different, and engagement of VE-cadherin in these two situations likely results in differences in activation of signaling pathways. For example, in monolayers, VE-cadherin localizes to cell-cell junctions and is physically linked to the actin cytoskeleton; this localization occurs when the cell meets a neighboring cell [156]. Thus, in single cells, engagement of VE-cadherin may result in biophysical changes which are not accounted for in our experiments and which cause softening of the cells.

In all experiments we observe that the cell periphery is statistically stiffer than the cell body. Previous studies have reported measurements that are both consistent with [172] and contradictory to [28] our finding. Possible reasons for disagreement in literature over whether the cell body or periphery is stiffer include the following: (a) differences in the amount of force applied to the cells and the timescale over which those

forces are exerted, both of which influence the measured mechanical properties of a viscoelastic material such as a cell; (b) differences in the maximum indentation fitted using the Hertz-Sneddon model, since very large indentations likely cause the stiff glass substrate to influence elastic measurements; and (c) differences in positioning of the AFM cantilever over the cell body, since the nucleus is the stiffest organelle in the cell (for review see Dahl *et al*., 2008 [173]) and is located in what we call the "cell body" region. Our force curves are taken by applying a small force, about 2 nN, over the course of one second. To eliminate the effects of the glass substrate, we fit our force curves to only the first 250 nanometers of indentation, which is small compared to the height of the cell, even at the periphery, which is about 600-800 nm in thickness, as measured by AFM topographic images. Further, because we are simultaneously obtaining AFM topographic images and force curves, we were able to choose to place the 25 force curve buffers at any region on the cell. While we did not know the exact position of the nucleus, our measurements show that consistently, the cell body is softer than the periphery, suggesting that we are not probing deep enough into the cell to "feel" the nuclear stiffness. Probing with deeper indentations into the cell could result in measurement of the stiffness of other structures within the cell, such as intermediate filaments, which have been shown to be important mechanotransducers within the cell [22, 174]. However, it has been shown that F-actin is the main contributor to cell stiffness [175], and that cell types with more pronounced F-actin networks are stiffer than cell types with less F-actin [176]. In previous reports, increased indentation depths led to two distinct slopes in the AFM force-distance curves [35, 177], corresponding to measurement of the stiffness of two distinct mechanical regions within the cell. Much further experimentation and

analysis are necessary to determine exactly which cellular structures and their interactions contribute to cellular stiffness. It would also be useful to identify whether the applied forces activate biochemical signaling pathways within the cell, perhaps through mechanosensitive transmembrane proteins such as syndecan-4 [178].

To summarize our observations regarding cell spreading, single cell to monolayer transition, and the effects of cell-cell adhesions in a monolayer, we created a schematic (Figure 4.8). In Figure 4.8A, the organization of cortical actin and stress fibers are based on the experimental observations of spreading cells, as previously described [157, 162]. According to these reports, a cell begins as a round sphere containing a layer of cortical actin. As it touches down onto the substrate and begins to form adhesions, actin polymerization initializes at the basal surface, with a layer of cortical actin remaining at the apical surface. At this point, there is probably still a low level of tension in the cell due to the immaturity of the F-actin filaments. The force of actin polymerization extends the periphery of the cell outward, and eventually mature stress fibers form, likely leading to an increase in internal tension within the cell. The final spread cell probably consists of a dense layer of highly cross-linked stress fibers stretched along the basal surface of the cell and an apical layer of cortical actin, which presumably also has undergone an increase in tension. We believe that this potential increase in tension of the F-actin architecture contributes to the overall increase in cell stiffness and is likely caused by myosin II, a motor protein known to cross-link actin filaments and subsequently pull on them. Previously, it has been shown that inhibition of myosin II via blebbistatin treatment leads to a decrease in cell stiffness also causes cell retraction [179]. This experimental observation agrees with our proposed model (Figure 4.8A); if we remove myosin II, the

stress fiber cross-links, the cell loses tension, causing relaxation of the actin cytoskeleton and a decrease in cell stiffness. Ultimately, in the cell spreading model, this would revert the cell to an earlier, softer, spreading state.

In Figure 4.8B, the transition from single cell to group to monolayer is summarized, according to our observations. Beginning in solitude, the spread cell contains a dense network of stress fibers, oriented locally in parallel groups. Eventually, more cells join the first cell and form what we refer to as a group, shown here as an island of four cells, all with cell-cell adhesions at the interior. While the F-actin architecture does not look significantly different from that of the single cell, we propose that the cells are extending outward at the periphery through actin polymerization, as evidenced by the increased size of both the cells and their FAs, yet they are still visibly connected to each other through cell-cell adhesions. The force of extension may generate more tension within the cells and thus an increase in cell stiffness. Then, as more and more cells enter the group, they begin packing and eventually form a monolayer. Note that in our schematic cartoon, the monolayer continues outward infinitely in all directions; pictured are cells at the interior. For reference, the compressive forces due to cell packing in the epithelial layer during morphogenesis have been measured to be quite sizeable [180, 181]. The stress fibers are arranged mainly around the periphery of the cell, suggesting that rearrangement has occurred due to the cell packing forces, resulting in softer cells. In a monolayer, there are less FAs per area, indicating that cell-substrate adhesion has decreased, but cell-cell adhesion has probably increased due to the formation of adherens junctions. The actin is linked to the cellular junctions through VE-cadherin, and the VE-

cadherin molecules on neighboring cells link to each other, creating a physical link between cells through which force can be transferred.

In Figure 4.8C, we propose a sketch which summarizes our observation on the effects of applying a VE-cadherin antibody or a low dose of cytoB, treatments which we and others have suggested to weaken cell-cell adhesions. Initially, the cell monolayer contains some degree of cell-cell and cell-substrate adhesions. Then, upon treatment to weaken the cell-cell adhesions, the cell-substrate adhesions become stronger as evidenced experimentally by larger and more area-dense FAs. Though we do not observe differences in F-actin architecture between the two monolayer states, the increased FAs suggest an increase in F-actin tension, resulting in a stiffer monolayer. Mechanically, the cell may seek to achieve a balance between cell-cell adhesion through cadherin activation and cell-substrate adhesion through integrin activation, and as one adhesion is decreased, the other increases [138, 182].

Figure 4.8. A schematic summarizes our observations of spreading cells and cells with varying degrees of cell-cell contact. **(A)** Prior to developing adhesions with the underlying substrate, the cell contains a layer of cortical actin beneath the membrane. This cortical actin network is soft compared with the parallel bundles of F-actin filaments (stress fibers) which polymerize and crosslink during spreading. Upon touching down on the substrate, the cell begins to adhere to the surface and actin polymerizes, causing the cell to extend outward onto its substrate. When it is fully spread, there exists a dense network of stress fibers which extend into the periphery of the cell, while a layer of cortical actin still remains. As the stress fibers contract, tension in the entire cell, including the cell body region, is increased. This generates the increased stiffness of the cell. **(B)** In the transition from a single cell to a network, the cells develop cell-cell contacts composed of numerous adhesion proteins. Because the cells have space around them to move, they likely extend outward through actin polymerization, while (visibly) still maintaining cell-cell contacts. Increased focal adhesion size at this point suggests that tension in the cell has increased, leading to increased cell stiffness. As more and more cells enter the group, they begin packing and eventually form a monolayer. Note that in our schematic cartoon, the monolayer continues outward infinitely in all directions; pictured are cells at the interior. Here, the stress fibers are arranged mainly around the periphery of the cell, suggesting that cell packing forces have caused rearrangement of F-actin, possibly resulting in softer cells. In a monolayer, there are less focal adhesions per area, indicating that cell-substrate adhesion has decreased, but likely cell-cell adhesion has increased. The actin is linked to the cellular junctions through VE-cadherin, and the

VE-cadherin molecules on neighboring cells link to each other, creating a physical link between cells through which force can be transferred. **(C)** Once in a monolayer, treatment with VE-cadherin antibody or a low dose of cytochalasin B presumably weaken cell-cell adhesions. Prior to treatment, the cells have some degree of cell-cell adhesion and cell-substrate adhesion. After treatment to weaken cell-cell adhesions, the cells develop stronger cell-substrate adhesions (larger focal adhesions), leading to increased tension, and thus increased stiffness, in the cells. If the monolayer is instead treated with a high dose of cytochalasin B, there is a complete loss of cell-cell adhesion, dissolution of focal adhesions, and decrease in cell stiffness due to the net depolymerization of actin filaments.

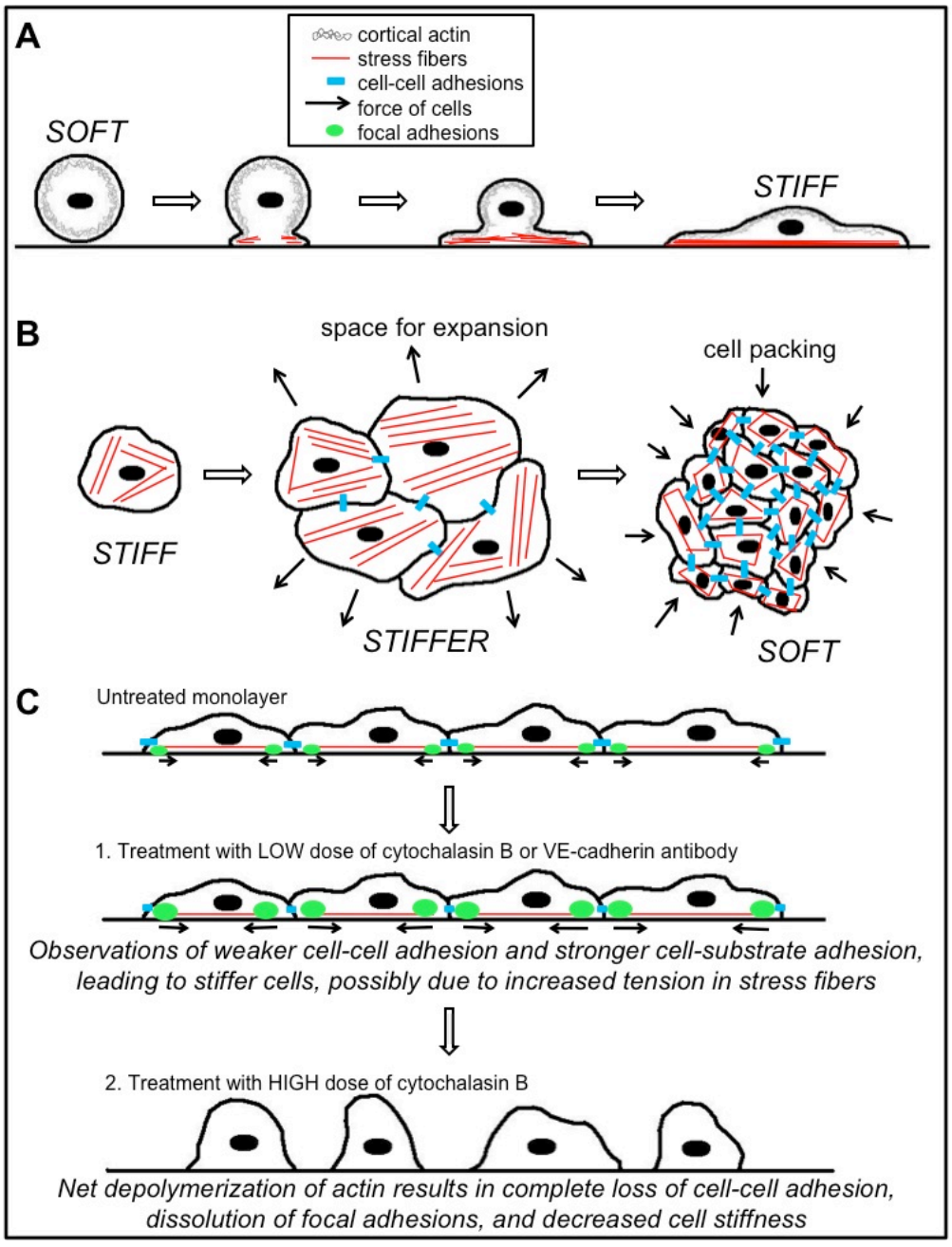

Previously, it has been shown that matrix properties such as substrate stiffness and extracellular matrix (ECM) coating affect cell-substrate adhesion, spreading area, and cell stiffness. In particular, cells have been found to spread less on softer surfaces and those with a low density of ECM protein at the surface, while cells spread more on stiffer surfaces and those with a higher density of ECM protein [54, 56, 60, 157, 183]. Further, cell stiffness increases as substrate stiffness increases [73-75] and as ECM density increases [184]. Together, these observations agree with our results, where increased spreading area correlates with increased cell stiffness. However, many of these experiments have been completed on single cells, and the role of substrate stiffness and ECM density in influencing cell-cell adhesion strength is only beginning to be understood. For example, Califano and Reinhart-King [54] have shown that softer surfaces with high ECM density promote formation and maintenance of cell-cell adhesions in EC networks, while EC networks do not form on stiffer surfaces with low ECM density. Further support of this idea is the work of de Rooj *et al.* [171], where epithelial cell-cell connections are disrupted through scattering on stiff surfaces and on those with high ECM density. These results suggest that both mechanical and chemical cues are incorporated as cells balance cell-cell and cell-substrate interactions. Further experiments where matrix mechanical and chemical properties are manipulated are definitely necessary to build upon our understanding of the relationships between cell morphology, cell stiffness, and cell-cell and cell-substrate adhesion.

4.5 Conclusions

In summary, cells within a monolayer are spatially confined due to the presence of neighbors and also have close adhesions with these neighbors at the junctions. In varying the degree of cell-cell contact in HUVECs (single cells, groups, and monolayers), we observe that increased cell stiffness roughly correlates with an increase in cell area. Further, we see that HUVECs stiffen as they spread onto a glass substrate. When we treat the cells with a low dose of cytoB or VE-cadherin antibody, treatments which presumably weaken cell-cell adhesions, we measure that cell-substrate adhesion increases, and the stiffness of cells within the monolayer approaches that of single cells. Our results together suggest that while morphology can roughly be used to predict cell stiffness, cell-cell interactions may play an important role in determining the mechanical properties of cells through maintenance of the balance between cell-cell and cell-substrate interactions. This biophysical balance may be disrupted in biological processes such as wound healing, angiogenesis, cancer cell metastasis, and immune cell transmigration.

5 Endothelial cells experience morphological, dynamical, and biomechanical changes in response to TNF-α †

5.1 Introduction

Tumor necrosis factor-alpha (TNF-α) is a cytokine produced by a variety of stromal cells, primarily monocytes and macrophages, as a result of an immune or inflammatory response. The vascular endothelium, which normally serves as a protective barrier between the blood vessel lumen and nearby tissues, undergoes a series of biological changes after binding TNF-α, resulting in increased permeability to both macromolecules [185] and immune cells (see Chapter 7). One of the most prominent biological changes is the increased expression of selectins, as well as adhesion molecules, including intercellular adhesion molecule-1 (ICAM-1) and vascular cell adhesion molecule-1 (VCAM-1), on the surface of the endothelium [186]. These molecules assist in the leukocyte adhesion cascade [186], which includes leukocyte migration along and transmigration through the vascular endothelium. At the same time, junctional molecules such as occludin and VE-cadherin dissociate away from the junctions, leading to decreased barrier function [187].

In addition to biological implications of TNF-α signaling, there is also evidence that TNF-α affects endothelial cell (EC) morphological and biomechanical properties. In this chapter, we utilize a variety of biophysical techniques to understand the links between EC morphology, biomechanics, and migratory dynamics after exposure of ECs to TNF-α. In this chapter we chose to evaluate single cells in order to simplify the

---

† This chapter is in preparation for submission to *Journal of Biomechanics*, as Stroka, K.M. and H. Aranda-Espinoza, Endothelial cells experience morphological, dynamical, and biomechanical changes in response to TNF- α.

system, since, for example, in Chapter 4 we showed that cell-cell adhesion affects EC stiffness. These changes in EC properties are key components of the inflammatory response, yet are often overshadowed by the biological changes that occur. We show that while, on average, TNF-α leads to significant alterations in cell shape and stiffness, there is actually a wide distribution of values for each of these properties, indicating a heterogeneous effect of TNF-α on cells. We also estimate cellular volume to be significantly larger after TNF-α treatment and use this result to connect observations of enhanced F-actin and decreased cell stiffness. In addition, our evaluation of migratory dynamics demonstrates an inverse correlation between cell aspect ratio and migration speed after TNF-α treatment, suggesting that cell shape may be an important functional regulator of EC migration during an inflammatory response. Finally, we address the basic mechanics of how the reorganization of F-actin filaments occurs; our experiments reveal that this occurs through a dynamic shift of existing filaments to an aligned configuration, rather than through depolymerization and repolymerization. Together, our results suggest a functional link between EC morphology, biomechanics, migration, and cytoskeletal dynamics during an inflammatory response.

5.2 Materials and methods

5.2.1 Cell culture

Human umbilical vein ECs (HUVECs) were purchased from Lifeline Cell Technology (Walkersville, MD) and cultured as previously described in Section 4.2.1. Glass coverslips (22x22 mm, Fisher Scientific, Pittsburgh, PA) were coated with 0.1 mg/mL fibronectin (Sigma, St. Louis, MO) for 2 hours at room temperature, and

HUVECs ($1x10^4$ total; passages 2-5) were plated onto the fibronectin-coated glass coverslips. Cells were incubated at 37°C, 5% CO_2, and 55% humidity overnight for approximately 16 hours and were subsequently treated with 25 ng/mL TNF-α or no treatment (control).

5.2.2 Cell staining

HUVECs were fixed in 0.5% glutaraldehyde (Ted Pella, Inc., Redding, CA) for 10 minutes and washed twice in phosphate buffered saline (PBS). Cells were then permeabilized and blocked for nonspecific binding as previously described in Section 4.2.2. Microtubules were stained by applying an anti-tubulin primary antibody (Invitrogen A11126, Carlsbad, CA) at 1:200 dilution (1 μg/mL) for 1 hour, followed by an anti-mouse Alexa488 secondary antibody (Invitrogen A11001) at 1:200 dilution (10 μg/mL). Primary and secondary antibodies were diluted in 2% bovine serum albumin with PBS. F-actin and nuclear DNA were stained as previously described in Section 4.2.2.

5.2.3 Cell transfection

Cells were transfected for GFP-actin using an Amaxa Nucleofector (Lonza, Walkersville, MD). Primary mammalian endothelial cell solutions (Lonza) were used in combination with program A-034 on the Nucleofector. After transfection, cells were plated onto fibronectin-coated glass coverslips and allowed to attach overnight. Cells were then rinsed and subsequently used in fluorescence timelapse microscopy experiments.

5.2.4 Atomic force microscopy

Young's moduli of live HUVECs were measured using an atomic force microscope (AFM; Agilent Technologies, Santa Clara, CA) as previously described in detail in Section 4.2.3. Briefly, a silicon nitride cantilever (Novascan, Ames, IA) with a spherical glass SiO_2 probe of diameter 5 μm was used to obtain typical force curve measurements on live HUVECs. Twenty-five force curves were taken on at least 10 cells for each condition (control and TNF-α), for a total of at least 250 force curves for each condition. Using a custom-written Matlab (The Mathworks, Natick, MA) program (Appendix A), data were fit to the Hertz-Sneddon model [144] for a paraboloid indenter [146], as previously described in Section 4.2.3. Cells were probed at both the "cell body" (raised portion) and "periphery" (near the base of the cell body, but not at the flattened lamellipodia). Indentations were much smaller (<20%) than the total cell height, indicating that the stiff glass substrate below the cell did not affect the force curves.

To estimate cell volume, the free and open source software Gwyddion was used. Cross-sectional plot profiles from AFM topograph images were taken across the major and minor axes of the cell (determined by eye). The plot profile was used to determine an approximate height of the cell body and periphery regions, as well as the lengths of the major and minor axes. Then, the cell volume was approximated by summing the volume of two ellipsoids, for the flattened portion of the cell and cell body, using the following equation:

$$\frac{4}{3}\pi\left[A_1B_1C_1 + A_2B_2\left(C_2 - C_1\right)\right]$$

where A_1 is the length of the minor axis of the flattened region, B_1 is the length of the major axis of the flattened region, C_1 is an estimate of the height of the flattened region,

A_2 is the length of the minor axis of the cell body, B_2 is the length of the major axis of the cell body, and C_2 is an estimate of the height of the cell body.

5.2.5 Microscopy

Phase contrast image timelapse sequences were taken in HUVEC culture media at 37°C, 5% CO_2, and 55% humidity using an Olympus IX71 (Olympus, Center Valley, PA) inverted microscope and a 10x/0.3 NA Ph1 objective. Images were captured using a QImaging Retiga-SRV charge-coupled device (CCD) digital camera (QImaging Corporation, Surrey, British Columbia, Canada) and IPLab software. Fluorescence images of GFP-actin-transfected cells were taken in HUVEC culture media at 37°C, 5% CO_2, and 55% humidity using an Olympus IX81 inverted microscope and a 60x/1.42 NA oil objective. Images were captured using a QImaging Rolera-MGi CCD digital camera (QImaging Corporation) and Slidebook software. Confocal images of cells stained for tubulin and F-actin were taken at room conditions using an Olympus IX81 scanning disk confocal microscope and a 6060x/1.42 NA oil objective. Images were captured using a Hammamatsu ORCA-ET CCD camera (Leeds Precision Instruments, Minneapolis, MN) using Slidebook software. Cell morphology (area and aspect ratio) were measured using ImageJ (NIH, Bethesda, MD). Cell speeds were calculated for each frame of the movie by dividing the cell's displacement by the time step (20 minutes). Then, a moving average of the previous 5 timepoints was plotted (as in Figures 5.3 and 5.4) to smooth the data.

5.3 Results

5.3.1 TNF-α results in a time-dependent, wide distribution of cell morphology

HUVECs were plated onto glass coverslips and given approximately 16 hours to spread; subsequently, phase contrast images were taken, and then the cells were treated with a physiological concentration of TNF-α (25 ng/mL) in culture medium. Phase contrast images were taken at 8 hours and 24 hours following treatment. Prior to TNF-α treatment, HUVECs displayed a distribution of areas (Figure 5.1A), while addition of TNF-α resulted in a shift of this distribution to the right after 8 hours of treatment (Figure 5.1B), and further to the right after 24 hours of treatment (Figure 5.1C). Importantly, at 24 hours, untreated (control) cell area was not different from cell area at 0 hours. Interestingly, the width of the distribution of areas became noticeably wider after 24 hours of TNF-α (Figure 5.1C). The increase in cell area throughout the course of treatment is also reflected in the average areas of untreated cells versus cells at 8 hours and 24 hours after addition of TNF-α ($P<0.001$) (Figure 5.1D).

HUVECs also underwent a change in aspect ratio due to TNF-α treatment. In comparison with the distribution of aspect ratios prior to treatment (Figure 5.1E), at 8 hours after addition of TNF-α, HUVECs were more elongated, as evidenced by the shift in the aspect ratio distribution peak to the right (Figure 5.1F). At 24 hours, the distribution shifted back to the left, though the distribution peak was still at a significantly larger aspect ratio than control cells (Figure 5.1G). The average aspect ratio of control cells versus cells at 8 hours and 24 hours after addition of TNF-α follows the trend of the distribution peaks and is statistically different ($P<0.001$) (Figure 5.1H).

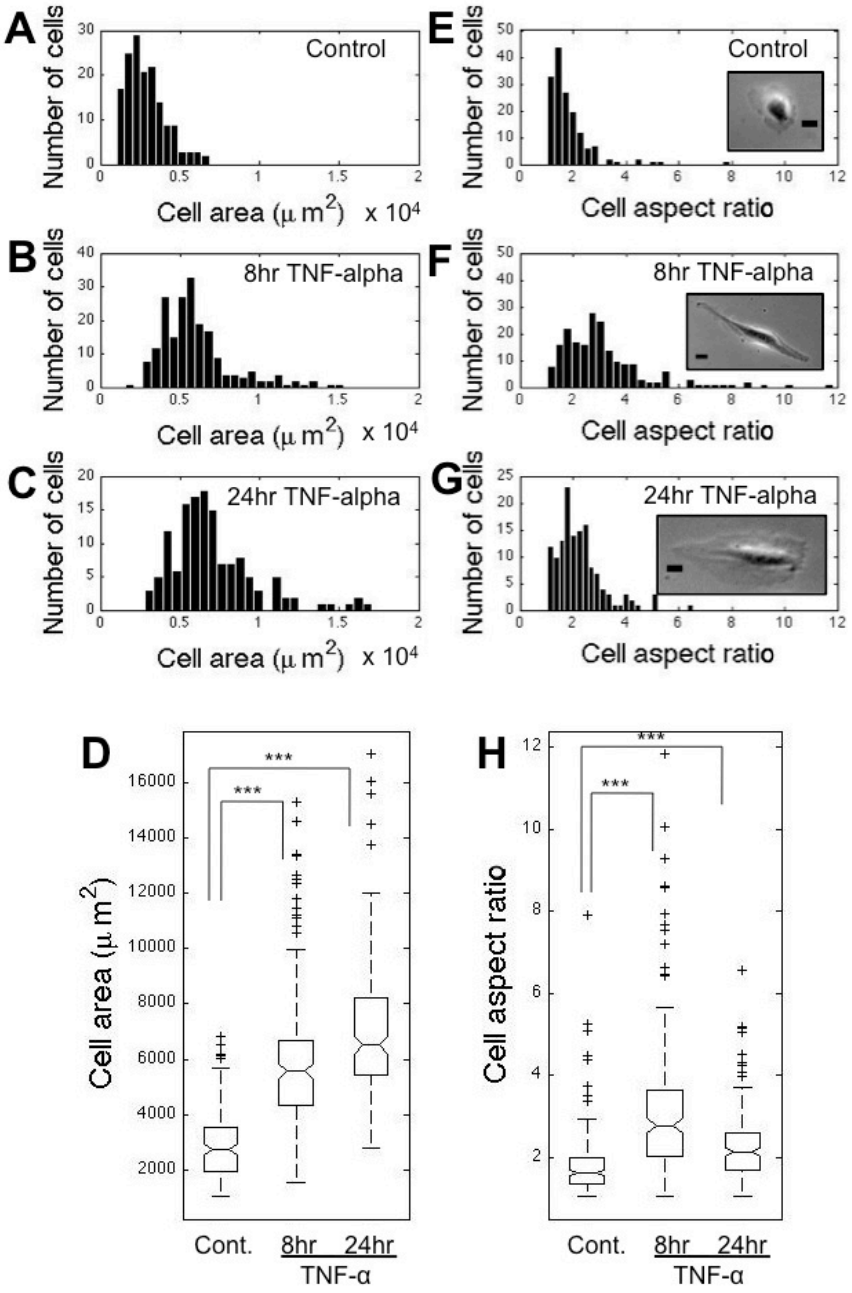

Figure 5.1. TNF-α induces changes in endothelial cell (EC) morphology. Shown are histograms of cellular area for **(A)** control, **(B)** 8-hour TNF-α-treated, and **(C)** 24-hour TNF-α-treated ECs. **(D)** Box and whisker plot indicates that average cellular area increases with TNF-α treatment. Also shown are histograms of cellular aspect ratio, calculated by dividing the length of the major axis by the minor axis, for **(E)** control, **(F)** 8-hour TNF-α-treated, and **(G)** 24-hour TNF-α-treated ECs. Insets in panels E, F, and G are representative images of cells for each condition. Scale bars for all insets are 20 μm. **(H)** Box and whisker plot indicates that average cellular aspect ratio increases with TNF-α treatment, with aspect ratios at 8 hours being significantly higher than those at 24 hours. *** indicates $P<0.001$ using Student's t-test.

5.3.2 TNF-α induces changes in cell biomechanical properties

Using AFM, we measured the stiffness (Young's modulus) of HUVECs, both at the periphery and cell body regions, as defined in Section 5.2.4. As we previously showed in Figure 4.3, the cell body region of control cells was softer than the periphery region (Figure 5.2A). The same trend was measured for cells after 24-hour exposure to TNF-α (Figure 5.2A). In addition, cells treated with TNF-α were softer than control cells at both the cell body and periphery regions ($P<0.001$) (Figure 5.2A). AFM deflection images of control (Figure 5.2B) and TNF-α-treated (Figure 5.2C) cells indicate the drastic changes in morphology that occurred in most cells after exposure to TNF-α. We also estimated cellular volume from the AFM topographic images, as described in the Section 8.2.4. Average estimated cell volume was larger for cells treated with TNF-α for 24 hours, in comparison with untreated control cells ($P<0.05$) (Figure 5.2D).

Figure 5.2. TNF-α induces changes in EC mechanical properties. **(A)** Box and whisker plot indicates EC stiffness decreases with 24-hour TNF-α treatment, both at the cell body and periphery regions, as measured by atomic force microscopy (AFM). *** indicates $P<0.001$ using Student's t-test. AFM deflection images of **(B)** control and **(C)** 24-hour TNF-α-treated ECs display the drastic change in morphology which occurs in most cells upon TNF-α exposure. AFM images are 90 μm by 90 μm. **(D)** Using AFM topographic information, cellular volume was estimated by summing the volume of two ellipsoids, for the flattened portion of the cell and cell body, using the equation and procedure outlined in Section 8.2.4. Top and side views of the relevant dimensions are shown. **(E)** Estimates of cellular volume for control and 24-hour TNF-α-treated ECs. * indicates $P<0.05$ using a Student's t-test.

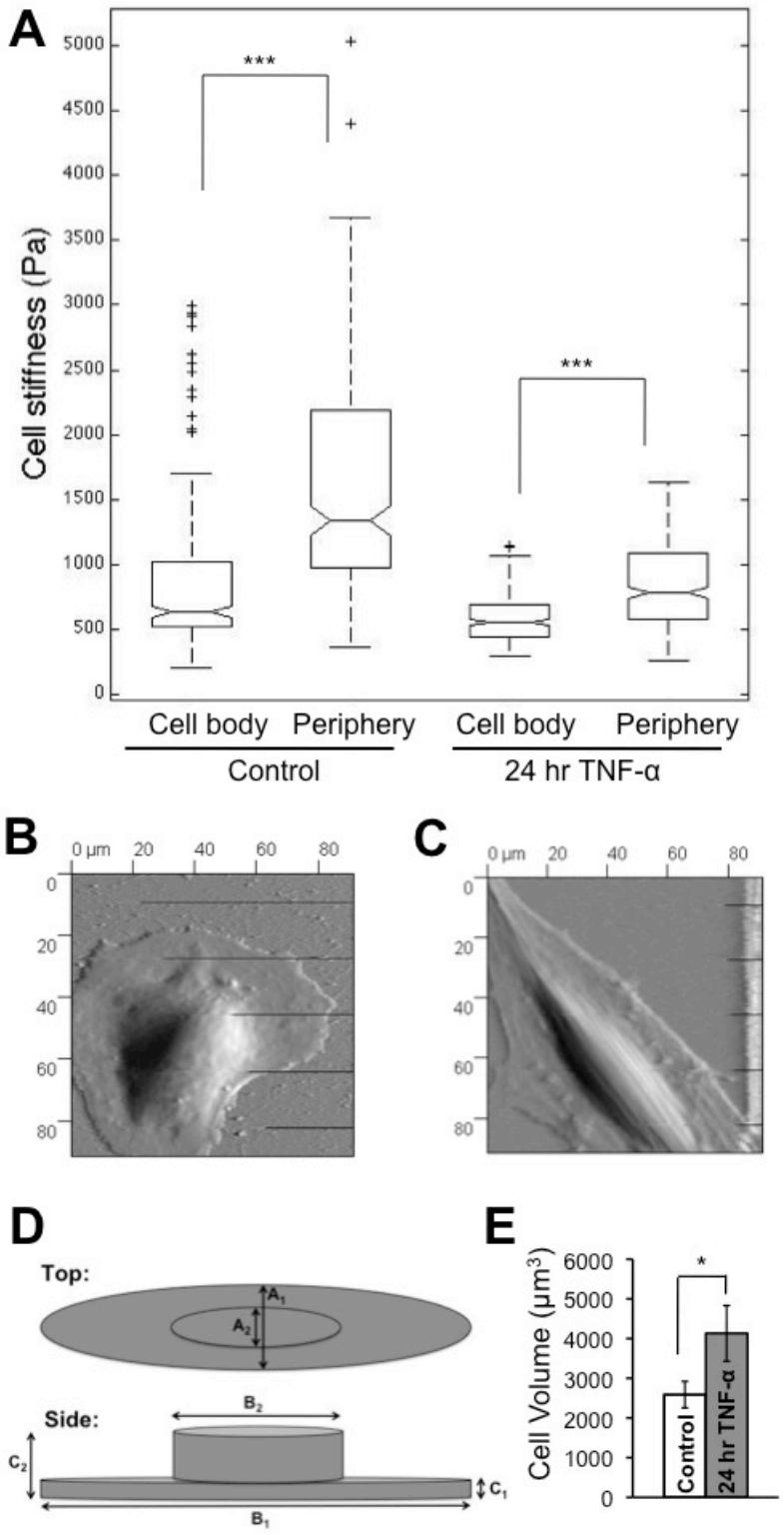

5.3.3 TNF-α induces inverse correlation between cell aspect ratio and migration speed

Using phase contrast timelapse microscopy we also evaluated the migratory behavior of HUVECs in response to TNF-α. In untreated control cells, aspect ratio and migration speed were not necessarily correlated. For example, in the representative cell shown in Figure 5.3A, as the time reaches point D on the plot, there is first a peak in speed that correlates with a peak in aspect ratio; however, the aspect ratio then drops off as the migration speed continues to increase. There is an additional peak in speed at point F, but this is not correlated with any changes in aspect ratio. Over the 24-hour period (of no treatment), the area of the control cell fluctuates and finally rises slightly. However, on average control cells are not larger after 24 hours. The change in aspect ratio at points C, D, E, and F on Figure 5.3A correspond to the phase contrast images shown in Figures 5.3C, 5.3D, 5.3E, and 5.3F, respectively.

In agreement with the average aspect ratio trends at 8 hours and 24 hours after addition of TNF-α (Figure 5.1H), most cells that we tracked individually experienced a peak in aspect ratio within the first 15 hours of TNF-α treatment, as in the representative cell shown in Figure 5.4A. Interestingly, in TNF-α-treated cells, aspect ratio was usually inversely correlated with cell migration speed (Figure 5.4A). For example, migration speed falls to the lowest value just before the aspect ratio peaks around point E in Figure 5.4A. Later, at point F, aspect ratio decreases rapidly as migration speed increases to a peak value. In addition, cell area increases steadily over 24 hours of TNF-α treatment (Figure 5.4B), which is in agreement with the average cell areas at 8 and 24 hours after addition of TNF-α (Figure 5.1D). The change in aspect ratio at points C, D, E, and F on

Figure 5.4A correspond to the phase contrast images shown in Figures 5.4C, 5.4D, 5.4E, and 5.4F, respectively.

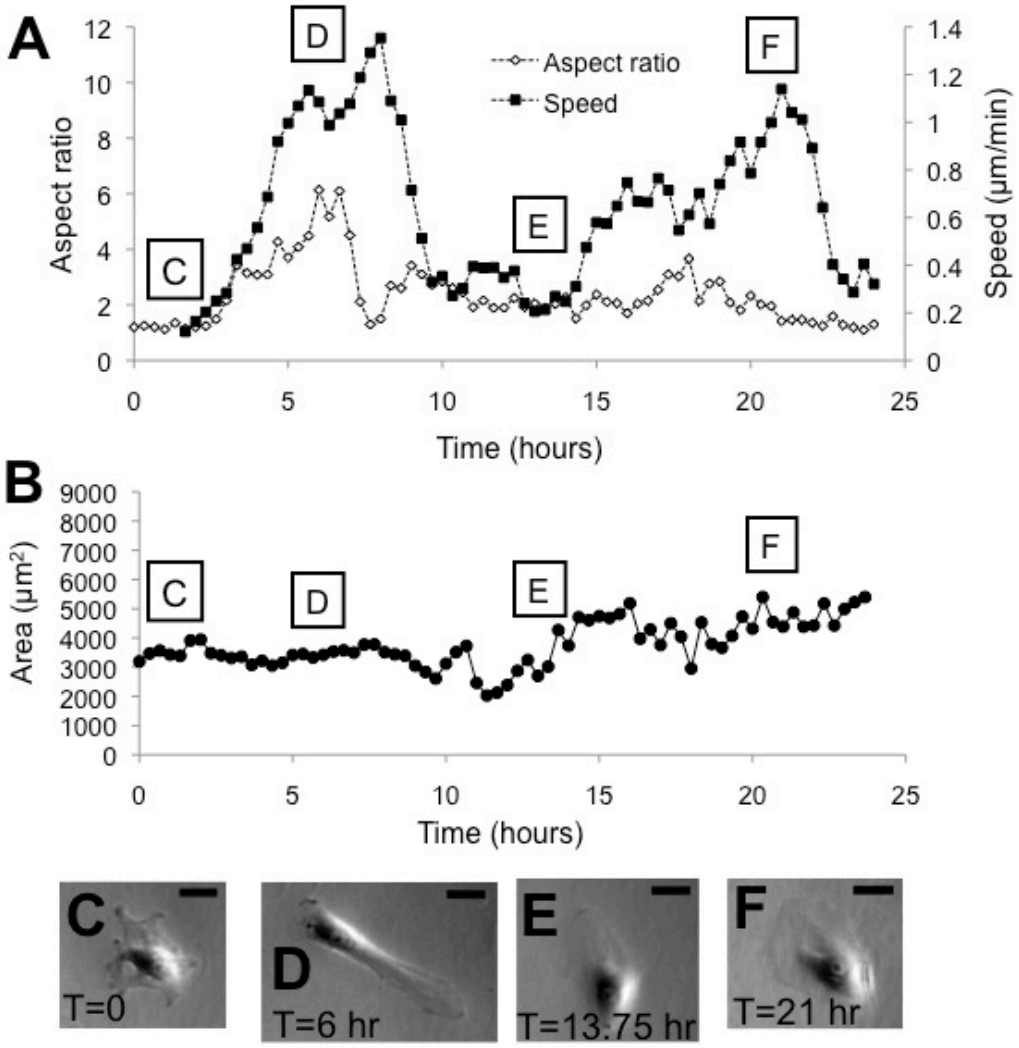

Figure 5.3. Cell speed is not necessarily correlated with aspect ratio in migrating control ECs. **(A)** Cell aspect ratio (primary axis) and speed (secondary axis) are plotted on the same axis for a migrating control cell (representative of 5 observed cells). **(B)** Cell area is plotted as a function of time. In panels A and B, time=0 corresponds to ~16 hours after plating cells. In panel A, letters C, D, E, and F correspond to timepoints relevant to the images shown in panels **(C)**, **(D)**, **(E)**, and **(F)**, respectively. Scale bar is 20 μm for all images.

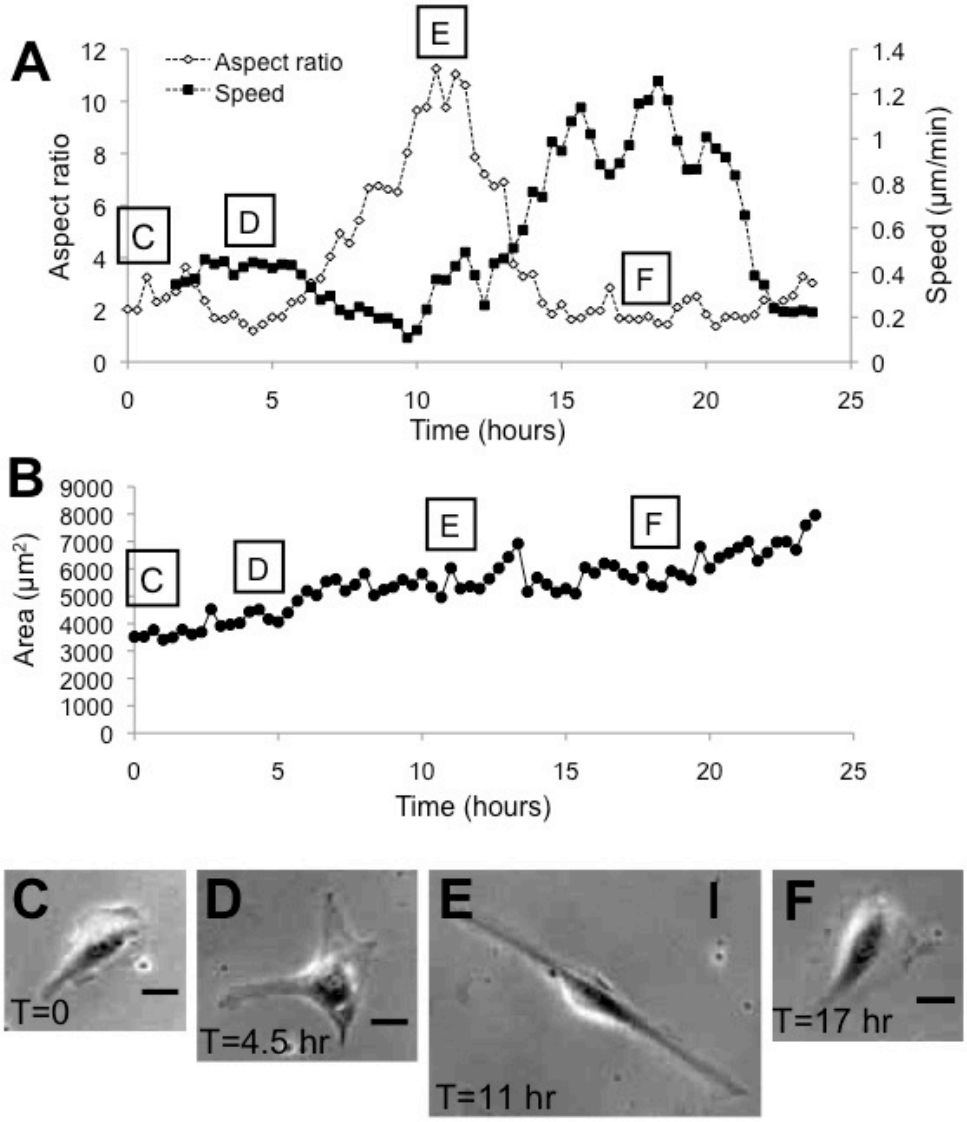

Figure 5.4. Cell speed is inversely correlated with aspect ratio in TNF-α-activated ECs. **(A)** Cell aspect ratio (primary axis) and speed (secondary axis) are plotted on the same axis for a migrating TNF-α-activated cell (representative of 5 observed cells). **(B)** Cell area is plotted as a function of time. In panels A and B, time=0 corresponds to ~16 hours after plating cells, which is the time when TNF-α was added to the cell media. In panel A, letters C, D, E, and F correspond to timepoints relevant to the images shown in panels **(C)**, **(D)**, **(E)**, and **(F)**, respectively. Scale bar is 20 µm for all images.

5.3.4 Actin and microtubule filaments align along cell major axis after TNF-α treatment

To evaluate the effects of TNF-α on the HUVEC cytoskeletal architecture, we stained for F-actin and immunostained for tubulin and captured confocal images of the cells. In control ECs, mature stress fibers formed and were arranged in parallel groups along the basal surface of the cells (Figure 5.5A). Microtubules were also present and were most densely arranged around the nucleus (Figure 5.5A). Activation of the cells with TNF-α induced significant changes in both the F-actin and microtubule organization of ECs. After 24-hour treatment with TNF-α, most cells' F-actin was arranged parallel to the major (long) axis of the cell (Figure 5.5B) Interestingly, microtubules followed the same pattern, as they were also mostly arranged parallel to the major axis of the cell, and thus were parallel to the F-actin (Figure 5.5B).

5.3.5 Actin rearranges dynamically upon exposure to TNF-α

In addition to a static evaluation of the effects of TNF-α on cytoskeletal architecture, we also wished to understand how the transition occurred dynamically. Specifically, we aimed to address the question of whether the F-actin reorganization involved depolymerization and repolymerization of actin, or whether it was simply a shift of existing actin fibers. Thus, we transfected HUVECs for GFP-actin and captured fluorescence images over the entire 24-hour period of TNF-α treatment. The timelapse sequence in Figure 5.6 indicates the dynamic shift of F-actin inward towards the nucleus as it aligns in parallel along the major axis of the cell.

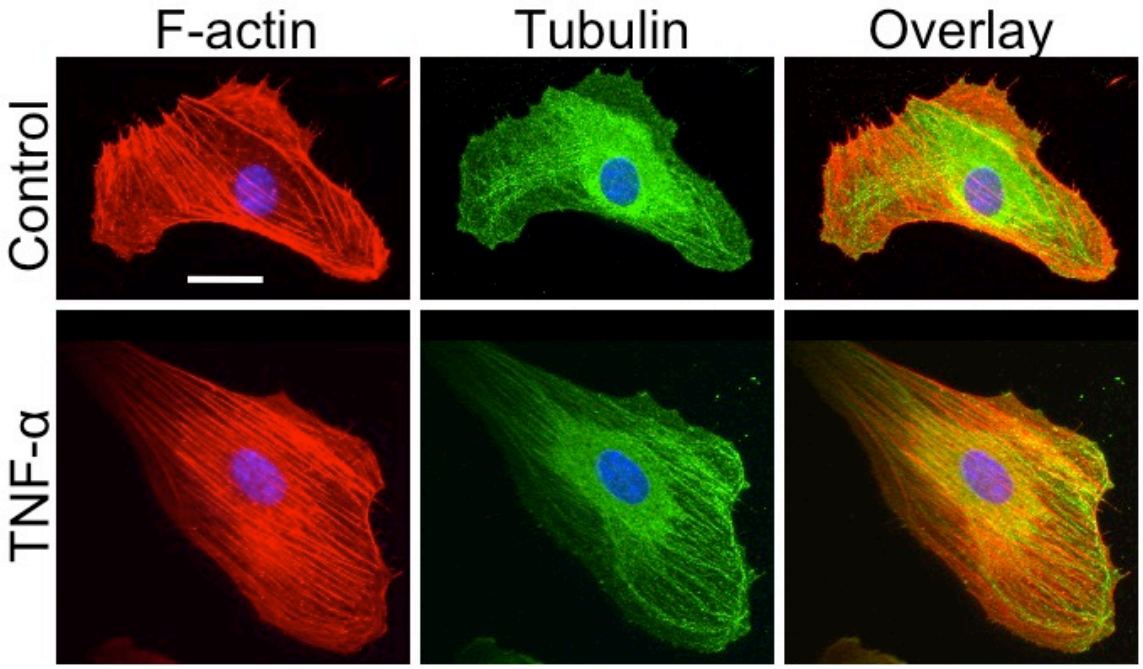

Figure 5.5. TNF-α exposure induces F-actin and microtubule alignment along cell major axis. ECs stained for F-actin (red) or DNA (blue) and immunostained for tubulin (green) are shown for control and 24-hour TNF-α-treated cells. An overlay of the red and green channels is also shown for each condition. Scale bar is 20 μm and applies to all images. The cells chosen are representative of at least 10 cells imaged.

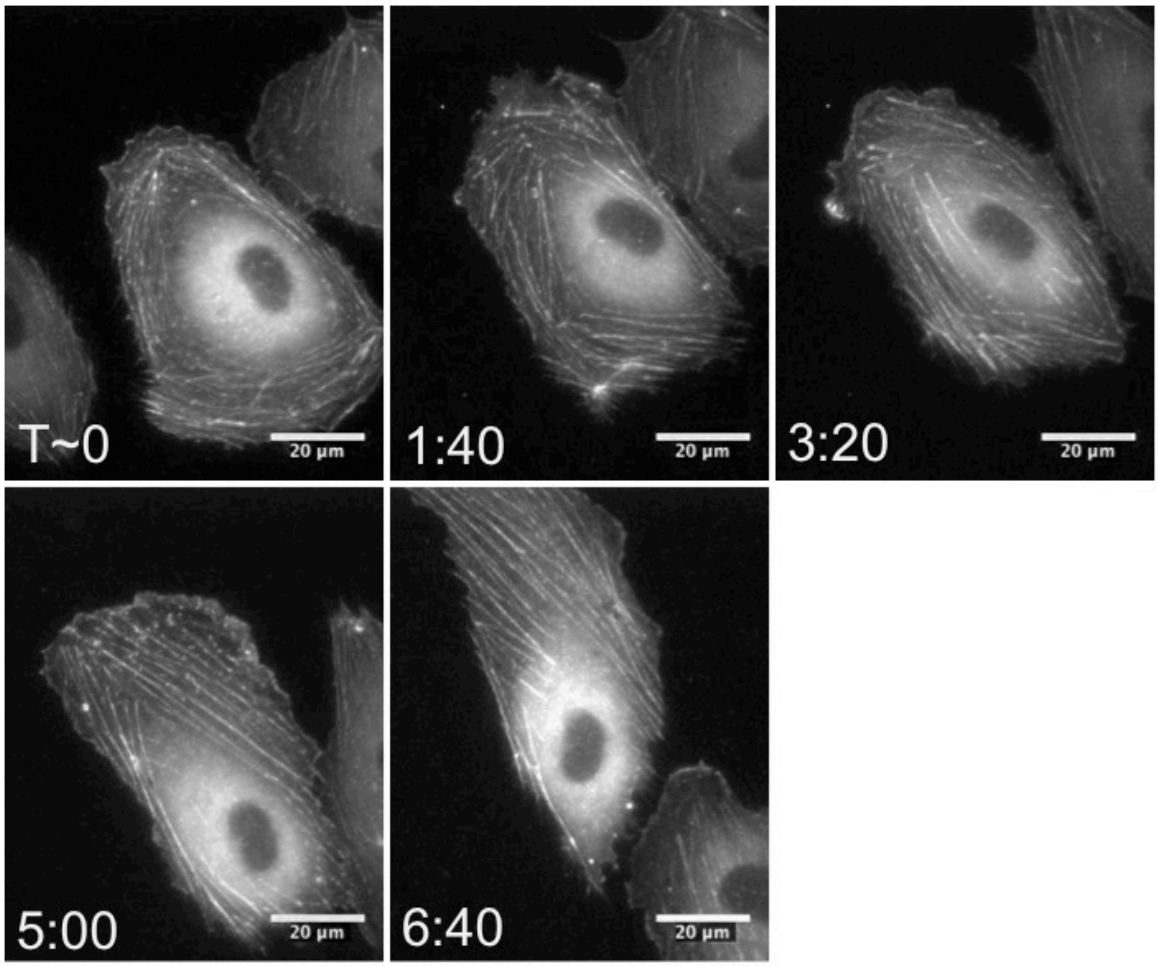

Figure 5.6. TNF-α-induced changes in the F-actin cytoskeleton involve a dynamic shift of existing actin filaments. ECs were nucleofected with GFP-actin and fluorescence images were captured after addition of TNF-α. Scale bar is 20 µm and applies to all images. T (lower left corner of each image) indicates the time (in hours:minutes format) after which TNF-α was added to the cell media.

5.4 Discussion

The immune response triggers a complicated sequence of events, one of which is release of the cytokine TNF-α from stromal cells such as monocytes and macrophages. TNF-α binds to the surface of the endothelium, initiating a signaling cascade that leads to drastic changes in junctional protein organization, adhesion molecule expression, permeability, morphology, and biomechanics. Here we focus on an often-ignored component of the inflammatory response, which is the link between EC morphology, biomechanics, migration, and cytoskeletal dynamics. These properties are important because, as we will see in Chapter 6, neutrophils are mechanosensitive and the biophysical properties of ECs are beginning to be understood as key regulators of the inflammatory response (Chapter 2).

While increases in cell area and aspect ratio have previously been reported as effects of TNF-α exposure [84, 187], here we demonstrate that this response is actually fairly heterogeneous, with a wide spread of values for both properties (Fig 5.1). In particular, the degree of elongation varies from the box-like morphology of untreated cells, to an extremely extended morphology (Figure 5.1F, inset), with aspect ratio around 10. In addition, the effect is time-dependent, with cell area increasing over 24 hours of exposure (Figure 5.1A-D). We also report, for the first time, a trend where aspect ratio peaks around 8 hours, and then drops off after 24 hours (Figure 5.1E-H). The dynamic shift of the F-actin over the first several hours of TNF-α treatment (Figure 5.6) indicates that changes in aspect ratio involve or are even caused by alterations in the cell's mechanical machinery, namely the cytoskeleton. This morphology behavior is also related to the migratory dynamics of the cell, as cell speed and aspect ratio are inversely

correlated in TNF-α-treated cells (Figure 5.4), but not in control cells (Figure 5.3). We suggest that this relationship arises because a high aspect ratio morphology is not adequate for efficient migration, and thus an elongated cell must first undergo deadhesion at the back end in order to migrate forward.

In addition, we hypothesized that the increased aspect ratio after 24 hours of TNF-α exposure is related to cell polarity, and thus we investigated the microtubule organization. Immunostaining for tubulin indicates that the microtubule network rearranges similar to F-actin, with filaments aligned parallel to the major length of the cell (Figure 5.5). Thus, the change in aspect ratio induced by TNF-α exposure can be explained by actin and microtubule arrangement and is also directly related to cell migration dynamics.

Changes in cell morphology and migration are often associated with biomechanical alterations. Here we show a decrease in cell stiffness after 24 hours of TNF-α exposure (Figure 5.2), which is consistent with previous reports [37]. This is the same time at which we observe both F-actin and microtubule cytoskeletal networks aligned parallel to the major axis of the cell (Figure 5.5). In addition, TNF-α exposure has been found to initiate Rho, ROCK, and myosin light chain kinase (MLCK) signaling pathways which are associated with cell contraction [187]. These data seem to be contradictory to a decrease in cell stiffness (Figure 5.2), as enhanced stress fibers and contractility are generally associated with increased cell stiffness [24]. However, we must also keep in mind that force measurements made by AFM utilize an indentation that is very small compared to the total height of the cell, and thus the Young's modulus measurements which we report are not necessarily reflective of the basal surface of the

cell, where the stress fibers are localized. Rather, our measurements are reflective of cell cytoplasmic or cortical actin stiffness. Thus, the significant increase in estimated cellular volume with TNF-α treatment (Figure 5.2E) can explain the decrease in cell stiffness, despite changes in F-actin that might suggest opposite effects on stiffness.

To our knowledge, we are the first to report an increase in EC volume after 24 hours of TNF-α treatment. An increase in stress fiber formation is a key characteristic of TNF-α treatment [187], as mentioned above. Likely, this event is accompanied by an influx of water and ions, and this could lead to changes in pressure that affect cell volume. Thus, while interesting, it is not surprising that TNF-α induces changes in overall cellular volume.

5.5 Conclusions

In conclusion, in this chapter we demonstrate that increases in cellular area, aspect ratio, and volume due to TNF-α exposure in single ECs are intrinsically related to cellular stiffness, migration behavior, and cytoskeletal organization and dynamics. Previously, much attention has been placed on the biological signaling due to cytokine exposure, though little work has focused on the biomechanics and dynamics of ECs in response to TNF-α. These biophysical properties of the vascular endothelium are key aspects of the immune response and are therefore likely to affect the efficiency of the leukocyte adhesion cascade. As one focus of Chapter 7, we will evaluate the effects of TNF-α on the biophysical properties of a confluent EC monolayer, and relate these changes to leukocyte migration and transmigration.

6 Neutrophils Display Biphasic Relationship between Migration and Substrate Stiffness†

6.1 Introduction

Cell migration has been established as essential for morphogenesis [188] and wound healing [189], as well as for tumor metastasis and angiogenesis [190]. Neutrophils are one type of migrating cell in the body's innate immune system and are the first line of defense against inflammation or infection. Infection in the body causes release of chemoattractant signals into the bloodstream and activation of endothelial cells (ECs) [49]. The neutrophil tethers to the EC wall through the cell adhesion molecules P-selectin and L-selectin, and then rolls and adheres firmly to the ECs as integrins on the neutrophil surface become activated [191]. Then, the neutrophil transmigrates through the EC wall into the intima of the blood vessel, where chemotaxis leads it to the source of infection. Finally, the neutrophil engulfs the infectious material through phagocytosis [49]. This entire process is often referred to as the leukocyte adhesion cascade.

Our experiments investigate neutrophil chemokinesis, or motility in a uniform concentration of chemoattractant. Neutrophils undergo chemokinesis during the middle phases of the leukocyte adhesion cascade, after they have attached and adhered to the EC wall. It has been reported that this stage of locomotion is necessary for transmigration to occur in monocytes [192]. Further, if the cells cannot transmigrate, they cannot travel to the source of infection and carry out their innate function. Because migration along the

---

† This chapter was originally published as Stroka, K.M. and H. Aranda-Espinoza (2009). Neutrophils display biphasic relationship between migration and substrate stiffness. *Cell Motility and the Cytoskeleton* **66**(6), 328-341. Permission was obtained from the publisher to use this material in the current dissertation.

EC wall is such an integral part of the leukocyte adhesion cascade, it is necessary to understand what factors influence motility during this stage.

Extensive work exists on the effects of adhesion proteins and integrin-ligand interactions on neutrophil motility [193-196]. Some work exists on the effects of shear stress on neutrophil adhesion and motility [196]. However, little is known about how neutrophil motility is affected by the stiffness of their physical environment. Studying these mechanical effects is important because often, changes in tissue stiffness indicate pathological conditions, such as in atherosclerosis and cancer. In order to develop new treatments for these conditions, a better understanding of how cells migrate on varying mechanical substrates is necessary.

EC stiffness is influenced by several known factors, as reviewed in Table 2.1. For example, ECs stiffen under shear stress as a function of the time exposed to and magnitude of the shear stress [28, 29]. Depleting the cholesterol from control bovine aortic ECs increases membrane stiffness, while enriching the cells with cholesterol does not affect the membrane stiffness [31]. Furthermore, cells can have a heterogeneous mechanical surface. For example, atomic force microscopy (AFM) experiments have revealed that the Young's modulus of human umbilical vein ECs ranges from 1.4 kPa near the edge of the cell to 6.8 kPa over the nucleus of the cell [41], while in bovine pulmonary aortic ECs the Young's modulus ranges from 0.2 to 2 kPa [42]. For comparison, by AFM measurements, cardiac cells have a stiffness of 100.3 kPa, while skeletal muscle cells are 24.7 kPa [41]. Therefore, there is heterogeneity in stiffness between different cell types and also within the same cell depending on location. Here, we are interested in how the mechanical properties of the substrate affect the immune

response, in particular, the morphology and motility of neutrophils. In our experiments, we are able to vary the stiffness of the substrate using polyacrylamide gels with different concentrations of crosslinker and thus use these gels to investigate neutrophil motility on surfaces of varying stiffness.

Previous research has shown that many types of cells respond to changes in substrate stiffness. For example, rat kidney epithelial cells, smooth muscle cells, and 3T3 fibroblasts spread less, exert smaller traction forces, and also display increased motility on flexible polyacrylamide substrates, as compared to stiffer substrates [25, 56, 61]. Bovine aortic endothelial cells (BAECs) also show increased spreading areas and spreading rates, as well as upregulation of α5 integrins on stiffer gels [56]. Substrate stiffness also affects neurite outgrowth and branching in neurons [62, 63], and directs differentiation of stem cells [64]. However, in contrast to other cell types, it has been reported that neutrophil perimeter after activation remains constant regardless of substrate stiffness, from surfaces as soft as 2 Pa to glass [56]. Results in this chapter contradict this report; here we show that substrate stiffness affects neutrophil morphology, spreading area, and motility. In particular, we demonstrate that there exists a robust biphasic relationship between the track speed and substrate stiffness. The stiffness of maximal motility increases when the ligand concentration on the surface of the gel is decreased. This biphasic behavior with substrate stiffness is consistent with results previously published for smooth muscle cells [197].

6.2 Materials and methods

6.2.1 Preparation of polyacrylamide gels

Polyacrylamide gels were attached to glass coverslips by a method previously described [198]. In brief, 22x22 mm glass coverslips (Fisher Scientific, Pittsburgh, PA) were flamed in a Bunsen burner, soaked in 0.1 M NaOH (Fisher Scientific, Pittsburgh, PA) and air-dried. The coverslips were coated with 3-aminopropyltrimethoxy silane (Sigma, St. Louis, MO) and fixed with 0.5% glutaraldehyde (Sigma, St. Louis, MO) in phosphate buffered saline (PBS). Polyacrylamide gels were prepared with varying concentrations of acrylamide (40% Acryl; Bio-Rad, Hercules, CA) and bisacrylamide (2% Bis; Bio-Rad, Hercules, CA) to vary stiffness. Concentrations used included 8% acrylamide + 0.2% bis, 8% acrylamide + 0.1% bis, 8% acrylamide + 0.07% bis, 8% acrylamide + 0.04% bis, and 5% acrylamide + 0.05% bis. Pre-gel solutions were degassed for 20 minutes in a vacuum chamber and polymerization was initiated with 10% ammonium persulfate (APS; Bio-Rad, Hercules, CA) and catalyzed with N,N,N',N'-Tetramethylethlenediamine (TEMED; Bio-Rad, Hercules, CA). 25 µL of gel solution was placed onto each activated coverslip and another coverslip (22 mm diameter; Fisher Scientific, Pittsburgh, PA) created a sandwich over the drop. The coverslip-gel assembly was inverted during polymerization. After polymerization the top coverslip was removed and gels (~80 µm thick, as measured by microscopy) were rinsed with 50 mM HEPES (Fisher Scientific, Pittsburgh, PA). 200 µL of 0.5 mg/mL sulfosucinimidyl 6 (4'-azido-2'-nitrophenyl-amino) hexanoate (sulfo-SANPAH; Pierce, Rockford, IL) in 50 mM HEPES, pH 8.5, with 0.05% dimethyl sulfoxide (DMSO; Fisher Scientific, Pittsburgh, PA) were pipetted onto the surface of each gel and exposed to UV light at a distance of 5 inches for

10 minutes. The sulfo-SANPAH was removed and the photoactivation procedure was repeated. Gels were rinsed twice with 50 mM HEPES, and 300 µL of either 10 µg/mL, 100 µg/mL, or 500 µg/mL fibronectin (FN; Sigma, St. Louis, MO) was placed onto the gels and allowed to react for 4 hours at room temperature. Substrates were then rinsed 3 times with PBS.

6.2.2 Determination of Young's moduli of gels

Bulk mechanical properties of the polyacrylamide gels were investigated using the Q-800 Dynamic Mechanical Analyzer (DMA; TA Instruments, New Castle, DE) and Q Series Explorer software. Bulk samples of height were cyclically compressed at 1 Hz to a strain of 1%. In this strain range the polyacrylamide gels are linearly elastic, with a linear stress-strain relationship and Young's modulus as the slope. 4-5 different samples of each gel were tested. This analysis resulted in values for Young's modulus of 2.8±0.5 kPa (5% acrylamide + 0.05% bis), 3.7±0.9 kPa (8% acrylamide + 0.04% bis), 5.2±1.6 kPa (8% acrylamide + 0.07% bis), 6.6±2.4 kPa (8% acrylamide + 0.1% bis), and 13.2±2.0 kPa (8% acrylamide + 0.2% bis). These values are consistent with previously published Young's moduli for gels composed of similar concentrations of acrylamide and bis [199].

6.2.3 Characterization of surface-bound fibronectin on gel surface

Polyacrylamide gels were coated with fibronectin, as discussed above. 2% bovine serum albumin (BSA; Sigma, St. Louis, MO) in PBS was applied to the gels for 30 minutes at room temperature. Gels were then incubated with 200 µL of 100 µg/mL

primary anti-fibronectin antibody (Abcam, Cambridge, MA) in 2% BSA+PBS for 1 hour at room temperature in a humidity chamber. Gels were washed 3 times in PBS, for 5 minutes each on a rocker. Gels were then incubated with 200 μL of a 1:100 dilution of the IgG antibody conjugated to Texas Red fluorescent probe (Abcam, Cambridge, MA) in 2% BSA+PBS for 1 hour at room temperature in a humidity chamber. Gels were washed 3 times in PBS, for 5 minutes each on a rocker. Fluorescence images were taken of the gels and relative intensity levels were quantified using ImageJ software. Polyacrylamide gels without protein and immunostained in the same way were used as a control.

6.2.4 Neutrophil isolation

Blood was taken from healthy human donors into BD Vacutainers containing K_3EDTA (Becktin Dickenson, Franklin Lakes, NJ) at the University of Maryland Health Center. 7 mL of blood were layered onto 4 mL of Polymorphprep media (AXIS-SHIELD PoC, Dundee, Scotland) and centrifuged at 23°C, 500g for 1 hour. Neutrophils were washed once in HBSS and centrifuged at 4°C, 350g for 10 minutes. Neutrophils were then resuspended in a buffer solution containing 10 mM HEPES and 0.1% human serum albumin (HSA; Sigma, St. Louis, MO) in HBSS. Methods were approved by the University of Maryland Institutional Review Board, and donors gave written consent.

6.2.5 Chemokinesis experiments

For each gel, a thin strip of vacuum grease was applied around a hole bored out of a small plastic Petri dish (Nunc, Rochester, NY) and the coverslip with gel attached was

pressed into the dish over the vacuum grease, forming a water-tight seal to contain liquid. Substrates were stored at 4°C in Hanks Balanced Salt Solution (HBSS; Gibco, Carlsbad, CA) overnight and sterilized under ultraviolet light for 15 minutes prior to plating cells.

A total of approximately 10^5 neutrophils in buffer solution were plated onto gels with 2 mM $MgCl_2$ (Sigma, St. Louis, MO), 1.5 mM $CaCl_2$ (Acros Organics, Morris Plains, NJ) for a total volume of 2 mL. Neutrophils were incubated for 5 minutes at 37°C, during which neutrophils remained passive. Neutrophils on gels were stimulated with 10 nM N-Formyl-Met-Leu-Phe (fMLF; Fisher Scientific, Pittsburgh, PA). Timelapse experiments were completed at 37°C using an Olympus IX71 inverted microscope. Images were captured every 10 seconds for a period of 30 minutes with a QImaging Retiga-SRV charge-coupled device digital camera (QImaging corporation, Surrey, British Columbia, Canada) at a magnification of 20X. All experiments were performed within 8 hours of obtaining human blood.

6.2.6 Quantification of motility

Centers of mass (in x,y coordinates) and areas of neutrophils were tracked through timelapse image sequences using ImageJ analysis software (National Institutes of Health, Bethesda, MD). Cell outlines were traced by hand in ImageJ for all images in each sequence. To obtain an estimate of the error associated with tracing cells by hand, the same cell was traced by hand 10 times each by three different people. The three resulting measurements for this particular cell's area (average ± standard deviation) were 258±4 μm^2, 259±2 μm^2, and 258±4 μm^2. For the same cell, the standard deviation associated with the centroid position measurements was about 0.03 μm using the same

method. Both Excel (Microsoft Corporation, Redmond, WA) and a self-written Matlab (The Math Works, Inc., Natick, MA) program (Appendix B) were used to quantify the spreading area, speed, and diffusion coefficient of neutrophils. The "overall" area of a given cell was time-averaged for all images in a timelapse sequence. Areas for each 5-minute time interval were also time-averaged (for 0-5 minutes, 5-10 minutes, 10-15 minutes, etc.).

Neutrophil track speed was calculated for each cell by time-averaging displacements of centroids for each time interval in the sequence and dividing by the time interval (Figure 6.1). Mean areas and speeds for 8-10 cells were averaged to give the total mean area or speed for one experiment. Experiments were repeated 3 times. Each independent experiment used blood from a different donor. Statistical significance was determined using a Student's t-test. Reported values are the averages of these three experiments, plus/minus the standard error.

Diffusion coefficients were calculated in the following way. To compute the sliding average of mean-squared displacements (MSD), the square of the distance traveled in the x-direction plus the square of the distance traveled in the y-direction was time-averaged for each time step λ and also for every time step $n*\lambda$, for every n up to the total number of time steps. This analysis was repeated for each neutrophil. The MSDs for every λ were averaged over all cells and MSD versus time was plotted. Neutrophil motility can be approximated as a nonlinear random walk according to the Langevin-type equation,

$$r^2 = 4D\,(t - \tau\,(1 - e^{-t/\tau}),$$

where r^2 is the two-dimensional mean-squared displacement, D is the random motility coefficient, t is time, and τ is the persistence time [200]. The linear portion of MSD versus time can be more simply fit to the equation $r^2 = 4Dt$, to obtain the random motility coefficient, D, which was confirmed to be of similar value to that obtained using the full Langevin equation. The exponent, α, in the power law relationship between mean square displacement and time ($r^2 \propto t^{\alpha}$) was determined by the slope of the natural log-log plot of r^2 versus t. Values of mean area (A), track speed (v), random motility coefficient (D), and α were averaged over 3 independent experiments to give the mean values and standard errors presented in this manuscript.

Finally, turning angles of neutrophils were calculated in the following way (Figure 6.1). The displacements of neutrophils between adjacent time steps, λ_n and λ_{n+1}, were used as vectors $\vec{d}_n$ and $\vec{d}_{n+1}$ and the angle between the vectors was computed using

$$\cos(\theta_n) = \frac{\vec{d}_n \cdot \vec{d}_{n+1}}{|\vec{d}_n||\vec{d}_{n+1}|} \quad .$$

The distribution of angles from three independent experiments for each substrate stiffness was used to form histograms.

6.3 Results

6.3.1 Fibronectin coating is independent of substrate stiffness

Immunostaining of the polyacrylamide gels with a primary anti-fibronectin antibody and secondary IgG antibody conjugated to Texas Red revealed similar fluorescence intensities on polyacrylamide gels with 100 µg/mL fibronectin. The 5% acrylamide gel was also coated with 500 µg/mL fibronectin and immunostained as

described above, resulting in a similar fluroscence intensity to the 8% acrylamide gels coated with 100 μg/mL fibronectin.

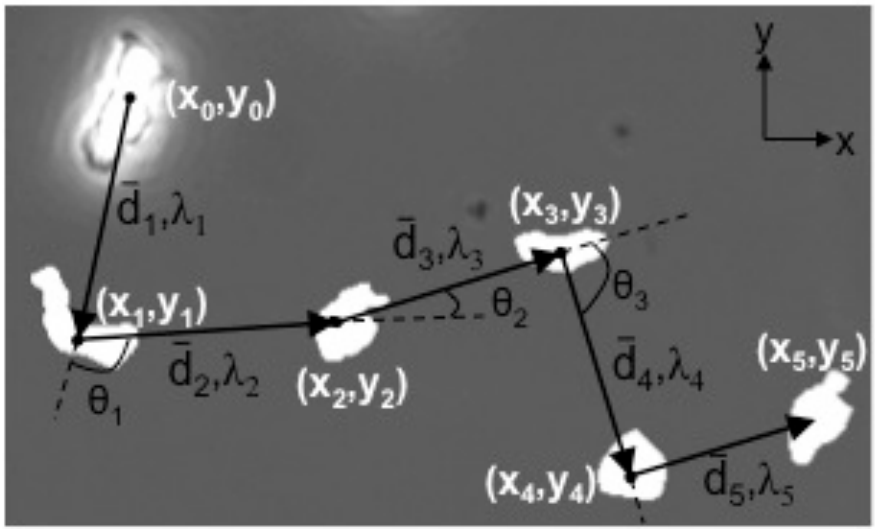

Figure 6.1. Method for quantification of neutrophil motility from a series of timelapse images. Positions of neutrophils are indicated in white, while their displacements from frame to frame are indicated with black arrows. The neutrophil begins at position $(x_0,y_0) = (0,0)$. The orientation of the coordinate system is shown in the upper right hand corner of the image. The first displacement takes place in the first timestep, λ_1, and the neutrophil travels a distance $\left|\vec{d}_1\right|$ during this time to end at position (x_1,y_1). Then, the neutrophil makes a turn at an angle of θ_1 from its original path, and during the second timestep λ_2, travels a distance $\left|\vec{d}_2\right|$ to its second position (x_2,y_2). This analysis continues through all frames of the sequence, as the neutrophil travels from position to position over the gel. Then, the speed of the neutrophil is calculated as the average magnitude of N displacements divided by the timestep: $v = \frac{\langle d \rangle}{\lambda}$, where $\langle d \rangle = \frac{1}{N}\sum_{n=1}^{N}\left|\vec{d}_n\right|$. The angle of turning, θ_n, is calculated using $\cos(\theta_n) = \frac{\vec{d}_n \cdot \vec{d}_{n+1}}{\left|\vec{d}_n\right|\left|\vec{d}_{n+1}\right|}$. Because cos(θ) is an even function, no distinction is made between left and right turns.

6.3.2 Neutrophil morphology depends on substrate stiffness

Neutrophils were isolated as explained in Section 6.2.4, plated on fibronectin-coated polyacrylamide gels, and activated with fMLF. Simple inspection of the neutrophils after activation indicates dramatic morphological differences on the gels of varying stiffness. We find that neutrophils on 13 kPa gels spread more than those on 4 kPa or 3 kPa, where the neutrophils are less spread (Figure 6.2). On 13 kPa, the cells are flattened on the gel substrate such that the nucleus and leading edge of the cell both appear dark in phase contrast microscopy images in comparison with the rest of the cell (Figure 6.2). Neutrophils on 4 kPa and 3 kPa appear brighter because the cell height is greater due to less adhesion and thus light is scattered by the cell. The presence of small protrusions over the body of the cells indicates that the cells are activated. Over the 30 minute timelapse, an average of 79% of cells display the well-spread isotropic characteristic morphology on 13 kPa, while only 19% and 8% display this well-spread morphology on 4 kPa and 3 kPa gels, respectively (Figure 6.3). Note that "well-spread" is defined here as having an area greater than about 120 μm^2. This was chosen considering that a passive neutrophil has a projected area of about 75 μm^2, while cells spread on the stiffest gel have an area of about 360 μm^2, at their largest spreading area (Figure 6.4A). Thus, an area of 120 μm^2 clearly separates characteristic morphologies on 4 kPa and 13 kPa. It is at the earlier time points when a small percentage of neutrophils are well-spread on the softer gels (Figure 6.3). A maximum percentage of cells are spread on all stiffnesses around 7.5 minutes. Following this time point, the cells on 4 kPa and 3 kPa begin to retract and display the morphology characteristic on 4 kPa or 3 kPa gels. Once retracted, these cells do not spread again. Note also that t=0 indicates the start of the

timelapse capture; this is within 30 seconds of fMLF addition. At this point, neutrophils have already begun to spread. Figure 6.3 indicates data for neutrophils spreading on 100 μg/mL fibronectin; similar spreading patterns were observed for neutrophils spreading on 10 μg/mL fibronectin.

Quantitatively, the mean spreading area (A) of neutrophils averaged over 30 minutes on 13 kPa (100 μg/mL fibronectin) is 310±70 μm^2, which is larger than on both the 3 kPa and 4 kPa gels ($P<0.05$), where the mean spreading areas are 70±20 μm^2 and 79±2 μm^2, respectively (Figure 6.4A) (see Section 6.2.6 for how areas were calculated). When averaged over 30 minutes, the area on 3 kPa and 4 kPa are not statistically different ($P>0.05$). The time evolution of spreading area in 5 minute intervals indicates that the average area on 13 kPa decreases throughout the 30 minute timelapse, but remains statistically larger than the areas on 4 kPa and 3 kPa at all time points ($P<0.05$). At t = 15, 20, and 25 minutes the area on 4 kPa is statistically larger than on 3 kPa ($P<0.05$). Figure 6.4B indicates the spreading area versus time for one characteristic cell on each of 3 kPa and 13 kPa gels, as well as two cells on 4 kPa. Two area versus time plots are included for 4 kPa to display a cell whose area remains fairly constant [4 kPa (1)] and also a cell which initially is well-spread, but then retracts and remains unspread for the remainder of the timelapse [4 kPa (2)]. The morphology through time for these same 4 cells is shown in Figure 6.4C, in 5 minute intervals. Neutrophils on 10 μg/mL also show an increase in area as stiffness increases.

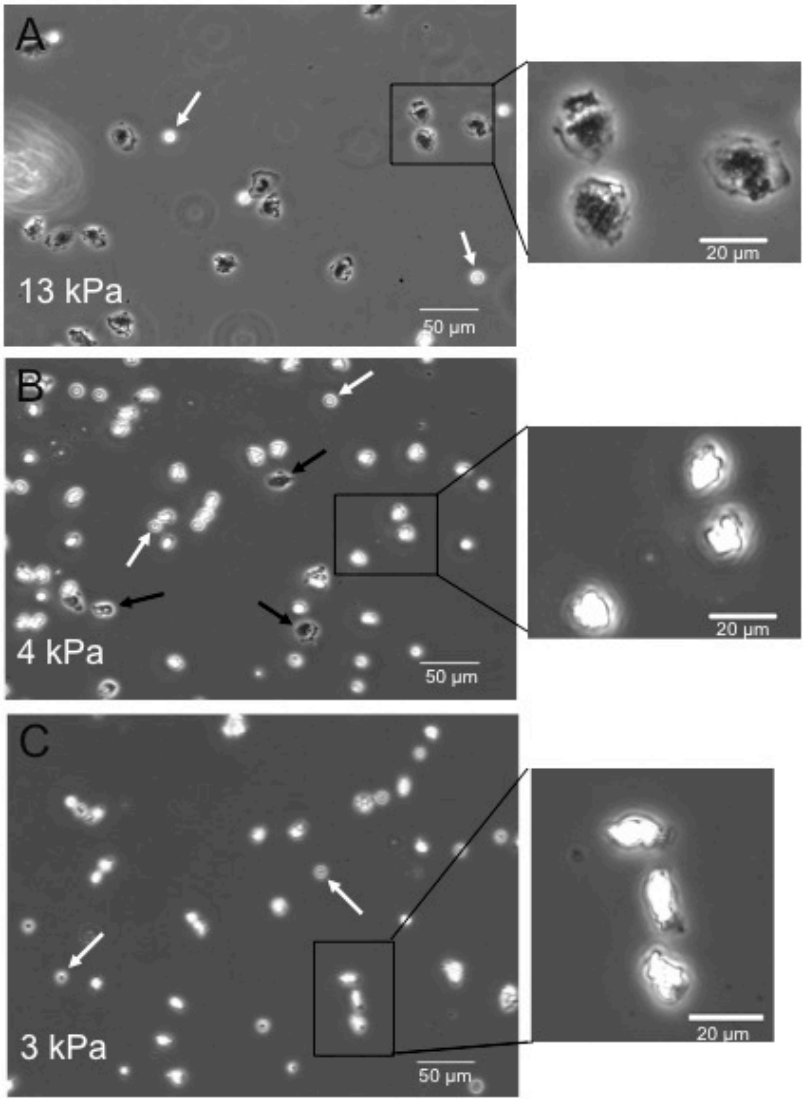

Figure 6.2. Effects of substrate stiffness on neutrophil morphology. Phase contrast images show cells exhibiting characteristic morphologies on **(A)** 13 kPa, **(B)** 4 kPa, and **(B)** 3 kPa fibronectin-coated (100 µg/mL) polyacrylamide gels after activation with a uniform concentration of 10 nM fMLF. Insets show magnified morphologies for each stiffness. The morphologies displayed in the insets indicate the morphologies of the majority of the cells on each gel. White arrows point to red blood cells. Neutrophils on 13 kPa **(A)** appear flattened and well-spread, with darker areas of the cells indicating the nucleus and leading edge. Neutrophils on 4 kPa **(B)** appear brighter because the cell height is greater than on 13 kPa since the cell is not well-spread, and thus light is scattered by the cell. The presence of small protrusions over the body of the cell indicates that the cell is activated. Black arrows point to examples of neutrophils on 4 kPa which initially spread similar to the characteristic morphology on 13 kPa gels. However, by t=20 minutes into the timelapse, the majority of these cells retract into the morphology characteristic on 4 kPa (see also Figure 6.3). Neutrophils on 3 kPa **(C)** appear similar to those on 4 kPa; however, though they are activated, neutrophils on 3 kPa do not attach, as observed in timelapse movies. As on 4 kPa, the presence of small protrusions over the body of the cell indicates that the cell is activated.

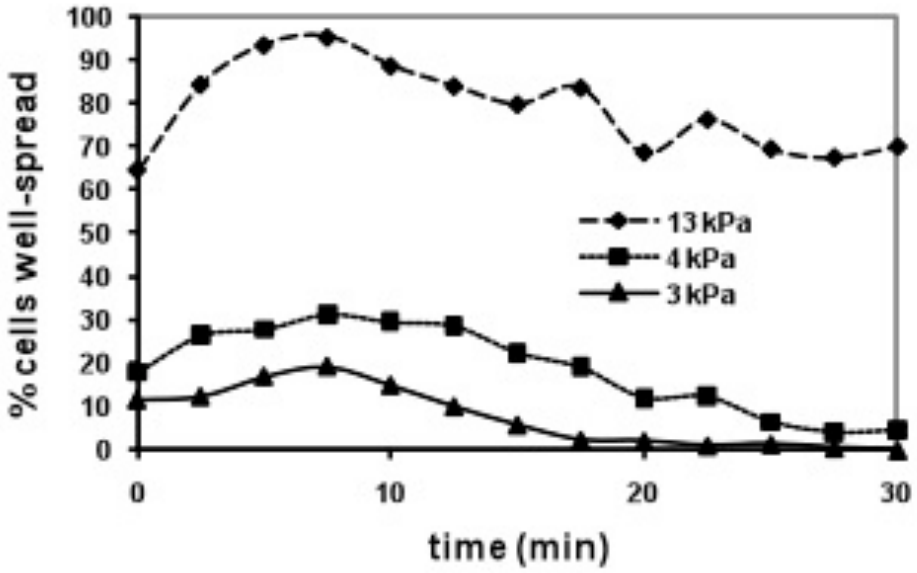

Figure 6.3. Percent of cells displaying well-spread morphology (characteristic of cells on 13 kPa polyacrylamide gel coated with fibronectin) on each of 13 kPa (N=77 cells on 4 gels from 3 blood donors), 4 kPa (N=134 cells on 6 gels from 3 blood donors), and 3 kPa (N=202 cells on 6 gels from 3 blood donors) in 2.5 minute time intervals after activation with a uniform concentration of 10 nM fMLF. The majority of neutrophils on 13 kPa spread initially and stay well-spread though the 30 minute timelapse. On 4 kPa and 3 kPa, some cells appear well-spread initially, but the majority of these cells retract by t=20 minutes and then stay unspread for the remainder of the timelapse. Results are shown for 100 μg/mL fibronectin, and similar spreading patterns are noticed for neutrophils on 10 μg/mL.

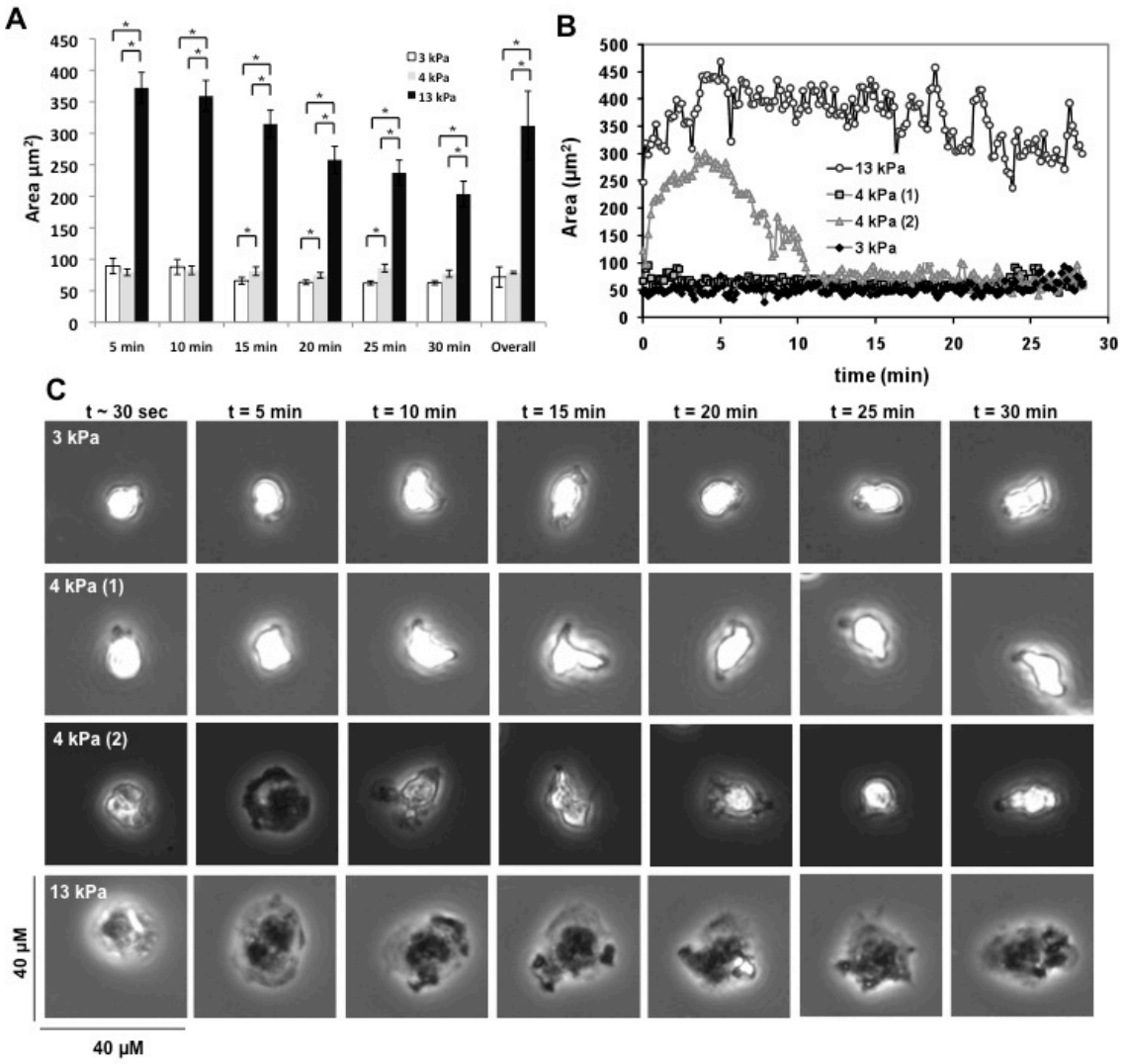

Figure 6.4. Effects of substrate stiffness on neutrophil area. **(A)** Time-averaged spreading area of neutrophils on fibronectin-coated polyacrylamide gels of varying stiffness over three independent experiments under control conditions during a chemokinetic response to 10 nM fMLF. Areas labeled "5 minutes" were averaged over 0-5 minutes. Areas labeled "10 minutes" were averaged 5-10 minutes, and so on. "Overall" areas were averaged over the entire 30 minute timelapse. Bars indicate mean of three experiments using different blood donors, and error bars represent standard error of three experiments. Asterisks indicate significance at 95% confidence using Student's t-test. **(B)** Spreading area versus time for one neutrophil on each of 13 kPa, 4 kPa, and 3 kPa fibronectin-coated (100 µg/mL) polyacrylamide gels during a chemokinetic response to 10 nM fMLF under control conditions. 4 kPa (1) data series shows area versus time for a neutrophil which displays unspread morphology characteristic of 4 kPa during the entire 15 minute time period. 4 kPa (2) data series shows area versus time for a neutrophil which initially spreads as on 13 kPa, but then retracts at t=7 minutes (see black arrows on Figure 6.2) and does not spread out again. Note also that t=0 corresponds to the beginning of the timelapse capture; this is within 30 seconds of adding fMLF. **(C)** Corresponding morphologies of single cells, for which the area versus time data is given in panel B. Images are shown in 5 minute time intervals. All images represent 40x40 µm.

6.3.3 Neutrophil migration speed is biphasic with substrate stiffness

The effect of time interval choice on neutrophil track speed was investigated (Figures 6.5A and 6.5B). As time interval (λ) increases from 10 seconds to 2 minutes, track speed decreases for neutrophils migrating on all stiffnesses, though the decrease in track speed is most apparent on 3 kPa gels, where cells do not migrate, but rather move randomly in place due to Brownian motion and changes in cell shape. Track speeds on 13 kPa (10 μg/mL fibronectin) are statistically different from speeds on all other stiffness for all λ (indicated by gray circles surrounding the data points in Figure 6.5A; $P<0.05$). Track speeds on 3 kPa (10 μg/mL fibronectin) become statistically different from speeds on both 5 kPa and 7 kPa at λ=50 seconds (Figure 6.A), but are not statistically different from speeds on 4 kPa at any interval. Track speeds on 13 kPa and 3 kPa (100 μg/mL) are statistically different from values on 4 kPa for all λ (Figure 6.5B).

Figure 6.5C shows the track speeds for a time interval of λ=10 seconds, while Figure 6.5D shows the track speeds for a time interval of λ=60 seconds. Choosing a time interval of 10 seconds does not reveal biphasic behavior between substrate stiffness and track speed for 10 μg/mL fibronectin (Figure 6.5C), but at λ=60 seconds the relationship is statistically biphasic (Figure 6.5D). Track speeds on 100 μg/mL are statistically biphasic for all time intervals, including 60 seconds (Figures 6.5B, 6.5C, and 6.5D).

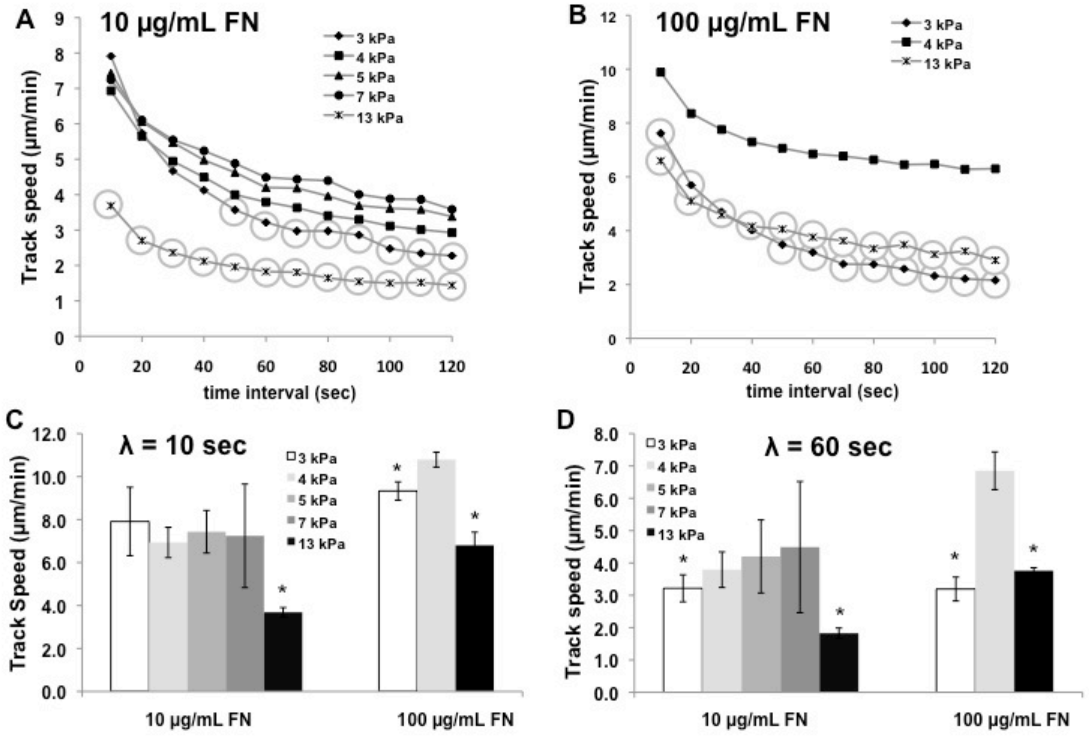

Figure 6.5. Neutrophil speed depends on substrate stiffness and amount of surface-bound fibronectin. **(A and B)** Average track speed of neutrophils versus time interval used for the calculation. Time intervals were varied from 10 seconds to 2 minutes, in 10 second time steps to investigate the effect of choosing a time interval on the track speed. Panel A indicates data for 10 µg/mL fibronectin (FN), while panel B indicates data for 100 µg/mL fibronectin. Data points circled in gray are statistically different from the maximum value at that time interval ($p<0.05$). **(C and D)** Track speed, using **(C)** time interval $\lambda=10$ seconds and **(D)** time interval $\lambda=60$ seconds, of neutrophils on fibronectin-coated (10 µg/mL and 100 µg/mL) polyacrylamide gels of varying stiffness under control conditions during a chemokinetic response to 10 nM fMLF. In panels A and B, bars indicate mean of three experiments using different blood donors, and error bars represent standard error of three experiments. Asterisks indicate statistical difference from maximum value at 95% confidence using Student's t-test.

6.3.4 Optimal stiffness for migration depends on amount of surface-bound fibronectin

Further, the optimal stiffness depends on ligand concentration. At 10 μg/mL fibronectin, the optimal stiffness is around 7 kPa (though 5 kPa is also statistically different from both 3 kPa and 13 kPa), while at 100 μg/mL, the optimal stiffness is lower, at 4 kPa (Figure 6.5D). For λ=60 seconds, values for mean track speeds of neutrophils on 13 kPa, 4 kPa, and 3 kPa (100 μg/mL) are 3.76±0.09 μm/min, 6.9±0.6 μm/min, and 3.2±0.4 μm/min, respectively. Values for mean track speeds on 13 kPa, 7 kPa, 5 kPa, 4 kPa, and 3 kPa (10 μg/mL) are 1.83±0.16 μm/min, 4.5±2.0 μm/min, 4.2±1.1 μm/min, 3.8±0.5 μm/min, and 3.2±0.4 μm/min, respectively. There is a statistical difference ($P<0.05$) between the maximum values on 4 kPa (100 μg/mL) and 7 kPa (10 μg/mL). Typical trajectories for neutrophils on polyacrylamide gels of varying stiffness are depicted in Figure 6.6.

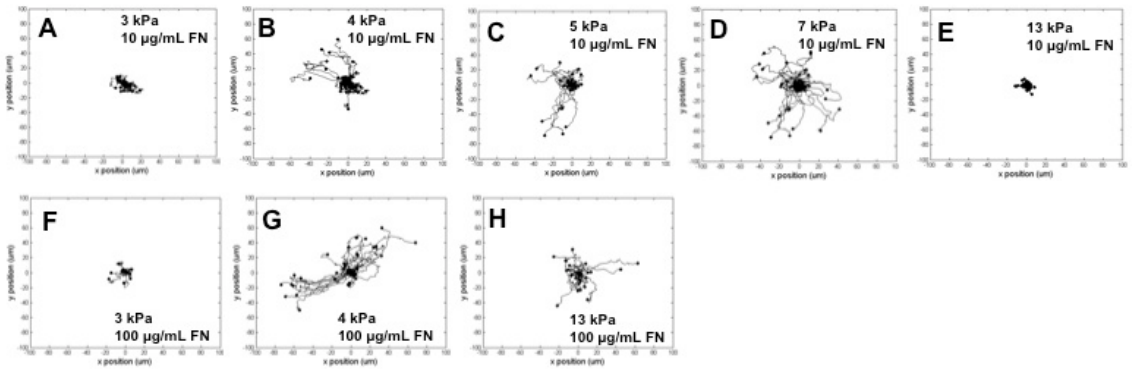

Figure 6.6. Typical trajectories of neutrophils on fibronectin-coated polyacrylamide gels following a chemokinetic response to 10 nM fMLF. Shown are trajectories from 20-30 cells, overlapped and with the starting positions centered at the origin. All plots range from (-100, 100) μm on both the x- and y- axes. Black dots indicate the ending position of the cell. **(A-E)** Trajectories on 10 μg/mL fibronectin. **(F-H)** Trajectories on 100 μg/mL fibronectin. **(A and F)** 3 kPa. **(B and G)** 4 kPa. **(C)** 5 kPa. **(D)** 7 kPa. **(E and H)** 13 kPa.

For comparison, previous studies on glass have reported the speed of neutrophils to be 15.3 μm/min [201] and 30 μm/min [202], though the protein coating conditions in those experiments vary from each other and from those in the present study. The speeds of neutrophils on our flexible gels are comparable to speeds found in more recent experiments, where neutrophil migration velocities were around 8 μm/min on plastic substrates coated with varying concentrations of E-selectin, platelet endothelial cell adhesion molecule type 1 (PECAM-1), and intercellular adhesion molecule type 1 (ICAM-1) [196]. Because glass susbtrates are not physiologically relevant, we chose to perform our experiments on flexible polyacrylamide gels in the range of stiffness of endothelial cells, which has been reported as 0.2 to 6.8 kPa [41, 42]. Thus, 13 kPa is a relatively stiff substrate. However, we expect that neutrophil speeds will be very low on gels that are even stiffer than those used in this study; this may be an interesting area for future study.

6.3.5 Random motility coefficient depends on substrate stiffness

The random motility (diffusion) coefficients of neutrophils are 0.49±0.15 $\mu m^2/s$, 1.9±0.3 $\mu m^2/s$, and 0.11±0.08 $\mu m^2/s$ on 13 kPa, 4 kPa, and 3 kPa polyacrylamide gels (100 μg/mL fibronectin), respectively. These values were calculated from the slope of the linear portion of plots of mean square displacement (MSD) versus time (Figure 6.7A). The resulting values for random motility coefficient are similar to those obtained using the full Langevin equation (see Section 6.2.6). The random motility coefficient is statistically smaller for neutrophils on 13 kPa and 3 kPa gels as compared to neutrophils migrating on the 4 kPa gel (Figure 6.7B) ($P<0.05$). There is no difference between

random motility coefficients on 13 kPa and on 3 kPa ($P>0.05$). Thus, neutrophils also display a biphasic behavior between the random motility coefficient and substrate stiffness, where about 4 kPa is the stiffness for optimal migration on 100 μg/mL fibronectin. On substrates coated with 10 μg/mL fibronectin, the random motility coefficient is 0.20±0.06 μm^2/sec, 0.39±0.24 μm^2/sec, 0.39±0.15 μm^2/sec, 0.32±0.12 μm^2/sec, and 0.07±0.01 μm^2/sec on 13 kPa, 7 kPa, 5 kPa, 4 kPa, and 3kPa, respectively, indicating that neutrophils diffuse most on 7 kpa or 5 kPa (Figure 6.7B). The maximum random motility coefficient on 10 μg/mL fibronectin (7 kPa) is statistically lower ($P<0.05$) than the maximum random motility coefficient on 100 μg/mL fibronectin (4 kPa).

For comparison, previous studies on glass have reported the diffusion coefficient of neutrophils to be 0.14 μm^2/sec [201] and 4 μm^2/s [202], though the protein coating conditions in those experiments vary from those in the present study. More recent experiments have found the diffusion coefficient of neutrophils on plastic substrates with varying concentrations of E-selectin, PECAM-1, and ICAM-1 to be in the range of about 0.25 to 1 μm^2/sec [196]. As previously mentioned, for the current study we focused on substrate stiffnesses in the range of stiffness of ECs, and comparatively, 13 kPa is a "stiff" substrate. We expect that neutrophil random motility coefficients on glass will be even lower than on the stiffest gels used in the current study.

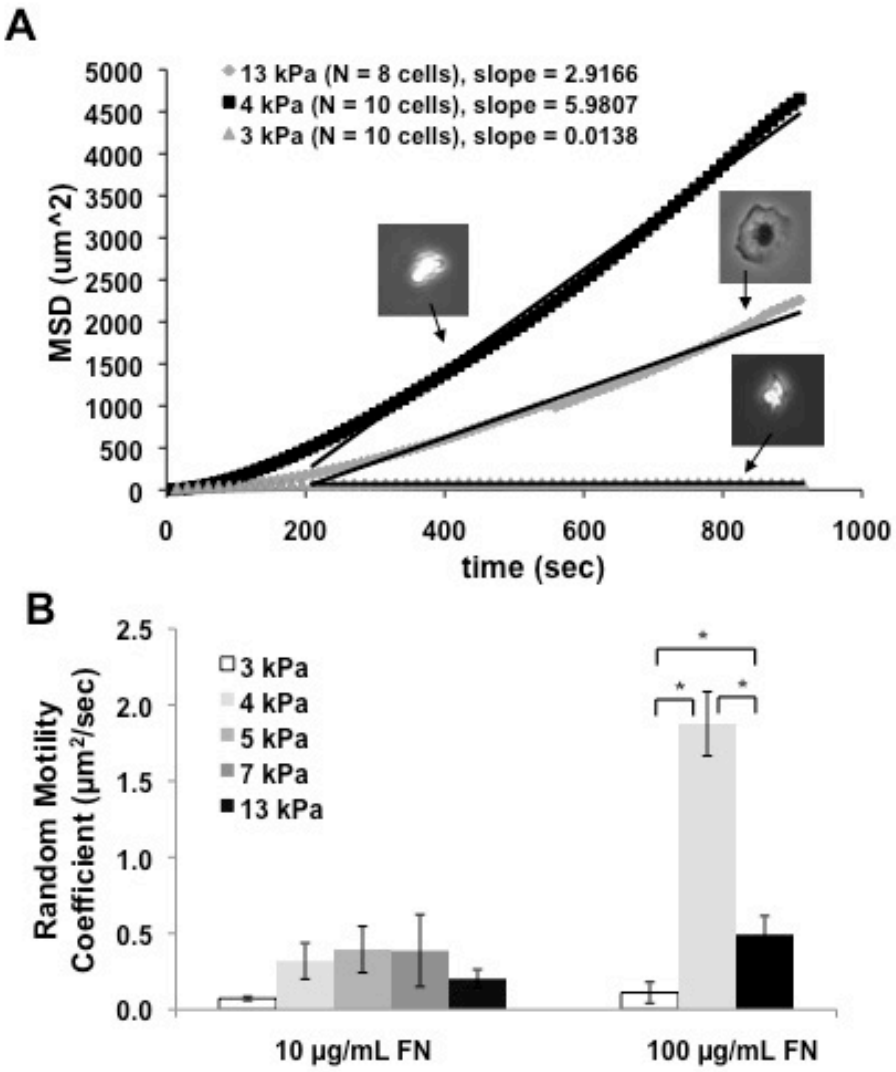

Figure 6.7. Random motility coefficient is biphasic with substrate stiffness. **(A)** Mean square displacement (MSD) versus time for neutrophils migrating on 100 μg/mL fibronectin-coated gels of varying stiffness under control conditions during a chemokinetic response to 10 nM fMLF. Each curve represents mean data for 8-10 cells on each stiffness (one experiment), as indicated in the plot legend. Images are 40 μm by 40 μm and represent characteristic morphology of neutrophils on each stiffness. The slope of the linear portion of each curve are also indicated with units $\mu m^2/s$ in the plot legend and are used to calculate the random motility coefficient. **(B)** Random motility coefficient of neutrophils on fibronectin-coated (10 μg/mL and 100 μg/mL) polyacrylamide gels of varying stiffness under control conditions during a chemokinetic response to 10 nM fMLF. Bars indicate mean of three experiments using different blood donors, and error bars represent standard error of three experiments. Asterisks indicate significance at 95% confidence using Student's t-test.

6.3.6 Neutrophil migration is superdiffusive

Natural log-log plots of MSD versus time, with a slope of α (Figure 6.8A), indicate that for neutrophils moving on 13 kPa, 4 kPa, and 3 kPa gels (100 µg/mL fibronectin), the value of α is 1.48±0.15, 1.57±0.02, and 0.9±0.4, respectively (Figure 6.8B). Meanwhile, on gels coated with 10 µg/mL fibronectin, the value of α is 1.42±0.05, 1.23±0.05, 1.34±0.06, 1.25±0.10, and 0.92±0.10 (Figure 6.8B). Note that $\alpha=1$ corresponds to random Brownian motion, $\alpha>1$ corresponds to superdiffusive motion, and $\alpha<1$ corresponds to subdiffusive motion. Thus, neutrophils display superdiffusive motion on 4 kPa, 5 kPa, 7 kPa, and 13 kPa gels, while motility on 3 kPa is closer to random motion. These values can be compared with recent results obtained in a similar way for neutrophils on plastic substrates of varying concentrations of E-selectin, PECAM-1, and ICAM-1; in these experiments, a natural log-log plot of MSD versus time resulted in a slope of ~1.42 [196].

6.3.7 Neutrophils are more persistent on stiff substrates

Substrate stiffness also affects the distribution of turning angles of neutrophils (Figure 6.9) (see Section 6.2.6). Note that in pure random, Brownian motion, all turning angles would be equally probable, resulting in a flat distribution, while in completely directed motion (i.e. chemotaxis), very small turning angles would be most probable [202]. On 4 kPa (Figure 6.9B) and 13 kPa (Figure 6.9C), smaller turning angles are much more probable, while on 3 kPa the distribution is more even (Fig 6.9A), and there is a less noticeable preference for smaller turning angles. In addition, frequency of angle occurrence drops off more quickly on 4 kPa than on 13 kPa, indicating more persistent

motion on 4 kPa. Data here (Figure 6.9) is shown for 100 µg/mL fibronectin; similar trends are observed for neutrophil turning angles on 10 µg/mL fibronectin.

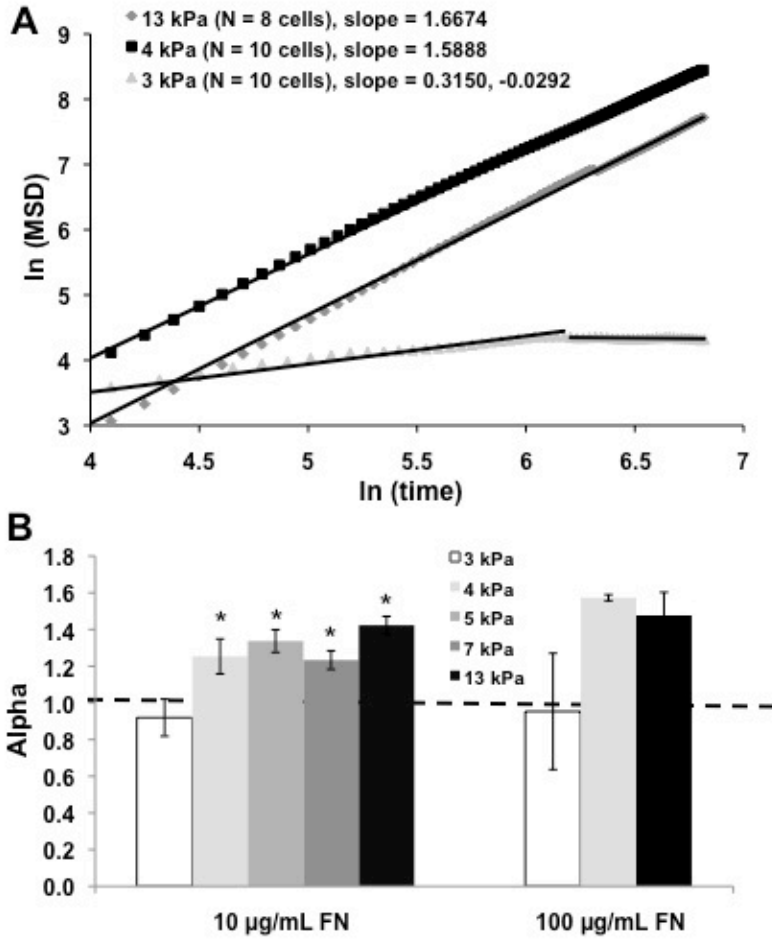

Figure 6.8. Slope of natural log-log plot of mean square displacement versus time reveals diffusive behavior of neutrophil migration. **(A)** Natural log-log plot of mean square displacement (MSD) versus time for neutrophils migrating on 100 µg/mL fibronectin-coated gels of varying stiffness under control conditions during a chemokinetic response to 10 nM fMLF. Each curve represents mean data for 8-10 cells on each stiffness (one representative experiment is shown), as indicated in the plot legend. On this log-log plot, the slope of the line is equal to the exponent (α) in power law relationship between mean square displacement and time. The second, negatively-sloping portion of data for 3 kPa indicates that the motility of neutrophils has significantly decreased. **(B)** Average α of three experiments for neutrophils on fibronectin-coated (10 µg/mL and 100 µg/mL) polyacrylamide gels of varying stiffness under control conditions during a chemokinetic response to 10 nM fMLF. Bars indicate mean of three experiments using different blood donors, and error bars represent standard error of three experiments. Asterisks indicate statistical difference from value on 3 kPa at 95% confidence using Student's t-test.

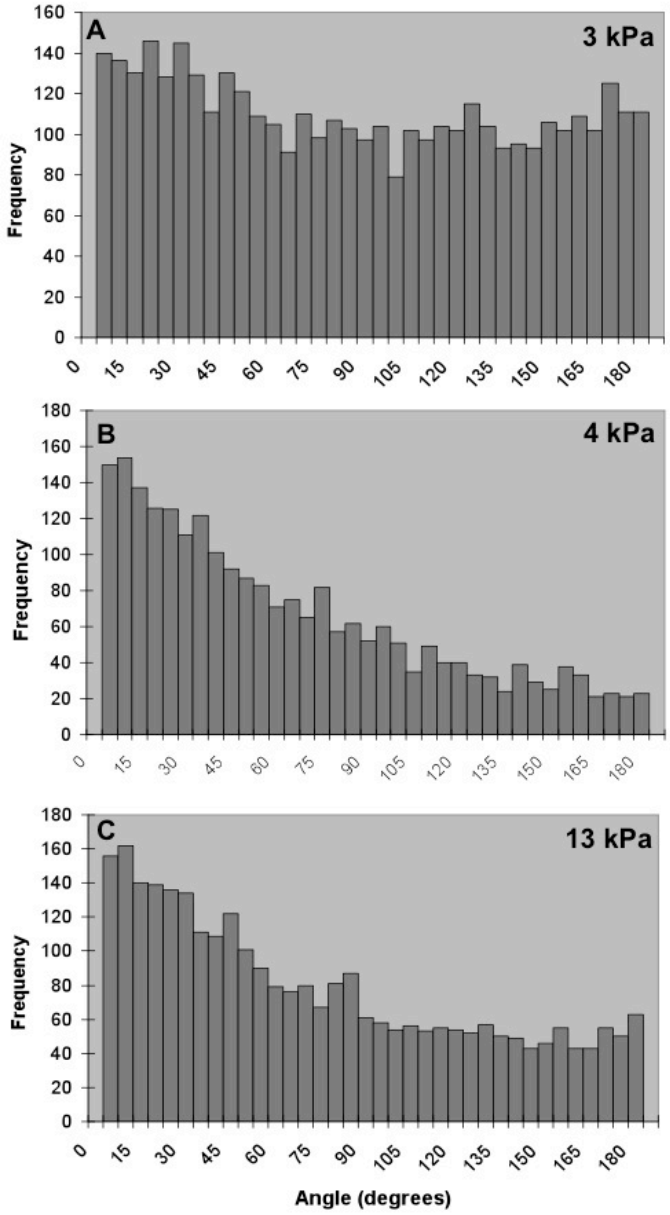

Figure 6.9. Histograms of turning angles from one frame to the next in 10 second time intervals for neutrophils moving on varying substrate stiffness, including **(A)** 3 kPa (N=28 cells), **(B)** 4 kPa (N=28 cells), and **(C)** 13 kPa (N=26 cells) polyacrylamide gels coated with 100 µg/mL fibronectin. Neutrophils were activated with a uniform concentration of 10 nM fMLF. Zero degrees corresponds to no turn; that is the neutrophil remains in the same path line as the previous frame. One hundred eighty degrees corresponds to a complete reversal of direction from one frame to the next. Angles in between may be either left or right hand turns. Because the motility was analyzed during chemokinesis, there will be an equal probability of left and right turns of the same magnitude. Note that there is a more even distribution of turning angles for neutrophils on 3 kPa, as compared to 4 kPa and 13 kPa, where the smaller turning angles are more probable.

6.4 Discussion

The leukocyte adhesion cascade is a key component of the immune response. Neutrophils are innately present in the bloodstream in their inactive state continuously exploring the EC wall for activated ECs. Once they find them, the neutrophils begin rolling along the EC wall, firmly attach, migrate along the wall, and finally, transmigrate through the EC wall towards the site of infection, where they engulf endogenous material. However, the ECs themselves present a heterogeneous surface stiffness to the neutrophils. Evidence for this comes from previous AFM experiments which have found that the Young's modulus of human umbilical vein ECs (HUVECs) ranges from 1.4 kPa to 6.8 kPa [41], depending on the location of the cell which is probed. Furthermore, the ECs present a variety of proteins to the neutrophil during the leukocyte adhesion cascade. Thus, determining if the neutrophils can actually "feel" the heterogeneity *in vivo* would be a very complex problem. In order to simplify this complex problem, in this chapter, we first performed experiments on polyacrylamide gels of homogeneous stiffness with one extracellular matrix protein (fibronectin, at concentrations of 10 μg/mL and 100 μg/mL) cross-linked to the gel.

Based on results from experiments using other cell types such as rat kidney epithelial cells and 3T3 fibroblasts [25, 56, 61], we hypothesized that a decrease in substrate stiffness would result in smaller neutrophil spreading areas and increased motility parameters (i.e. speed and random motility coefficient). The trend in our results for the intermediate stifffnesses and the stiffest gels supports this hypothesis. That is, neutrophils on intermediate stiffnesses spread less (Figure 6.4), migrate faster (Figure 6.5), and have a larger random motility coefficient (Figure 6.7) than on the stiffest 13 kPa

polyacrylamide gels, for both 10 μg/mL and 100 μg/mL fibronectin. Further, the area of neutrophils on both ligand concentrations increases monotonically with substrate stiffness.

However, the motility data for neutrophils on 3 kPa gels do not fit this monotonic trend. Neutrophils on 3 kPa gels (10 μg/mL and 100 μg/mL fibronectin) "bounce" around with a track speed (λ = 10 seconds) close to that on the intermediate stiffnesses (Figure 6.5C); however the random motility coefficient is markedly reduced on 3 kPa (Figure 6.7), most likely because the neutrophils are unable to migrate on such a soft surface. This lack of migration is presumably due to lack of attachment to the polyacrylamide gel.

Because it is difficult to define a speed in a random walk, we also chose to evaluate the track speeds of the neutrophils as a function of time interval, λ (Figures 6.5A and 6.5B). Formally, we would expect the diffusive speeds to fall off with $t^{-1/2}$, since diffusive speed is the time derivative of the square root of the MSD, and MSD = 4Dt for a two dimensional random walk. As we increase the time interval used to calculate track speed, the track speed decreases for neutrophils on all stiffnesses in the range tested, with the track speed on 3 kPa decreasing most significantly for both 10 μg/mL and 100 μg/mL fibronectin. Therefore, the misleadingly high value for track speed assuming λ = 10 seconds (Figure 6.5C) on 3 kPa most likely arises because the distance traveled due to random motion is of similar magnitude to the distance traveled, more persistently, during migration of neutrophils on the stiffer gels. Thus, it would make more sense to report the track speed of neutrophils assuming a larger time interval, such as λ = 60 seconds (Figure 6.5D), where the track speeds on 3 kPa are statistically less than the track speed on 4 kPa for 100 μg/mL fibronectin, and on 5 kPa and 7 kPa for 10 μg/mL fibronectin. These

analyses demonstrate that careful consideration must be taken when choosing a time interval for calculating speed during a random walk. If an appropriate time interval is not chosen, biphasic behavior may not be revealed.

These results suggest that there exists an optimum extracellular stiffness which promotes neutrophil motility, and that stiffness is around 4 kPa on 100 µg/mL fibronectin and around 7 kPa on 10 µg/mL fibronectin. Thus, the optimum stiffness for neutrophil random motility shifts to a lower value for a higher ligand concentration. For intermediate and stiff gels, the maximum values of track speed and random motility coefficient are significantly larger on gels coated with 100 µg/mL fibronectin, as compared with 10 µg/mL fibronectin, indicating that neutrophils are ligand-sensing as well as mechano-sensing. Interestingly, the optimum gel stiffnesses are close to the range of stiffness of the innate neutrophil substrate, the vascular endothelium. However, as already suggested, neutrophils do feel a heterogeneous surface stiffness, and thus their motility may vary as they migrate across the EC. Also as previously discussed, the step of the leukocyte adhesion cascade which involves migration along the EC wall is critical for transmigration of monocytes [192], and thus we expect it to be necessary for neutrophil transmigration as well. For example, our results show 4 kPa is optimal (for 100 µg/mL fibronectin), if a large diffusion coefficient or track speed is necessary for the immune response. However, these results cannot predict what substrate stiffness is best for neutrophil transmigration; Chapter 7 will explore this idea.

The morphology and spreading areas of the neutrophils on 13, 4, and 3 kPa (10 µg/mL and 100 µg/mL fibronectin) suggest that they are most strongly adhered on 13 kPa (Figures 6.2 and 6.4). Though we did not directly measure adhesion of the neutrophils on

the gels of varying compliance, it is obvious by simple observation of small perturbations of the cells in the timelapse movies that most neutrophils on 3 kPa gels do not attach. These neutrophils on 3 kPa move randomly but do not displace significantly from their initial positions at any given time. It is also obvious that those few which spread initially detach from the substrate by t = 20 minutes (Figure 6.3). We can compare these spreading areas of activated neutrophils on gels of varying stiffness to the expected area for an inactive neutrophil of diameter 10 μm which projects a circular shape of area ~75 μm^2 onto the substrate. Then, the spreading areas on 3 kPa and 4 kPa are similar to that of an inactive neutrophil, providing further evidence that there is little attachment to those substrates. In the activated state, the cell area may increase or decrease slightly due to the break in isotropy and subsequent changes in shape, even with little attachment to the substrate. For a neutrophil to be well-attached, it must extend membrane as it flattens out in order to bind to extracellular matrix proteins on the substrate surface, resulting in an increase in area. Thus, the significantly larger spreading area on 13 kPa at all time points (Figure 6.5A), for both concentrations of ECM proteins tested, suggests that those cells are more strongly adhered than the cells on 3 kPa or 4 kPa.

The results for random motility coefficient and track speed (λ = 60 seconds) lead us to propose a biphasic relationship between stiffness and migration, where, for the range of stiffnesses tested, neutrophil migration on intermediate stiffnesses around 4 kPa is maximal (Figure 6.10) for 100 μg/mL fibronectin, while 7 kPa is optimal for migration on 10 μg/mL. As expected, cell area is *not* biphasic with substrate stiffness, but rather monotonic, since neutrophils on soft surfaces do not attach, while neutrophils on stiffer surfaces strongly adhere.

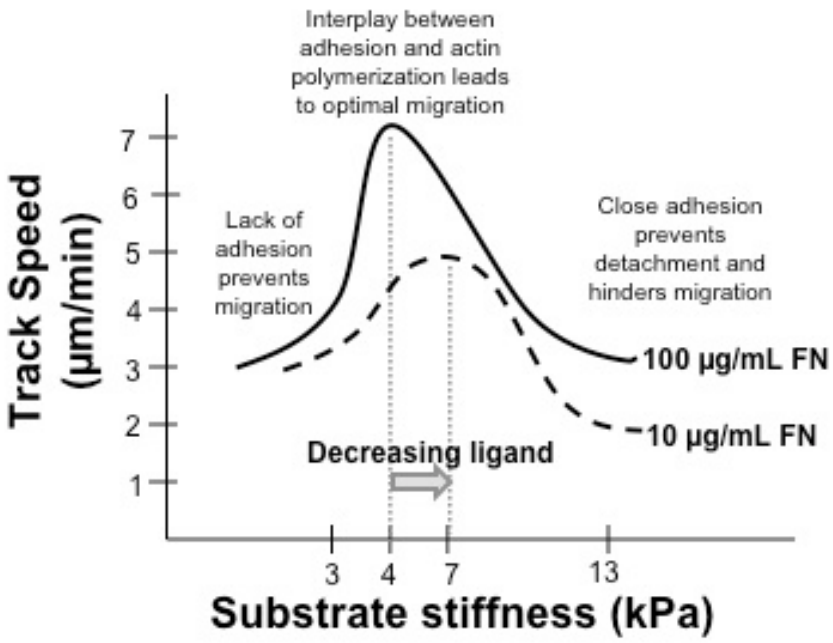

Figure 6.10. Proposed biphasic relationship between the track speed, ligand concentration, and substrate stiffness during neutrophil chemokinetic migration. At low stiffness (~3 kPa), even though there is actin polymerization, a lack of adhesion to the substrate prevents migration because the cell cannot exert traction forces. At high stiffness (~13 kPa), close adhesion to the substrate prevents detachment and therefore hinders migration. At high protein concentration (100 μg/mL), the optimal stiffness is around 4 kPa, while at low protein concentration (10 μg/mL), the optimal stiffness shifts to 7 kPa. At the intermediate stiffnesses, there is an interplay between adhesion and actin polymerization which leads to optimal migration. Note that the shape of the curve is only a qualitative representation of the biphasic behavior.

Biphasic relationships between adhesion and cell speed have been previously reported for cells on substrates with varying protein concentrations [203]. Biphasic relationships between substrate stiffness and cell speed have also been reported for primary human aortic smooth muscle cells (SMCs) on polycrylamide gels of varying stiffness [197] and, more recently, for mouse fibroblasts in collagen gels of varying stiffness [204]. Most likely, this is due to an interplay between adhesion (force which hinders forward migration) and actin polymerization (force which facilitates forward

motion). This biphasic relationship has also been explained by an interplay between focal adhesion dynamics and contractility due to myosin [205]. Cell migration involves the regulation of actin polymerization to protrude the leading edge forward, adhesion of the leading edge, contraction at the rear of the cell, and finally, detachment at the rear of the cell, resulting in net forward movement. It has been shown that neutrophils exert the largest traction forces at the uropod, or rear, of the cell body, which acts as an anchor [206]. We hypothesized that on stiffer surfaces (such as 13 kPa), the cell cannot efficiently release adhesions, resulting in slowed migration. Interestingly, rear detachment of the cell has been reported to be the rate-limiting step in cell migration [207]. On soft surfaces (such as 3 kPa), the cell cannot migrate efficiently because it cannot exert traction forces or anchor the leading edge without adhesion. Intermediate stiffnesses offer the ideal mechanical environment for a balance between adhesion and actin polymerization, resulting in optimal migration. Our results are consistent with those reported for human aortic SMCs, where the migration speed is biphasic with substrate stiffness, with the optimal value increasing for a lower protein concentration on the surface of the gel [197]. This shift in optimal stiffness presumably occurs because as ECM density is decreased, adhesion to the substrate also decreases, which interrupts the optimal interplay between actin polymerization and adhesion. Because cells attach more stongly to stiffer substrates, a stiffer gel is necessary to increase the level of adhesion on low ECM densities, thus returning the optimal balance.

We must also address the inconsistency between our data and that presented by Yeung *et al*. [56], where it was reported that neutrophil circumference does not depend on substrate stiffness. The discrepancy may first be explained by the fact that the stiffest

gel used in their experiments was around a shear modulus of 500 Pa (approximately equal to Young's modulus of 1.5 kPa). According to our data (Figure 6.4A), neutrophils on 1.5 kPa would display similar area to those on 3 kPa, which is also close to that of a passive neutrophil. Thus, in the range of gel stiffnesses they investigated, changes in cell area would not have been noticed. Further discrepancies may be found due to the time at which the cell area or circumference was measured. For example, if they had waited for a very long time ($t >> 30$ minutes) before imaging the cells, then they may not have noticed that the neutrophils take on a well-spread morphology during the first 30 minutes of spreading. Figure 6.4A indicates that neutrophil spreading area on 13 kPa decreases over the 30 minute timelapse, so it is possible that at much later times the cells are no longer well-spread. One possible explanation for this result is that the neutrophil chemoattractant receptors have become desensitized to the fMLF at later times, and the cells may retract as a result. Our own experiments reveal that cells remain well-spread on 13 kPa for at least an hour following activation with fMLF, but it is unknown what the spreading behavior is at later times.

Neutrophils seem to be very fine-tuned to changes in substrate stiffness, as they display very different behaviors in the range 3 kPa to 13 kPa. This is not surprising, considering mesenchymal stem cells respond very differently to substrate stiffnesses of 1 kPa and 10 kPa by differentiating into neurogenic or myogenic cells, respectively [64]. Detection of substrate stiffness is possibly carried out by the tension-sensitive talin1 molecules which link actin polymers to integrins on the neutrophil surface [18]. Integrins on the neutrophil surface then bind to the fibronectin on the gel. However, it is likely that without sufficient mechanical tension (as on 3 kPa) on talin1, the signals for adhesion and

migration will not be propagated to the cell. In contrast, on 13 kPa, there may be an excess of mechanical tension on talin1, thus leading to strong adhesion.

Neutrophils on 4 kPa and 13 kPa gels clearly demonstrate superdiffusive or driven motion, with an α (exponent in power law relationship between mean square displacement and time) greater than 1 (Figure 6.8). This occurs most likely due to the active component of their migration (i.e. actin polymerization). However, neutrophils on 3 kPa gels display random motion, as evidenced by a mean α closer to 1 (Figure 6.8), as well as a fairly even distribution of turning angles between 0 and 180 degrees (Figure 6.9A). The second portion of data for 3 kPa (Figure 6.8A) of close to zero slope indicates that the motility of neutrophils has significantly decreased, most likely because the chemoattractant receptors on the neutrophil surface have saturated, or because the cell is not actually migrating. We compared our results with numerical simulations and reveal that pure random motility produces an even distribution of turning angles, D = 0.05 $\mu m^2/s$, and $\alpha \approx 1$, indicating that neutrophils on the 3 kPa gel are not adhering. Furthermore, this indicates that neutrophils move randomly on 3 kPa but with persistent directionality on 4 kPa and 13 kPa. Persistence in motion is driven by actin polymerization, and morphologically the cell is polarized. The distribution of turning angles on varying stiffness also points to persistent motion on 4 kPa and 13 kPa (Figures 6.9B and 6.9C), where smaller turning angles occur more frequently during the first 30 minutes of migration after activation with fMLF. Further, the distribution falls off more quickly at lower turning angles for 4 kPa, as compared to 13 kPa, suggesting that neutrophils on 4 kPa are more persistent than those on 13 kPa. Thus, on soft gels, the distribution of turning angles is close to even, indicating no preference for one particular

turning angle. On intermediate stiffness gels, there is an extreme preference for low turning angles, suggesting persistent motion. On stiff gels, the distribution falls off slower than on intermediate stiffness, but small turning angles are preferenced more than on soft gels, indicating intermediate persistence.

Though a small percentage of neutrophils on 4 kPa and 3 kPa initially appear well-spread, the observation that most of them retract *irreversibly* by t=20 minutes after activation (Figure 6.3) suggests that the cells on 3 kPa and 4 kPa which display initial spreading (Figures 6.4B and 6.4C) are simply testing the conditions of their environment. However, future experiments would need to be carried out in order to test this hypothesis.

It could be argued that a greater porosity in softer gels leads to more absorption of protein into the gel and thus less protein on the surface of the gel. This would explain why neutrophils on softer gels do not spread as greatly as those on stiffer gels. However, to rule out this possibility, we immunostained fibronectin on the surface of the gel using a primary anti-fibronectin antibody and secondary antibody conjugated to Texas Red. Quantification of the fluorescence intensity reveals that the fibronectin coating on gels composed of 8% acrylamide is constant, while the fibronectin coating on gels composed of 5% acrylamide (3 kPa gel) is two times less than that on the 8% acrylamide gels for a theoretical fibronetin concentration (in solution) of 100 µg/mL. However, if the solution concentration is increased to 500 µg/mL, then the fluorescence intensity is of similar value to that on the 8% gels, indicating a similar fibronectin density on the surface of the gel. On 3 kPa gels coated with 500 µg/mL, the cells still do not attach and therefore the spreading patterns are similar to those in Figures 6.2C and 6.4C. The insensitivity of cells on soft gels to increased ligand density is consistent with previous reports for rat smooth

muscle cells [60]. Additionally, previous research has shown that the concentration of protein coating on polyacrylamide gels of similar acrylamide concentration remains constant, regardless of bis concentration [25]. Thus, we expect that substrate stiffness can be decoupled from ligand density, though both factors have a significant effect on cytoskeletal regulation during cell migration. Use of polyacrylamide gels coated with varying concentrations of fibronectin in these experiments allows us to investigate the effects of substrate stiffness and ligand density independently from each other.

6.5 Conclusions

We have demonstrated that neutrophil motility and morphology during chemokinesis depend on the stiffness of the substrate according to a biphasic relationship which has been reported in other cell types, but not yet in neutrophils and which exists over a narrow stiffness range, from 3 kPa to 13 kPa, which is reminiscent of the stiffness found in endothelial cells. Neutrophil response to stiffness during chemokinesis is biphasic with an optimum stiffness that is higher for a lower concentration of surface protein. Further, for the intermediate to stiff range of gels, increased migration is observed with a higher concentration of protein on the surface. Therefore, neutrophils are both ligand-sensing and mechano-sensing. Presumably, this relationship is based on a competition between adhesiveness and actin polymerization. In the next chapter (Chapter 7), we will explore whether this mechanosensitivity is relevant to neutrophil migration along and transmigration through their innate substrate, the vascular endothelium.

7 Subendothelial Matrix Stiffness Influences Neutrophil Transmigration via Myosin Light Chain Kinase-Dependent Cell Contraction†

7.1 Introduction

Leukocyte transmigration through the vascular endothelium is a crucial step in the normal immune response. However, it is a complicated biological process that involves many proteins and requires a coordinated effort between the leukocytes and endothelial cells (ECs). The biophysical aspects of leukocyte transmigration are also important, as mechanical force transmission is an essential regulator of vascular homeostasis. It is likely that the mechanical properties of the vasculature depend on both vessel size (large vessels versus microvasculature) and location (soft brain versus stiffer muscle or tumor). Further, in the cardiovascular disease of atherosclerosis, the arteries stiffen [113, 115, 116, 119] as an increased number of leukocytes penetrate the endothelium, and tumor vasculature is also stiffer [114]. However, it is unknown how changes in vasculature stiffness affect the behavior of the ECs lining the blood vessel, or the behavior of the leukocytes migrating along and transmigrating through the endothelium. Interestingly, polymorphonuclear neutrophils are capable of sensing differences in both substrate stiffness and surface-bound adhesion proteins (Chapter 6). Therefore, we would expect neutrophils to be capable of sensing similar changes that may occur in their physiological substrate, the endothelium.

---

† This chapter was adapted from Stroka, K.M. and H. Aranda-Espinoza (2011). Endothelial cell substrate stiffness influences neutrophil transmigration via myosin light chain kinase-dependent cell contraction. *Blood* 118(6), 1632-1640. © The American Society of Hematology. Permission was obtained from the publisher to use this material in the current dissertation.

The mechanical properties of ECs are affected by a number of physiological factors, including shear stress [30], cholesterol content [31, 154], and oxidized low-density lipoprotein [32], as reviewed in Section 2.4. Furthermore, neutrophil adherence to ECs increases EC stiffness, likely due to signaling cascades that induce rearrangement of the actin cytoskeleton [38, 39]. However, little is known about the effects of substrate stiffness on the biophysical properties of healthy or inflamed EC monolayers. Single EC stiffness increases with substrate stiffness [73], though cells in monolayer may show different behavior than single cells, as the degree of cell-cell adhesion also contributes to cell stiffness (Chapter 4).

Neutrophil adherence to the endothelium has been shown to regulate EC gap formation through a cytosolic calcium-dependent mechanism [208]. Myosin light chain kinase (MLCK) is activated downstream of calcium-calmodulin binding and phosphorylates myosin light chain, which activates myosin and induces EC contraction, leading to formation of gaps and subsequent regulation of neutrophil transmigration [209, 210]. Consistent with this cascade, leukocyte adhesion and transmigration increase the magnitude of EC traction forces exerted onto the substrate [82, 92]. Because cells are capable of exerting larger traction forces onto stiffer substrates [61], the MLCK-mediated signaling cascade induced by neutrophil adhesion may depend on the mechanical properties of the EC substrate, possibly leading to changes in transmigration.

In this work, we designed an *in vitro* model of the vascular endothelium (Chapter 3) to explore the role of EC substrate stiffness in neutrophil transmigration. Neutrophils primarily transmigrate in the microvasculature, the mechanical properties of which likely vary with health and in different regions of the body. Thus, we used fibronectin-coated

polyacrylamide gel substrates of varying physiologically-relevant stiffness [43, 119, 120] (0.42 kPa - 280 kPa). We plated human umbilical vein endothelial cells (HUVECs) onto the gels, allowed them to form monolayers, and activated them with tumor necrosis factor-alpha (TNF-α) to stimulate an inflammatory response. TNF-α treatment induced significant changes in the endothelium, including softening, local alignment, enlargement, elongation, and cytoskeletal rearrangement. We then added neutrophils to the endothelium (Figure 7.1A) and observed transmigration. Interestingly, neutrophil transmigration increased with increasing substrate stiffness below the endothelium. To explain this, we first evaluated the effects of substrate stiffness on a range of HUVEC properties, including inter-cellular adhesion molecule-1 (ICAM-1) expression, cell stiffness, F-actin organization, cell morphology, and cell-substrate adhesion. Once the HUVECs were activated with TNF-α, these properties could not account for the higher fraction of transmigrated neutrophils on stiffer substrates. Meanwhile, inhibition of MLCK or myosin II decreased transmigration on stiff substrates, while transmigration on soft substrates was unaffected. In addition, on stiff substrates, we observed formation of large holes in the monolayers as ECs retracted; hole formation initiated as neutrophil transmigration reached a maximum. These results provide strong evidence that neutrophil transmigration is regulated by MLCK-mediated generation of intercellular gaps through EC contraction, and that this phenomenon depends on substrate stiffness. These results may also be associated with cardiovascular disease biology, where increased arterial stiffness is coupled with increased leukocyte transmigration.

7.2 Materials and methods

7.2.1 Substrate preparation and characterization

Thin polyacrylamide gels were attached to glass coverslips by a method first described by Wang and Pelham [198] and described in detail in Section 6.2.1. Concentrations in this work included 15% acrylamide + 1.2% bis (280 kPa), 8% acrylamide + 0.2% bis (13 kPa), 8% acrylamide + 0.07% bis (5 kPa), 8% acrylamide + 0.04% bis (4 kPa), 5% acrylamide + 0.05% bis (3 kPa), 3% acrylamide + 0.1% bis (0.87 kPa), and 3% acrylamide + 0.06% bis (0.42 kPa). Gels (~80 μm thick) were coated with 0.1 mg/mL fibronectin (Sigma, St. Louis, MO), also as previously described in Section 6.2.1. Young's moduli of the gels were determined using dynamic mechanical analysis and atomic force microscopy (Section 6.2.2) and characterization of surface-bound fibronectin was done using immunofluorescence to ensure equal protein presentation with stiffness (Section 6.2.3). For experiments on glass, coverslips (22x22 mm, Fisher Scientific, Pittsburgh, PA) were coated with 0.1 mg/mL fibronectin for 2 hours at room temperature.

7.2.2 Cell culture and treatments

HUVECs were purchased from Lifeline Cell Technology (Walkersville, MD) and cultured as previously described in Section 4.2.1. Human brain microvascular ECs (HBMECs; Applied Cell Biology Research Institute, Kirkland, WA) were cultured as previously described [211]. Cells (passages 2-5; $4x10^5$ total) were plated onto fibronectin-coated glass coverslips or polyacrylamide gels and grown for approximately 48 hours until monolayer formation. Cells were then treated with 25 ng/mL human TNF-

α (Fisher Scientific) for the final 24 hours prior to experiments. To further increase permeability of monolayers [166-168], following TNF-α activation, HUVECs were treated with 10 ng/mL cytochalasin B (cytoB; Sigma) or with 1:100 dilution (10 µg/mL) of VE-cadherin antibody (Sigma V1514) for 1 hour at 37˚C just prior to experiments and then washed once with phosphate buffered saline (PBS), as previously described in Section 4.2.1. To inhibit MLCK or myosin II, HUVEC monolayers were pretreated with 15 µM ML-7 (Sigma) or 15 µM blebbistatin, respectively, for 8 minutes and then washed with PBS prior to adding neutrophils. For some experiments, neutrophils were treated in suspension with 15 µM ML-7 for 8 minutes, centrifuged, and resuspended in buffer solution. Treatments with dimethyl sulfoxide (DMSO; Fisher Scientific) or anti-human IgG (Fc specific) antibody (Sigma I9135) were used for vehicle controls as appropriate.

7.2.3 Transmigration assays

Neutrophils were isolated from human blood as previously described in Section 6.2.4. Methods were approved by the University of Maryland Institutional Review Board. Following TNF-α treatment, EC monolayers were washed once with PBS and replaced with fresh media, or treated as described above. A total of approximately $10x10^5$, $5x10^5$, or $2x10^5$ neutrophils were plated onto the EC monolayer and allowed to gravitate down to the monolayer for about 30-60 seconds. Phase contrast images were then captured for 30 minutes as the neutrophils migrated along and transmigrated through the EC monolayers. Microscopy was completed at 37°C, 5% CO_2 and 55% humidity using an inverted microscope (Olympus IX71, Center Valley, PA). Images were captured with a QImaging Retiga-SRV charge-coupled device (CCD) digital camera (QImaging Corporation,

Surrey, British Columbia, Canada) using IPLab software (Becton, Dickinson and Company, Franklin Lakes, NJ). Fraction of neutrophil transmigration was calculated by dividing the number of neutrophils which transmigrated in a particular 30 minute sequence by the total number of neutrophils (typically around 50) in the first frame of that sequence. Neutrophils which entered or exited the field of view later during the sequence were not counted. All experiments were repeated at least 3 times. Neutrophil injury to the monolayer was quantified by counting the number of visible holes in the monolayer in images at various timepoints after plating neutrophils. Number of holes was normalized to total image area. Outlines of holes were traced by hand and area was quantified using ImageJ (National Institutes of Health, Bethesda, MD). Neutrophil migration speeds along the endothelium were determined as outlined in Section 6.2.6. Times for neutrophils to complete transmigration were measured starting at the timepoint just before the first darkened piece of cell was observed in phase contrast microscopy (indicating that transmigration had initiated), and ending at the first timepoint when the entire cell was darkened (indicating that the cell had completely traversed the monolayer).

7.2.4 Cell staining

HUVEC monolayers were fixed, permeabilized, and blocked for non-specific binding as previously described in Section 4.2.2. Cells were stained with antibodies for β-catenin (to visualize cellular borders) and vinculin (to quantify focal adhesions), or with phalloidin-TRITC (to label F-actin) or Hoechst stain (to label cell DNA), as previously described in Section 4.2.2. For ICAM-1 staining, non-permabilized HUVECs were

treated with 10 µg/mL monoclonal anti-human ICAM-1 antibody (R&D Systems BBA3, Minneapolis, MN) for 1 hour, followed by 5 µg/mL anti-mouse Alexa 488 secondary antibody (Invitrogen A11001, Carlsbad, CA) for 1 hour. Fluorescence microscopy was completed at room temperature on immunostained HUVECs using an inverted microscope (Olympus IX81). Images were captured with a Hamamatsu ORCA-ER CCD digital camera (Leeds Precision Instruments, Minneapolis, MD) using Slidebook software (Intelligent Imaging Innovations, Inc., Denver, CO). Cell morphology (area and aspect ratio) and vinculin punctate size and density were measured using the fluorescence images and Image J as previously described in Section 4.2.6. Here, β-catenin-stained cell morphology was measured by applying an edge detector filter, thresholding the images, and then using the particle analyzer in ImageJ.

7.2.5 Viral transfection

HUVECs were transfected with VE-cadherin-GFP (VEcadGFP) using an adenovirus (AdV), which was received as a gift from Dr. William Luscinskas (Harvard University). Construction of the VEcadGFP plasmid and transference to an adenovirus expression vector were previously described in work from Dr. Luscinskas's lab [98]. HUVECs were plated onto fibronectin-coated polyacrylamide gels as discussed in Section 7.2.2 and given 1-2 hours to spread. After attachment and spreading, 3 µL of AdV-VEcadGFP were added to the cells with 2 mL media. HUVECs were incubated for 1-2 days, and finally 25 ng/mL TNF-α was added for an additional 24 hours. Over 24 hours, significant removal of VEcadGFP from the junctions was noticed using

fluorescence timelapse microscopy; however, the signal was still strong enough at 24 hours to obtain data.

7.2.6 Atomic force microscopy

Young's moduli of live HUVEC monolayers were measured using an atomic force microscope (AFM; Agilent, Santa Clara, CA) with a silicon nitride cantilever (Novascan, Ames, IA) with a spherical glass SiO_2 probe of diameter 5 μm. The AFM methods have previously been described in detail in Section 4.2.3. Gel substrates with HUVEC monolayers attached were positioned under the AFM tip and typical force curves were captured for at least 100 different locations along each of 3 independent samples per condition. In a custom-written Matlab (The MathWorks, Natick, MA) program, data were fit to the Hertz-Sneddon model [144] for a paraboloid indenter [146]:

$$F_{paraboloid} = \frac{4}{3}\left(\frac{E}{1-\upsilon^2}\right)R^{1/2}\delta^{3/2},$$

where $F_{paraboloid}$ is the force exerted by the paraboloid indenter, E is the Young's modulus of the cell, R is the radius of curvature of the indenter, and δ is the distance of the indenter from the sample. The cells were assumed to be nearly incompressible [152] and therefore it was assumed that $\upsilon = 0.45$ was the Poisson's ratio of the elastic halfspace. The Young's modulus was found for each force curve using the fitting algorithm and average Young's modulus was computed by averaging all force curves for a given condition.

Gels were ~80 μm thicker than the indentation depth (<200nm), so that the stiffness of the glass coverslip did not affect force curves. Cells within the monolayers

were probed at both the "cell body" (the raised portion), as well as at the cell "periphery" (near the base of the cell body, but not at the cell-cell junctions to avoid the thinnest part of the cell). Indentations were much smaller than the height of the sample (several microns, as measured by confocal microscopy), even at the "periphery" location. In addition, cells were probed with small forces (~2 nN). Thus, it is very unlikely that the substrate stiffness below the HUVECs affected the force curves.

7.2.7 Statistical analysis

Statistical tests were done between pairs of data using a Student's t-test, or among groups of data using analysis of variance (ANOVA), where $P<0.05$ indicated statistical significance. Following ANOVA, multiple comparisons were done using Tukey's honestly significant difference criterion. All measurements reported in this article are in the format mean ± standard error.

7.3 Results

7.3.1 Neutrophil transmigration increases with stiffness below the endothelium

We created an *in vitro* model of the vascular endothelium, where the blood vessel layers below the endothelium were represented by fibronectin-coated polyacrylamide gels of a range of stiffnesses (Figure 7.1A). HUVECs, typical cells to represent the endothelium for leukocyte transmigration *in vitro*, were plated at high density onto the gels to form monolayers. The endothelium was activated with TNF-α in order to induce an inflammatory response. Neutrophils were plated onto the endothelium, and we observed neutrophil activation and migration along the monolayer. Subsequently, a

fraction of neutrophils transmigrated through the endothelium (Figures 7.1B and 7.1C). Neutrophil transmigration was easily observed in phase contrast microscopy and was identified by a change in phase of the neutrophils, from white to dark (Fig 7.1D). Neutrophils in the process of transmigrating contained both a white portion still on top of the endothelium, as well as a dark portion already beneath the endothelium (Figure 7.1D; white arrows). Transmigration typically occurred within about 30 seconds to several minutes. Interestingly, we observed increased neutrophil transmigration through HUVEC monolayers with increased substrate stiffness (Figure 7.1B). From 0.42 kPa to 5 kPa, the fraction of transmigration increased linearly with substrate stiffness ($r^2 = 0.99$). Similar results were obtained using HBMECs (Figure 7.1B).

Figure 7.1. Neutrophil transmigration increases within increasing subendothelial matrix stiffness. **(A)** HUVECs were plated onto fibronectin-coated polyacrylamide gels of varying stiffness from 0.42 kPa to 280 kPa. After monolayer formation, HUVECs were treated with TNF-α to induce an inflammatory response. Neutrophils were isolated from human blood and plated onto the HUVEC monolayer**. (B)** The fraction of neutrophils which transmigrated was quantified as a function of the stiffness below the HUVECs. Bars indicate average fraction of transmigrated cells, while error bars indicate standard error of 3-8 experiments (N = 6, 8, 4, 6, 8, 3, 7, 3 from 0.42 kPa, 0.87 kPa, 3 kPa, 4 kPa, 5 kPa, 13 kPa, 280 kPa, and glass (~50 GPa), respectively). **(C)** Data from panel B, up to 5 kPa, are plotted with a linear fit ($r^2 = 0.99$). Statistical significance for panels B-C is indicated by *** ($P<0.001$), ** ($P<0.005$), or ^ ($P<0.05$), using a t-test in comparison with 5 kPa value of same cell type. **(D)** Shown is an example of a phase contrast timelapse image sequence of 4 neutrophils, 2 of which transmigrate through the endothelium. Scale bar is 10 μm and applies to all images. T=0 is time just prior to initiation of transmigration in the first cell. White arrows point to the phase-darkened portion of the neutrophil as it transmigrates through the endothelium. At T=75 seconds, the white arrowhead points to a neutrophil which possibly initiates but does not complete transmigration. In the final frame, the 2 darkened neutrophils are between the endothelium and the gel, while the 2 white neutrophils are on top of the endothelium.

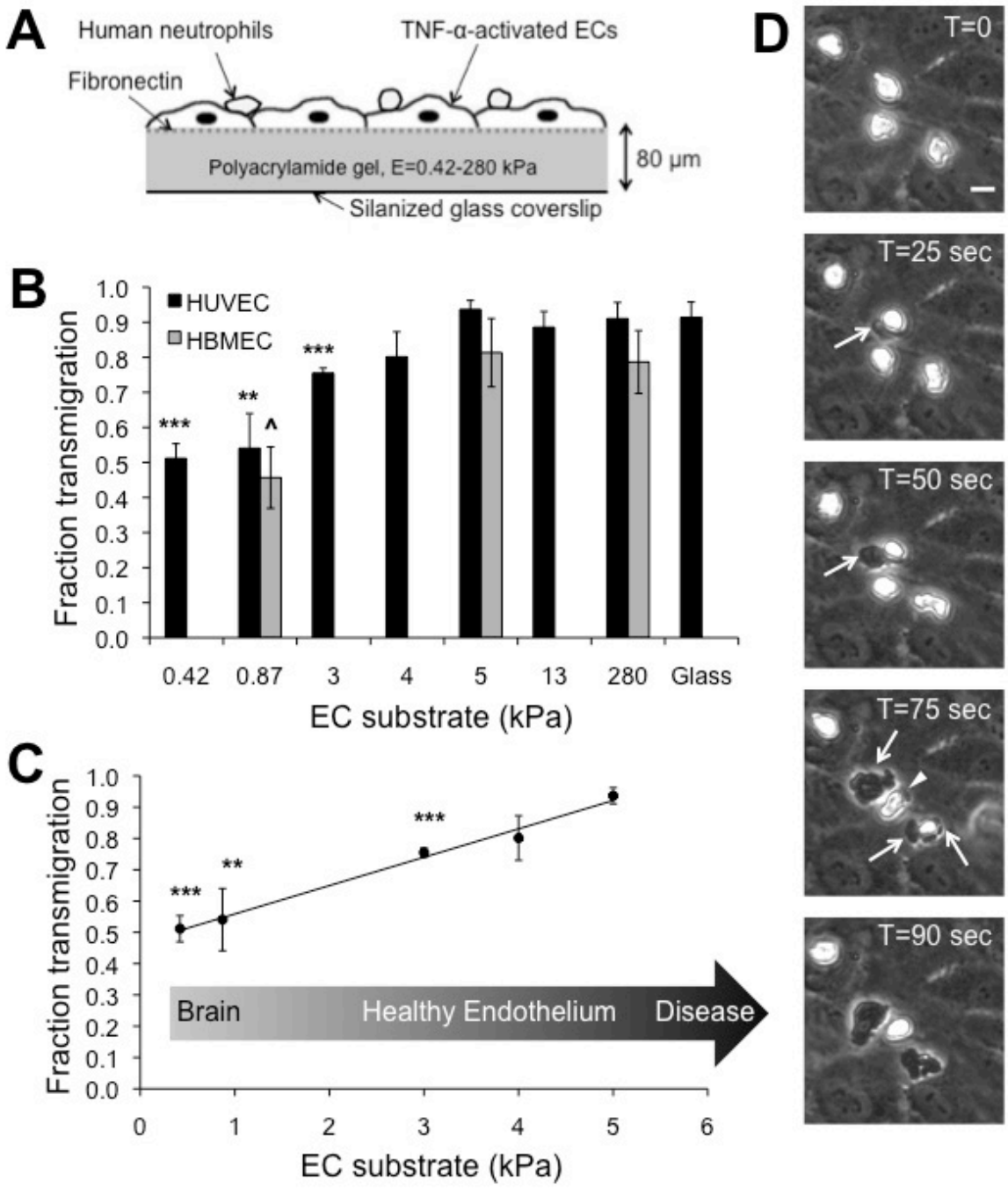

7.3.2 Neutrophils transmigrate primarily via the paracellular pathway

As discussed in Section 2.9, neutrophils are able to transmigrate through two different pathways: (1) the paracellular route and (2) the transcellular route. When neutrophils take the paracellular route, they can squeeze between ECs along the border ("bicellular"), or between three ECs at the tricellular junction. *In vivo*, neutrophils preferentially take the tricellular mode of transmigration in mouse cremaster muscle microvessels, as measured using intravital microscopy [212]. Neutrophils have also been shown to preferentially transmigrate at tricellular junctions *in vitro* [213].

Here, we wished to determine whether subendothelial matrix stiffness affects the mode of transmigration. Using an adenovirus, we transfected HUVECs for VEcadGFP to observe the location of the cell-cell junctions live, during transmigration. We simultaneously captured phase contrast images of the neutrophils and fluorescence images of EC VEcadGFP, and overlaid them to determine the point of transmigration in relation to the EC borders. We observed transmigration via all three pathways: at bicellular junctions (Figure 7.2), at tricellular junctions (Figure 7.3), and via the transcellular route (Figure 7.4).

In addition, we quantified the relative contributions of each of these routes to the total amount of transmigration (Figure 7.5). In our experiments, the paracellular pathway comprised a significantly higher fraction of transmigration than the transcellular pathway, for all stiffnesses ($P<0.05$). Transcellular transmigration accounted for less than 7% of total transmigration on all stiffness (Figure 7.5). By trend, neutrophils slightly favored the bicellular route over the tricellular routes, though there was no statistical difference between the two pathways for any substrate stiffness (Figure 7.5).

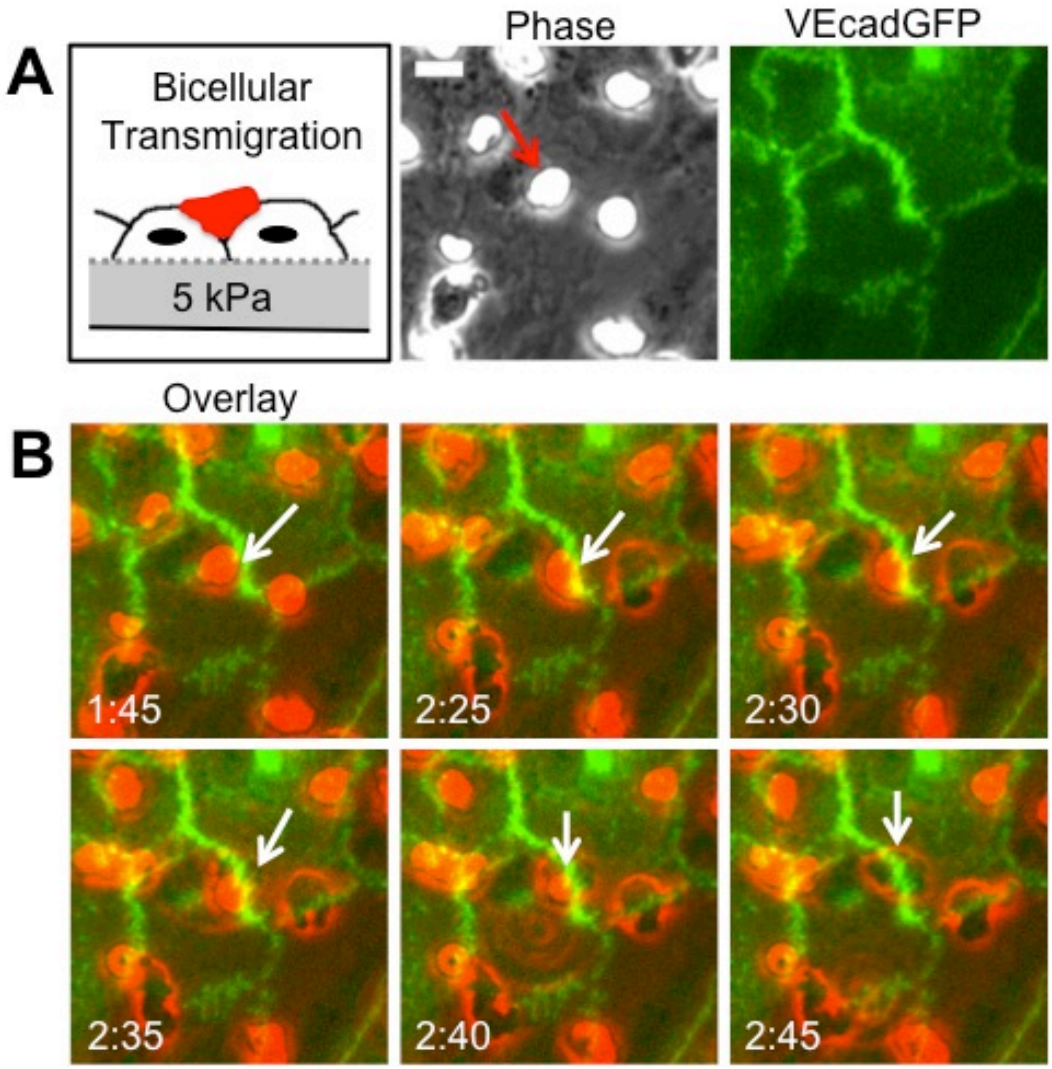

Figure 7.2. Example of neutrophil transmigration through the **bicellular** pathway. **(A)** The schematic indicates the method of bicellular transmigration, by which a neutrophil (red) squeezes through at the junction of two cells. Also shown in panel A are a phase contrast image and fluorescence image of VEcadGFP. The red arrow points to the neutrophil of interest, which transmigrates through the bicellular pathway. **(B)** Overlay of the phase contrast (red) and VEcadGFP (green) images indicates that the neutrophil of interest, now shown by the white arrow, transmigrates right at the cell-cell junctions (green). In each image in panel B, the time in the lower left-hand corner is in minutes:seconds format and indicates the time after plating neutrophils on the endothelium. Scale bar in phase contrast image in panel A is 10 μm and applies to all images. **Note that the VEcadGFP (green) image is the same for all timepoints and therefore does not show dislocation of VE-cadherin from the junction as the neutrophil transmigrates.**

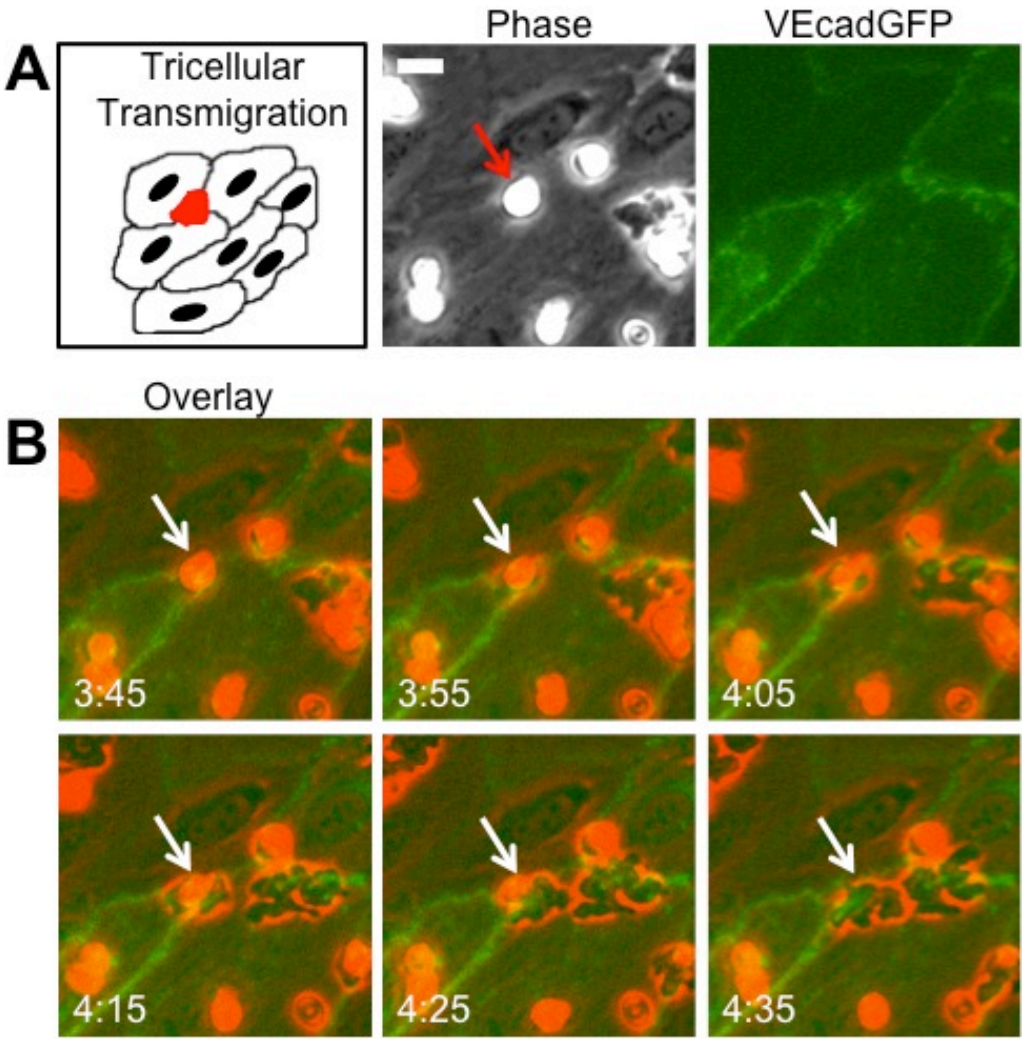

Figure 7.3. Example of neutrophil transmigration through the **tricellular** junctions of ECs. **(A)** The schematic indicates the method of tricellular transmigration, by which a neutrophil (red) squeezes through at the junction of three cells. Also shown in panel A are a phase contrast image and fluorescence image of VEcadGFP. The red arrow points to the neutrophil of interest, which transmigrates through the tricellular pathway. **(B)** Overlay of the phase contrast (red) and VEcadGFP (green) images indicates that the neutrophil of interest, now shown by the white arrow, transmigrates right at the intersection of three ECs. In each image in panel B, the time in the lower left-hand corner is in minutes:seconds format and indicates the time after plating neutrophils on the endothelium. Scale bar in phase contrast image in panel A is 10 μm and applies to all images. **Note that the VEcadGFP (green) image is the same for all timepoints and therefore does not show dislocation of VE-cadherin from the junction as the neutrophil transmigrates.**

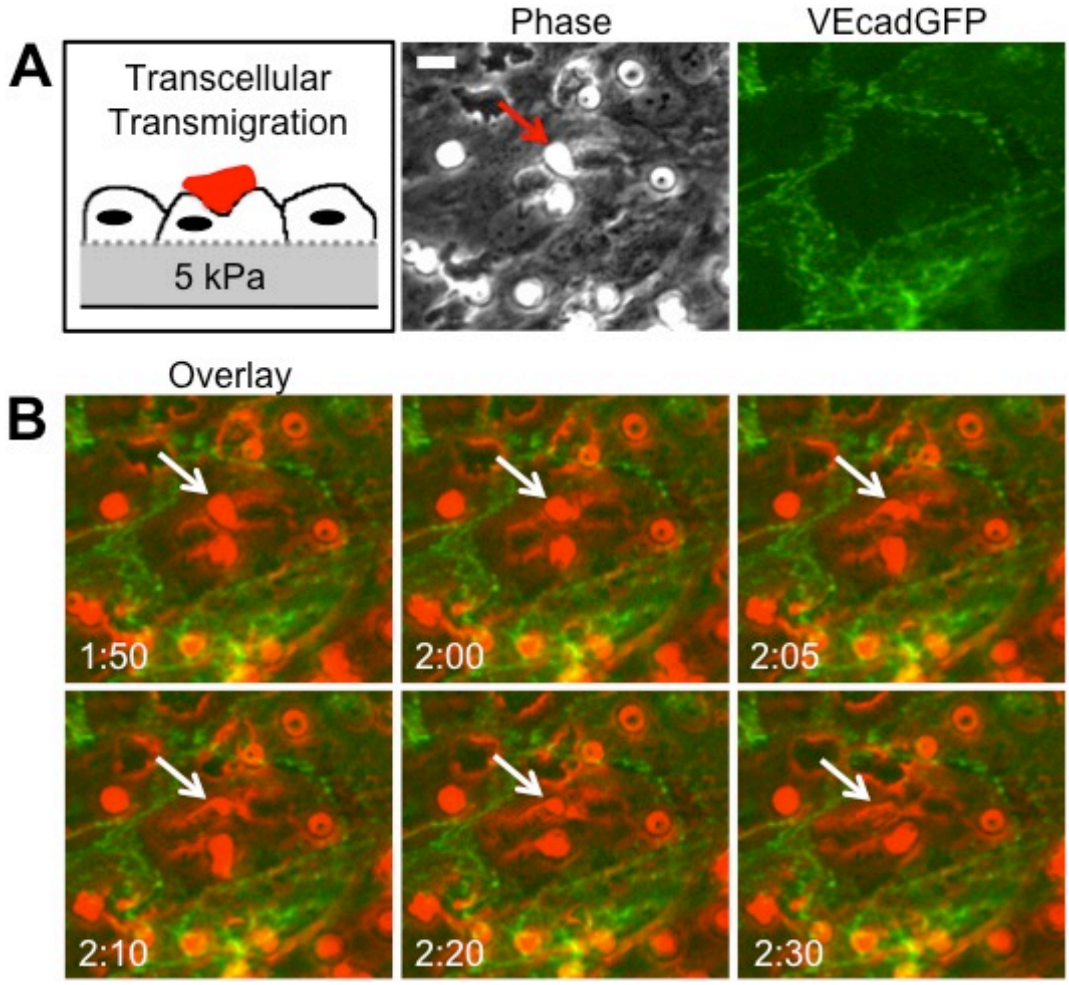

Figure 7.4. Example of neutrophil transmigration through the **transcellular** pathway. **(A)** The schematic indicates the method of transcellular transmigration, by which a neutrophil transmigrates through the body of an EC, far from the cell-cell junctions. Also shown in panel A are a phase contrast image and fluorescence image of VEcadGFP. The red arrow points to the neutrophil of interest, which transmigrates through the transcellular pathway. **(B)** Overlay of the phase contrast (red) and VEcadGFP (green) images indicates that the neutrophil of interest, now shown by the white arrow, transmigrates far from the cell-cell junctions (green). In each image in panel B, the time in the lower left-hand corner is in minutes:seconds format and indicates the time after plating neutrophils on the endothelium. Scale bar in phase contrast image in panel A is 10 μm and applies to all images. **Note that the VEcadGFP (green) image is the same for all timepoints.**

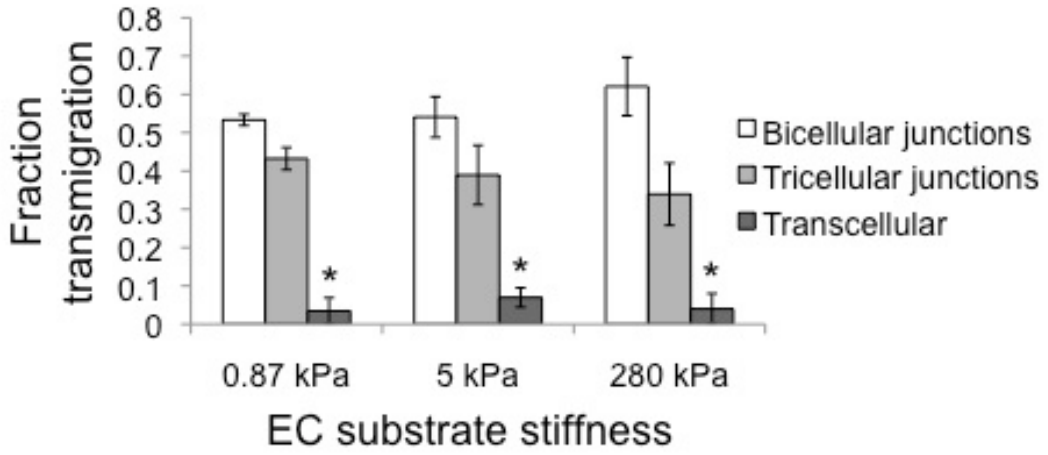

Figure 7.5. Neutrophils transmigrate through HUVECs primarily via the paracellular route (specifically, the bicellular route or at tricellular junctions. For each subendothelial matrix stiffness, the fraction of transmigration is the number of neutrophils that transmigrated via a particular route, divided by the total number of neutrophils that transmigrated (not the total number of cells). Bars are average of 3 experiments, while error bars indicate standard error. * indicates $P<0.05$ with paracellular and tricellular junctions data for the same substrate stiffness.

7.3.3 ICAM-1 expression does not depend on substrate stiffness

TNF-α activation of HUVECs is known to upregulate ICAM-1, which was necessary for neutrophil transmigration according to two experiments which we performed: (1) If the HUVECs were not activated using TNF-α, there was low ICAM-1 expression, and we observed that only ~1% of neutrophils transmigrated (Figure 7.6). (2) If the HUVECs were activated using TNF-α, but then ICAM-1 was blocked using an antibody, we observed the fraction of transmigration drop off with increasing antibody

concentration on all substrates (Figure 7.6). Thus, we quantified ICAM-1 expression on the apical surface of TNF-α-activated HUVEC monolayers using an ICAM-1 antibody and a fluorescent secondary antibody, combined with fluorescence imaging (Figure 7.7A). Quantification of the fluorescence intensity revealed no difference ($P>0.05$) in ICAM-1 expression in TNF-α-activated HUVECs on 0.87 kPa, 5 kPa, and 280 kPa substrates (Figure 7.7B).

7.3.4 Stiffness of TNF-α-activated HUVEC monolayers varies little with substrate stiffness

Using AFM, we obtained deflection images (Figure 7.8A) and then measured the stiffness (Young's modulus) of control and TNF-α-activated HUVEC monolayers on varying substrates, at both the cell body and periphery locations (Figure 7.8B). Deflection images of control monolayers revealed more disorganization on soft, 0.87 kPa substrates than on stiffer 5 kPa or 280 kPa substrates (Figure 7.8A; top). Average stiffness of the control endothelium increased with increasing substrate stiffness at both the cell body and periphery (Figure 7.8B; $P<0.001$). However, upon treatment with TNF-α, the HUVECs on all substrates elongated, aligned, and enlarged, and no differences were observed between the three substrates in the AFM deflection images (Figure 7.8A; bottom). Further, while the stiffness of the TNF-α-activated endothelium still increased with substrate stiffness at both the cell body and periphery (Figure 7.8B; $P<0.001$), the trend was much less dramatic. Interestingly, the endothelium softened with TNF-α treatment on the stiffer substrates ($P<0.001$). In varying substrate stiffness, the stiffness of the TNF-α-

activated endothelium changed only to a small degree (~50 Pa at the cell body and ~300 Pa at the periphery).

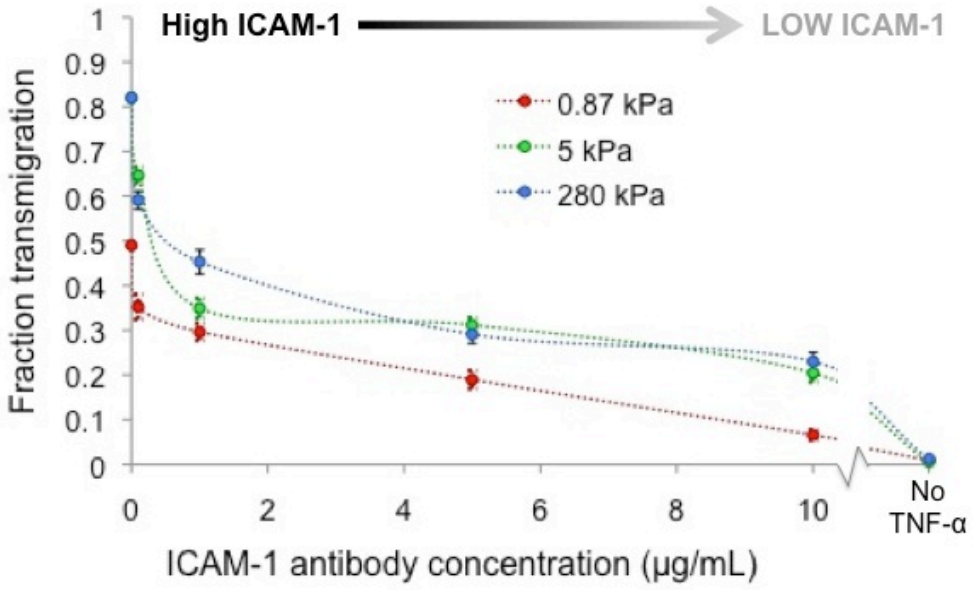

Figure 7.6. Neutrophil transmigration depends on endothelial cell ICAM-1 presentation. HUVECs on varying substrates (087, 5, and 280 kPa) were treated with TNF-α for 24 hours, washed with PBS, treated with varying concentrations of ICAM-1 antibody (0.1, 1, 5, and 10 μg/mL) for 1 hour, and washed again with PBS. Neutrophils were plated onto the endothelium, and 10 images were taken in various locations across the monolayer at 15 minutes after addition of neutrophils in order to visualize and subsequently quantify the fraction of transmigrated neutrophils. Data points are also shown for no ICAM-1 antibody (0 μg/mL; high ICAM-1) after TNF-α treatment, as well as for no TNF-α treatment (low ICAM-1). Data points represent average fraction of transmigrated cells, while bars indicate standard error. Dotted lines connecting data points do not represent data but are included to guide the eye.

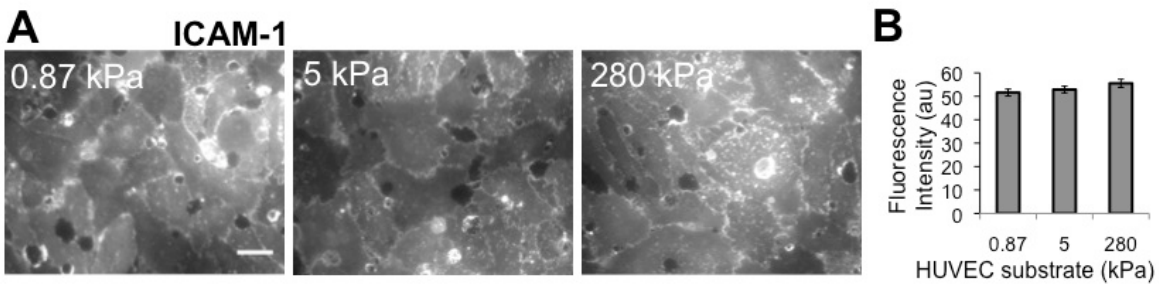

Figure 7.7. Immunostaining indicates no change in ICAM-1 expression with substrate stiffness. ICAM-1 was measured as a function of HUVEC substrate stiffness using a fluorescently-tagged antibody to ICAM-1 on non-permeabilized TNF-α-activated HUVEC monolayers. Fluorescence images were taken over many locations on the non-permeabilized HUVEC monolayer surface **(A)**, and intensity (in arbitrary units, au) was quantified using ImageJ software **(B)**. Scale bar in panel A is 20 μm and applies to all images. Substrate stiffness is indicated in the upper left corner of each image in panel A. Bars indicate average of at least 20 images from each of 2 independent experiments, while error bars indicate standard error. ANOVA indicates that $P>0.05$ among stiffnesses.

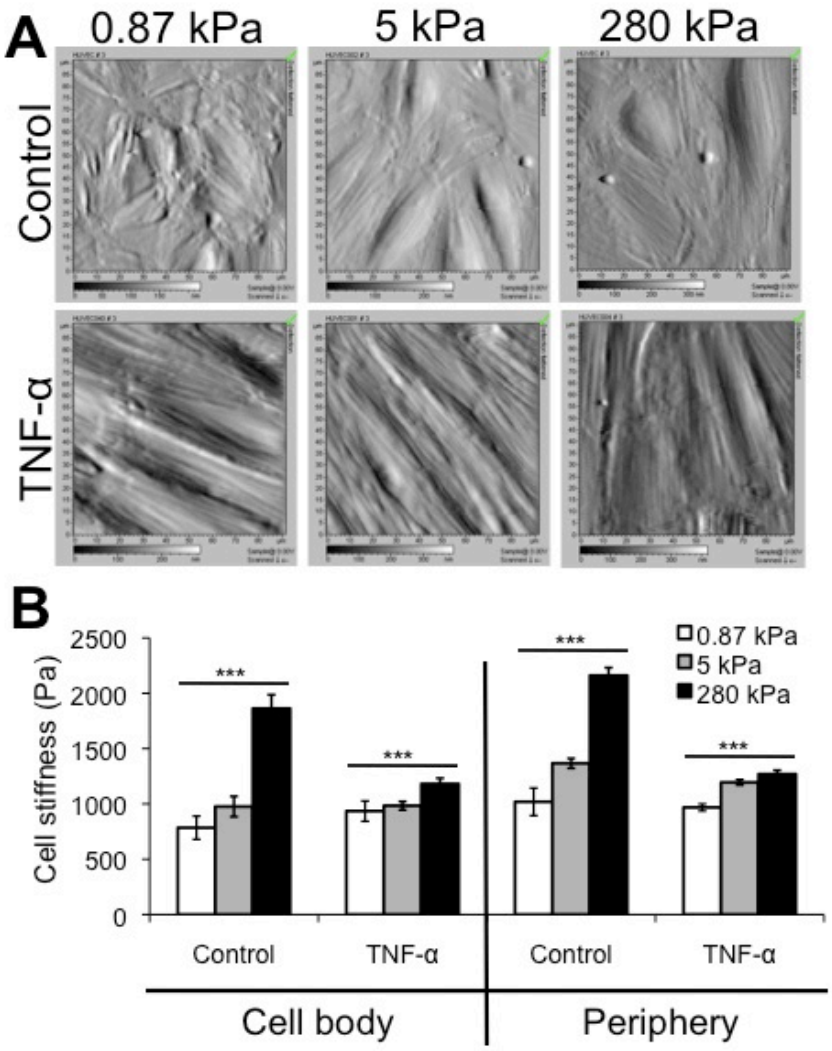

Figure 7.8. Atomic force microscopy data reveals only a slight increase in TNF-α-activated HUVEC stiffness with substrate stiffness. **(A)** Atomic force microscopy (AFM) was used to obtain deflection images for HUVEC monolayers on 0.87 kPa, 5 kPa, and 280 kPa substrates, both under control and TNF-α-treated conditions. Deflection images are 90 µm by 90 µm. **(B)** AFM was also used to quantify the Young's modulus ("stiffness") of HUVEC monolayers as a function of substrate stiffness in the control (no TNF-α) and after TNF-α treatment. The stiffness of the "cell body" region (raised portion of the cell) and periphery (flattened region just around the raised portion) were quantified separately. Bars indicate average stiffness from N force curves from 3 independent experiments, while error bars indicate standard error. N=47, 50, 89 on control monolayers on 0.87 kPa, 5 kPa, and 280 kPa, respectively, at the cell body. N=381, 351, 334 on control monolayers on 0.87 kPa, 5 kPa, and 280 kPa, respectively, at the periphery. N=96, 121, 160 on TNF-α-activated monolayers on 0.87 kPa, 5 kPa, and 280 kPa, respectively, at the cell body. N=396, 357, 399 on TNF-α-activated monolayers on 0.87 kPa, 5 kPa, and 280 kPa, respectively, at the periphery. *** indicates $P<0.001$ using ANOVA. On 280 kPa, $P<0.001$ between control and TNF-α at both cell body and periphery using Student's t-test.

7.3.5 Neutrophil transmigration injures the endothelium on stiff substrates

Prior to neutrophil transmigration, HUVEC monolayers on soft and stiff substrates were visually intact, according to phase contrast images. Interestingly, monolayers on soft substrates were nearly always still intact following neutrophil transmigration (Figure 7.9A). In contrast, neutrophil transmigration created large holes in the monolayers on stiff substrates (Figures 7.9B, 7.9C, and 7.9D), indicating EC injury. Holes initiated as the HUVECs retracted, though they retained cell-cell adhesion on the sides opposite to retraction. In some cases, significant neutrophil accumulation beneath the endothelium created large holes and prevented healing (Figure 7.9D), while often the endothelium was able to heal smaller holes (Figure 7.9E). Hole formation was usually initiated by neutrophils which had already transmigrated and which changed in morphology from highly protrusive (Figure 7.10; T=0.92 to T=2.25 minutes), to more isotropic and spread-out (Figure 7.10; T=5.83 minutes). Hole formation began at 25 minutes after plating neutrophils (about the same time when the maximum fraction of neutrophils had transmigrated), reached a peak by 45 minutes, and subsequently dropped off (Figure 7.11A). Holes were observed similarly when $10x10^5$ or $5x10^5$ neutrophils were added to the endothelium, while very few holes were observed with $2x10^5$ neutrophils (Figures 7.11A and 7.11B). Holes were also significantly larger on 5 kPa or 280 kPa substrates in comparison with 0.87 kPa (Figure 7.11C).

7.3.6 Decreasing cell-cell adhesion increases transmigration on soft substrates

To determine whether endothelial cell-cell adhesion changed with substrate stiffness, we varied the degree of cell-cell adhesion by preconditioning the TNF-α-

activated endothelium for one hour with one of two treatments: (1) 10 ng/mL cytoB or (2) VE-cadherin antibody, both of which have previously been shown to decrease cell-cell adhesion [166-168]. With VE-cadherin antibody treatment, there was increased transmigration on soft 0.87 kPa substrates in comparison with the IgG antibody control ($P<0.05$), yet no change in transmigration on stiff 280 kPa substrates in comparison with the control ($P>0.05$) (Figure 7.12A). Transmigration was not statistically different with cytoB treatment for any substrates.

7.3.7 Inhibition of MLCK normalizes effects of substrate stiffness

We investigated the role of MLCK-mediated EC contraction in neutrophil transmigration as a function of substrate stiffness using the selective MLCK inhibitor ML-7 [214] (Figure 7.12B). Transmigration through ML-7-treated HUVECs on stiff substrates (5 kPa and 280 kPa; 58±6% and 67±5% transmigration, respectively) was reduced nearly to the level as on soft substrates with the same treatment (0.87 kPa; 45±5% transmigration) (Figure 7.12B). On 5 kPa and 280 kPa, transmigration was significantly reduced with respect to the DMSO vehicle control (Figure 7.12B; $P<0.01$), while transmigration on the soft 0.87 kPa substrate was not affected. Treatment of HUVECs with blebbistatin to inhibit myosin II had the same effect as ML-7 treatment (Figure 7.12B). Very few holes formed on all substrates with ML-7 treatment. ICAM-1 expression was not affected by ML-7 treatment on any substrate (Figure 7.13). As expected, transmigration of ML-7-treated neutrophils through untreated (TNF-α only) ECs was reduced on all substrates (Figure 7.12B).

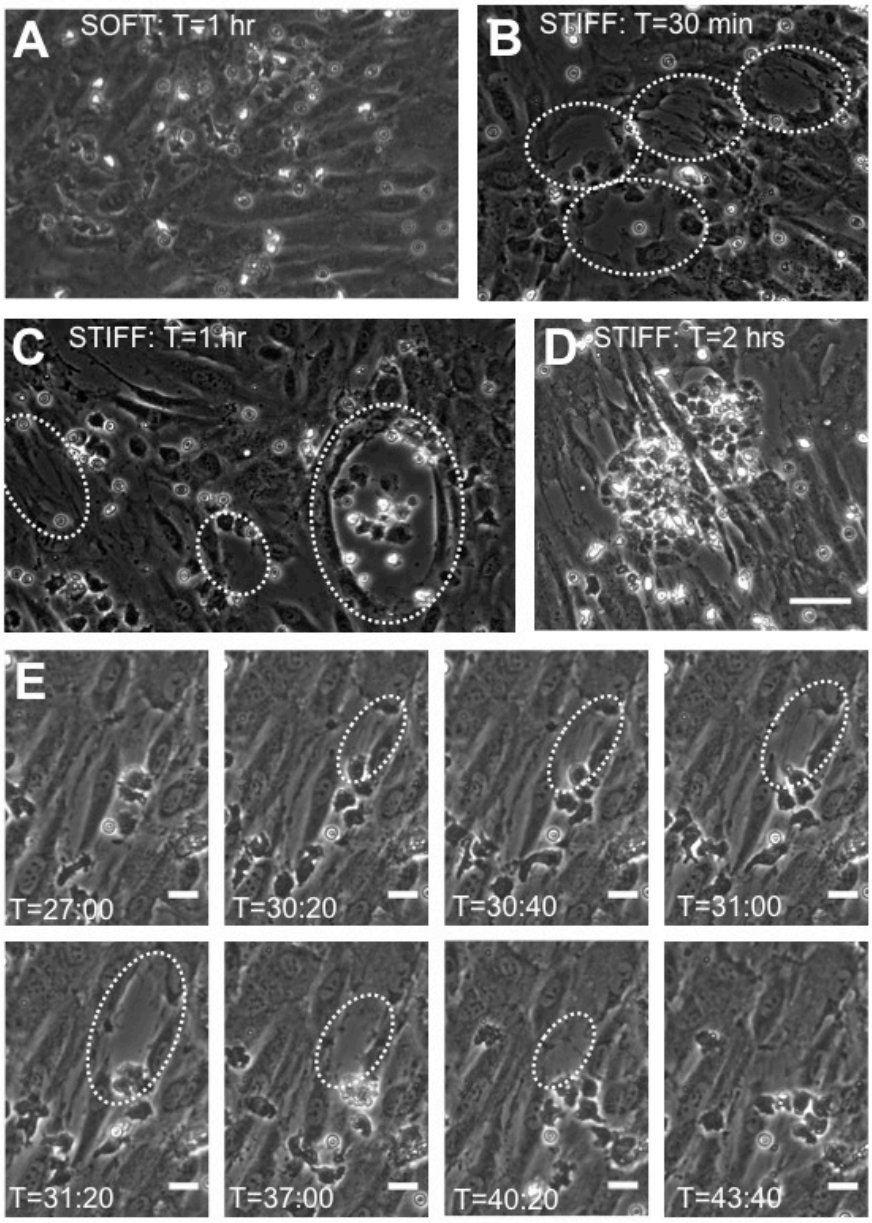

Figure 7.9. Neutrophil transmigration on stiff substrates causes injury to the monolayer; small holes reseal while larger ones do not. Shown are representative phase contrast images of the HUVEC monolayer following neutrophil transmigration on **(A)** a soft (0.87 kPa) substrate, and **(B-C)** stiff (280 kPa) substrates. Time after plating neutrophils onto the HUVEC monolayers (T) is shown at the top of each image. Large holes commonly form in monolayers on stiff substrates after transmigration and are outlined in panels B-C by white dotted lines. **(D)** Also shown is a phase contrast image of a monolayer on a 280 kPa substrate at approximately 2 hours after plating neutrophils. Significant neutrophil accumulation in the area of the hole has occurred. The scale bar in panel D is 50 μm and applies to images in panels A-D. **(E)** Shown is a time sequence of a hole forming and then healing on a 5 kPa substrate. Time after plating neutrophils is indicated at the bottom of each image. The scale bars on all images in panel E are 20 μm.

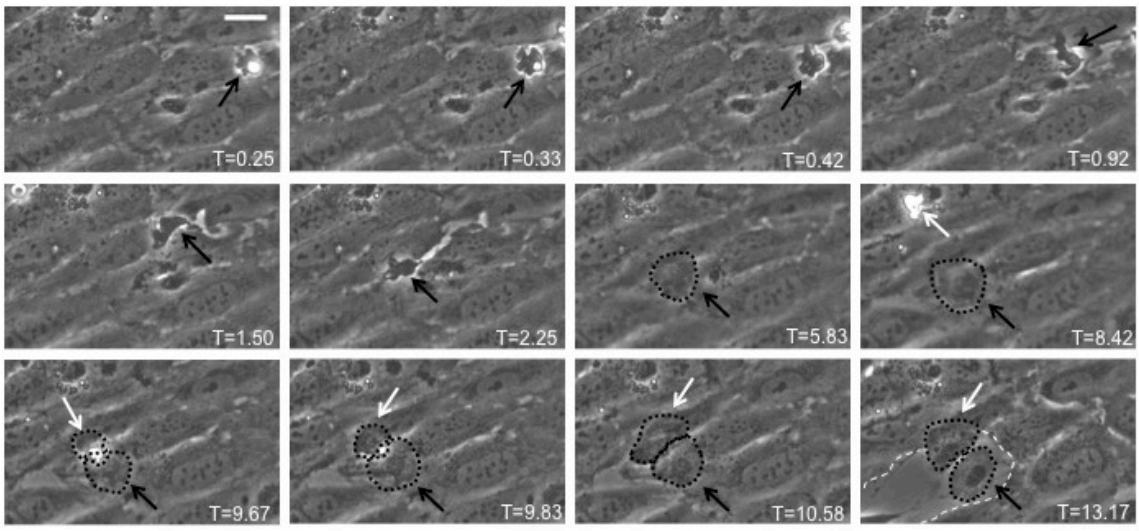

Figure 7.10. Change in neutrophil morphology, from protrusive to round, after transmigration leads to injury of the endothelium on a stiff substrate. Phase contrast time sequence of two neutrophils as they migrate on top of a HUVEC monolayer on a 280 kPa gel and then transmigrate. The time after plating (T) is shown in minutes and the scale bar is 20 μm and applies to all images in panel E. Black arrows point to the first neutrophil of interest (Cell 1), while the white arrows point to a second neutrophil of interest (Cell 2). Cell 1 is in the middle of transmigrating in the first image and transmigrates completely by T=0.42. At T=5.83, it drastically changes morphology and spreads out in an isotropic fashion (Cell 1 is outlined in black dotted line for clarity when it is under the endothelium). Then, at T=8.42 Cell 2 enters the view, migrates toward Cell 1 and then transmigrates (black dotted outline in T=9.67 and T=9.83). By T=10.58, Cell 2 has completely transmigrated and both cells have spread out nearly isotropically, instead of taking on the spindly-like morphology normally seen in neutrophils which are migrating under the HUVEC monolayer. After both cells have transmigrated and spread out, the HUVEC monolayer rips apart (white dotted line at T=13.17), exposing Cell 1 and Cell 2 spread out on the now-bare gel.

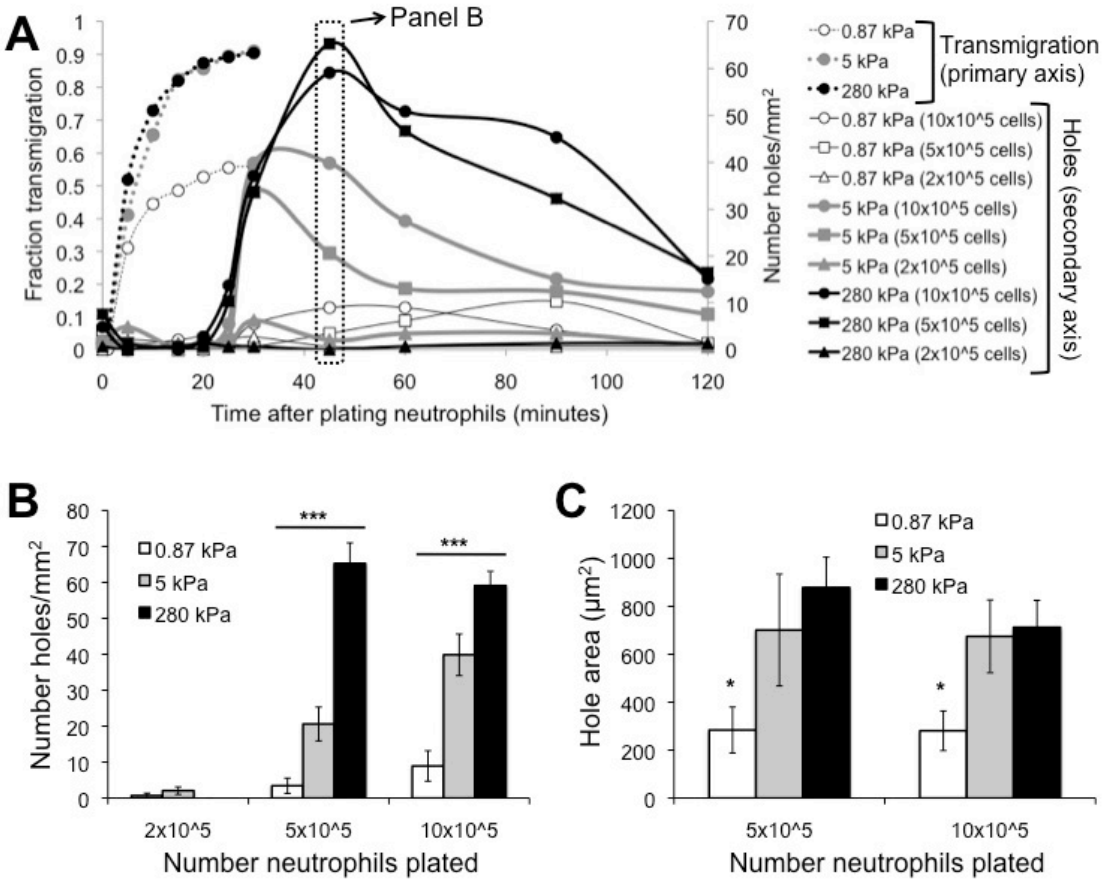

Figure 7.11. Endothelial cell hole formation begins when neutrophil transmigration has reached a maximum. **(A)** Fraction of neutrophils which have transmigrated (primary vertical axis) as a function of time after addition of neutrophils is shown for varying substrates (0.87, 5, 280 kPa). Also plotted is the number of holes per area (secondary vertical axis) as a function of time after addition of neutrophils, for varying substrates and number of neutrophils plated. **(B)** Data from panel A at T=45 minutes is highlighted. Shown is the number of holes per area on each of the substrates, with varying numbers of neutrophils. **(C)** The area of holes at T=45 minutes is quantified for varying substrate stiffness and number of neutrophils plated. Bars indicate average, while error bars indicate standard error. * and *** indicate $P<0.05$ and $P<0.001$, respectively, using ANOVA.

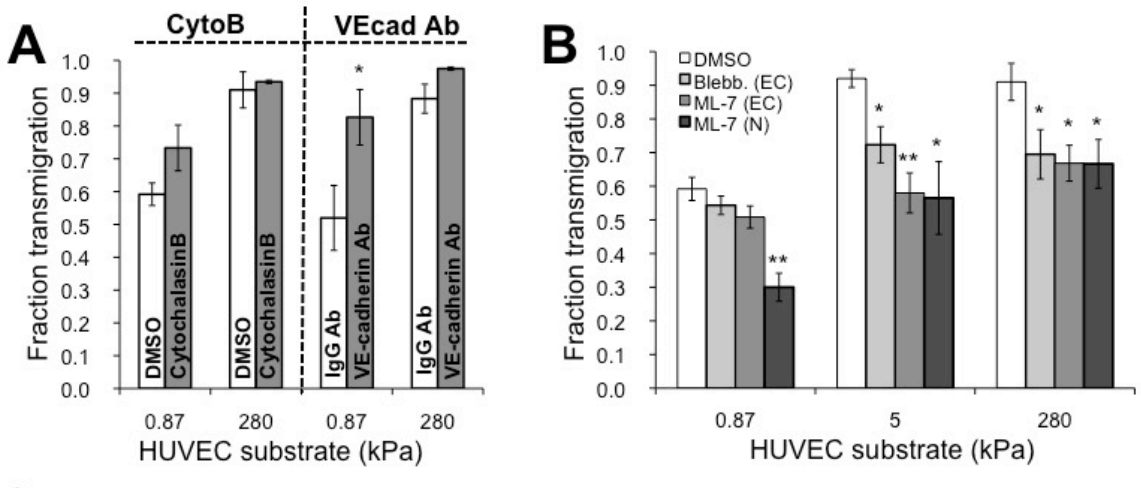

Figure 7.12. MLCK mediates substrate stiffness-dependent neutrophil transmigration. **(A)** TNF-α-activated HUVEC monolayers were pre-treated with appropriate control (DMSO or IgG antibody), cytochalasin B (cytoB), or VE-cadherin antibody (VEcad Ab) for one hour. Neutrophils were plated onto the HUVECs and the fraction of transmigration was quantified on soft (0.87 kPa) and stiff (280 kPa) substrates. **(B)** TNF-α-activated HUVEC monolayers were pre-treated with DMSO, blebbistatin, or ML-7. Neutrophils were plated onto the HUVECs and the fraction of transmigration was quantified on soft (0.87 kPa), intermediate (5 kPa), and stiff (280 kPa) substrates. Also shown is the fraction of transmigration for ML-7-treated neutrophils through TNF-α-treated monolayers. In panel B, the legend indicates whether the endothelial cells (EC) or neutrophils (N) were treated with the drug. Bars in panels A-B indicate average fraction of transmigrated cells, while error bars indicate standard error from at least 3 independent experiments. In panel A * indicates $P<0.05$ with IgG antibody control using Student's t-test. In panel B * indicates $P<0.05$ and ** indicates $P<0.01$ between treated monolayers and DMSO control using Student's t-test.

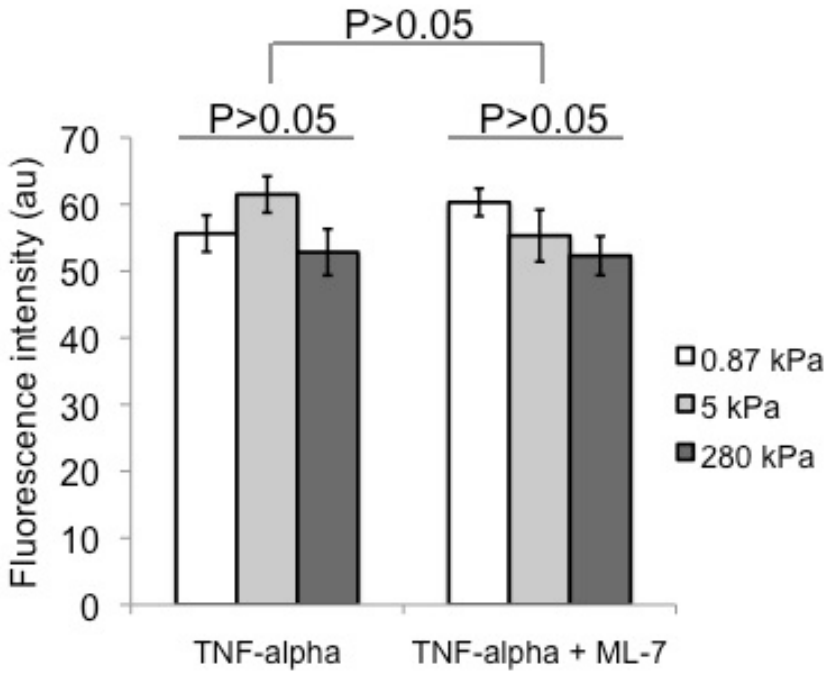

Figure 7.13. Immunostaining indicates no change in ICAM-1 expression with substrate stiffness after treatment with TNF-α and ML-7. ICAM-1 was measured as a function of HUVEC substrate stiffness using a fluorescently-tagged antibody to ICAM-1 on TNF-α-activated and TNF-α-activated plus ML-7-treated HUVEC monolayers. Fluorescence images were taken over many locations on the HUVEC monolayer surface, and intensity was quantified using ImageJ software. Bars indicate average of at least 20 images from each substrate, while error bars indicate standard error.

7.3.8 TNF-alpha abrogates effects of substrate stiffness on F-actin organization

Using phalloidin-actin staining, we evaluated the organization of the F-actin cytoskeleton as a function of substrate stiffness for control monolayers and those treated with TNF-α. In control monolayers on soft 0.87 kPa substrates, the F-actin was more disorganized, with less developed stress fibers, as compared with control monolayers on stiff 280 kPa substrates, where the actin fibers appeared longer, straighter, and more organized (Figure 7.14; white arrowheads). Once the HUVECs were treated with TNF-α, the F-actin architecture did not appear noticeably different on soft and stiff substrates; the stress fibers were extended and mature on all substrates (Figure 7.15; white arrowheads), as observed by fluorescence microscopy. F-actin staining also revealed the elongation, alignment, and enlargement of the HUVECs with TNF-α treatment (Figure 7.15), as compared with untreated cells (Figure 7.14).

7.3.9 HUVEC morphology in a monolayer does not depend on substrate stiffness

We first measured the area of single cells with no cell-cell contacts, as a function of substrate stiffness, and found that single cell area increased with substrate stiffness (Figure 7.16A; $P<0.001$). We then immunostained the monolayers using a β-catenin antibody as a marker of cell borders (Figures 7.14 and 7.15) to evaluate the morphology of cells within the monolayer. As previously described in Chapter 4, cells in monolayer were much smaller than single cells. However, once the cells were in monolayer, cell area was independent of substrate stiffness, and this was true for both control and TNF-α-activated HUVECs (Figure 7.16A). Similarly, the aspect ratio of cells within the control and TNF-α-activated monolayers did not depend on substrate stiffness (Figure 7.16B;

P>0.05). However, it was apparent that TNF-α treatment itself caused an in increase in both cell area (Figure 7.16A; P<0.001) and aspect ratio on all substrates (Figure 7.16B; P<0.001), which was in agreement with the F-actin staining (Figure 7.15). As a result of similar morphology, monolayers treated with TNF-α also displayed a similar cell density of approximately $1.7x10^4$ cells/mm^2.

7.3.10 Focal adhesion size and density of HUVEC monolayers do not depend on substrate stiffness

To evaluate the amount of cell-substrate adhesion as a function of substrate stiffness, we immunostained the HUVEC monolayers for vinculin, a marker of focal adhesions (FAs) [154; See also Section 4.3.6]. Fluorescence images (Figure 7.17A) and subsequent processed binary images (Figure 7.17B) displayed the punctate FAs, which we quantified in terms of density (number per area) and area (size of individual FAs). While there were less FAs per area in TNF-α-activated HUVEC monolayers compared with the control (Figure 7.17C), neither the density nor area of FAs in both control and TNF-α-activated monolayers depended on substrate stiffness (Figures 7.17C and 7.17D; P>0.05).

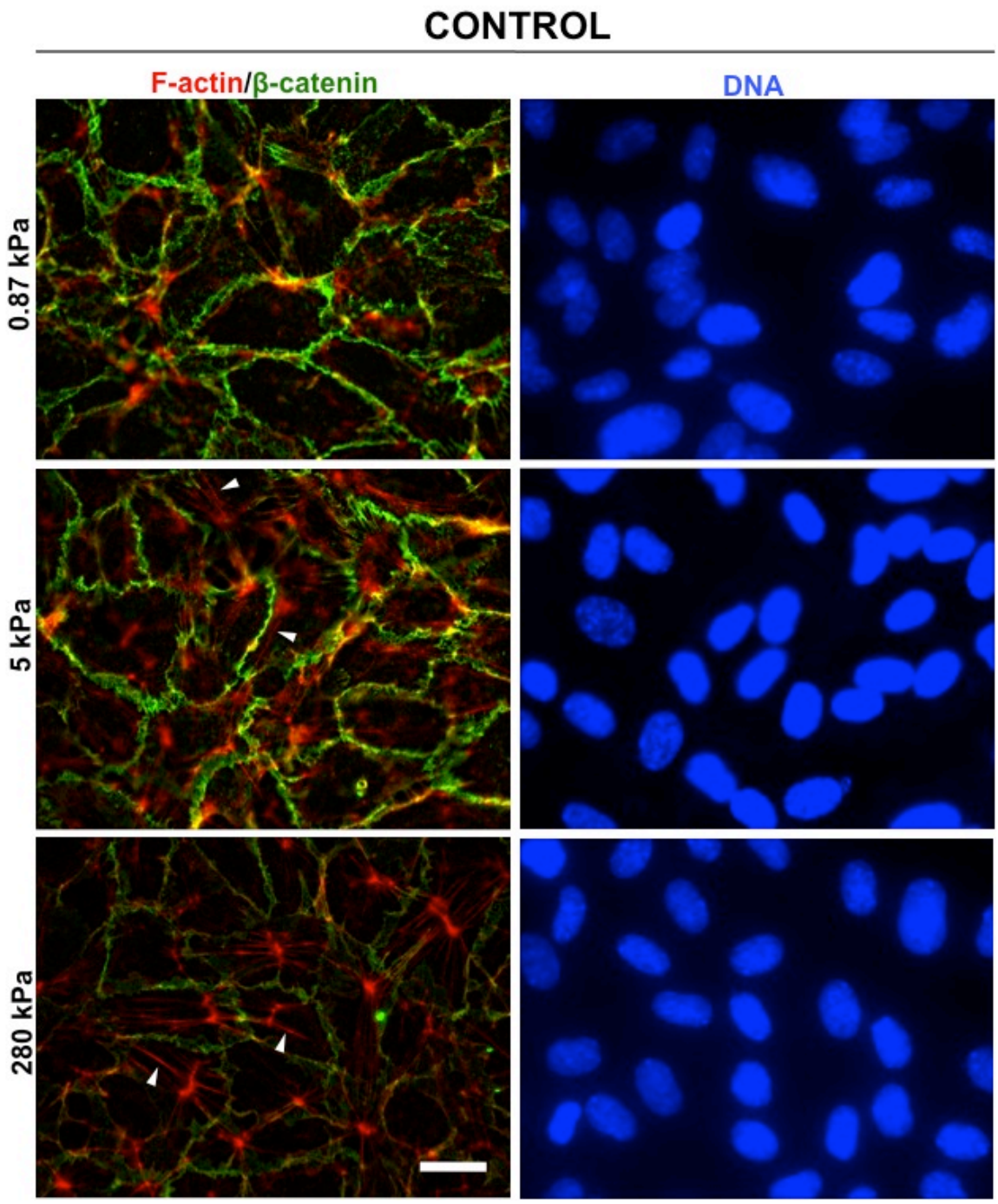

Figure 7.14. Untreated HUVECs in monolayer form more mature F-actin stress fibers on stiffer substrates. HUVECs were immunostained for β-catenin (green) and stained for F-actin (red) and DNA (blue), and fluorescence images were taken. Scale bar is 20 μm and applies to all images. DNA image corresponds to same group of cells as those shown for F-actin/β-catenin. White arrowheads point to examples of F-actin stress fibers.

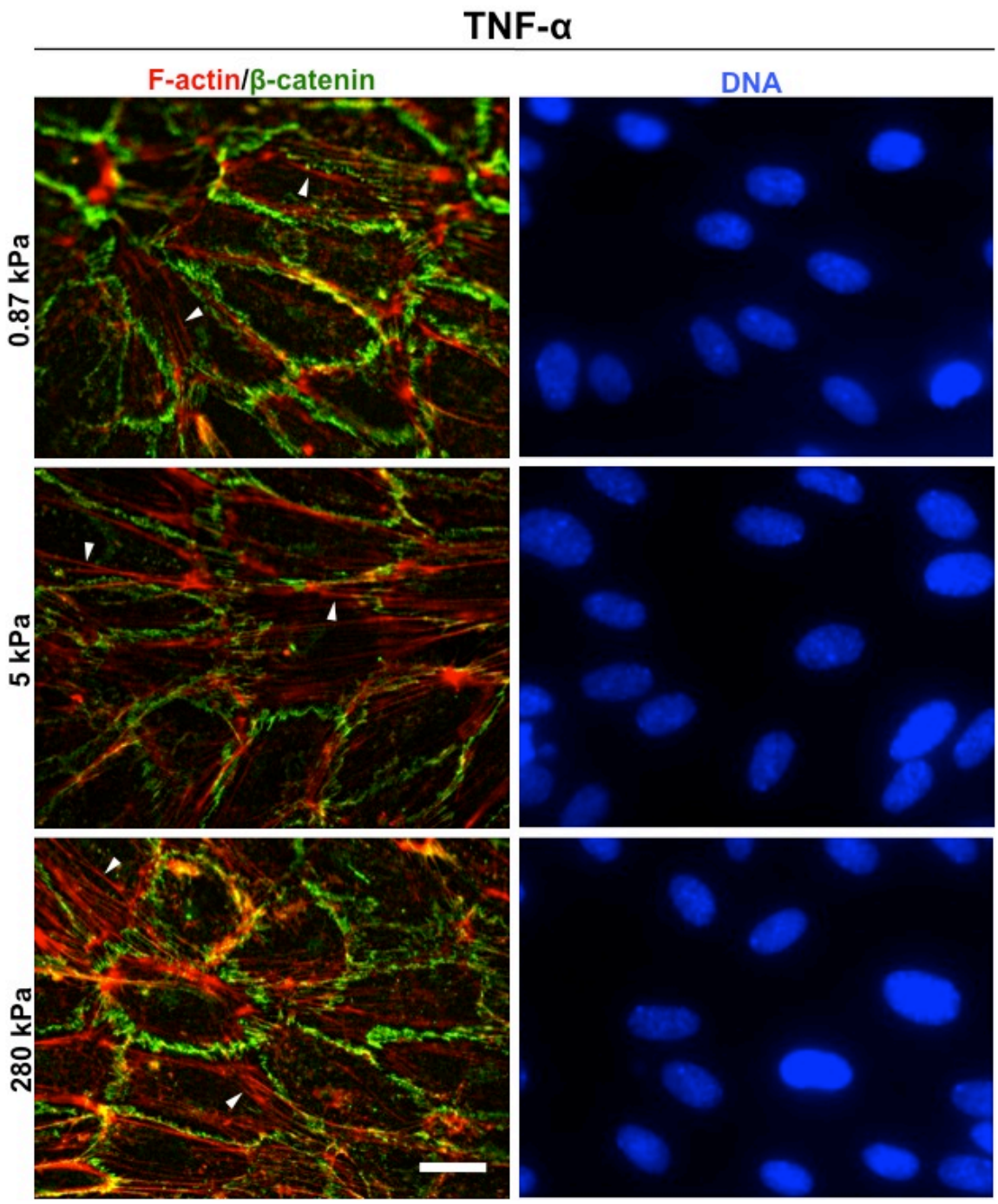

Figure 7.15. TNF-α-treated HUVECs in monolayer form mature F-actin stress fibers on all substrates. TNF-α-treated HUVECs were immunostained for β-catenin (green) and stained for F-actin (red) and DNA (blue), and fluorescence images were taken. Scale bar is 20 μm and applies to all images. DNA image corresponds to same group of cells as those shown for F-actin/β-catenin. White arrowheads point to examples of F-actin stress fibers.

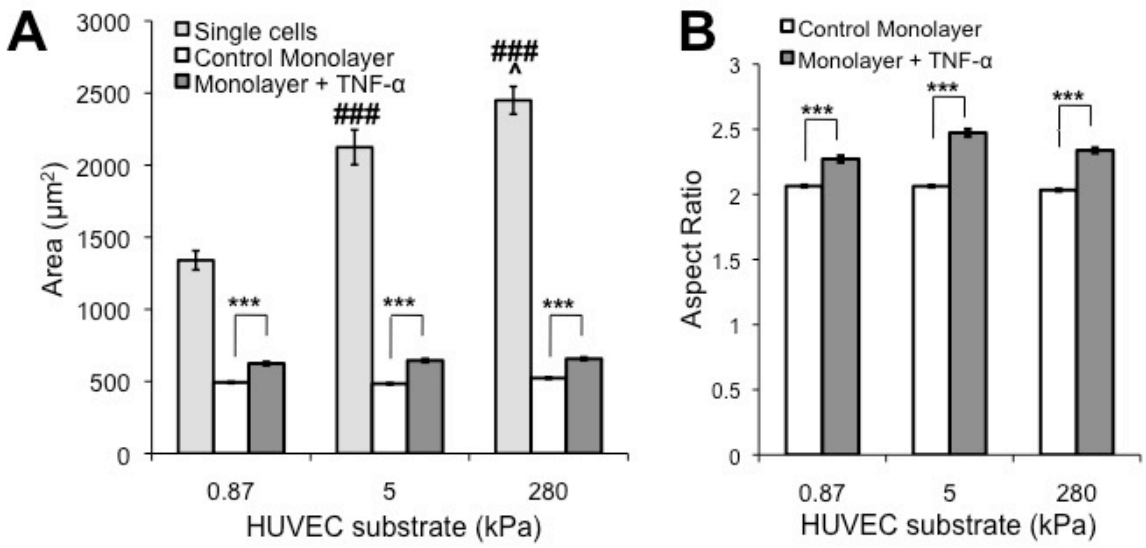

Figure 7.16. HUVEC morphology in a monolayer does not depend on substrate stiffness. **(A)** HUVEC area was quantified for single cells, control monolayers, and TNF-α-activated monolayers as a function of substrate stiffness. **(B)** HUVEC aspect ratio was quantified for control and TNF-α-activated monolayers. Aspect ratio is defined as length divided by width when cell shape is fit to an ellipse. Bars indicate average area of N cells from 2 independent experiments, while error bars indicate standard error. N=115, 142, 127 for single cells on 0.87 kPa, 5 kPa, and 280 kPa, respectively. N=8932, 8766, and 6890 for cells within control monolayers on 0.87 kPa, 5 kPa, and 280 kPa, respectively. N=1655, 1788, 2783 for cells within TNF-α-activated monolayers on 0.87 kPa, 5 kPa, and 280 kPa, respectively. ### indicates $P<0.001$ with single cells on 0.87 kPa substrate, while ^ indicates $P<0.05$ with single cells on 5 kPa substrate using ANOVA. *** indicates $P<0.001$ using Student's t-test.

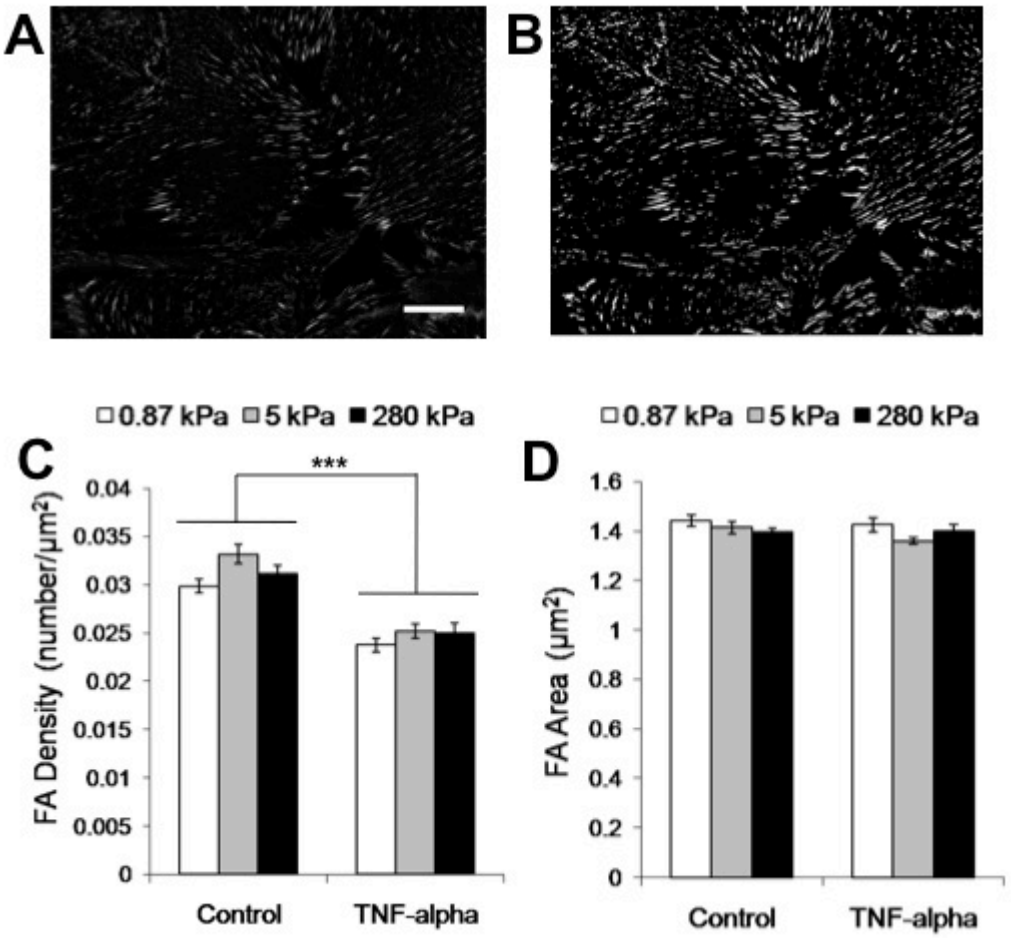

Figure 7.17. HUVEC monolayer focal adhesion (FA) size and density do not depend on substrate stiffness. **(A)** HUVEC monolayers were immunostained for vinculin in order to visualize FAs. Images were processed and made binary **(B)** in order to quantify FA density **(C)** and area **(D)** as a function of substrate stiffness and monolayer treatment (control and TNF-α). Bars indicate average density or area from at least 20 images from each of 3 independent experiments, while error bars indicate standard error. In panel C, $P>0.05$ between stiffnesses for both control and TNF-α, using ANOVA. $P<0.001$ between control and TNF-α for all stiffnesses using Student's t-test, indicated by ***. In panel D, $P>0.05$ between stiffnesses for both control and TNF-α, using ANOVA. $P>0.05$ between control and TNF-α for each stiffness using Student's t-test. Scale bar in A represents 20 μm and applies to panels A and B.

7.3.11 Neutrophil migration speed along the endothelium does not depend on subendothelial matrix stiffness

In addition to transmigration, we also wished to evaluate neutrophil migration along the endothelium. Figure 7.11A (primary vertical axis) shows that neutrophils did not all transmigrate at the same time after being added to the endothelium; they spent varying amounts of time migrating along the endothelium before transmigrating through it. On average, this time was around 5 minutes and was independent of subendothelial matrix stiffness ($P>0.05$) (Figure 7.18A). Meanwhile, the speed at which those cells migrated was also independent of subendothelial matrix stiffness ($P>0.05$) (Figure 7.18B) and was significantly faster than cells migrating on polyacrylamide gels alone (Figure 6.5).

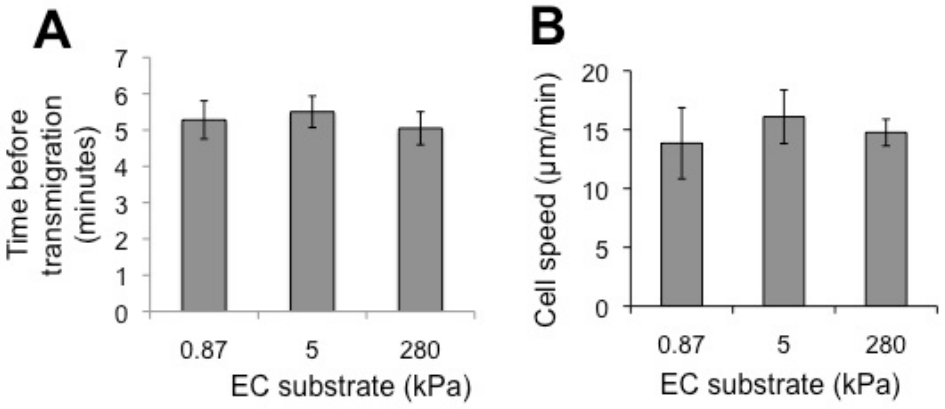

Figure 7.18. Neutrophil migration along the endothelium prior to transmigration does not depend on subendothelial matrix stiffness. Shown are **(A)** average time that neutrophils spent migrating before transmigrating, as well as **(B)** average neutrophil speed while migrating along the endothelium before transmigrating, both as a function of subendothelial matrix stiffness. Bars indicate average, while error bars indicate standard error. For panel A, N=136, 176, and 153 for 0.87 kPa, 5 kPa, and 280 kPa substrates, respectively. For panel B, N=60, 66, and 101 neutrophils for 0.87 kPa, 5 kPa, and 280 kPa substrates, respectively. $P>0.05$ among all substrates in panels A and B using ANOVA.

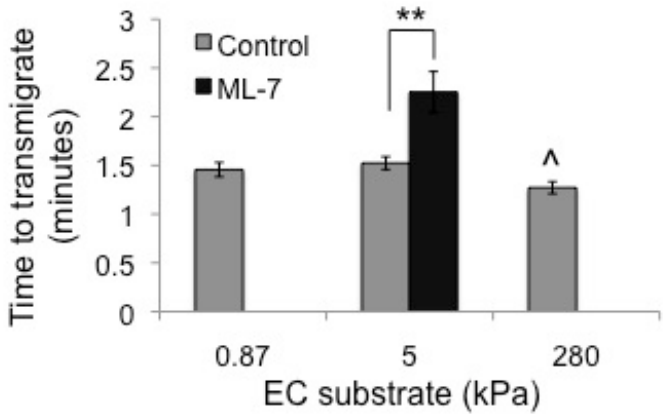

Figure 7.19. Time to transmigrate through the endothelium varies weakly with substrate stiffness, and ML-7 treated neutrophils take significantly longer to transmigrate. Bars indicate average, while error bars indicate standard error. For control neutrophils, N=136, 176, and 153 for 0.87 kPa, 5 kPa, and 280 kPa, respectively. N=65 for ML-7-treated neutrophils on 5 kPa. ** indicates $P<0.01$ using a Student's t-test. ^ indicates $P<0.05$ with 0.87 kPa and 5 kPa using ANOVA. Times were measured starting at the timepoint just before the first darkened piece of cell was observed in phase contrast microscopy (indicating that transmigration had initiated), and ending at the first timepoint when the entire cell was darkened (indicating that the cell had completely traversed the monolayer). No data is shown for ML-7-treated neutrophils on 0.87 kPa and 280 kPa.

7.4 Discussion

Neutrophil transmigration is an important physiological process in the normal immune response and occurs in blood vessels whose mechanical properties likely depend on location within the body, size, and health. In this chapter, we evaluated the effects of vessel stiffness on both the endothelium properties and neutrophil transmigration. In our *in vitro* model, we observed that the fraction of transmigrating neutrophils increased with increasing stiffness below the endothelium, in both large vessel endothelium (HUVECs) and also in microvasculature endothelium (HBMECs) (Figure 7.1B). Because substrate stiffness is known to control many biological and biomechanical properties of cells, we

evaluated an array of properties of the endothelium to explain this behavior, including EC monolayer ICAM-1 expression, stiffness, morphology, cell-substrate adhesion, cell-cell adhesion, and cell contraction. Our results provide strong evidence that substrate stiffness changes cell-cell adhesion through MLCK-dependent cell contraction.

Previous work regarding neutrophil transmigration has mostly utilized glass (stiffness ~50 GPa) or transwell filters as substrates. It is likely that blood vessel stiffness depends not only on the size and health of the vessel, but also on the location within the body, since tissues such as brain, muscle, and tumors vary in mechanical properties [64, 215]. Therefore, it is more physiologically relevant to perform *in vitro* transmigration experiments on softer substrates in the kilopascal range of stiffness. Here, we vary the substrate stiffness of the endothelium in a controlled way in order to evaluate its contribution to neutrophil transmigration.

Our results indicate that neutrophil transmigration involves an interplay between EC contraction, neutrophil contraction, and ICAM-1 signaling. It is known that neutrophil binding to ICAM-1 on the surface of the endothelium [208-210, 216] initiates MLCK-dependent EC contraction, which should depend on the stiffness below the endothelium, since cells are able to exert larger traction forces on stiffer substrates [61]. Here, inhibition of myosin-II dependent EC contraction by targeting myosin II or upstream MLCK in HUVECs not only reduced transmigration on intermediate (5 kPa) and stiff (280 kPa) substrates in comparison with the vehicle control, but reduced it nearly to the level of transmigration on soft substrates (Figure 7.12B). Meanwhile, transmigration on the soft (0.87 kPa) substrate was unaffected (Figure 7.12B), likely because contraction was already suppressed due to ECs' inability to exert large traction

forces on a soft substrate [61]. Stiff substrates likely promote contraction through mechanotransduction events in EC integrin to extracellular matrix adhesions, possibly through talin activation [199]. Consistent with these results, it has been shown that inhibition of contraction reduces cell stiffness [217].

Together, these results support the situation described by the schematic in Figure 7.20. Contractile forces (black arrows) due to actin-myosin activation are larger on stiff substrates and create intercellular gaps that are more permissible for neutrophil penetration; contraction is suppressed by soft substrates. When MLCK is inhibited, contractile forces on stiff substrates are reduced, leading to less transmigration, while inhibition of MLCK does not further reduce contractile forces on soft substrates, leading to no change in transmigration. The schematic in Figure 7.21 summarizes how our results fit into the known MLCK-mediated signaling pathway initiated by neutrophil adhesion to the endothelium. The fact that neutrophil transmigration occurs primarily via the paracellular route (Figure 7.5) corroborates the idea that substrate stiffness-dependent intercellular gap formation, mediated by MLCK activation, accounts for the transmigration behavior. Because transcellular transmigration does not depend on substrate stiffness (Figure 7.5), it seems likely that MLCK inhibition reduces paracellular transmigration without affecting transcellular transmigration; however, further experiments could address this hypothesis.

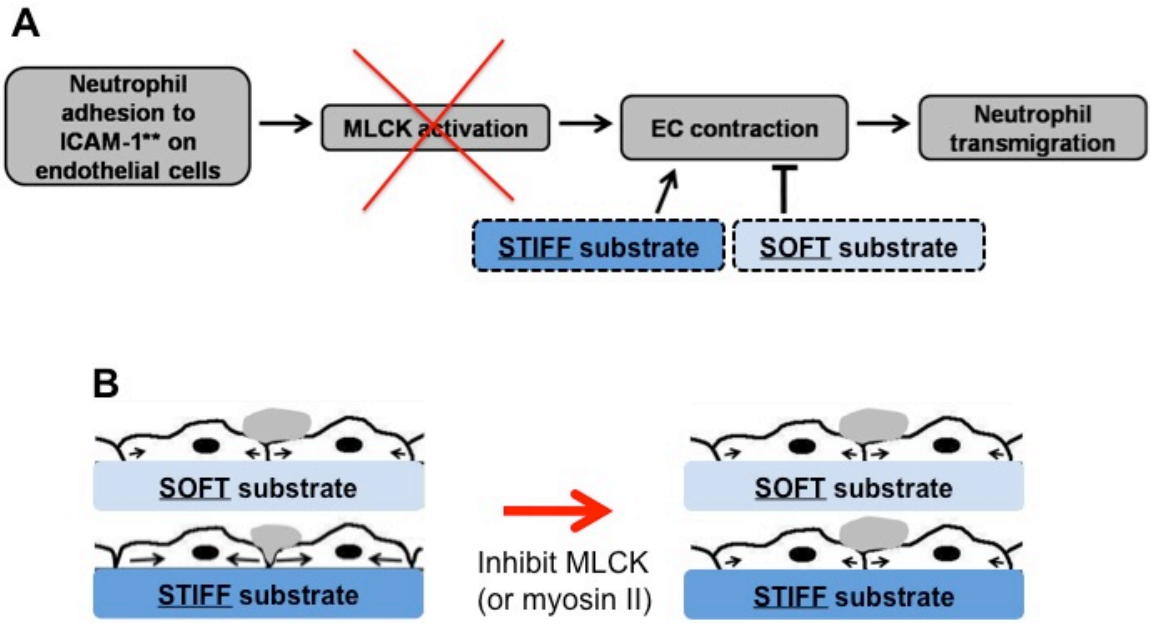

Figure 7.20. Schematic illustrating a possible mechanism for how pretreatment of HUVEC monolayers with ML-7 eliminates the effects of substrate stiffness in neutrophil transmigration. **(A)** Summary of the pathway initiated by neutrophil adhesion to the endothelium, and how our manipulation of substrate stiffness contributes to the pathway. **(B)** Prior to ML-7 treatment (left), neutrophil adherence to the endothelium induces a signaling cascade which activates MLCK and results in endothelial cell contraction (black arrows) and gap formation. Because the cells can exert more traction on a stiffer substrate, they are capable of creating larger gaps on the stiff substrate, ultimately allowing more neutrophils to transmigrate through. Treatment of the endothelium with ML-7 (effectively inhibiting MLCK; red X in panel A) causes inhibition of contraction on the stiff substrate. The soft substrate is unaffected, possibly because contraction was already suppressed to some degree, and ML-7 treatment did not produce further effects.

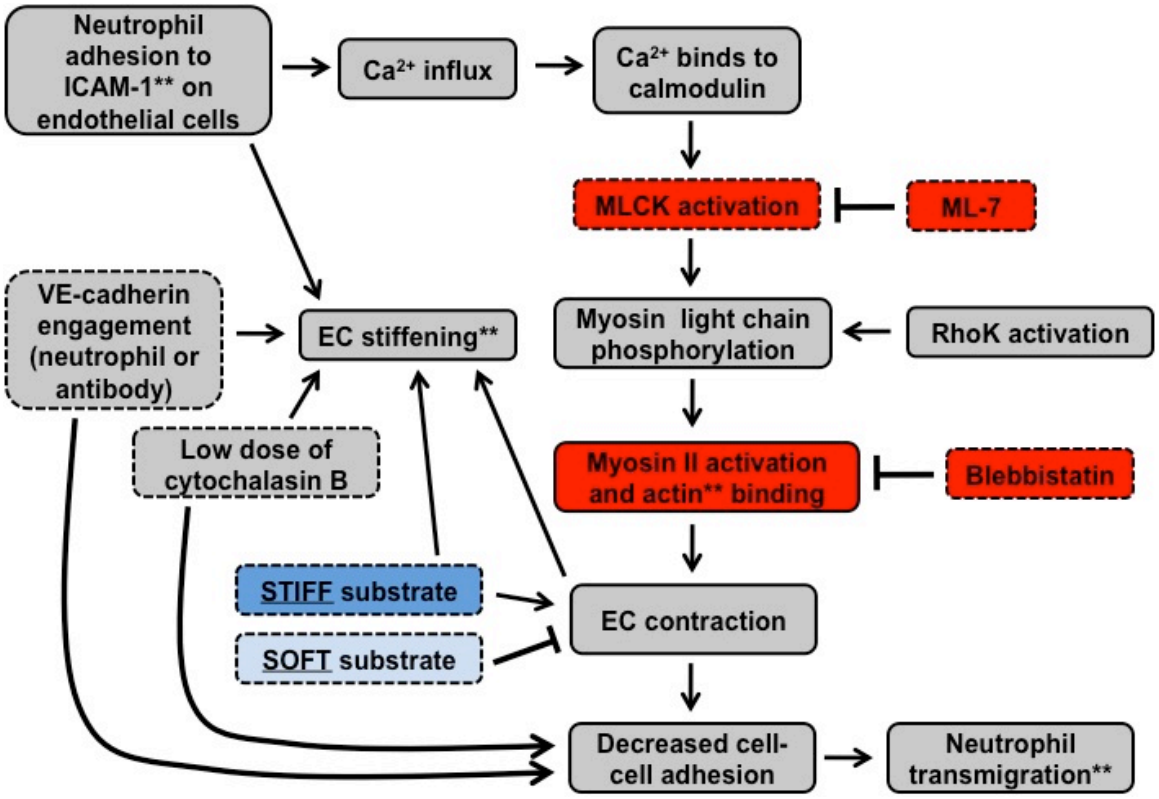

Figure 7.21. Signaling cascade initiated by neutrophil adhesion to ECs is affected by substrate mechanical properties. This flowchart indicates how our results fit into the signaling cascade initiated by neutrophil adhesion to ICAM-1 on the endothelium. Cellular components labeled by ** were measured here using various microscopic techniques, while those outlined with dotted lines were varied experimentally. Contractility-affecting drugs used in this work and affected molecules are indicated by red fill. Contribution of our manipulation of subendothelial matrix stiffness is indicated by blue fill.

TNF-α is known to increase EC permeability to macromolecules both *in vivo* and *in vitro* [185] through long-term reorganization of junctional proteins such as occludin, junctional adhesion molecule-A (JAM-A), and the membrane-associated protein ZO-1, and not via Rho-, ROCK- and MLCK-mediated EC contraction [187]. Specifically, inhibiting MLCK during TNF-α treatment does not interfere with the increase in EC

permeability over the 24 hour activation period [187]. Therefore, in our experiments, treatment of the HUVECs with ML-7 for one hour prior to transmigration assays did not reverse the effects of TNF-α-mediated permeability. Thus, the decrease in neutrophil transmigration that we observed through ML-7-treated endothelium on intermediate (5 kPa) and stiff (280 kPa) substrates (Figure 7.12B) reflects changes in EC contraction due to substrate stiffness (Figures 7.20 and 7.21) and not due to a reversal of TNF-α-mediated permeability.

In explaining the result that stiff substrates promote neutrophil transmigration, we must also rule out possible effects of substrate stiffness on other properties of the endothelium. We have previously demonstrated that neutrophils are sensitive both to the stiffness of their substrate and also to the concentration of adhesion protein on the surface of their substrate (Chapter 6). In our *in vitro* model, prior to transmigration, the endothelium is the neutrophil "substrate." Therefore, it makes sense that neutrophils would be sensitive to changes in either the amount of adhesion protein on the apical surface of the HUVECs, or to the actual stiffness of the monolayer. However, because ICAM-1 immunostaining indicated no change in the amount of ICAM-1 with substrate stiffness (Figure 7.7), it is unlikely that differences in this adhesion protein can explain the differences in transmigration behavior. Further, treatment with TNF-α to induce inflammatory conditions softened the monolayers on stiff substrates (Figure 7.8B), which is in agreement with previous studies on glass [37]. After this treatment, the average stiffness of the endothelium varied only 50-300 Pa between substrates (Figure 7.8B), depending on location. While the monolayer is fairly heterogeneous (Figures 4.3E, 4.3F, and 4.3G) it is unlikely that neutrophil mechanosensing of endothelium stiffness caused

an increase in transmigration from 51% to 91% from 0.42 kPa to 280 kPa, as mechanosensing typically occurs with changes in stiffness in the kilopascal range, not hundreds of pascals (Chapter 6). However, it is still possible that the small but significant increase in EC stiffness is a reflection of increased contractility on stiffer substrates.

In addition to ICAM-1 expression and cell stiffness, we also investigated whether HUVEC F-actin organization, morphology (area and aspect ratio), or FAs (number per area or size) could explain the increased transmigration on stiffer substrates; however, none of these properties could account for the behavior (Figures 7.14, 7.15, 7.16, and 7.17; further discussion starts in the following paragraph). Finally, neutrophils adhered to and migrated with similar speeds on all endothelium regardless of substrate stiffness, indicating that their ability to move to a suitable location for transmigration was not hindered on soft substrates (Figure 7.18).

As neutrophils transmigrate through ECs, they depolymerize and rearrange the EC actin cytoskeleton locally [112]. Substrate stiffness has been shown to regulate F-actin architecture in single cells; specifically, single ECs on stiffer substrates develop more organized, well-developed stress fibers [73]. Here, we showed that F-actin arrangement in the control (no TNF-α) endothelium also depended on substrate stiffness in a way similar to single cells (Figure 7.10). It could potentially be more difficult for a neutrophil to traverse a more actin-dense monolayer, such as the control monolayers on stiff substrates (Figure 7.14). While neutrophils are capable of transmigrating through both the transcellular and paracellular pathways (Figures 7.2, 7.3, and 7.4), they prefer the paracellular (between cell-cell junctions) route (Figure 7.5, see also ref. [84]), where, in the control monolayers, the actin appeared most dense (Figure 7.14). However, TNF-α

abrogated the effects of substrate stiffness on actin cytoskeleton, as stress fibers on all substrates were well-developed, aligned, and oriented throughout the entire cell, not just at the cell periphery (Figure 7.15). In this case, neutrophils encountered an equally-dense actin cytoskeleton on all substrate stiffnesses, indicating that differences in HUVEC F-actin arrangement cannot account for the transmigration behavior.

Because neutrophils preferentially use the paracellular route for transmigration (Figure 7.5, see also ref. [84]), it is possible that the morphology of individual HUVECs within the monolayer directs the frequency of transmigration. For example, HUVEC area or aspect ratio could influence the probability of a neutrophil being at the HUVEC cell borders versus middle at any given time, thus directing its ability to transmigrate, assuming the paracellular route is preferential. However, we did not observe differences in area (Figure 7.16A) or aspect ratio (Figure 7.16B) of individual HUVECs within control or TNF-α-activated monolayers, indicating that differences in EC morphology within the monolayer do not contribute to substrate stiffness-dependent neutrophil transmigration.

It is clear that activation of the inflammatory response by TNF-α induces many morphological changes in the endothelium, including F-actin rearrangement (Figure 7.15), local cell alignment (Figure 7.15), enlargement (Figure 7.16A), and elongation (Figure 7.16B) of HUVECs within the monolayer. These TNF-α-mediated changes in cell morphology are Rho/ROCK dependent, as they are prevented by ROCK inhibition [187]. TNF-α also induces phosphorylation of focal adhesion kinase and paxillin [218], and causes cytoskeletal rearrangement (Figure 7.15), possibly by activation of the small guanosine-trisphosphate (GTP)-binding proteins Rho, Rac, and Cdc42 [52]. Thus, in

addition to ICAM-1 upregulation and junctional protein reorganization, TNF-α also induces many cellular morphological changes, though those changes do not depend on substrate stiffness (Figures 7.14, 7.15 and 7.16).

The large holes in the endothelium that we observed as a result of neutrophil transmigration on stiff substrates (Figures 7.9B, 7.9C, and 7.9D) suggest three possibilities: (1) there was less EC-substrate adhesion on stiff substrates, (2) there was less endothelial cell-cell adhesion on stiff substrates, or (3) increased transmigration resulted in elevated neutrophil protease activity, causing cleavage of cell-substrate and cell-cell adhesions on stiff substrates. Because initial FA patterns were the same with substrate stiffness, as measured by vinculin punctate staining (Figure 7.17), we ruled out the first explanation. However, it could still be possible that neutrophil adhesion and subsequent transmigration caused rearrangement of the endothelium FA structure as a function of substrate stiffness. Evidence for this arises from Figure 7.10, where a change in neutrophil morphology, transitioning from protrusive to round, likely disrupted EC-substrate adhesions. This would be an interesting avenue for future exploration. Secondly, a reduction in cell-cell adhesion on stiff substrates may partially explain hole formation. The result that neutrophil transmigration was increased on soft substrates, but not stiff substrates, by decreasing cell-cell adhesion with a VE-cadherin antibody (Figure 7.12A) suggests that cell-cell adhesion was compromised on stiff substrates to a greater degree than soft substrates following TNF-α treatment; this could promote hole formation as well as neutrophil transmigration.

A third explanation for the formation of holes in the monolayers could be due to protease release by the neutrophils as they migrated between the gels and the

endothelium. Neutrophil injury to the endothelium has previously been observed *in vitro* [219, 220], and can be inhibited by tryptic, elastase, and serine protease inhibitors [220]. In this case, hole formation on the stiff substrates could be due to the fact that nearly twice as many neutrophils transmigrated in comparison with soft substrates (Figure 7.1B), resulting in more proteases. To address this, we simply halved the number of neutrophils added to the surface of the endothelium ($10x10^5$ to $5x10^5$) and observed transmigration (Figure 7.11A). Interestingly, holes still formed with $5x10^5$ neutrophils, and were similar in density and size to $10x10^5$ neutrophils (Figures 7.11B and 7.11C), indicating that it was not simply the number of transmigrated neutrophils which influenced hole formation on the stiff substrates. Thus, it seems plausible that increased contractile forces in ECs on stiff substrates promote retraction as neutrophil proteases act on the ECs. Further evidence for this hypothesis is our observation that ML-7 inhibits hole formation in ECs on stiff substrates.

Further reduction of the number of neutrophils plated ($2x10^5$) eliminated hole formation, signifying that neutrophils were responsible for hole formation, and that a threshold number were needed. Interestingly, the kinetics of hole formation aligned with neutrophil transmigration; that is, hole formation began around 25 minutes after plating neutrophils, about the same time when a maximum fraction of neutrophils had transmigrated (Figure 7.11A). Thus, it is likely that protease release by neutrophils, in combination with increased contractile forces to promote retraction in ECs on stiffer substrates, led to significant EC injury. The following experiment was used to further test this hypothesis.

First, neutrophils were plated onto EC monolayers on soft (0.87 kPa) and stiff (280 kPa) substrates and given 40 minutes to interact with the endothelium. During this time, neutrophils were presumably releasing proteases. After 40 minutes, the solution from each of the dishes was collected from the dish and centrifuged, and the (cell-free) supernatant, which should have contained any proteases released into the media during the 40 minute interaction period, was isolated. Then, this conditioned media from the 0.87 kPa substrate was added to a fresh monolayer on a 280 kPa substrate (without neutrophils), while the conditioned media from the 280 kPa substrate was added to a fresh monolayer on a 0.87 kPa substrate (also without neutrophils). Thus, this experiment allowed us to test whether the difference in hole production with substrate stiffness could have been a result of differential protease production. Interestingly, no holes formed on either substrate, indicating that the physical interaction of neutrophils with the endothelium was necessary for holes to form. Thus, we propose the holes formed due to a combination of (a) protease release by neutrophils, (b) the physical interaction of neutrophils with the endothelium, and (c) the increased contractility of ECs on stiffer substrates.

So far in this discussion we have focused on the physical state of the endothelium and showed that it plays a significant role in neutrophil transmigration. However, the biophysical properties of neutrophils are also important contributors to this complex process. For example, in Figure 7.12, we displayed that MLCK-mediated contraction in *neutrophils* also contributes to the ability of neutrophils to transmigrate. However, interestingly, neutrophil transmigration is not completely blocked upon inhibition of MLCK (Figure 7.12B). While we cannot rule out the possibility that MLCK may not

have completely been inhibited, we hypothesize that neutrophil actin polymerization still allows the neutrophils to complete transmigration; if this is true, then we expect that the timescale for transmigration is different. Indeed, on 5 kPa gels, the time for neutrophils to traverse the monolayer was significantly longer for ML-7-treated neutrophils than untreated neutrophils (Figure 7.19), suggesting a different or modified mechanism for transmigration. Also in support of this hypothesis is the fact that treatment of neutrophils with latrunculin, an acting-disrupting drug, completely abolished neutrophil transmigration.

Interestingly, the average time for untreated neutrophils to complete transmigration varied only slightly with subendothelial matrix stiffness, though it was statistically shorter for neutrophils transmigrating through ECs on 280 kPa, in comparison with 0.87 kPa and 5 kPa (Figure 7.19). This suggests that as long as they have the mechanical machinery intact (i.e. mechanisms for contraction and actin polymerization), and once they find a suitable place on the endothelium for transmigration, they complete the process within a similar amount of time, regardless of the substrate.

In addition, the result that transmigration of ML-7-treated neutrophils was not completely blocked on soft substrates suggests that ICAM-1 levels (and likely other signaling molecules such as platelet EC adhesion molecule-1, PECAM-1) were high enough to support transmigration, even though neutrophil contraction was inhibited by drug treatment and EC contraction was reduced by substrate stiffness. Indeed, ICAM-1 is an important player and is necessary for transmigration, as the fraction of transmigrated neutrophils was directly related to the amount of ICAM-1 on the surface of the

endothelium, even on stiff substrates where contraction was higher (Figure 7.6). Specifically, when the ECs were not treated with TNF-α (low ICAM-1), we observed only ~1% transmigration on all substrates (Figure 7.6). These results provide evidence that even though EC contraction promotes transmigration, it alone is not sufficient to support transmigration – signaling by adhesion molecules such as ICAM-1 is also necessary.

A technical issue that we must address is the possibility that ML-7 leached out from the ECs after treatment and affected the neutrophils. Indeed, treatment of neutrophils (without treating the ECs) with ML-7 reduces transmigration on all substrates (Figure 7.12B). These results indicate that if leaching did occur after EC treatment with ML-7, we would see a reduction in transmigration on all substrates, not just the stiff ones. However, we only observed a decrease in transmigration on stiff substrates, while transmigration on soft substrates was unaffected, signifying that leaching of ML-7 from the ECs did not occur.

7.5 Conclusions

In summary, we have developed an *in vitro* model of the vascular endothelium using polyacrylamide gels of varying stiffness to investigate the effects of vasculature stiffness, both on the endothelium and on neutrophil transmigration. Interestingly, we observed a linear increase in transmigration from very soft (0.42-0.87 kPa) to the "healthy" range of subendothelial layer stiffness (3-5 kPa), reaching a threshold value in the "disease" stiffness range, from 13 or 280 kPa (Figures 7.1B and 7.1C).

Our results provide strong evidence that neutrophil transmigration is regulated by MLCK-mediated generation of intercellular gaps through EC contraction, and that substrate stiffness mediates this response. Neutrophil transmigration also promotes EC retraction and large hole formation in endothelium on stiff substrates, an event which is further indicative of increased contractility. Myosin light chains may also be phosphorylated by Rho kinase during neutrophil transmigration [221] (Figure 7.21), and therefore further experiments could test whether Rho kinase-dependent cell contraction also plays a role in how the endothelium substrate stiffness affects neutrophil transmigration.

Our results suggest that neutrophil transmigration may vary with blood vessel mechanical properties, depending on location within the body and size. Further, these results may be associated with cardiovascular disease biology, where increased vascular stiffness is coupled with increased leukocyte transmigration. In addition, this work may be relevant to cancer cell metastasis or stem cell homing, both of which involve cell transmigration across the endothelium. While this chapter focused on transmigration through TNF-α-activated endothelium, in the next chapter (Chapter 8), we quantify the effects of subendothelial matrix stiffness on neutrophil transmigration through an endothelium that has been treated with oxLDL, another important physiological factor relevant to cardiovascular disease.

8 OxLDL and subendothelial matrix stiffness promote neutrophil transmigration through enhanced endothelial cell ICAM-1 and contractility †

8.1 Introduction

Oxidation of low-density lipoproteins (LDLs) in the body has been correlated with various pathological conditions, including atherosclerosis, diabetes mellitus, and autoimmune diseases (for review, see [222]). Elevated oxidized low density lipoproteins (oxLDL) levels in the bloodstream have been identified as a risk factor for development of coronary artery disease and plaque formation [223-227]. Exposure of the vascular endothelium to oxLDL leads to endothelial cell (EC) damage and dysfunction, including disruption of cell-cell adhesion [228, 229], as well as impairment of nitric oxide release [230]. Interestingly, *in vivo* studies have demonstrated that oxLDL affects both large vessels and microvasculature and promotes leukocyte adhesion and transmigration in microvasculature [229, 231, 232]. In addition, EC exposure to oxLDL enhances monocyte invasion through the endothelium *in vitro* [110]. These changes in EC-leukocyte interactions are likely partially due to upregulation of adhesion molecules necessary for leukocyte adherence and transmigration, including intercellular cell adhesion molecule-1 (ICAM-1), vascular cell adhesion molecule-1 (VCAM-1), and platelet endothelial cell adhesion molecule-1 (PECAM-1) [110, 233, 234].

In addition to increased adhesion molecule expression, EC exposure to oxLDL also leads to reorganization of lipid rafts, as indicated by loss of the lipid raft marker

---

† This chapter has been submitted for publication as Stroka, K.M., I. Levitan, and H. Aranda-Espinoza, OxLDL and substrate stiffness promote neutrophil transmigration through enhanced endothelial cell ICAM-1 and contractility, *Journal of Biomechanics* (under review).

GM_1 [32], and to changes in lipid order, as observed by Laurdan two-photon imaging [235]. Concurrently, the cells also undergo changes in biomechanical properties, including increased contractility [32], stiffness [32, 33], and ability to realign with flow [236]. It has been proposed that oxLDL acts as a cholesterol acceptor, removing cholesterol from the plasma membrane [32, 236]. Indeed, increases in cell stiffness [31, 32] and traction forces [154] have also been measured in cholesterol-depleted cells, though actin-disrupting drugs abrogate this cell stiffening [31]; these results support the idea that oxLDL exposure or direct cholesterol removal triggers biomechanical changes through modification of the plasma membrane-cytoskeleton complex [31].

While the above-mentioned work demonstrates that oxLDL affects the biomechanical properties of the endothelium, there is also evidence that the subendothelial layers of blood vessels stiffen in cardiovascular disease. Clinically, pulse wave velocity measurements have demonstrated increased vasculature stiffness in patients with atherosclerosis or hypertension [115, 116], and because these waves also reflect deep into microvasculature, it is believed that there is also a change in microvasculature stiffness. However, these measurements are unable to specify which parts of the blood vessel change biomechanically. Several *in vitro* studies have recently addressed this issue by scraping away the endothelium, or by cross-sectioning the artery to measure the media layer. Using these methods, the reported stiffness of healthy subendothelial matrices has ranged from 2.5 kPa to 8 kPa [43, 119, 120], while arteries in ApoE-null mice, a model for atherosclerosis, are much stiffer, around 28 kPa [119]. These experiments indicate that the mechanical properties of the subendothelial matrix in vasculature vary significantly in cardiovascular disease. In addition, it is possible, though

not yet proven, that the stiffness of microvasculature in a particular tissue varies with the stiffness of that tissue; for example, brain is very soft (300-500 Pa), while collagenous bone is much stiffer (~100 kPa) [64, 122].

Using an *in vitro* model of the vascular endothelium, we have previously shown in Chapter 7 that stiffer EC substrates promote neutrophil transmigration through tumor necrosis factor-α (TNF-α)-activated endothelium (Figure 7.1). This substrate stiffness-dependent transmigration is due to biophysical changes that occur in the endothelium; stiffer substrates support larger myosin light chain kinase (MLCK)-mediated contractile forces upon neutrophil adherence to the endothelium. Presumably, larger contractile forces lead to formation of intercellular gaps that promote transmigration. Also in Chapter 7, we showed that the fraction of transmigrated cells depends on the amount of ICAM-1 available for binding on the surface of the ECs, independent of substrate stiffness (Figure 7.6). Because oxLDL exposure also leads to upregulation of ICAM-1 and increased contractility in ECs, we hypothesized that treatment of the endothelium with oxLDL also affects transmigration in a substrate stiffness-dependent way. In particular, we wanted to explore transmigration of neutrophils, which primarily transmigrate in microvasculature, where oxLDL exposure has been shown to affect leukocyte-EC interactions, and where vessel stiffening is relevant in cardiovascular disease.

In this work we used the *in vitro* model of the vascular endothelium (see Chapters 3 and 7) to explore the interplay between oxLDL and substrate stiffness in neutrophil transmigration. We prepared fibronectin-coated polyacrylamide gels of varying physiological stiffness (0.87 kPa, 5 kPa, and 280 kPa). Human umbilical vein endothelial

cells (HUVECs) formed confluent monolayers on these substrates, and we subsequently treated the HUVECs with 25 μg/mL oxLDL, which is within the physiological range for patients with coronary artery disease (4). After 24 hours, oxLDL treatment increased ICAM-1 expression on all substrates, though the final amount of ICAM-1 was independent of substrate stiffness. We plated human neutrophils onto the surface of the endothelium and found that oxLDL treatment of the endothelium promoted transmigration on all substrates, and stiff substrates further promoted transmigration. Inhibition of MLCK-dependent contractile forces reduced transmigration on all substrates and eliminated the dependence of substrate stiffness on transmigration. These results provide further evidence that efficient transmigration requires both ICAM-1 expression and EC contractile forces, and that exposure of the vascular endothelium to oxLDL in cardiovascular disease has significant implications for the immune response in stiffening blood vessels.

8.2 Materials and methods

8.2.1 Preparation of substrates

Thin (~80 μm) polyacrylamide gel substrates were prepared on activated coverslips as first described by Wang and Pelham [198] and as used previously in our work (Sections 6.2.1 and 7.2.1; see also ref. [122]). Concentrations in this work included 15% acrylamide + 1.2% bis (280 kPa), 8% acrylamide + 0.07% bis (5 kPa), and 3% acrylamide + 0.1% bis (0.87 kPa). After sulfo-SANPAH treatment and UV activation, gels were coated with 0.1 mg/mL fibronectin, also as previously described in our work (Sections 6.2.1 and 7.2.1; see also ref. [122]). Dynamic mechanical analysis and atomic

force microscopy were used to measure the mechanical properties of the gels, while immunofluorescence staining was used to characterize the surface-bound fibronectin in order to ensure equal protein amounts with varied gel stiffness (Section 6.2.3; see also ref. [122]).

8.2.2 Cell culture and treatments

HUVECs were purchased from Lifeline Cell Technology (Walkersville, MD) and cultured as previously described (Section 4.2.1). Cells (passages 2-5, $4x10^5$ total) were plated onto fibronectin-coated polyacrylamide gels and formed monolayers within 2 days, as previously described in Section 7.2.2. After 2 days, cells were treated with 25 μg/mL oxLDL for the final 24 hours prior to transmigration experiments. In some assays, cells were treated with oxLDL for only the final hour prior to experiments. To inhibit MLCK, HUVECs were pre-treated with 10 μM ML-7 (Sigma, St. Louis, MO) for 8 minutes prior to transmigration assays. For removal of cholesterol, HUVECs were pre-treated with 5 mM methyl-β-cyclodextrin (MβCD; Fisher Scientific) for one hour prior to transmigration assays. To block ICAM-1, cells were pre-treated with 10 μg/mL monoclonal anti-human ICAM-1 (R&D Systems BBA3, Minneapolis, MN) for one hour prior to transmigration assays.

8.2.3 Cholesterol reagents

Normal human plasma, prepared in acid citrate dextrose, was purchased from a blood bank (Life Source, Chicago). LDL was isolated by sequential centrifugation in KBr between the density ranges 1.019 to 1.063g ml^{-1}. The preparation was dialyzed against

three changes of 10mM Tris/HCl buffer, pH 7.4, containing 0.15 M NaCl and 1 mM EDTA at 4°C to remove KBr. To proceed to the copper oxidation, the further dialysis against PBS (pH 7.4) was performed to reduce the EDTA presence. Copper sulfate was then added to LDL with a final concentration of 25 μM. The oxidation was set in 37°C for 16 hours and stopped by adding 1 mM EDTA. Oxidation level of oxLDL was assayed by measuring the content of thiobarbituric acid-reactive substances (TBARS) in LDL and oxLDL by using TBARS Assay Kit (ZeptoMetrix, Buffalo, NY). The average TBARS value was 21.8±5.1 nanomoles per MDA per milligram of LDL protein for oxLDL.

8.2.4 Transmigration assays

Neutrophils were isolated from human blood as previously described in Section 6.2.4. Protocols were approved by the University of Maryland Institutional Review Board. Transmigration experiments were completed also as previously described in Section 7.2.3. Following oxLDL treatment, HUVECs were washed thoroughly with PBS, and fresh regular HUVEC media was added. Neutrophils (~$1x10^6$ total) were added to the HUVEC monolayer and allowed to gravitate to the EC apical surface for about 30-60 seconds. Phase contrast microscopy was used to capture timelapse images of the EC-neutrophil interactions for 30 minutes. Microscopy was completed at 37°C, 5% CO_2 and 55% humidity using an inverted microscope (Olympus IX71, Center Valley, PA). Images were captured with a QImaging Retiga-SRV charge-coupled device (CCD) digital camera (QImaging Corporation, Surrey, British Columbia, Canada) using IPLab software (Becton, Dickinson and Company, Franklin Lakes, NJ). Fraction of neutrophil transmigration was quantified, as previously described (Section 7.2.3), by dividing the

number of neutrophils which transmigrated any time during the 30 minute timelapse by the total number of neutrophils in the first frame of that sequence. Neutrophils which entered or exited the field of view after the first frame of the sequence were not counted. All experiments were repeated at least 3 times. Hole area and density were quantified as previously described (Section 7.2.3).

8.2.5 Cell staining

HUVECs were fixed, blocked for non-specific binding, and immunostained for ICAM-1 as previously described (Section 7.2.4). Alternatively, HUVECs were fixed, permeabilized, blocked for non-specific binding, and immunostained with antibodies to β-catenin to label cell borders, or stained with phalloidin-TRITC to label F-actin, both as previously described in Section 7.2.4. Fluorescence microscopy was completed at room temperature on immunostained HUVECs using an inverted microscope (Olympus IX81). Images were captured with a Hamamatsu ORCA-ER CCD digital camera (Leeds Precision Instruments, Minneapolis, MD) using Slidebook software (Intelligent Imaging Innovations, Inc., Denver, CO).

8.2.6 Statistical analysis

Student's t-tests were used to perform statistical analysis on pairs of data, while analysis of variance (ANOVA) was used among groups of data, where $P<0.05$ indicated statistical significance. Following ANOVA, Tukey's honestly significant difference criterion was used for multiple comparisons. All measurements reported in this article are in the format mean ± standard error.

8.3 Results

8.3.1 Stiff substrates promote neutrophil transmigration through oxLDL-treated HUVECs

Using our *in vitro* model of the vascular endothelium, we observed activation of neutrophils (Figure 8.1A; white arrowheads) and subsequent transmigration through oxLDL-treated HUVECs using phase contrast microscopy (Figure 8.1A, bottom). Meanwhile, few neutrophils on untreated HUVECs were activated (Figure 8.1A, top). Neutrophils on top of the endothelium appeared bright white, while transmigration events could be identified by the phase-darkened portions of the neutrophils between the endothelium and the gel (Figure 8.1A, bottom; white arrows). We found that 24-hour treatment of HUVECs with oxLDL promoted neutrophil transmigration on all substrates, in comparison with untreated HUVECs ($P<0.001$) (Figure 8.1B). In addition, transmigration increased with the stiffness of the substrate below the endothelium (Figure 8.1B), from 26% transmigration through ECs on 0.87 kPa, to 54% on 5 kPa ($P<0.01$). Transmigration on even stiffer substrates (280 kPa) was about 41% and was not different from 5 kPa ($P>0.05$). Meanwhile, 1-hour treatments of oxLDL or MβCD in the endothelium did not lead to neutrophil transmigration, similar to untreated ECs. Some neutrophils (~15%) were not activated after being plated onto an oxLDL-treated endothelium, but the fraction not activated was independent of substrate stiffness (Figure 8.1C).

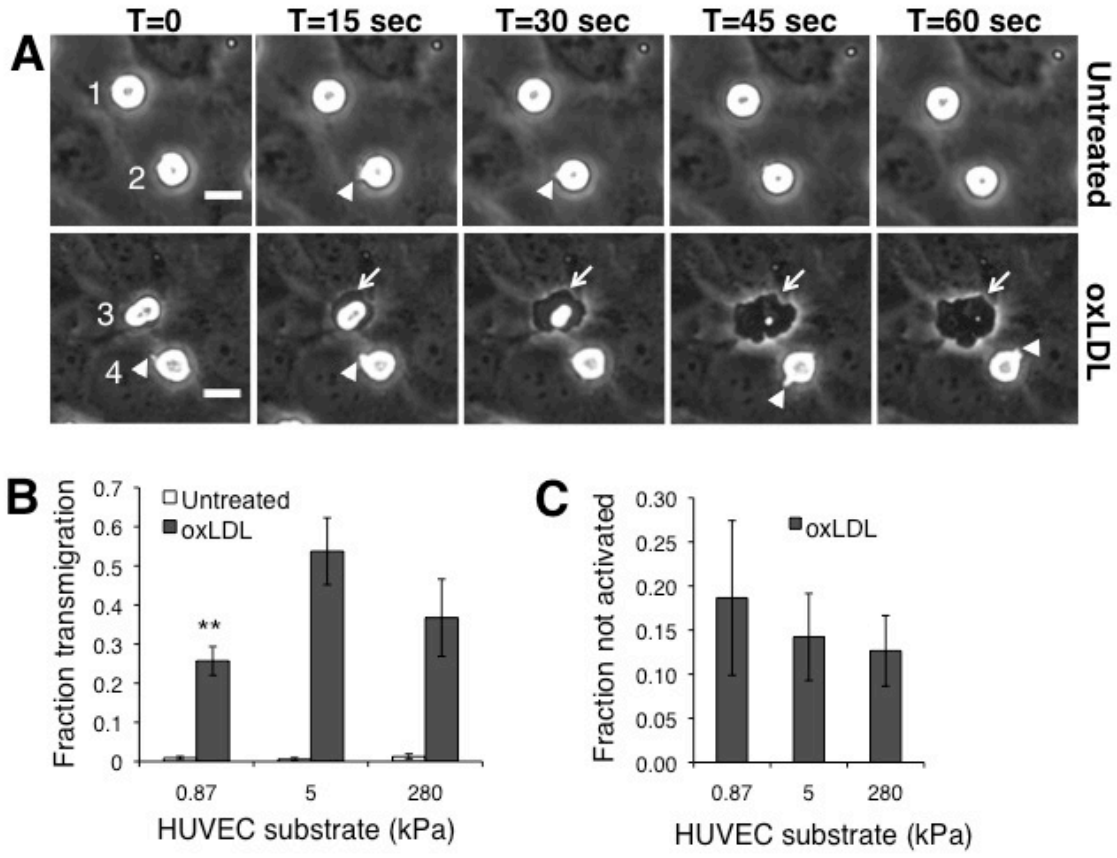

Figure 8.1. Stiffer substrates promote neutrophil transmigration through oxLDL-treated HUVECs. **(A, top)** Phase contrast time sequence of two neutrophils on untreated HUVECs. Cell labeled with "1" does not activate, while cell labeled with "2" does activate, as indicated by protrusive morphology (white arrowheads). **(A, bottom)** Also shown is a phase contrast time sequence of two neutrophils on 24-hour oxLDL-treated HUVECs. Cell labeled with "3" transmigrates through the endothelium (portion beneath the endothelium indicated by white arrow), while cells labeled with "4" is activated (white arrowheads) but does not transmigrate. Transmigration is indicated by a change in phase from bright white (on top of the endothelium) to darkened (between the endothelium and the gel; white arrows). T=0 corresponds to the time when transmigration begins in cell 1. Scale bar is 10 μm and applies to all images. Both untreated (top) and oxLDL-treated (bottom) are on 5 kPa substrate. **(B)** Fraction of transmigrated neutrophils through untreated or oxLDL-treated HUVECs, as a function of substrate stiffness. **, $P<0.01$, one-way ANOVA followed by Tukey's honestly significant difference criterion. Bars are averages of at least 8 experiments, while error bars indicate standard error. **(C)** Fraction of neutrophils not activated as a function of substrate stiffness. Bars are averages of 4 experiments, while error bars indicate standard error. $P>0.05$ by ANOVA.

8.3.2 ICAM-1 expression on oxLDL-treated HUVEC monolayer apical surface is independent of substrate stiffness

We have previously shown that neutrophil transmigration is proportional to the amount of ICAM-1 available for binding on the surface of TNF-α-activated endothelium (Figure 7.6). To evaluate the amount of ICAM-1 on the apical surface of the oxLDL-treated endothelium, we immunostained non-permeabilized HUVECs, captured fluorescence images, and quantified fluorescence intensity as a function of substrate stiffness (Figures 8.2A and 8.2B). For both untreated and 24-hour oxLDL-treated HUVECs, ICAM-1 intensity was independent of substrate stiffness ($P>0.05$), though on all substrates there was an increase in ICAM-1 expression after 24 hours of oxLDL treatment ($P<0.05$) (Figures 8.2A and 8.2B).

8.3.3 Blocking ICAM-1 eliminates oxLDL-induced transmigration on all substrates

To evaluate the role of oxLDL-induced ICAM-1 expression in neutrophil transmigration, ICAM-1 on the apical surface of the endothelium was blocked using an ICAM-1 antibody. In this blockade assay, neutrophil transmigration was significantly reduced to the level of the untreated controls (Figure 8.2C). Further, blocking ICAM-1 eliminated the effects of substrate stiffness on transmigration, as there was no difference in transmigration between the substrates.

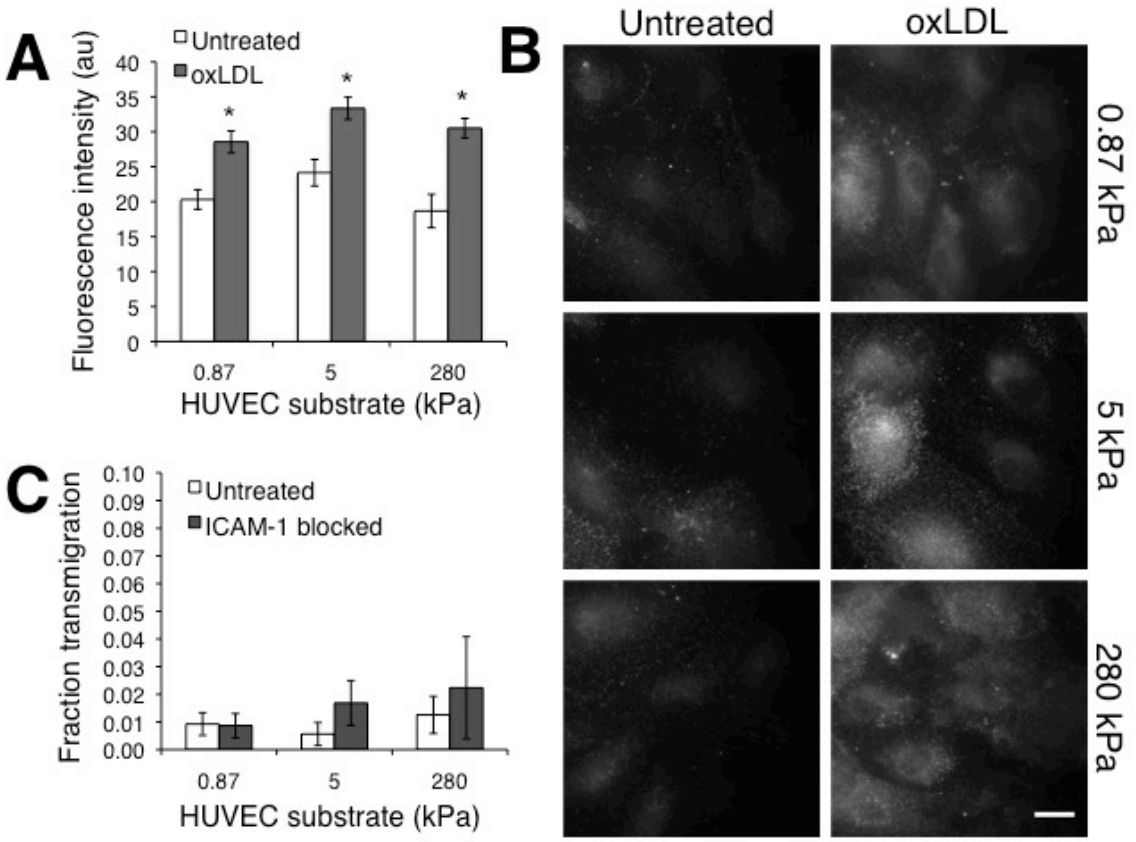

Figure 8.2. ICAM-1 expression is enhanced in oxLDL-treated HUVECs, and blocking ICAM-1 significantly reduces transmgiration on all substrates. **(A)** HUVECs were immunostained for ICAM-1 and fluorescence images were taken at many different locations across each of at least 3 different monolayers for each substrate. Bars indicate average, while error bars indicate standard error. $P>0.05$ by ANOVA across substrates for untreated and oxLDL-treated HUVECs. For each substrate, * indicates that $P<0.05$ between control and oxLDL using a t-test. **(B)** Representative fluorescence images of HUVEC monolayers immunostained for ICAM-1. Scale bar is 20 μm and applies to all images in panel B. **(C)** HUVECs were treated with an ICAM-1 antibody and neutrophil transmigration was quantified as a function of substrate stiffness. Bars indicate average, while error bars indicate standard error of at least 3 experiments. No statistical difference was found between the untreated and oxLDL-treated HUVECs, nor was there any dependence on substrate stiffness for either case ($P>0.05$).

8.3.4 Neutrophil transmigration injures the oxLDL-treated endothelium on stiff substrates

OxLDL is known to cause EC dysfunction, and here we investigated how subsequent leukocyte transmigration through the endothelium might further damage the ECs. In untreated or 1 hour oxLDL-treated ECs (the cases where there was <1% transmigration), we observed intact monolayers up to 2 hours after addition of neutrophils. Remarkably, we observed formation of large holes, on the order of thousands of square microns, after neutrophil transmigration through oxLDL-treated endothelium (Figure 8.3). Both the size of the holes ($P<0.001$) and number per area ($P<0.01$) increased with increasing EC substrate stiffness (Figures 8.3A and 8.3B). By 2 hours after plating neutrophils, holes did not reseal; in fact, holes on 280 kPa were significantly larger than at 1 hour ($P<0.001$; Figure 8.3B). Histograms of hole area at 1 hour and 2 hours (Figures 8.3C and 8.3D) indicate that at 2 hours, there were about half as many small holes (~1000 μm^2) in comparison with 1 hour; meanwhile, there was a greater amount of larger holes at 2 hours. Monolayers on soft substrates (0.87 kPa) were usually still intact 1 hour after plating neutrophils (Figure 8.3E), while monolayers on stiffer substrates (5 kPa and 280 kPa) were severely disrupted (Figure 8.3F).

8.3.5 OxLDL treatment induces EC stress fiber formation on all substrates

We observed oxLDL-treated HUVEC morphology and found no visible changes as a function of substrate stiffness (Figure 8.4A). We also labeled F-actin and observed mature stress fibers in oxLDL-treated HUVECs on all substrates (Figure 8.4B). These

results can be compared with untreated cells that developed less stress fibers on softer substrates (Figure 8.4B).

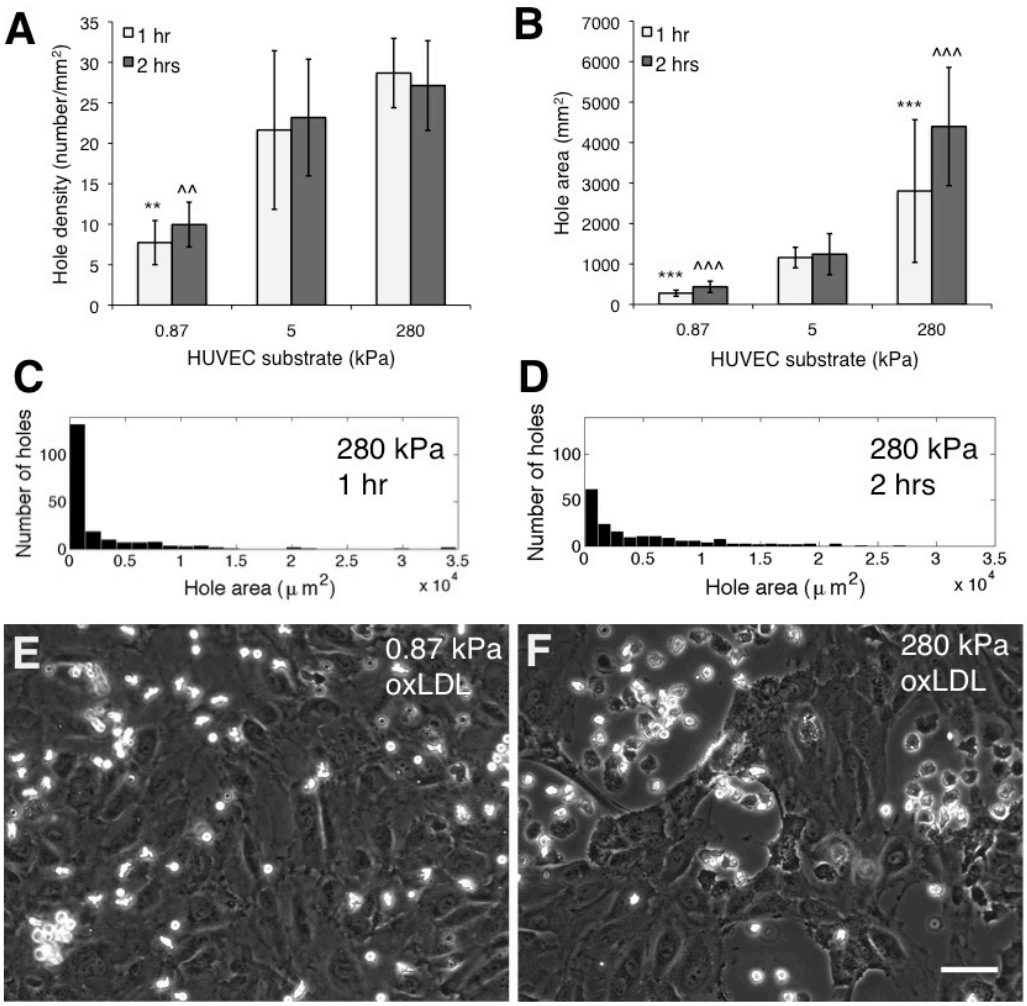

Figure 8.3. Stiff substrates promote hole formation in the oxLDL-treated endothelium following neutrophil transmigration. **(A)** Quantification of hole density as a function of subendothelial matrix stiffness at 1 hour and 2 hours after plating neutrophils. ** indicates P<0.01 by ANOVA followed by Tukey's honestly significant difference criterion. Bars are averages of 4 experiments, while error bars indicate standard error**. (B)** Quantification of hole area as a function of substrate stiffness at 1 hour and 2 hours after plating neutrophils. *** indicates P<0.001 with 5 kPa at 1 hour, while ^^^ indicates P<0.001 with 5 kPa at 2 hours. In addition, P<0.001 between hole areas at 1 hour and 2 hours for 280 kPa. **(C)** Histogram of hole areas for HUVECs on 280 kPa at 1 hour after plating neutrophils. **(D)** Histogram of hole areas for HUVECs on 280 kPa at 2 hours after plating neutrophils. **(E)** Phase contrast image of mostly intact HUVEC monolayer on a soft (0.87 kPa) substrate, 1 hour after plating neutrophils. **(F)** Phase contrast image of HUVEC monolayer on a stiff (280 kPa) substrate, 1 hour after plating neutrophils. Large holes have formed in the monolayer. Scale bar is 50 μm and also applies to panel E.

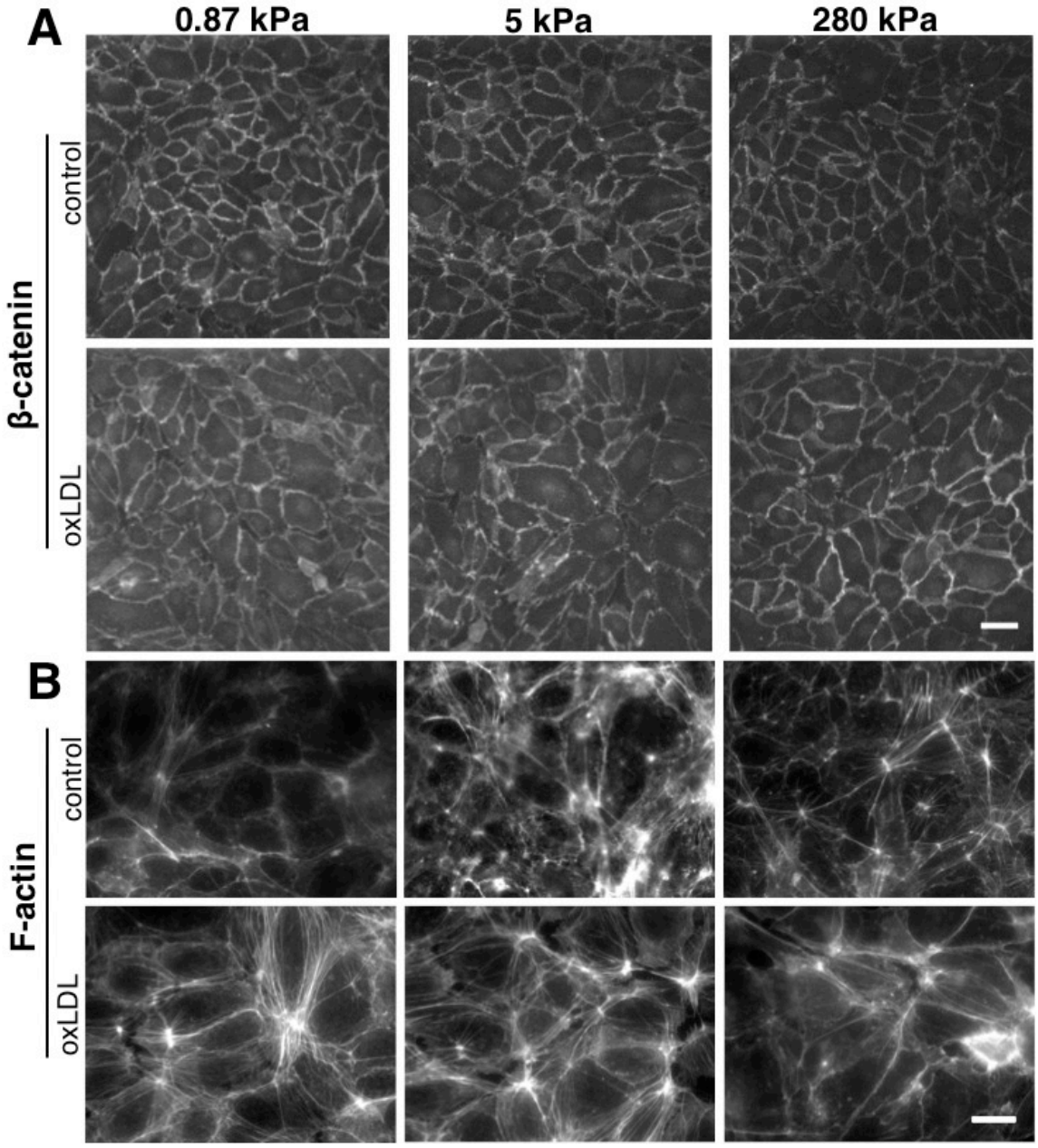

Figure 8.4. HUVEC morphology in the monolayer is independent of substrate stiffness. **(A)** OxLDL-treated HUVEC monolayers on all substrates were immunostained for β-catenin as a marker of cell borders. **(B)** Untreated and oxLDL-treated HUVEC monolayers were stained for F-actin. Scale bar for panel A, β-catenin images, is 50 μm, while scale bar for panel B, F-actin images, is 20 μm. Substrate stiffness is indicated at the top of each column.

8.3.6 Inhibition of MLCK-mediated EC contraction normalizes effects of substrate stiffness

Previously, we have shown that MLCK-mediated EC contraction promotes neutrophil transmigration through TNF-α-activated endothelium (Chapter 7). Here, we wished to evaluate the possible mechanism by which substrate stiffness promotes neutrophil transmigration through oxLDL-treated endothelium. We hypothesized that MLCK was also playing a role in this case, and therefore we suppressed contraction in the HUVECs by pretreating the monolayers with 10 μM ML-7 to inhibit MLCK. In these experiments, neutrophil transmigration was significantly reduced on all substrates, but there was no dependence of transmigration on substrate stiffness (Figure 8.5). Further, inhibition of MLCK prevented hole formation in the endothelium after neutrophil transmigration. Interestingly, a higher concentration of ML-7 (15 μM) completely disrupted the monolayer even before adding neutrophils, while a lower concentration (5 μM) had no effect on transmigration.

Figure 8.5. Inhibition of MLCK-mediated EC contraction reduces transmigration on all substrates and normalizes the effects of substrate stiffness. HUVECs were pretreated with ML-7 to inhibit MLCK and neutrophil transmigration was quantified for each substrate. Bars indicate average, while error bars indicate standard error of at least 3 experiments. Statistical significance between oxLDL-treated HUVECs and oxLDL+ML-7-treated HUVECs is indicated by * ($P<0.05$), ** ($P<0.01$), or *** ($P<0.001$).

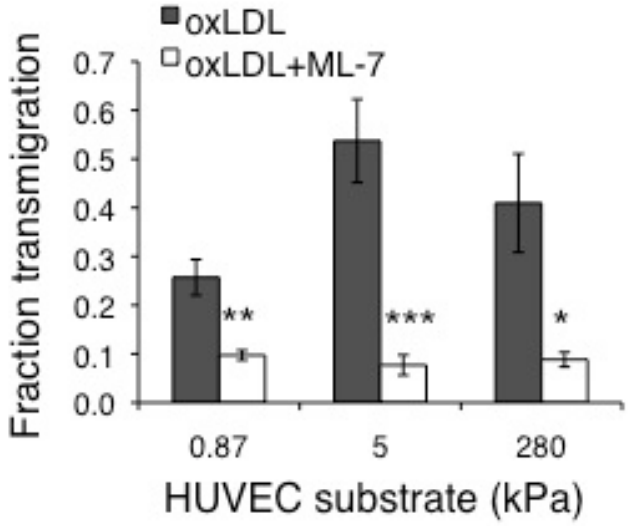

8.4 Discussion

Elevated levels of oxLDL in the bloodstream and increased vasculature stiffness are both associated with cardiovascular disease in patients. Here, we used an *in vitro* model of the vascular endothelium to explore the combined effects of oxLDL exposure and subendothelial matrix stiffening on neutrophil transmigration. Leukocyte transmigration is a complicated biophysical process and requires an interplay between signaling events and mechanical forces (Chapters 2 and 7) and thus we hypothesized that the immune response would depend on both EC oxLDL exposure and substrate stiffness. Indeed, we observed that oxLDL exposure of the endothelium promoted transmigration on all substrates, with stiff substrates further promoting transmigration (Figure 8.1B).

Though EC contractility is enhanced even after only 1-hour exposure to oxLDL [32], we observed few activated neutrophils and no transmigration after this treatment, indicating that contractility by itself does not promote transmigration. After 24 hours of

oxLDL treatment, ICAM-1 expression was enhanced on the apical surface of the endothelium on all substrates (Figures 8.2A and 8.2B), in agreement with previous reports [234]. Blocking ICAM-1 after oxLDL treatment reduced transmigration down to the amount through untreated endothelium (Figure 8.2C), indicating that enhanced ICAM-1 expression following oxLDL treatment accounted for the increase in neutrophil transmigration that we observed in comparison with untreated cells (Fig 8.1B). Further evidence of similarities of ICAM-1 expression with substrate stiffness comes from our result that the fraction of non-activated neutrophils did not depend on substrate stiffness (Figure 8.1C). OxLDL treatment of ECs has previously been shown to enhance monocyte transmigration by about 20% compared to controls in transwell assays [237]. Due to differences in experimental methods, it is difficult to compare this increase in transmigration with our results for neutrophil transmigration (Figure 8.1B); however, it is evident that the general trend is the same for neutrophils and monocytes.

Not only did 24-hour oxLDL treatment promote transmigration, but it did so in a substrate stiffness-dependent manner, with stiff substrates (5 kPa and 280 kPa) further promoting transmigration (Figure 8.1B). Recently, direct measurements of traction forces in islands of ~15 ECs demonstrated larger contractile forces in EC monolayers on stiffer substrates [238]. Thus, increased EC contraction on stiffer substrates leads to more transmigration (Figure 8.1B) in the presence of the same amount of ICAM-1 (Figures 8.2A and 8.2B). This is the same trend we found for transmigration through TNF-α-activated endothelium (Chapter 7) though the fractions of transmigration through oxLDL-treated ECs were reduced by about half in comparison with those for TNF-α-activated ECs for all substrates (Figures 8.1B and 7.1B). It is possible that the differences in

neutrophil transmigration between oxLDL treatment and TNF-α treatment are due to variance in ICAM-1 expression or cell contractility, or both, though further experiments would be necessary to corroborate that hypothesis. However, it is clear that both treatments point to an interplay between adhesion molecules such as ICAM-1 and contractility (substrate stiffness) to mediate transmigration.

F-actin staining revealed stress fiber formation in EC monolayers on all substrates, including 0.87 kPa (Figure 8.4). These results can be compared with F-actin organization in untreated HUVEC monolayers, where we observed more stress fibers on stiffer substrates (Figure 8.4B). Stress fibers are necessary for cell contraction, suggesting that oxLDL increased contraction on all substrates in comparison with untreated cells, before addition of neutrophils. However, F-actin organization by itself cannot be used as a measure of contractility. Here, increased transmigration (Figure 8.1B) and hole formation (Figure 8.3) on stiff substrates are both indicators of larger contractile forces in ECs on stiffer substrates. We have previously shown that neutrophil transmigration through TNF-α-activated endothelium is mediated by MLCK-dependent contractile forces in ECs (Chapter 7). Specifically, neutrophil adherence to the endothelium initiates a signaling cascade that activates MLCK, leading to EC contraction and possibly intercellular gap formation. Stiff substrates support these contractile forces, while soft substrates suppress them (Chapter 7). To determine whether MLCK-mediated EC contraction also plays a role in neutrophil transmigration through oxLDL-treated endothelium, we inhibited MLCK in ECs and observed transmigration and EC hole formation. Transmigration was reduced down to about 10% on all substrates, and the dependence on substrate stiffness was eliminated (Figure 8.5). Because transmigration

was higher on stiffer substrates (5 kPa and 280 kPa) with oxLDL treatment alone (Figure 8.1B), MLCK inhibition affected transmigration on stiff substrates to a higher degree than soft substrates (0.87 kPa). These results indicate higher contractility in HUVECs on stiff substrates after oxLDL treatment and possibly after neutrophil binding to ICAM-1, and this contractility promoted neutrophil transmigration. Meanwhile, MLCK inhibition also prevented hole formation on stiff substrates, signifying the importance of EC contractility in hole formation. Thus, we conclude that the substrate stiffness-dependent neutrophil transmigration and EC injury were due to MLCK-mediated contractile forces.

We have previously shown that neutrophil transmigration leads to formation of large holes (on the order of thousands of square microns) in TNF-α-activated endothelium on stiff substrates 5 kPa and above (Figure 7.9). Interestingly, transmigration of many different types of metastatic tumor cells also leads to hole formation in the endothelium [219]. Here, we observed similar injury after neutrophil transmigration through oxLDL-treated ECs, where hole size and density increased with increasing substrate stiffness (Figure 8.3). We have previously characterized the kinetics of hole formation in relation to neutrophil transmigration through TNF-α-activated ECs, showing that hole formation initiates a few minutes after a maximum fraction of neutrophils has transmigrated (Figure 7.11). However, for the case of TNF-α-treated ECs, the endothelium was mostly able to reseal the holes by 2 hours after plating neutrophils. Here, with oxLDL treatment, the injury was actually more severe, as the endothelium did not reseal the holes by 2 hours (Figures 8.3A and 8.3B), even though the fraction of neutrophil transmigration was significantly reduced in comparison with TNF-α. For example, on the 5 kPa substrate, 54% of neutrophils transmigrated through oxLDL-

treated HUVECs (Figure 8.1B) versus 94% through TNF-α-activated HUVECs (Figure 7.1B). The histograms of hole size in Figures 8.3C and 8.3D indicate one of two possibilities at 2 hours: either about half of the smaller holes actually became larger, or that the smaller holes healed, while more larger holes formed. For both oxLDL and TNF-α treatments, holes are likely due to proteases released by neutrophils either during transmigration or after transmigration, as they migrate between the endothelium and the gel. These proteases could cleave endothelial cell-cell and/or cell-substrate adhesions, and larger EC contractile forces on stiffer substrates could promote retraction as proteases act on them, leading to large holes. Also, neutrophil transmigration and subsequent migration beneath the monolayer could weaken endothelial cell-cell and/or cell-substrate adhesions. If this type of injury also occurs *in vivo* due to the presence of oxLDL, transmigration through the endothelium in stiffened vasculature could add another layer of complication to the molecular and cellular events in cardiovascular disease.

8.5 Conclusions

In summary, we showed that 24-hour oxLDL treatment of the vascular endothelium promoted neutrophil transmigration, with stiff EC substrates further promoting transmigration. ICAM-1 expression was enhanced on all substrates after 24-hour oxLDL treatment, an effect that accounted for the promotion of transmigration in comparison with the untreated controls. Meanwhile, 1-hour oxLDL treatment did not lead to neutrophil transmigration, even though contractility was enhanced at this point. In addition, large holes formed in the monolayers on stiff substrates following neutrophil transmigration and were further indicators of enhanced contractile forces in ECs on stiff

substrates. Using an inhibitor of MLCK in oxLDL-treated ECs, we showed that MLCK-mediated EC contractility was responsible for the dependence of substrate stiffness on transmigration and hole formation in the monolayers. Thus, it is clearly an interplay between ICAM-1 and MLCK-dependent contractile forces which mediate neutrophil transmigration through oxLDL-treated endothelium. Stiff substrates and enhanced ICAM-1 after oxLDL treatment together maximally promote transmigration. These results indicate that microvasculature stiffness, which likely varies depending on tissue location and health, is an important regulator of the immune response in the presence of oxLDL. These results also suggest that the effects of EC exposure to oxLDL during the onset of atherosclerosis depend on the biomechanical changes that take place in vasculature as the disease develops.

9 Summary and Conclusions

Leukocyte transmigration plays a pivotal role both in the normal immune response and also in the development of cardiovascular disease, including atherosclerosis and stroke. A vast amount of work has been dedicated to biological aspects of transmigration, including cytokine exposure, junctional protein organization in the endothelium, and signaling pathways. However, even though cardiovascular disease is associated with vascular stiffening, the biomechanical properties of the subendothelial matrix have, until this point, been largely ignored with respect to the immune response. Here, we investigated important aspects of EC biomechanics, leukocyte mechanosensing, and EC contraction-mediated neutrophil transmigration using an *in vitro* model of the vascular endothelium that takes into account the flexibility of the matrix below the endothelium.

9.1 Cell-cell adhesion and TNF-α affect EC biomechanics

We first evaluated the effects of two key components of our *in vitro* model, cell-cell adhesion and TNF-α exposure, on EC biomechanical properties. Biological processes such as atherogenesis, wound healing, cancer cell metastasis, and immune cell transmigration rely on a delicate balance between cell-cell and cell-substrate adhesion; however, the effects of cell-cell interactions on the mechanical properties of cells have received little attention. Here, we used atomic force microscopy (AFM) to measure the Young's modulus of live ECs. In varying the degree of cell-cell contact in ECs (single cells, groups, and monolayers), we observed that increased cell stiffness correlated with an increase in cell area. Further, we observed that ECs stiffened as they spread onto a

substrate. When we weakened cell-cell junctions, we observed that cell-substrate adhesion increased, and the stiffness of cells within the monolayer approached that of single cells. Our results suggest that while morphology can roughly be used to predict cell stiffness, cell-cell interactions play a significant role in determining the mechanical properties of individual cells in tissues by careful maintenance of cell tension homeostasis.

The immune response triggers a complicated sequence of events, one of which is release of the cytokine TNF-α from stromal cells such as monocytes and ECs. TNF-α binds to the surface of the endothelium, initiating a biological signaling cascade that leads to drastic changes in junctional protein organization, adhesion molecule expression, and permeability. Here we explored other less-studied effects of TNF-α on ECs, including cell morphology, biomechanics, migration, and cytoskeletal dynamics. We found that TNF-α induced a wide distribution of cell area and aspect ratio, with these properties increasing on average. Meanwhile, ECs treated with TNF-α softened, and we associated this with significant increases in estimated cellular volume. In addition, our evaluation of migratory dynamics demonstrated an inverse correlation between cell aspect ratio and migration speed after TNF-α treatment, suggesting that cell shape may be an important functional regulator of EC migration during an inflammatory response. Finally, we addressed the basic mechanics of how the reorganization of F-actin filaments occurs during TNF-α treatment, and we demonstrated a dynamic shift of existing actin filaments. Together, these results suggest a functional link between EC morphology, biomechanics, migration, and cytoskeletal dynamics during an inflammatory response.

9.2 Neutrophils are mechanosensitive

Knowing that a variety of factors can influence EC biomechanical properties, we next explored whether neutrophils are mechanosensitive – that is, whether they are capable of detecting changes in substrate stiffness and using that information to direct their behavior. Thus, we investigated the effects of substrate stiffness on neutrophil morphology and motility parameters such as random motility coefficient, speed, and distribution of turning angles of neutrophils during chemokinesis. Human neutrophils were plated onto fibronectin-coated polyacrylamide gels of varying stiffness and timelapse images were taken with phase contrast microscopy. Our results showed a biphasic behavior between neutrophil motility and substrate stiffness, with the optimum stiffness for motility depending on the concentration of fibronectin on the surface of the gel. This biphasic behavior most likely arises because neutrophils on soft gels are less adherent, preventing production of traction forces, while neutrophils on stiff gels adhere strongly, resulting in decreased migration. At intermediate stiffness, however, neutrophils can attain optimal motility as a function of extracellular matrix coating. Thus, we demonstrated that neutrophils are indeed mechanosensitive, suggesting that biomechanical changes which occur in vascular could influence the immune response. Therefore, our next step was to evaluate the effects of EC biomechanics and subendothelial matrix stiffness on neutrophil transmigration.

9.3 Subendothelial matrix stiffness directs the immune response

In a novel *in vitro* model, we mimicked blood vessels of varying mechanical properties using fibronectin-coated polyacrylamide gels of varying physiological

stiffness, plated with human EC monolayers that were activated with TNF-α or oxLDL. Interestingly, neutrophil transmigration increased with increasing substrate stiffness below the endothelium. We hypothesized that some sort of biophysical change in the endothelium produced this result, and thus we evaluated the effects of substrate stiffness on an array of EC (and neutrophil) properties (Figure 9.1). EC intercellular adhesion molecule-1 expression, stiffness, cytoskeletal arrangement, morphology, and cell-substrate adhesion could not account for the dependence of transmigration on EC substrate stiffness. We also explored the role of cell contraction and observed that large holes formed in endothelium on stiff substrates several minutes after neutrophil transmigration reached a maximum. Interestingly, for ECs treated with TNF-α, these holes healed after two hours of adding neutrophils, while holes in ECs treated with oxLDL did not heal within that time, indicating that transmigration through the endothelium in stiffened vasculature could add another layer of complication to the molecular and cellular events in cardiovascular disease. Further, suppression of contraction through inhibition of MLCK eliminated the effects of substrate stiffness by reducing transmigration and preventing hole formation in ECs on stiff substrates. These results provide strong evidence that neutrophil transmigration is regulated by MLCK-mediated endothelial cell contraction and that this event depends on subendothelial matrix stiffness. Thus, not only did we identify the relationship between subendothelial matrix stiffness and transmigration, but we also discovered the molecular mechanism responsible for that relationship.

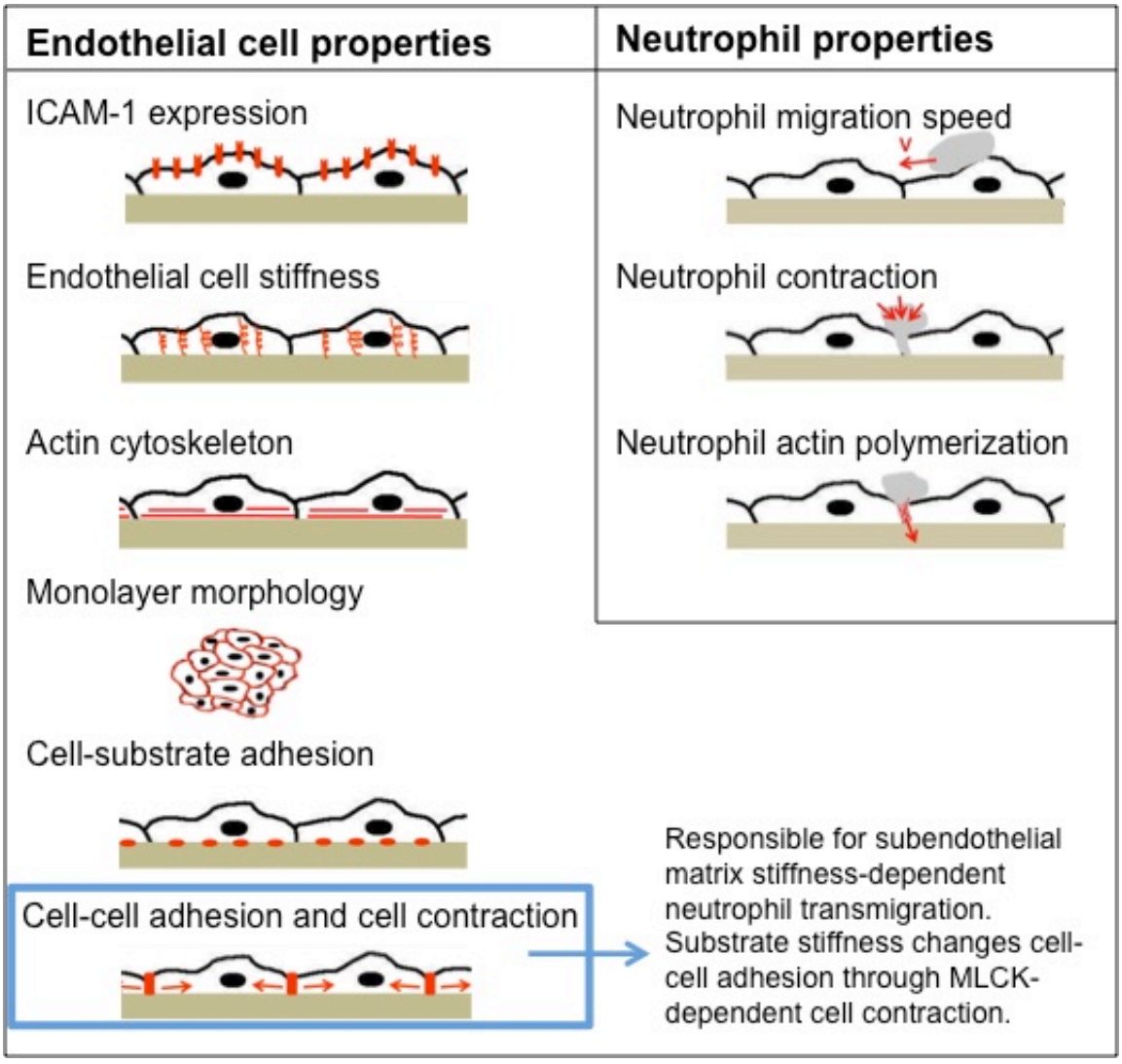

Figure 9.1. Summary of the biophysical properties of the endothelium and neutrophils which could have accounted for the subendothelial matrix stiffness-dependent neutrophil transmigration behavior.

9.4 Concluding remarks

Our results suggest that neutrophil transmigration varies with blood vessel mechanical properties, depending on health, tissue type, and size. Thus microvasculature stiffness, which likely varies depending on tissue type and health, is likely an important regulator of the immune response in the presence of either TNF-α or oxLDL. These results may be associated with cardiovascular disease biology, where increased vascular stiffness is coupled with increased leukocyte transmigration. These results also suggest that the biomechanical changes that take place in vasculature as cardiovascular disease develops could be exacerbating the situation. Finally, this work may also be relevant to cancer cell metastasis or stem cell homing, both which involve cell transmigration across the endothelium.

10 Future Work and Outlook

The work in this dissertation has motivated the start of many additional projects, all which will contribute to a more comprehensive understanding of the biophysical aspects of vasculature and the immune response. For example, this dissertation has only focused on one type of immune cell (neutrophils), and now we are using the *in vitro* model developed in this dissertation to study both monocyte and metastatic cancer cell transmigration. Shear stress could be added as an additional component of the model using either a parallel plate flow chamber or microfluidics, since this dissertation approximated the low shear stresses experienced in microvasculature by using static conditions. In addition, further experiments could identify the role of EC contractility in directing paracellular versus transcellular transmigration. Below we outline several projects that are motivated by the results presented in this dissertation.

10.1 Paracellular versus transcellular transmigration

As discussed in Section 2.9, leukocyte transmigration can occur via one of two pathways: (1) the paracellular route (through cell-cell junctions), or (2) the transcellular route (through the body of the EC). In Chapter 7, we combined our *in vitro* model for transmigration with transfection of ECs using an adenovirus for GFP-VE-cadherin in order to label cell-cell junctions. Though we observed mostly paracellular transmigration, others have observed robust transcellular transmigration both *in vivo* and *in vitro*. In the future, it would be useful to identify key factors that promote transcellular transmigration and also to determine whether EC contraction plays a role in transcellular transmigration. For example, if there exists a model where the transcellular pathway comprises a

significant percentage of total transmigration, perhaps inhibition of MLCK reduces paracellular transmigration and increases the frequency of transcellular transmigration due to a decrease in intercellular gap formation. Subendothelial matrix stiffness could also play a role in determining how MLCK inhibition affects paracellular versus transcellular transmigration.

It would also be useful to study EC actin dynamics during transcellular transmigration. Currently, it is not well understood how leukocytes transmigrate via this pathway, nor is it known how the EC cytoskeleton rearranges to accommodate transmigration. Though, if a leukocyte passes through the body of an EC, it is obvious that the EC stress fibers must be affected in some way. Our preliminary data indicates that large holes form in the actin cytoskeleton due to initiation of neutrophil transcellular transmigration (Figures 10.1 and 10.2), which could indicate that actin is being depolymerized during this process, or that the actin is being physically pushed down or to the side by the neutrophil. Confocal microscopy could be used to explore this process. If actin depolymerization is the explanation, then further experiments could identify the specific molecular and physical contributions of ECs and neutrophils that result in such dramatic reorganization of the EC actin cytoskeleton.

Figure 10.1. Initiation of neutrophil transmigration (red arrow) leads to formation of a large hole in the F-actin cytoskeleton (green, left) of a HUVEC. A phase contrast image is also shown at the right, for the timepoint (T=9:40) when the hole begins to form. The neutrophil of interest is indicated by the red arrow in the phase contrast image, while the red outline in the GFP-actin image at T=9:40 corresponds to the outline of that neutrophil. Protrusions extending from the neutrophil in the phase contrast image indicate that transmigration has initiated. Scale bar on phase contrast image is 20 μm and also applies to all GFP-actin images. Times shown are in minutes:seconds format, where T=0 is the time when neutrophils were plated onto the endothelium.

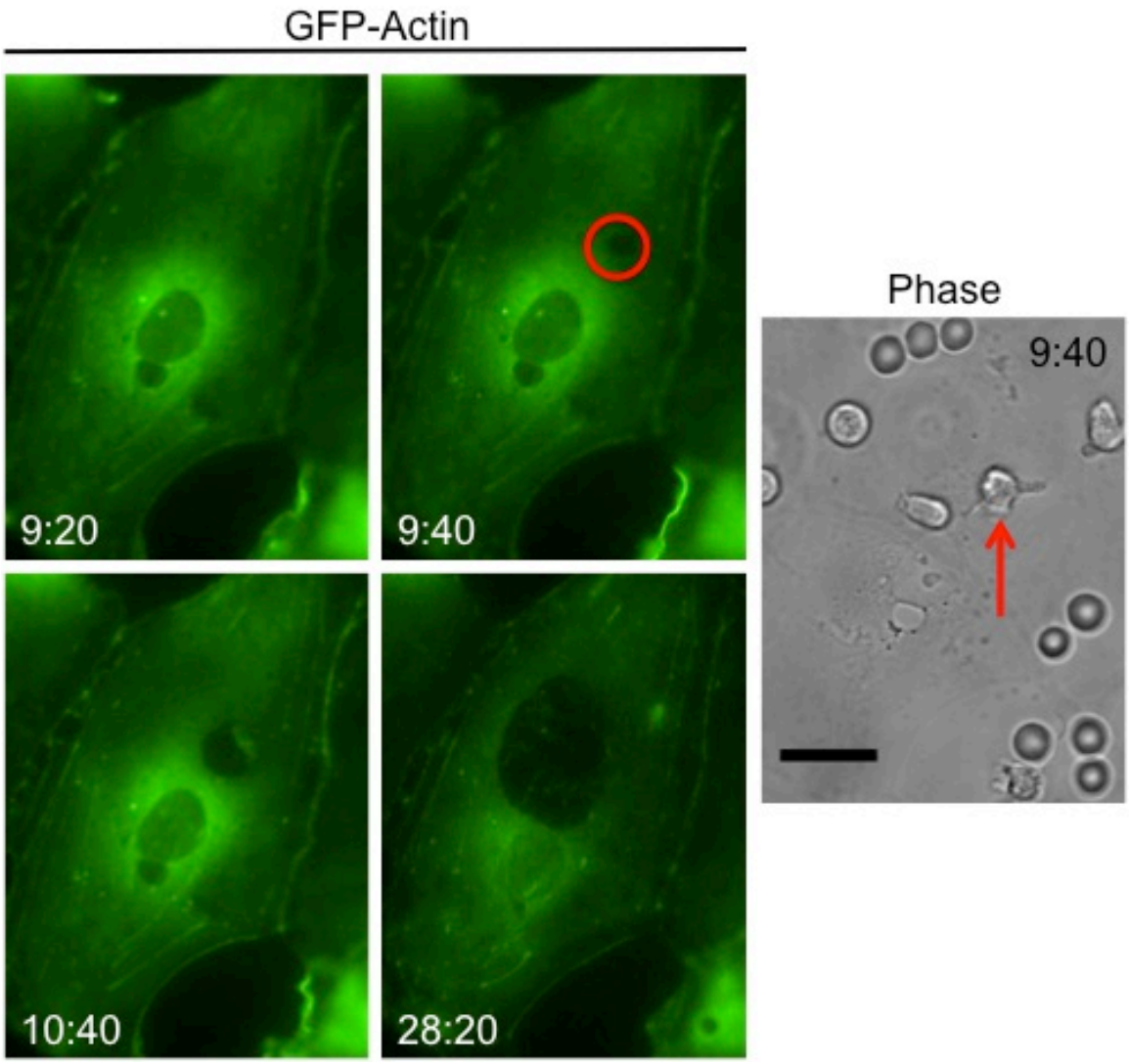

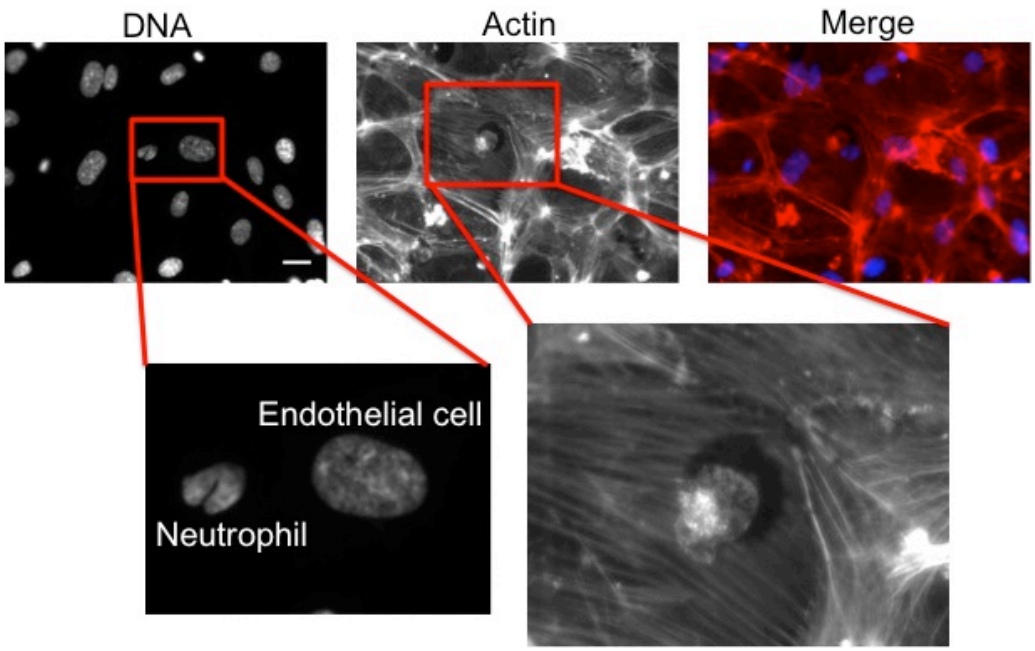

Figure 10.2. Neutrophil leaves a large hole in EC F-actin after transmigration. Cells were fixed at at 10 minutes after adding neutrophils to the endothelium. Cells were stained for F-actin (red) and DNA (blue). Neutrophils and ECs can easily be distinguished by the size and shape of the nucleus (bottom left image). A large hole in the EC stress fibers can be seen in the lower right image, with the disorganized, brighter actin of the neutrophil just next to it. Scale bar is 20 μm.

10.2 Role of neutrophil cytoskeleton during transmigration

In this dissertation we showed that the physical state of the endothelium plays a significant role in neutrophil transmigration. Though, the biophysical properties of neutrophils are also important contributors to this complex process. For example, in Figure 7.12, we displayed that MLCK-mediated contraction in *neutrophils* also contributes to the ability of neutrophils to transmigrate. Given these results, it would also be interesting to evaluate which components of the cellular cytoskeleton are necessary for transmigration. We treated the neutrophils with latrunculin-A, an actin-disrupting drug that binds actin monomers, preventing polymerization. With this treatment, neutrophils

were not able to migrate along or transmigrate through the monolayer, indicating that actin polymerization is a crucial factor for transmigration.

In addition to actin, microtubules are key regulators of neutrophil polarity during migration [239], though their potential role in transmigration has not yet been studied. Our preliminary experiments have shown that treating neutrophils with taxol, a mictrobule filament-stabilizing drug, results in a significantly reduced fraction of transmigration. Thus, microtubule dynamics do seem to play a role in transmigration. Treatment of neutrophils with nocodazole, a microtubule polymerization-disrupting drug, will be the target of future experiments. In addition to determining the effects of these drugs on how many neutrophils transmigrate, we will also evaluate whether the time to complete transmigration is different when microtubules are either stabilized or depolymerized. Thus, future work will identify specific proteins comprising the mechanical machinery in neutrophils that allow these cells to physically exert force as they push their way through the endothelial barrier. It will also be important to consider how cytoskeletal dynamics and cell contractile forces may act in concert to direct transmigration.

10.3 Measurement of traction forces during transmigration

An important next step in this work will be to actually quantify the traction forces exerted by endothelial cells during transmigration, as a function of subendothelial matrix stiffness. Traction force microscopy has become a popular tool to make such measurements, as fluorescent marker beads can be embedded in the polyacrylamide gels and displacements of these beads can be used to measure forces exerted dynamically by

cells. Mathematically, computation of forces exerted by single cells is relatively easy and common in today's research, in comparison with forces of monolayers, which are much more complicated. Recently, a method for measuring forces in islands of ECs (mini-monolayers, or groups of 10-15 cells) has been established using micropatterning techniques, and used to show that traction forces in groups of ECs increase as subendothelial matrix stiffness increases [238]. We are in contact with this group and plan to collaborate with them to measure EC traction force generation during neutrophil transmigration as a function of subendothelial matrix stiffness. Using their methods, it will also be possible to calculate intercellular stresses (cell-cell forces) in addition to traction stresses (cell-substrate forces) as a function of substrate stiffness.

10.4 Analysis of neutrophil "hotspots"

Interestingly, in our results, neutrophil migration through the endothelium on stiff substrates (approximately 5 kPa and above) occurs at specific "hotspots" in the monolayer, where one neutrophil transmigrates through the endothelium, and many neutrophils subsequently follow through the same hole. Recently, similar results have been shown for monocytes, and the authors of this study attribute what we call transmigratory "hotspots" to transmigration-induced junctional molecule rearrangement (specifically, increased PECAM-1 and decreased VE-cadherin), which increases EC permeability and places the endothelium in a more "leukocyte-leaky" state [240]. Another reasonable hypothesis is that the leukocytes release chemoattractant molecules as they transmigrate, which attract other leukocytes to the area. Alternatively, the distribution of adhesion molecules along the endothelium could be heterogeneous, and

leukocytes could simply be collectively choosing to transmigrate at the most favorable spots. However, in our work, this same "hotspot" phenomenon is not seen on softer substrates below 5 kPa, suggesting that the cell mechanics are involved. For example, perhaps the enhanced EC contractility on stiffer substrates actually varies locally, and leukocytes choose to exploit this feature, resulting in many leukocytes transmigrating in the same location. Further experiments could test the relative contribution of cell mechanics, adhesion molecule distribution, and chemoattractant release to transmigration via "hotspots" on stiff substrates.

10.5 Neutrophil migration below the endothelium

In Figure 7.18 we showed that neutrophil migration above the endothelium does depend on the stiffness of the substrate below the endothelium. This makes sense, since the ICAM-1 presentation was the same, while the stiffness of the ECs was not different enough for the neutrophils to detect. However, an interesting question is what happens once the neutrophils transmigrate and begin migrating below the endothelium. At that point, they are in direct contact with the substrate, so it could be hypothesized that their migration in that situation would be more similar to neutrophils on bare gels (without ECs), as in Chapter 6. However, we must also take into account the presence of the ECs above the neutrophils; in this case, it is actually a quasi-3D situation.

Interestingly, neutrophil morphology below the monolayer is quite different from the morphology above the monolayer (Figure 10.3). Above the monolayer, neutrophils appear bright white and mostly rounded in phase contrast microscopy, while below the monolayer they darken and take on a protrusive, spindly-like morphology. We

hypothesize that this change in morphology occurs due to the EC-substrate adhesions, which prevent the neutrophils from spreading out completely in an isotropic fashion. This could be tested by transfecting the ECs for GFP-vinculin and observing EC focal adhesion dynamics in relation to neutrophil migration below the monolayer.

As neutrophils migrate below the endothelium, they are presented with the stiffness of the substrate below them, as well as the stiffness of the ECs above them. Another experiment using a sandwich of polyacrylamide gels could test the response of neutrophils to two different stiffnesses (one above them and one below them). It would be interesting to determine whether the top surface or bottom surface is more responsible for directing neutrophil morphology and migration dynamics.

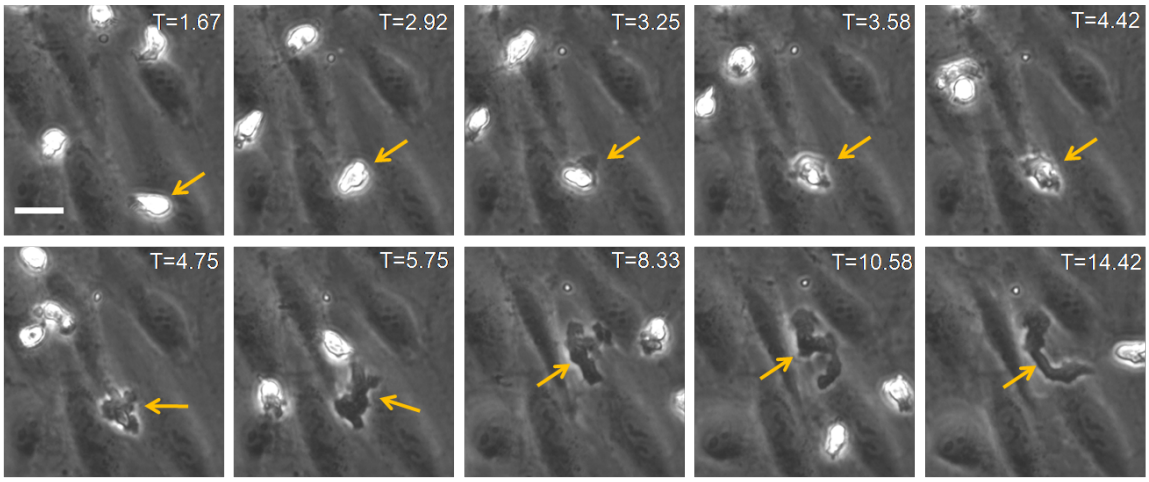

Figure 10.3. Characteristic migration along and below the endothelium. Shown is a phase contrast time sequence of a neutrophil transmigrating through a HUVEC monolayer. The time after plating (T) is shown in minutes and the scale bar is 20 μm. The orange arrows follow the cell of interest from frame to frame. Transmigration is indicated by the change in phase, from the bright white cell on top of the HUVECs, to the darkened spread-out cell underneath the HUVECs. In this case, the HUVECs are plated on top of a 5 kPa polyacrylamide gel. Transmigration begins at T=3.25 and by T=4.75 the neutrophil has completely transmigrated and begins migrating between the HUVECs and the gel. In the last four frames, it is evident that the neutrophil migrates with a very different morphology under the HUVECs than it does on top of the HUVECs. Once underneath, it sends out long, thin spindly protrusions, possibly in order to migrate around strong adhesions between the HUVECs and the gel substrate.

10.6 Metastatic cancer cell transmigration

The process of cancer metastasis also involves some form of cell transmigration through the endothelial barrier. During metastasis, cancer cells break away from the primary tumor site, intravasate into the bloodstream, circulate in the bloodstream, extravasate through the endothelium and out of the vasculature, and invade a tissue distant from the primary tumor location. Metastatic cancers are usually much harder to treat, as the disease is no longer localized to a single tumor in a particular tissue. Thus, it would be useful to either (a) prevent cancer cells from detaching from the primary tumor site in the first place, or (b) inhibit their ability to enter or exit the bloodstream. The methods developed in this dissertation have the potential to address the latter situation.

We plated HBMECs (also used as model of microvasculature endothelium in Chapter 7) onto fibronectin-coated glass dishes or soft polyacrylamide gels and allowed them to form a confluent monolayer. Then, we added metastatic breast cancer cells (MDA-MB-231 cell line) onto the endothelium, and captured timelapse images over 24 hours as the cancer cells interacted with the endothelium. We expected to observe transmigration events similar to neutrophils, where the invading cells squeezed between or through the endothelium; however, instead the cancer cells became incorporated into the monolayer. These preliminary data suggest that cancer cell transmigration may involve a two-step process, whereby metastatic cancer cells first incorporate into the endothelium, and then migrate under the monolayer. If this is true, then the mechanism of cancer cell extravasation is actually quite different from immune cells; this result could have significant impact on the cancer field.

10.7 Collagen gel assays

In our *in vitro* model, we specifically chose to use polyacrylamide gels due to the ability to manipulate their mechanical properties independent of protein presentation. However, in doing this, we also prevented the neutrophils from completing the next step of transmigration, which is invasion of the basement membrane and subsequent layers of the blood vessel. It would be interesting to use a collagen gel in place of the polyacrylamide gel and evaluate hole formation in the endothelium. Perhaps, for example, if the neutrophils can invade the collagen gel after they transmigrate through the endothelium, then there will be less hole formation, due to (1) less neutrophil migration directly below the ECs, and (2) proteases acting on the collagen gel rather than the endothelial cell-cell junctions or cell-substrate adhesions. It would also be interesting to load the collagen gels with bacteria, setting up a chemoattractant gradient. Then, the activation state of the endothelium could be measured by evaluating ICAM-1 expression, and neutrophil transmigration could be analyzed. Using this model, the role of smooth muscle cells could be included, as they could be incorporated into the collagen gel.

10.8 Mathematical modeling and simulations of transmigration

Because neutrophil transmigration is such a complicated biophysical process, it may be possible to model it mathematically, or develop simulations to describe it. This is an area that has not at all been explored by anyone to date. For example, to develop a mathematical model of transmigration, we could relate the rate of transmigration to the forces of actin polymerization and neutrophil contractile forces. This type of model

would take into account the biophysical properties of the neutrophils; however, more complex models could also take into account the EC intercellular forces.

We could also use computer simulations to explore how the number and distribution of possible "hotspots" for transmigration affects the fraction of cells that transmigrate. These hotspots would represent the places in the endothelium conducive for transmigration (e.g. places where ECs contract to form intercellular gaps). Specifically, we could address the question of whether increased transmigration on stiff substrates is due to there being more hotspots versus larger hotspots on those substrates. To do this, we could first define a certain number of hotspots (N) and their location (it would be easiest to assume a random distribution). We could also define the size (D) of the hotspot (~100 nm is the size of hole in the endothelium known to be created by neutrophils as they transmigrate). Then, we could set up a simulation of a particle's random motility, assigning a diffusion coefficient based on known experimental motility parameters. If the particle moves into the space occupied by a hole, it counts as transmigration. A defined number of particles (P) could be introduced into the simulation and allowed to migrate randomly for a defined amount of time (30 minutes, as in our experimental assays). Then, N and D could be varied systematically in the simulations to evaluate the relative contributions of hotspot number and size to transmigration.

10.9 Outlook

Our work displays the importance of taking into account blood vessel stiffness in *in vitro* models for transmigration; systems using glass or plastic substrates can no longer be considered physiologically relevant. In this dissertation we discover important links

between the biophysical state of the endothelium and the transmigration step of the immune response. This aspect of transmigration had not yet been studied, and the field will benefit from further exploration of the mechanical properties of both the endothelium itself and subendothelial matrix stiffness.

11 Appendix

Appendix A: Matlab code for AFM force curve analysis

Script:

```
% Written by Kimberly M. Stroka

clear all
close all
clc

file_ext = 'HUVEC042'; % Adjust for data file name
file_ext_base1 = '.xls';
file_ext_base2a = '-raw.fig';
file_ext_base2b = '-fit.fig';
file_base = 'C:\Documents and Settings\Kim Murley Stroka\My
Documents\AFM HUVECs\070909 HUVECs on glass\monolayer 2\flexgrid
images\'; % Adjust for data folder name
output_base = 'C:\Documents and Settings\Kim Murley Stroka\My
Documents\AFM HUVECs\test\'; % Adjust output folder
file_name = [file_base, file_ext, file_ext_base1];
output_file = [output_base, file_ext, file_ext_base1];
fig_file1 = [output_base, file_ext, file_ext_base2a];
fig_file2 = [output_base, file_ext, file_ext_base2b];

% The following command calls the “Function” below.
AFM_102709_flexgrid(file_name, output_file, fig_file1, fig_file2)
```

Function:

```
function[] = AFM_102709_flexgrid(file_name, output_file, fig_file1,
fig_file2)

% Written by Kimberly M. Stroka

% ------Preparation of data files:

% For 2000 data points, imports Excel files
% Need to change *.ivs (PicoScan) or *.mi (Picoview) files to *.txt in
% DOS command prompt. Then need to open each file in Excel and save as
% Excel file instead of text delimited.

% Be sure to enter deflection sensitivity (volt_conv - Line 24), spring
% constant of the cantilever (Line 211), radius of curvature of
cantilever (Line 211), and Poisson ratio (Line 211) into program.

% In Figure 1, magenta dot indicates end of "cut" data. Green dots
% indicate region of data which is being fit in Figure 2.
% In Figure 2, data points are blue, while red line is the Hertz-
% Sneddon fit.
```

```
% -----Parameters to adjust prior to running program:

volt_conv =1;   %nm/V conversion (enter 1 if data already converted)

% -----Parameters to be adjusted if fit is not good

cut =200;       % Cuts several of the first data points in case data is
% very noisy in the beginning
beg_slope = -0.08;     % This defines the slope where the program will
% begin fitting the data. The data prior to this will be cut.
t = 50;         % This defines the number of data points to be fit

% -----Read in and preprocess data

Youngs_mod = [];
R_squared = [];
name = {};

figure(2)
f_ = clf;
figure(f_);

for m =0:24

    if m == 0
        cellsA = 'A108:A2107';
        cellsB = 'B108:B2107';
    end
    if m == 1
        cellsA = 'A2119:A4118';
        cellsB = 'B2119:B4118';
    end
    if m == 2
        cellsA = 'A4130:A6129';
        cellsB = 'B4130:B6129';
    end
    if m == 3
        cellsA = 'A6141:A8140';
        cellsB = 'B6141:B8140';
    end
    if m == 4
        cellsA = 'A8152:A10151';
        cellsB = 'B8152:B10151';
    end
    if m == 5
        cellsA = 'A10163:A12162';
        cellsB = 'B10163:B12162';
    end
    if m == 6
        cellsA = 'A12174:A14173';
        cellsB = 'B12174:B14173';
    end
    if m == 7
        cellsA = 'A14185:A16184';
        cellsB = 'B14185:B16184';
    end
    if m == 8
```

```
    cellsA = 'A16196:A18195';
    cellsB = 'B16196:B18195';
end
if m == 9
    cellsA = 'A18207:A20206';
    cellsB = 'B18207:B20206';
end
if m == 10
    cellsA = 'A20218:A22217';
    cellsB = 'B20218:B22217';
end
if m == 11
    cellsA = 'A22229:A24228';
    cellsB = 'B22229:B24228';
end
if m == 12
    cellsA = 'A24240..A26239';
    cellsB = 'B24240..B26239';
end
if m == 13
    cellsA = 'A26251:A28250';
    cellsB = 'B26251:B28250';
end
if m == 14
    cellsA = 'A28262:A30261';
    cellsB = 'B28262:B30261';
end
if m == 15
    cellsA = 'A30273:A32272';
    cellsB = 'B30273:B32272';
end
if m == 16
    cellsA = 'A32284:A34283';
    cellsB = 'B32284:B34283';
end
if m == 17
    cellsA = 'A34295:A36294';
    cellsB = 'B34295:B36294';
end
if m == 18
    cellsA = 'A36306:A38305';
    cellsB = 'B36306:B38305';
end
if m == 19
    cellsA = 'A38317:A40316';
    cellsB = 'B38317:B40316';
end
if m == 20
    cellsA = 'A40328:A42327';
    cellsB = 'B40328:B42327';
end
if m == 21
    cellsA = 'A42339:A44338';
    cellsB = 'B42339:B44338';
end
if m == 22
    cellsA = 'A44350:A46349';
    cellsB = 'B44350:B46349';
```

```
    end
    if m == 23
        cellsA = 'A46361:A48360';
        cellsB = 'B46361:B48360';
    end
    if m == 24
        cellsA = 'A48372:A50371';
        cellsB = 'B48372:B50371';
    end


%d = x-axis = distance from sample (nm)
%z = y-axis = deflection of cantilever (nm)
d = XLSREAD(file_name,1, cellsA);
z = XLSREAD(file_name,1, cellsB)*volt_conv;

figure(1); subplot(5,5,m+1)
plot(d(1:1000),z(1:1000))
hold on

%-----Cut out first several points, # defined by "cut"
d2 = [d(cut:end)];
z2 = [z(cut:end)];

%-----Calculate derivative of raw data

dzdd = [];
for n = 2:length(d2)
    x = [(z2(n)-z2(n-1))/(d2(n)-d2(n-1))];
    dzdd = [dzdd;x];
end

%-----Check slope of each point with the point 10 points ahead

dzdd2 = [];
for n = 2:length(d2)-50
    x10 = [(z2(n+9)-z2(n-1))/(d2(n+9)-d2(n-1))];
    dzdd2 = [dzdd2;x10];
end

%-----Substract out z_o and d_o and cut out unwanted data at beginning

q = 1;
g = 1;
while (q==g)
    g = g + 1;
   if dzdd2(g)>beg_slope
       d3 = [d2(g:end)];
       z3 = [z2(g:end)];
       q = q + 1;
   end
end

d4 = [d3]-d3(1);
z4 = [z3]-z3(1);
dzdd = [dzdd(q:end)];
```

```
start_pt = cut+g;
end_pt = start_pt+t;
figure(1)
plot(d(cut),z(cut),'mo','MarkerFaceColor','m','MarkerSize',2)
plot(d(start_pt),z(start_pt),'go','MarkerFaceColor','g','MarkerSize',2)
plot(d(end_pt),z(end_pt),'go','MarkerFaceColor','g','MarkerSize',2)

%-----Cut out unwanted data at end

d5 = [d4(1:t)];
z5 = [z4(1:t)];

%-----Reflect around y-axis; convert to meters

d6 = -[d5].*10^-9;
z6 = [z5].*10^-9;

%----------------Fit to Sneddon-Hertz Model for spherical probe

%-----Create fit

ft_ = fittype({'(((((((4/(3*0.008))*(1/(1-0.45^2))*((2.5*10^-
6)^(1/2))*x^(3/2))))) ))'} ,...
     'dependent',{'y'},'independent',{'x'},'coefficients',{'E'});

%-----Fits this model using new data

[cf_, good] = fit(d6,z6,ft_ );

%-----Set up figure to receive datasets and fits

figure(2)
legh_ = []; legt_ = {};   % handles and text for legend
xlim_ = [Inf -Inf];       % limits of x axis
ax_ = subplot(5,5,m+1);
%ax_ = subplot(1,1,1);
set(ax_,'Box','on');
axes(ax_); hold on;

%-----Plot data originally in dataset "z6 vs. d6"

d6 = d6(:);
z6 = z6(:);

if m==2
    d_periph=d6;
    z_periph=z6;
end

if m==15
    d_top=d6;
    z_top=z6;
end
```

```
h_ = line(d6,z6,'Parent',ax_,'Color',[0.333333 0 0.666667],...
     'LineStyle','none', 'LineWidth',1,...
     'Marker','.', 'MarkerSize',12);
xlim_(1) = min(xlim_(1),min(d6));
xlim_(2) = max(xlim_(2),max(d6));
legh_(end+1) = h_;
legt_{end+1} = 'Data';


%-----Nudge axis limits beyond data limits

if all(isfinite(xlim_))
   xlim_ = xlim_ + [-1 1] * 0.01 * diff(xlim_);
   set(ax_,'XLim',xlim_)
end

%-----Plot the fit and save results

h_ = plot(cf_,'fit',0.95);
legend off;  % turn off legend from plot method call
set(h_(1),'Color',[1 0 0],'LineStyle','-', 'LineWidth',2,'Marker',
'none', 'MarkerSize',6);
legh_(end+1) = h_(1);
legt_{end+1} = 'Hertz model fit';

hold off;
legend(ax_,legh_, legt_);
xlabel('Distance (m)'); ylabel('Deflection (m)')
legend off;
%axis([0,5*10^-7,0,10*10^-7]);
Youngs_mod(m+1) = cf_.E;
R_squared(m+1) = good.rsquare;
Force(m+1) = z3(1); % Force initially applied (not yet multiplied by k)

end

Youngs_mod'
R_squared'

nameX = {'A'; 'B'; 'C'; 'D'; 'E'; 'F'; 'G'; 'H'; 'I'; 'J'; 'K'; 'L';
'M'; 'N'; 'O'; 'P'; 'Q'; 'R'; 'S'; 'T'; 'U'; 'V'; 'W'; 'X'; 'Y'};

file_nameX = {file_name};
summary1 = {'Young"s modulus (Pa)', 'R-squared', 'Force (nm)/k'};
summary2 = [Youngs_mod.', R_squared.', Force.'];

xlswrite(output_file, file_nameX, 1, 'A1');
xlswrite(output_file, nameX, 1, 'A3');
xlswrite(output_file, summary1, 1, 'B2');
xlswrite(output_file, summary2, 1, 'B3');

F1 = figure(1);
F2 = figure(2);

saveas(F1, fig_file1);
saveas(F2, fig_file2);
```

Appendix B: Matlab code for neutrophil migration analysis

```
% Written by Kimberly M. Stroka
% Adjust parameters in first section

clc
close all
clear all

%-----Set the following parameters before beginning:

end_time = 1800;              % seconds; total time of timelapse
time_step = 10;               % seconds; time between images
MSD_start_time = time_step;  % seconds; start time to use for MSD
% calculation; should be multiple of time_step
MSD_end_time = 0;             % seconds; end time to use for MSD
% calculation,; use value of 0 to use best fit length instead of
% specified value
angle_bin = 100;       % number of bins to use for histogram of angles
r2_cutoff = 0.99;      % cutoff value of correlation coefficient for
% linear fit of MSD vs. time
total_cells = 10;      % total number of files (1 file per cell
% tracked) for this gel; can go up to 10 cells for this program
scale =  1;            % number of microns per pixel (=1 if already
% converted in ImageJ)
scale2 = 1;            % number of microns^2 per pixel (=1 if already
% converted in ImageJ)

hist_title = {'TITLE'}; % This title will be used for all figures

file_name = 'C:\Documents and Settings\Kim Murley Stroka\My
Documents\NEUTROPHIL PROJECT\Chemokinesis Analysis\Raw Data\3 kpa
(10ugml) - 1\'; % Adjust folder and file names below
file1 = [file_name, 'Results1.xls'];
file2 = [file_name, 'Results2.xls'];
file3 = [file_name, 'Results3.xls'];
file4 = [file_name, 'Results4.xls'];
file5 = [file_name, 'Results5.xls'];
file6 = [file_name, 'Results6.xls'];
file7 = [file_name, 'Results7.xls'];
file8 = [file_name, 'Results8.xls'];
file9 = [file_name, 'Results9.xls'];
file10 = [file_name, 'Results10.xls'];


%------Begin calculating data:

end_length = end_time/time_step;
MSD_start = MSD_start_time/time_step;
MSD_end = MSD_end_time/time_step;
theta_all = [0];

for cell_no = 1:total_cells
    if cell_no == 1
        file = file1;
    end
```

```
    if cell_no == 2
        file = file2;
    end
    if cell_no == 3
        file = file3;
    end
    if cell_no == 4
        file = file4;
    end
    if cell_no == 5
        file = file5;
    end
    if cell_no == 6
        file = file6;
    end
    if cell_no == 7
        file = file7;
    end
    if cell_no == 8
        file = file8;
    end
    if cell_no == 9
        file = file9;
    end
    if cell_no == 10
        file = file10;
    end


% -----Read in data

    x = XLSREAD(file,1,'C2:C181')*scale;
    y = XLSREAD(file,1,'D2:D181')*scale;
    A = XLSREAD(file,1,'B2:B181')*scale2;

    x = x(1:end_length);
    y = y(1:end_length);
    A = A(1:end_length);
    t = [0:length(x)-1].*time_step;
    t2 = t(2:end);


% -----Plot Area vs. Time

    Avg_area(cell_no) = mean(A);
    figure(1); subplot(5,2,cell_no);
    plot(t,A,'o',t,Avg_area(cell_no),'r','MarkerSize',3);
    title(hist_title); xlabel('Time (sec)'); ylabel('Area (um^2)');
    axis([0,t(end),0,max(A)]);

    Avg_area5(cell_no) = mean(A(1:30));
    Avg_area10(cell_no) = mean(A(31:60));
    Avg_area15(cell_no) = mean(A(61:90));
    Avg_area20(cell_no) = mean(A(91:120));
    Avg_area25(cell_no) = mean(A(121:150));
    Avg_area30(cell_no) = mean(A(151:end));
```

```
% -----Plot Cell Trajectories

    xo = x-x(1);
    yo = y-y(1);

    figure(2)
    plot(xo,yo); title(hist_title); xlabel('x position (um)');
    ylabel('y position (um)')
    axis([-200,200,-200,200]);
    hold on
    plot(xo(end),yo(end),'or','MarkerSize',5')
    hold on


% -----Plot Angle vs. Time

    for m = 2:(length(x)-2)
        xx(m) = xo(m+1)-(xo(m));
        yy(m) = yo(m+1)-(yo(m));
        xx(m+1) = xo(m+2)-xo(m+1);
        yy(m+1) = yo(m+2)-yo(m+1);
        theta(m-1) = acos((xx(m)*xx(m+1)+yy(m)*yy(m+1))/((sqrt(xx(m)^2
            +yy(m)^2))*(sqrt(xx(m+1)^2+yy(m+1)^2))));
    end

    theta = theta.*(180/pi);
    theta_all = [theta_all theta];

    figure(3); subplot(5,2,cell_no)
    plot(t2(1:end-2),theta);
    title('Angle versus time')
    xlabel('Time (sec)'); ylabel('Angle (deg)'); axis tight
    figure(4)
    subplot(5,2,cell_no);
    hist(theta,angle_bin)
    title(hist_title); xlabel('Angle (deg)'); ylabel('Frequency');
    axis tight

% -----Calculate and plot mean square displacement

    for m = 1:length(x)-1
        for n = 1:(length(x)-m)
            msd(n) = (x(n+m)-x(n))^2+(y(n+m)-y(n))^2;
        end
        avg_msd(cell_no,m) = mean(msd);
    end

    figure(6); subplot(5,2,cell_no);
    plot(t2,avg_msd(cell_no,:),'o','MarkerSize',3); title(hist_title);
    xlabel('Time(sec)'); ylabel('MSD (um^2/sec)'); axis tight

% ----Calculate track velocity, end-to-end distance, and contour length

    for n = 1:(length(x)-1)
        msdv(n) = (x(n+1)-x(n))^2+(y(n+1)-y(n))^2;
```

```
        x_step(n) = (x(n+1)-x(n));
        y_step(n) = (y(n+1)-y(n));
    end
    sqrt_msd = msdv.^1/2;
    v = sqrt_msd./time_step;
    speed(cell_no) = mean(v)*60; % um/min
    R_ee(cell_no) = sqrt((x(end)-x(1))^2+(y(end)-y(1))^2);
    L_contour(cell_no) = sum(sqrt_msd);


end

% -----CALCULATE AVERAGE VALUES

Avg_areaALL = mean(Avg_area)       % um^2
StDev_area = std(Avg_area)         % um^2

Avg_area5ALL = mean(Avg_area5)
Avg_area10ALL = mean(Avg_area10)
Avg_area15ALL = mean(Avg_area15)
Avg_area20ALL = mean(Avg_area20)
Avg_area25ALL = mean(Avg_area25)
Avg_area30ALL = mean(Avg_area30)

Avg_speed = mean(speed)             % um/min
StDev_speed = std(speed)            % um/min

Avg_R_ee = mean(R_ee)               % um
Avg_L_contour = mean(L_contour)     % um

MSD = mean(avg_msd);

figure(7); subplot(2,1,1);
plot(t2,MSD,'o','MarkerSize',3); title(hist_title);
xlabel('Time (sec)'); ylabel('MSD (um^2)');

figure(7); subplot(2,1,2);
plot(log(t2),log(MSD),'o','MarkerSize',3); title(hist_title);
xlabel('log(Time)'); ylabel('log(MSD)');

figure(8);
hist(theta_all(2:end),angle_bin); title(hist_title);
xlabel('Angle (deg)'); ylabel('Frequency'); axis tight


% -----Fit Linear portion of MSD vs. time to Diffusion Equation
% -----MSD=4*D*t

t2 = t2(MSD_start:end);
MSD = MSD(MSD_start:end);

if MSD_end_time == 0
    R = corr2(t2,MSD);
    for m = 1:length(t2)
        if R^2<r2_cutoff
            t2 = t2(1:end-m);
```

```
            MSD = MSD(1:end-m);
            R = corr2(t2,MSD);
        end
    end
else
    t2 = t2(1:MSD_end);
    MSD = MSD(1:length(t2));
end

t_fine = [0:0.1:t2(end)];
t_fine2 = [t2(2):0.1:t2(end)];
a = polyfit(t2,MSD,1)
b = polyfit(log(t2(2:end)),log(MSD(2:end)),1)
MSD_fitted = polyval(a,t_fine);
log_MSD_fitted = polyval(b,log(t_fine2));

lin_fit = ['Linear fit, D = slope/4 = ', num2str(a(1)/4)];
lin_fit2 = ['Linear fit, slope = ', num2str(b(1))];

figure(9); subplot(2,1,1); plot(t2,MSD,'o','MarkerSize',3); hold on
figure(9); subplot(2,1,1); plot(t_fine,MSD_fitted,'r','LineWidth',2');
title(hist_title); xlabel('time (sec)'); ylabel('MSD (um^2)')
legend('Simulation Data',lin_fit); axis tight

figure(9); subplot(2,1,2);
plot(log(t2(2:end)),log(MSD(2:end)),'o','MarkerSize',3); hold on
figure(9); subplot(2,1,2);
plot(log(t_fine2),log_MSD_fitted,'r','LineWidth',2');
title(hist_title); xlabel('log(time)'); ylabel('log(MSD)')
legend('Simulation Data',lin_fit2)
```

12 Bibliography

1. Delves, P. J. and Roitt, I. M. (2000) The immune system. New England Journal of Medicine 343, 37-49.

2. Strell, C. and Entschladen, F. (2008) Extravasation of leukocytes in comparison to tumor cells. Cell Commun Signal 6, 10.

3. Lucchinetti, C., Bruck, W., Parisi, J., Scheithauer, B., Rodriguez, M., Lassmann, H. (2000) Heterogeneity of multiple sclerosis lesions: implications for the pathogenesis of demyelination. Ann Neurol 47, 707-17.

4. Noseworthy, J. H., Lucchinetti, C., Rodriguez, M., Weinshenker, B. G. (2000) Multiple sclerosis. N Engl J Med 343, 938-52.

5. Bailey, S. L., Carpentier, P. A., McMahon, E. J., Begolka, W. S., Miller, S. D. (2006) Innate and adaptive immune responses of the central nervous system. Crit Rev Immunol 26, 149-88.

6. Hickey, W. F. (1999) Leukocyte traffic in the central nervous system: the participants and their roles. Semin Immunol 11, 125-37.

7. Encyclopedia Britannica, Inc. (2007) Search titel: Atherosclerosis, Web site: http://www.britannica.com/EBchecked/topic/40908/atherosclerosis, Accessed September 1, 2011.

8. Davies, P. F. (1995) Flow-mediated endothelial mechanotransduction. Physiol Rev 75, 519-60.

9. Helmke, B. P. and Davies, P. F. (2002) The cytoskeleton under external fluid mechanical forces: hemodynamic forces acting on the endothelium. Ann Biomed Eng 30, 284-96.

10. Walpola, P. L., Gotlieb, A. I., Langille, B. L. (1993) Monocyte adhesion and changes in endothelial cell number, morphology, and F-actin distribution elicited by low shear stress in vivo. Am J Pathol 142, 1392-400.

11. Kim, D. W., Gotlieb, A. I., Langille, B. L. (1989) In vivo modulation of endothelial F-actin microfilaments by experimental alterations in shear stress. Arteriosclerosis 9, 439-45.

12. Goode, T. B., Davies, P. F., Reidy, M. A., Bowyer, D. E. (1977) Aortic endothelial cell morphology observed in situ by scanning electron microscopy during atherogenesis in the rabbit. Atherosclerosis 27, 235-51.

13. Nerem, R. M., Levesque, M. J., Cornhill, J. F. (1981) Vascular endothelial morphology as an indicator of the pattern of blood flow. J Biomech Eng 103, 172-6.

14. Levesque, M. J. and Nerem, R. M. (1985) The elongation and orientation of cultured endothelial cells in response to shear stress. J Biomech Eng 107, 341-7.

15. Chien, S., Li, S., Shyy, Y. J. (1998) Effects of mechanical forces on signal transduction and gene expression in endothelial cells. Hypertension 31, 162-9.

16. Papadaki, M. and Eskin, S. G. (1997) Effects of fluid shear stress on gene regulation of vascular cells. Biotechnol Prog 13, 209-21.

17. Braddock, M., Schwachtgen, J. L., Houston, P., Dickson, M. C., Lee, M. J., Campbell, C. J. (1998) Fluid Shear Stress Modulation of Gene Expression in Endothelial Cells. News Physiol Sci 13, 241-246.

18. Jiang, G., Giannone, G., Critchley, D. R., Fukumoto, E., Sheetz, M. P. (2003) Two-piconewton slip bond between fibronectin and the cytoskeleton depends on talin. Nature 424, 334-7.

19. del Rio, A., Perez-Jimenez, R., Liu, R., Roca-Cusachs, P., Fernandez, J. M., Sheetz, M. P. (2009) Stretching single talin rod molecules activates vinculin binding. Science 323, 638-41.

20. Davies, P. F., Robotewskyj, A., Griem, M. L. (1994) Quantitative studies of endothelial cell adhesion. Directional remodeling of focal adhesion sites in response to flow forces. J Clin Invest 93, 2031-8.

21. Shiu, Y. T., Li, S., Marganski, W. A., Usami, S., Schwartz, M. A., Wang, Y. L., Dembo, M., Chien, S. (2004) Rho mediates the shear-enhancement of endothelial cell migration and traction force generation. Biophys J 86, 2558-65.

22. Helmke, B. P., Goldman, R. D., Davies, P. F. (2000) Rapid displacement of vimentin intermediate filaments in living endothelial cells exposed to flow. Circ Res 86, 745-52.

23. Helmke, B. P., Rosen, A. B., Davies, P. F. (2003) Mapping mechanical strain of an endogenous cytoskeletal network in living endothelial cells. Biophys J 84, 2691-9.

24. Wang, N., Tolic-Norrelykke, I. M., Chen, J., Mijailovich, S. M., Butler, J. P., Fredberg, J. J., Stamenovic, D. (2002) Cell prestress. I. Stiffness and prestress are closely associated in adherent contractile cells. Am J Physiol Cell Physiol 282, C606-16.

25. Pelham, R. J., Jr. and Wang, Y. (1997) Cell locomotion and focal adhesions are regulated by substrate flexibility. Proc Natl Acad Sci U S A 94, 13661-5.

26. Wojciak-Stothard, B. and Ridley, A. J. (2003) Shear stress-induced endothelial cell polarization is mediated by Rho and Rac but not Cdc42 or PI 3-kinases. J Cell Biol 161, 429-39.

27. Deguchi, S., Fukamachi, H., Hashimoto, K., Iio, K., Tsujioka, K. (2009) Measurement and finite element modeling of the force balance in the vertical section of adhering vascular endothelial cells. J Mech Behav Biomed Mater 2, 173-85.

28. Sato, M., Nagayama, K., Kataoka, N., Sasaki, M., Hane, K. (2000) Local mechanical properties measured by atomic force microscopy for cultured bovine endothelial cells exposed to shear stress. J Biomech 33, 127-35.

29. Theret, D. P., Levesque, M. J., Sato, M., Nerem, R. M., Wheeler, L. T. (1988) The application of a homogeneous half-space model in the analysis of endothelial cell micropipette measurements. J Biomech Eng 110, 190-9.

30. Sato, M., Levesque, M. J., Nerem, R. M. (1987) Micropipette aspiration of cultured bovine aortic endothelial cells exposed to shear stress. Arteriosclerosis 7, 276-86.

31. Byfield, F. J., Aranda-Espinoza, H., Romanenko, V. G., Rothblat, G. H., Levitan, I. (2004) Cholesterol depletion increases membrane stiffness of aortic endothelial cells. Biophys J 87, 3336-43.

32. Byfield, F. J., Tikku, S., Rothblat, G. H., Gooch, K. J., Levitan, I. (2006) OxLDL increases endothelial stiffness, force generation, and network formation. J Lipid Res 47, 715-23.

33. Chouinard, J. A., Grenier, G., Khalil, A., Vermette, P. (2008) Oxidized-LDL induce morphological changes and increase stiffness of endothelial cells. Exp Cell Res 314, 3007-16.

34. Oberleithner, H., Riethmuller, C., Schillers, H., MacGregor, G. A., de Wardener, H. E., Hausberg, M. (2007) Plasma sodium stiffens vascular endothelium and reduces nitric oxide release. P Natl Acad Sci USA 104, 16281-16286.

35. Oberleithner, H., Callies, C., Kusche-Vihrog, K., Schillers, H., Shahin, V., Riethmuller, C., MacGregor, G. A., de Wardener, H. E. (2009) Potassium softens vascular endothelium and increases nitric oxide release. P Natl Acad Sci USA 106, 2829-2834.

36. Callies, C., Schon, P., Liashkovich, I., Stock, C., Kusche-Vihrog, K., Fels, J., Strater, A. S., Oberleithner, H. (2009) Simultaneous mechanical stiffness and electrical potential measurements of living vascular endothelial cells using combined atomic force and epifluorescence microscopy. Nanotechnology 20, 175104.

37. Kang, I., Panneerselvam, D., Panoskaltsis, V. P., Eppell, S. J., Marchant, R. E., Doerschuk, C. M. (2008) Changes in the hyperelastic properties of endothelial cells induced by tumor necrosis factor-alpha. Biophys J 94, 3273-85.

38. Wang, Q. and Doerschuk, C. M. (2000) Neutrophil-induced changes in the biomechanical properties of endothelial cells: roles of ICAM-1 and reactive oxygen species. J Immunol 164, 6487-94.

39. Wang, Q., Chiang, E. T., Lim, M., Lai, J., Rogers, R., Janmey, P. A., Shepro, D., Doerschuk, C. M. (2001) Changes in the biomechanical properties of neutrophils and endothelial cells during adhesion. Blood 97, 660-8.

40. Kataoka, N., Iwaki, K., Hashimoto, K., Mochizuki, S., Ogasawara, Y., Sato, M., Tsujioka, K., Kajiya, F. (2002) Measurements of endothelial cell-to-cell and cell-to-substrate gaps and micromechanical properties of endothelial cells during monocyte adhesion. Proc Natl Acad Sci U S A 99, 15638-43.

41. Mathur, A. B., Collinsworth, A. M., Reichert, W. M., Kraus, W. E., Truskey, G. A. (2001) Endothelial, cardiac muscle and skeletal muscle exhibit different viscous and elastic properties as determined by atomic force microscopy. J Biomech 34, 1545-53.

42. Pesen, D. and Hoh, J. H. (2005) Micromechanical architecture of the endothelial cell cortex. Biophys J 88, 670-9.

43. Engler, A. J., Richert, L., Wong, J. Y., Picart, C., Discher, D. (2004) Surface probe measurements of the elasticity of sectioned tissue, thin gels and polyelectrolyte multilayer films: Correlations between substrate stiffness and cell adhesion. Surface Science 570, 142-154.

44. Mathur, A. B., Truskey, G. A., Reichert, W. M. (2000) Atomic force and total internal reflection fluorescence microscopy for the study of force transmission in endothelial cells. Biophys J 78, 1725-35.

45. Charras, G. T. and Horton, M. A. (2002) Single cell mechanotransduction and its modulation analyzed by atomic force microscope indentation. Biophys J 82, 2970-81.

46. Ueki, Y., Sakamoto, N., Ohashi, T., Sato, M. (2009) Morphological responses of vascular endothelial cells induced by local stretch transmitted through intercellular junctions. Experimental Mechanics 49, 125-134.

47. Osawa, M., Masuda, M., Kusano, K., Fujiwara, K. (2002) Evidence for a role of platelet endothelial cell adhesion molecule-1 in endothelial cell mechanosignal transduction: is it a mechanoresponsive molecule? J Cell Biol 158, 773-785.

48. Gray, D. S., Liu, W. F., Shen, C. J., Bhadriraju, K., Nelson, C. M., Chen, C. S. (2008) Engineering amount of cell-cell contact demonstrates biphasic proliferative regulation through RhoA and the actin cytoskeleton. Exp Cell Res 314, 2846-2854.

49. Alberts, B., Johnson, A., Lewis, J., Raff, M., Roberts, K., Walter, P. (2002) Molecular Biology of the Cell. Garland Science, Taylor & Francis Group.

50. Sawa, Y., Sugimoto, Y., Ueki, T., Ishikawa, H., Sato, A., Nagato, T., Yoshida, S. (2007) Effects of TNF-alpha on leukocyte adhesion molecule expressions in cultured human lymphatic endothelium. J Histochem Cytochem 55, 721-33.

51. Blum, M. S., Toninelli, E., Anderson, J. M., Balda, M. S., Zhou, J., O'Donnell, L., Pardi, R., Bender, J. R. (1997) Cytoskeletal rearrangement mediates human microvascular endothelial tight junction modulation by cytokines. Am J Physiol 273, H286-94.

52. Wojciak-Stothard, B., Entwistle, A., Garg, R., Ridley, A. J. (1998) Regulation of TNF-alpha-induced reorganization of the actin cytoskeleton and cell-cell junctions by Rho, Rac, and Cdc42 in human endothelial cells. J Cell Physiol 176, 150-65.

53. Stolpen, A. H., Guinan, E. C., Fiers, W., Pober, J. S. (1986) Recombinant tumor necrosis factor and immune interferon act singly and in combination to reorganize human vascular endothelial cell monolayers. Am J Pathol 123, 16-24.

54. Califano, J. P. and Reinhart-King, C. A. (2008) A balance of substrate mechanics and matrix chemistry regulates endothelial cell network assembly. Cellular and Molecular Bioengineering 1, 122-132.

55. Sieminski, A. L., Hebbel, R. P., Gooch, K. J. (2004) The relative magnitudes of endothelial force generation and matrix stiffness modulate capillary morphogenesis in vitro. Exp Cell Res 297, 574-84.

56. Yeung, T., Georges, P. C., Flanagan, L. A., Marg, B., Ortiz, M., Funaki, M., Zahir, N., Ming, W., Weaver, V., Janmey, P. A. (2005) Effects of substrate stiffness on cell morphology, cytoskeletal structure, and adhesion. Cell Motil Cytoskeleton 60, 24-34.

57. Reinhart-King, C. A., Dembo, M., Hammer, D. A. (2008) Cell-cell mechanical communication through compliant substrates. Biophys J 95, 6044-51.

58. Harley, B. A., Kim, H. D., Zaman, M. H., Yannas, I. V., Lauffenburger, D. A., Gibson, L. J. (2008) Microarchitecture of three-dimensional scaffolds influences cell migration behavior via junction interactions. Biophys J 95, 4013-24.

59. Peyton, S. R. and Putnam, A. J. (2005) Extracellular matrix rigidity governs smooth muscle cell motility in a biphasic fashion. J Cell Physiol 204, 198-209.

60. Engler, A., Bacakova, L., Newman, C., Hategan, A., Griffin, M., Discher, D. (2004) Substrate compliance versus ligand density in cell on gel responses. Biophys J 86, 617-28.

61. Lo, C.-M., Wang, H.-B., Dembo, M., Wang, Y.-L. (2000) Cell movement is guided by the rigidity of the substrate. Biophysical Journal 79, 144-152.

62. Flanagan, L. A., Ju, Y. E., Marg, B., Osterfield, M., Janmey, P. A. (2002) Neurite branching on deformable substrates. Neuroreport 13, 2411-5.

63. Gunn, J. W., Turner, S. D., Mann, B. K. (2005) Adhesive and mechanical properties of hydrogels influence neurite extension. J Biomed Mater Res A 72, 91-7.

64. Engler, A. J., Sen, S., Sweeney, H. L., Discher, D. E. (2006) Matrix elasticity directs stem cell lineage specification. Cell 126, 677-89.

65. Fereol, S., Fodil, R., Labat, B., Galiacy, S., Laurent, V. M., Louis, B., Isabey, D., Planus, E. (2006) Sensitivity of alveolar macrophages to substrate mechanical and adhesive properties. Cell Motil Cytoskeleton 63, 321-40.

66. Erler, J. T. and Weaver, V. M. (2009) Three-dimensional context regulation of metastasis. Clin Exp Metastasis 26, 35-49.

67. Paszek, M. J., Zahir, N., Johnson, K. R., Lakins, J. N., Rozenberg, G. I., Gefen, A., Reinhart-King, C. A., Margulies, S. S., Dembo, M., Boettiger, D., Hammer, D. A., Weaver, V. M. (2005) Tensional homeostasis and the malignant phenotype. Cancer Cell 8, 241-54.

68. Majno, G. and Joris, I. (1996) Cells, Tissues, and Disease: Principles of General Pathology. Blackwell Science, Worcester, Massachusetts.

69. Feinberg, A. W., Schumacher, J. F., Brennan, A. B. (2009) Engineering high-density endothelial cell monolayers on soft substrates. Acta Biomater 5, 2013-24.

70. Friedland, J. C., Lee, M. H., Boettiger, D. (2009) Mechanically activated integrin switch controls alpha5beta1 function. Science 323, 642-4.

71. Deroanne, C. F., Lapiere, C. M., Nusgens, B. V. (2001) In vitro tubulogenesis of endothelial cells by relaxation of the coupling extracellular matrix-cytoskeleton. Cardiovasc Res 49, 647-58.

72. Kumar, S., Maxwell, I. Z., Heisterkamp, A., Polte, T. R., Lele, T. P., Salanga, M., Mazur, E., Ingber, D. E. (2006) Viscoelastic retraction of single living stress fibers and its impact on cell shape, cytoskeletal organization, and extracellular matrix mechanics. Biophys J 90, 3762-73.

73. Byfield, F. J., Reen, R. K., Shentu, T. P., Levitan, I., Gooch, K. J. (2009) Endothelial actin and cell stiffness is modulated by substrate stiffness in 2D and 3D. J Biomech 42, 1114-9.

74. Ghosh, K., Pan, Z., Guan, E., Ge, S., Liu, Y., Nakamura, T., Ren, X. D., Rafailovich, M., Clark, R. A. (2007) Cell adaptation to a physiologically relevant ECM mimic with different viscoelastic properties. Biomaterials 28, 671-9.

75. Solon, J., Levental, I., Sengupta, K., Georges, P. C., Janmey, P. A. (2007) Fibroblast adaptation and stiffness matching to soft elastic substrates. Biophys J 93, 4453-61.

76. Winer, J. P., Oake, S., Janmey, P. A. (2009) Non-linear elasticity of extracellular matrices enables contractile cells to communicate local position and orientation. PLoS One 4, e6382.

77. Yamamura, N., Sudo, R., Ikeda, M., Tanishita, K. (2007) Effects of the mechanical properties of collagen gel on the in vitro formation of microvessel networks by endothelial cells. Tissue Eng 13, 1443-53.

78. Vader, D., Kabla, A., Weitz, D., Mahadevan, L. (2009) Strain-induced alignment in collagen gels. PLoS One 4, e5902.

79. Stroka, K. M. and Aranda-Espinoza, H. (2009) Neutrophils display biphasic relationship between migration and substrate stiffness. Cell Motil Cytoskeleton 66, 328-341.

80. Jannat, R. A., Robbins, G. P., Ricart, B. G., Dembo, M., Hammer, D. A. (2010) Neutrophil adhesion and chemotaxis depend on substrate mechanics. J Phys-Condens Mat 22, -.

81. Oakes, P. W., Patel, D. C., Morin, N. A., Zitterbart, D. P., Fabry, B., Reichner, J. S., Tang, J. X. (2009) Neutrophil morphology and migration are affected by substrate elasticity. Blood 114, 1387-1395.

82. Rabodzey, A., Alcaide, P., Luscinskas, F. W., Ladoux, B. (2008) Mechanical forces induced by the transendothelial migration of human neutrophils. Biophys J 95, 1428-38.

83. Stroka, K. M. and Aranda-Espinoza, H. (2011) Endothelial cell substrate stiffness influences neutrophil transmigration via myosin light chain kinase-dependent cell contraction. Blood 118, 1632-1640.

84. Yang, L., Froio, R. M., Sciuto, T. E., Dvorak, A. M., Alon, R., Luscinskas, F. W. (2005) ICAM-1 regulates neutrophil adhesion and transcellular migration of TNF-alpha-activated vascular endothelium under flow. Blood 106, 584-92.

85. Dustin, M. L. and Springer, T. A. (1988) Lymphocyte Function Associated Antigen-1 (Lfa-1) Interaction with Intercellular-Adhesion Molecule-1 (Icam-1) Is One of at Least 3 Mechanisms for Lymphocyte Adhesion to Cultured Endothelial-Cells. J Cell Biol 107, 321-331.

86. Lawson, C. and Wolf, S. (2009) ICAM-1 signaling in endothelial cells. Pharmacol Rep 61, 22-32.

87. Muller, W. A. (1995) The role of PECAM-1 (CD31) in leukocyte emigration: studies in vitro and in vivo. J Leukoc Biol 57, 523-8.

88. O'Brien, C. D., Lim, P., Sun, J., Albelda, S. M. (2003) PECAM-1-dependent neutrophil transmigration is independent of monolayer PECAM-1 signaling or localization. Blood 101, 2816-2825.

89. Feng, D., Nagy, J. A., Pyne, K., Dvorak, H. F., Dvorak, A. M. (2004) Ultrastructural localization of platelet endothelial cell adhesion molecule (PECAM-1, CD31) in vascular endothelium. Journal of Histochemistry & Cytochemistry 52, 87-101.

90. Dufour, E. M., Deroche, A., Bae, Y., Muller, W. A. (2008) CD99 is essential for leukocyte diapedesis in vivo. Cell Commun Adhes 15, 351-63.

91. Lou, O., Alcaide, P., Luscinskas, F. W., Muller, W. A. (2007) CD99 is a key mediator of the transendothelial migration of neutrophils. J Immunol 178, 1136-43.

92. Liu, Z. J., Sniadecki, N. J., Chen, C. S. (2010) Mechanical Forces in Endothelial Cells during Firm Adhesion and Early Transmigration of Human Monocytes. Cellular and Molecular Bioengineering 3, 50-59.

93. Vestweber, D. (2007) Adhesion and signaling molecules controlling the transmigration of leukocytes through endothelium. Immunol Rev 218, 178-96.

94. Baumgartner, W., Hinterdorfer, P., Ness, W., Raab, A., Vestweber, D., Schindler, H., Drenckhahn, D. (2000) Cadherin interaction probed by atomic force microscopy. Proc Natl Acad Sci U S A 97, 4005-10.

95. Vestweber, D., Winderlich, M., Cagna, G., Nottebaum, A. F. (2009) Cell adhesion dynamics at endothelial junctions: VE-cadherin as a major player. Trends Cell Biol 19, 8-15.

96. Yamada, S., Pokutta, S., Drees, F., Weis, W. I., Nelson, W. J. (2005) Deconstructing the cadherin-catenin-actin complex. Cell 123, 889-901.

97. Abe, K. and Takeichi, M. (2008) EPLIN mediates linkage of the cadherin catenin complex to F-actin and stabilizes the circumferential actin belt. Proceedings of the National Academy of Sciences of the United States of America 105, 13-9.

98. Shaw, S. K., Bamba, P. S., Perkins, B. N., Luscinskas, F. W. (2001) Real-time imaging of vascular endothelial-cadherin during leukocyte transmigration across endothelium. J Immunol 167, 2323-30.

99. Alcaide, P., Newton, G., Auerbach, S., Sehrawat, S., Mayadas, T. N., Golan, D. E., Yacono, P., Vincent, P., Kowalczyk, A., Luscinskas, F. W. (2008) p120-Catenin regulates leukocyte transmigration through an effect on VE-cadherin phosphorylation. Blood 112, 2770-9.

100. Wee, H., Oh, H. M., Jo, J. H., Jun, C. D. (2009) ICAM-1/LFA-1 interaction contributes to the induction of endothelial cell-cell separation: implication for enhanced leukocyte diapedesis. Exp Mol Med 41, 341-8.

101. Wojcikiewicz, E. P., Koenen, R. R., Fraemohs, L., Minkiewicz, J., Azad, H., Weber, C., Moy, V. T. (2008) LFA-1 binding destabilizes the JAM-A homophilic interaction during leukocyte transmigration. Biophys J. 96, 285-93.

102. Carman, C. V. and Springer, T. A. (2008) Trans-cellular migration: cell-cell contacts get intimate. Current Opinion in Cell Biology 20, 533-540.

103. Riethmuller, C., Nasdala, I., Vestweber, D. (2008) Nano-surgery at the leukocyte-endothelial docking site. Pflugers Arch 456, 71-81.

104. Carman, C. V., Jun, C. D., Salas, A., Springer, T. A. (2003) Endothelial cells proactively form microvilli-like membrane projections upon intercellular adhesion molecule 1 engagement of leukocyte LFA-1. J Immunol 171, 6135-44.

105. van Buul, J. D., Allingham, M. J., Samson, T., Meller, J., Boulter, E., Garcia-Mata, R., Burridge, K. (2007) RhoG regulates endothelial apical cup assembly downstream from ICAM1 engagement and is involved in leukocyte trans-endothelial migration. J Cell Biol 178, 1279-93.

106. Wojcikiewicz, E. P., Abdulreda, M. H., Zhang, X., Moy, V. T. (2006) Force spectroscopy of LFA-1 and its ligands, ICAM-1 and ICAM-2. Biomacromolecules 7, 3188-95.

107. Barreiro, O., Zamai, M., Yanez-Mo, M., Tejera, E., Lopez-Romero, P., Monk, P. N., Gratton, E., Caiolfa, V. R., Sanchez-Madrid, F. (2008) Endothelial adhesion receptors are recruited to adherent leukocytes by inclusion in preformed tetraspanin nanoplatforms. J Cell Biol 183, 527-42.

108. Yang, L., Kowalski, J. R., Yacono, P., Bajmoczi, M., Shaw, S. K., Froio, R. M., Golan, D. E., Thomas, S. M., Luscinskas, F. W. (2006) Endothelial cell cortactin

coordinates intercellular adhesion molecule-1 clustering and actin cytoskeleton remodeling during polymorphonuclear leukocyte adhesion and transmigration. J Immunol 177, 6440-9.

109. Carman, C. V., Sage, P. T., Sciuto, T. E., de la Fuente, M. A., Geha, R. S., Ochs, H. D., Dvorak, H. F., Dvorak, A. M., Springer, T. A. (2007) Transcellular diapedesis is initiated by invasive podosomes. Immunity 26, 784-97.

110. Hashimoto, K., Kataoka, N., Nakamura, E., Tsujioka, K., Kajiya, F. (2007) Oxidized LDL specifically promotes the initiation of monocyte invasion during transendothelial migration with upregulated PECAM-1 and downregulated VE-cadherin on endothelial junctions. Atherosclerosis 194, e9-17.

111. Birukova, A. A., Arce, F. T., Moldobaeva, N., Dudek, S. M., Garcia, J. G., Lal, R., Birukov, K. G. (2009) Endothelial permeability is controlled by spatially defined cytoskeletal mechanics: atomic force microscopy force mapping of pulmonary endothelial monolayer. Nanomedicine 5, 30-41.

112. Isac, L., Thoelking, G., Schwab, A., Oberleithner, H., Riethmuller, C. (2010) Endothelial f-actin depolymerization enables leukocyte transmigration. Analytical and bioanalytical chemistry 399, 2351-8.

113. Zieman, S. J., Melenovsky, V., Kass, D. A. (2005) Mechanisms, pathophysiology, and therapy of arterial stiffness. Arterioscler Thromb Vasc Biol 25, 932-43.

114. Weaver, V. (2011) Tissue Stiffness and Breast Cancer Invasion. Abstract presented at Biophysical Society Annual Meeting March 7, 2011.

115. Blacher, J., Asmar, R., Djane, S., London, G. M., Safar, M. E. (1999) Aortic pulse wave velocity as a marker of cardiovascular risk in hypertensive patients. Hypertension 33, 1111-1117.

116. Boutouyrie, P., Tropeano, A. I., Asmar, R., Gautier, I., Benetos, A., Lacolley, P., Laurent, S. (2002) Aortic stiffness is an independent predictor of primary coronary events in hypertensive patients - A longitudinal study. Hypertension 39, 10-15.

117. Mao, Y., Sun, Q., Wang, X., Ouyang, Q., Han, L., Jiang, L., Han, D. (2009) In vivo nanomechanical imaging of blood-vessel tissues directly in living mammals using atomic force microscopy. Applied Physics Letters 95, 013704.

118. Levy, B. I., Ambrosio, G., Pries, A. R., Struijker-Boudier, H. A. (2001) Microcirculation in hypertension: a new target for treatment? Circulation 104, 735-40.

119. Kothapalli, D., Liu, S., Byfield, F. J., Castagnino, P., Xu, T., Hawthorne, E., Phillips, M. C., Lund-Katz, S., Janmey, P. A., Assoian, R. K. (2010) Apolipoprotein E controls matrix protein synthesis and arterial stiffness. American Society of Cell Biology Annual Meeting December 14, 2010.

120. Peloquin, J., Huynh, J., Williams, R. M., Reinhart-King, C. A. (2011) Indentation measurements of the subendothelial matrix in bovine carotid arteries. J Biomech 44, 815-21.

121. Klein, E. A., Yin, L., Kothapalli, D., Castagnino, P., Byfield, F. J., Xu, T., Levental, I., Hawthorne, E., Janmey, P. A., Assoian, R. K. (2009) Cell-cycle control by physiological matrix elasticity and in vivo tissue stiffening. Curr Biol 19, 1511-8.

122. Norman, L. L. and Aranda-Espinoza, H. (2010) Cortical neuron outgrowth is insensitive to substrate stiffness. Cellular and Molecular Bioengineering 3, 398-414.

123. Paszek, M. J., Zahir, N., Johnson, K. R., Lakins, J. N., Rozenberg, G. I., Gefen, A., Reinhart-King, C. A., Margulies, S. S., Dembo, M., Boettiger, D., Hammer, D. A., Weaver, V. M. (2005) Tensional homeostasis and the malignant phenotype. Cancer cell 8, 241-254.

124. Dejana, E. (2004) Endothelial cell-cell junctions: Happy together. Nat Rev Mol Cell Bio 5, 261-270.

125. Davies, P. F., Barbee, K. A., Volin, M. V., Robotewskyj, A., Chen, J., Joseph, L., Griem, M. L., Wernick, M. N., Jacobs, E., Polacek, D. C., dePaola, N., Barakat, A. I. (1997) Spatial relationships in early signaling events of flow-mediated endothelial mechanotransduction. Annu Rev Physiol 59, 527-49.

126. Ko, K. S., Arora, P. D., McCulloch, C. A. (2001) Cadherins mediate intercellular mechanical signaling in fibroblasts by activation of stretch-sensitive calcium-permeable channels. J Biol Chem 276, 35967-77.

127. Shay-Salit, A., Shushy, M., Wolfovitz, E., Yahav, H., Breviario, F., Dejana, E., Resnick, N. (2002) VEGF receptor 2 and the adherens junction as a mechanical transducer in vascular endothelial cells. Proc Natl Acad Sci U S A 99, 9462-7.

128. Ladoux, B., Anon, E., Lambert, M., Rabodzey, A., Hersen, P., Buguin, A., Silberzan, P., Mege, R.-M. (2010) Strength Dependence of Cadherin-Mediated Adhesions. Biophysical Journal 98, 534–542.

129. Lampugnani, M. G., Zanetti, A., Breviario, F., Balconi, G., Orsenigo, F., Corada, M., Spagnuolo, R., Betson, M., Braga, V., Dejana, E. (2002) VE-cadherin regulates endothelial actin activating Rac and increasing membrane association of Tiam. Mol Biol Cell 13, 1175-89.

130. Etienne-Manneville, S. and Hall, A. (2002) Rho GTPases in cell biology. Nature 420, 629-35.

131. Juliano, R. L. (2002) Signal transduction by cell adhesion receptors and the cytoskeleton: functions of integrins, cadherins, selectins, and immunoglobulin-superfamily members. Annu Rev Pharmacol Toxicol 42, 283-323.

132. Blaschuk, O. W. and Devemy, E. (2009) Cadherins as novel targets for anti-cancer therapy. European Journal of Pharmacology 625, 195-198.

133. Adams, C. L. and Nelson, W. J. (1998) Cytomechanics of cadherin-mediated cell-cell adhesion. Current Opinion in Cell Biology 10, 572-577.

134. Chen, C. S., Mrksich, M., Huang, S., Whitesides, G. M., Ingber, D. E. (1997) Geometric control of cell life and death. Science 276, 1425-8.

135. Nelson, C. M. and Chen, C. S. (2003) VE-cadherin simultaneously stimulates and inhibits cell proliferation by altering cytoskeletal structure and tension. Journal of Cell Science 116, 3571-3581.

136. Nelson, C. M. and Chen, C. S. (2002) Cell-cell signaling by direct contact increases cell proliferation via a PI3K-dependent signal. Febs Lett 514, 238-242.

137. Fagotto, F. and Gumbiner, B. M. (1996) Cell contact-dependent signaling. Developmental Biology 180, 445-454.

138. Lauffenburger, D. A. and Griffith, L. G. (2001) Who's got pull around here? Cell organization in development and tissue engineering. P Natl Acad Sci USA 98, 4282-4284.

139. Califano, J. P. and Reinhart-King, C. A. (2010) Substrate stiffness and cell area predict cellular traction stresses in single cells and cells in contact. Cellular and Molecular Bioengineering 3, 68-75.

140. Farhadifar, R., Roper, J. C., Algouy, B., Eaton, S., Julicher, F. (2007) The influence of cell mechanics, cell-cell interactions, and proliferation on epithelial packing. Current Biology 17, 2095-2104.

141. Trepat, X., Wasserman, M. R., Angelini, T. E., Millet, E., Weitz, D. A., Butler, J. P., Fredberg, J. J. (2009) Physical forces during collective cell migration. Nature Physics 5, 426-430.

142. Hoffman, B. D. and Crocker, J. C. (2009) Cell Mechanics: Dissecting the Physical Responses of Cells to Force. Annual Review of Biomedical Engineering 11, 259-288.

143. Vinckier, A. and Semenza, G. (1998) Measuring elasticity of biological materials by atomic force microscopy. FEBS Letters 430, 12-6.

144. Sneddon, I. N. (1965) The relation between load and penetration in the axisymmetric boussinesq problem for a punch of arbitrary profile. Int. J. Eng. Sci. 3, 47-57.

145. Svaldo Lanero, T., Cavalleri, O., Krol, S., Rolandi, R., Gliozzi, A. (2006) Mechanical properties of single living cells encapsulated in polyelectrolyte matrixes. J Biotechnol 124, 723-31.

146. Weisenhorn, A. L., Khorsandit, M., Kasast, S., Gotzost, V., Butt, H.-J. (1993) Deformation and height anomaly of soft surfaces studied with an AFM. Nanotechnology 4, 106-113.

147. Rotsch, C. and Radmacher, M. (2000) Drug-induced changes of cytoskeletal structure and mechanics in fibroblasts: an atomic force microscopy study. Biophys J 78, 520-35.

148. Wakatsuki, T., Schwab, B., Thompson, N. C., Elson, E. L. (2001) Effects of cytochalasin D and latrunculin B on mechanical properties of cells. Journal of Cell Science 114, 1025-1036.

149. Reinhart-King, C. A. (2008) Endothelial cell adhesion and migration. Angiogenesis: In Vitro Systems 443, 45-64.

150. Butt, H. J. and Jaschke, M. (1995) Calculation of Thermal Noise in Atomic-Force Microscopy. Nanotechnology 6, 1-7.

151. Hutter, J. L. and Bechhoefer, J. (1993) Calibration of Atomic-Force Microscope Tips. Review of Scientific Instruments 64, 1868-1873.

152. Lin, L. A. G., Liu, A. Q., Yu, Y. F., Zhang, C., Lim, C. S., Ng, S. H., Yap, P. H., Gao, H. J. (2008) Cell compressibility studies utilizing noncontact hydrostatic pressure measurements on single living cells in a microchamber. Applied Physics Letters 92, 233901.

153. Rico, F., Roca-Cusachs, P., Gavara, N., Farre, R., Rotger, M., Navajas, D. (2005) Probing mechanical properties of living cells by atomic force microscopy with blunted pyramidal cantilever tips. Phys Rev E Stat Nonlin Soft Matter Phys 72, 021914.

154. Norman, L. L., Oetama, R. J., Dembo, M., Byfield, F., Hammer, D. A., Levitan, I., Aranda-Espinoza, H. (2010) Modification of Cellular Cholesterol Content Affects Traction Force, Adhesion and Cell Spreading. Cellular and Molecular Bioengineering 3, 151-162.

155. Axelrod, D. (2001) Total internal reflection fluorescence microscopy in cell biology. Traffic 2, 764-774.

156. Nelson, C. M., Pirone, D. M., Tan, J. L., Chen, C. S. (2004) Vascular endothelial-cadherin regulates cytoskeletal tension, cell spreading, and focal adhesions by stimulating RhoA. Mol Biol Cell 15, 2943-53.

157. Reinhart-King, C. A., Dembo, M., Hammer, D. A. (2005) The dynamics and mechanics of endothelial cell spreading. Biophys J 89, 676-89.

158. Geiger, B. and Bershadsky, A. (2001) Assembly and mechanosensory function of focal contacts. Curr Opin Cell Biol 13, 584-92.

159. Waterman-Storer, C. M., Salmon, W. C., Salmon, E. D. (2000) Feedback interactions between cell-cell adherens junctions and cytoskeletal dynamics in Newt lung epithelial cells. Molecular Biology of the Cell 11, 2471-2483.

160. Vitorino, P. and Meyer, T. (2008) Modular control of endothelial sheet migration. Genes & Development 22, 3268-3281.

161. Balaban, N. Q., Schwarz, U. S., Riveline, D., Goichberg, P., Tzur, G., Sabanay, I., Mahalu, D., Safran, S., Bershadsky, A., Addadi, L., Geiger, B. (2001) Force and focal adhesion assembly: a close relationship studied using elastic micropatterned substrates. Nature Cell Biology 3, 466-472.

162. Bereiterhahn, J., Luck, M., Miebach, T., Stelzer, H. K., Voth, M. (1990) Spreading of Trypsinized Cells - Cytoskeletal Dynamics and Energy-Requirements. Journal of Cell Science 96, 171-188.

163. Gauthier, N. C., Rossier, O. M., Mathur, A., Hone, J. C., Sheetz, M. P. (2009) Plasma membrane area increases with spread area by exocytosis of a GPI-anchored protein compartment. Mol Biol Cell 20, 3261-72.

164. Rawicz, W., Olbrich, K. C., McIntosh, T., Needham, D., Evans, E. (2000) Effect of chain length and unsaturation on elasticity of lipid bilayers. Biophys J 79, 328-39.

165. Angst, B. D., Marcozzi, C., Magee, A. I. (2001) The cadherin superfamily: diversity in form and function. Journal of Cell Science 114, 629-641.

166. Corada, M., Mariotti, M., Thurston, G., Smith, K., Kunkel, R., Brockhaus, M., Lampugnani, M. G., Martin-Padura, I., Stoppacciaro, A., Ruco, L., McDonald, D. M., Ward, P. A., Dejana, E. (1999) Vascular endothelial-cadherin is an important determinant of microvascular integrity in vivo. P Natl Acad Sci USA 96, 9815-9820.

167. Gotsch, U., Borges, E., Bosse, R., Boggemeyer, E., Simon, M., Mossmann, H., Vestweber, D. (1997) VE-cadherin antibody accelerates neutrophil recruitment in vivo. Journal of Cell Science 110, 583-588.

168. Hordijk, P. L., Anthony, E., Mul, F. P. J., Rientsma, R., Oomen, L. C. J. M., Roos, D. (1999) Vascular-endothelial-cadherin modulates endothelial monolayer permeability. Journal of Cell Science 112, 1915-1923.

169. Zhu, A. J. and Watt, F. M. (1996) Expression of a dominant negative cadherin mutant inhibits proliferation and stimulates terminal differentiation of human epidermal keratinocytes. Journal of Cell Science 109, 3013-3023.

170. Levenberg, S., Katz, B. Z., Yamada, K. M., Geiger, B. (1998) Long-range and selective autoregulation of cell-cell or cell-matrix adhesions by cadherin or integrin ligands. Journal of Cell Science 111, 347-357.

171. de Rooij, J., Kerstens, A., Danuser, G., Schwartz, M. A., Waterman-Storer, C. M. (2005) Integrin-dependent actomyosin contraction regulates epithelial cell scattering. J Cell Biol 171, 153-164.

172. Roca-Cusachs, P., Alcaraz, J., Sunyer, R., Samitier, J., Farre, R., Navajas, D. (2008) Micropatterning of single endothelial cell shape reveals a tight coupling between nuclear volume in G1 and proliferation. Biophys J 94, 4984-95.

173. Dahl, K. N., Ribeiro, A. J. S., Lammerding, J. (2008) Nuclear shape, mechanics, and mechanotransduction. Circulation Research 102, 1307-1318.

174. Wang, N. and Stamenovic, D. (2002) Mechanics of vimentin intermediate filaments. Journal of muscle research and cell motility 23, 535-40.

175. Gardel, M. L., Nakamura, F., Hartwig, J. H., Crocker, J. C., Stossel, T. P., Weitz, D. A. (2006) Prestressed F-actin networks cross-linked by hinged filamins replicate mechanical properties of cells. Proc Natl Acad Sci U S A 103, 1762-7.

176. Cai, X. F., Xing, X. B., Cai, J. Y., Chen, Q., Wu, S. X., Huang, F. C. (2010) Connection between biomechanics and cytoskeleton structure of lymphocyte and Jurkat cells: An AFM study. Micron 41, 257-262.

177. Kasas, S., Wang, X., Hirling, H., Marsault, R., Huni, B., Yersin, A., Regazzi, R., Grenningloh, G., Riederer, B., Forro, L., Dietler, G., Catsicas, S. (2005) Superficial and deep changes of cellular mechanical properties following cytoskeleton disassembly. Cell Motility and the Cytoskeleton 62, 124-132.

178. Bellin, R. M., Kubicek, J. D., Frigault, M. J., Kamien, A. J., Steward, R. L., Barnes, H. M., DiGiacomo, M. B., Duncan, L. J., Edgerly, C. K., Morse, E. M., Park, C. Y., Fredberg, J. J., Cheng, C. M., Leduc, P. R. (2009) Defining the role of syndecan-4 in mechanotransduction using surface-modification approaches. P Natl Acad Sci USA 106, 22102-22107.

179. Martens, J. C. and Radmacher, M. (2008) Softening of the actin cytoskeleton by inhibition of myosin II. Pflugers Arch 456, 95-100.

180. Hutson, M. S., Tokutake, Y., Chang, M. S., Bloor, J. W., Venakides, S., Kiehart, D. P., Edwards, G. S. (2003) Forces for morphogenesis investigated with laser microsurgery and quantitative modeling. Science 300, 145-149.

181. Foty, R. A., Pfleger, C. M., Forgacs, G., Steinberg, M. S. (1996) Surface tensions of embryonic tissues predict their mutual envelopment behavior. Development 122, 1611-1620.

182. Ryan, P. L., Foty, R. A., Kohn, J., Steinberg, M. S. (2001) Tissue spreading on implantable substrates is a competitive outcome of cell-cell vs. cell-substratum adhesivity. P Natl Acad Sci USA 98, 4323-4327.

183. Isenberg, B. C., DiMilla, P. A., Walker, M., Kim, S., Wong, J. Y. (2009) Vascular Smooth Muscle Cell Durotaxis Depends on Substrate Stiffness Gradient Strength. Biophysical Journal 97, 1313-1322.

184. Bhadriraju, K. and Hansen, L. K. (2002) Extracellular matrix- and cytoskeleton-dependent changes in cell shape and stiffness. Exp Cell Res 278, 92-100.

185. Goldblum, S. E., Hennig, B., Jay, M., Yoneda, K., McClain, C. J. (1989) Tumor necrosis factor alpha-induced pulmonary vascular endothelial injury. Infection and immunity 57, 1218-26.

186. Dustin, M. L. and Springer, T. A. (1988) Lymphocyte function-associated antigen-1 (LFA-1) interaction with intercellular adhesion molecule-1 (ICAM-1) is one of at least three mechanisms for lymphocyte adhesion to cultured endothelial cells. J Cell Biol 107, 321-31.

187. Mckenzie, J. A. G. and Ridley, A. J. (2007) Roles of Rho/ROCK and MLCK in TNF-alpha-induced changes in endothelial morphology and permeability. J Cell Physiol 213, 221-228.

188. Juliano, R. L. and Haskill, S. (1993) Signal transduction from the extracellular matrix. J Cell Biol 120, 577-85.

189. Martin, P. (1997) Wound healing--aiming for perfect skin regeneration. Science 276, 75-81.

190. Bernstein, L. R. and Liotta, L. A. (1994) Molecular mediators of interactions with extracellular matrix components in metastasis and angiogenesis. Curr Opin Oncol 6, 106-13.

191. Pearson, J. D. (1999) Vascular Adhesion Molecules and Inflammation. In *Progress in Inflammation Research* (M. J. Parnham, ed) Birkhauser Verlag, Basel, Switzerland 260.

192. Schenkel, A. R., Mamdouh, Z., Muller, W. A. (2004) Locomotion of monocytes on endothelium is a critical step during extravasation. Nat Immunol 5, 393-400.

193. Cox, E. A. and Huttenlocher, A. (1998) Regulation of integrin-mediated adhesion during cell migration. Microsc Res Tech 43, 412-9.

194. Shao, J. Y. and Hochmuth, R. M. (1999) Mechanical anchoring strength of L-selectin, beta2 integrins, and CD45 to neutrophil cytoskeleton and membrane. Biophys J 77, 587-96.

195. Molteni, R., Fabbri, M., Bender, J. R., Pardi, R. (2006) Pathophysiology of leukocyte-tissue interactions. Curr Opin Cell Biol 18, 491-8.

196. Smith, L. A., Aranda-Espinoza, H., Haun, J. B., Hammer, D. A. (2007) Interplay between shear stress and adhesion on neutrophil locomotion. Biophys J 92, 632-40.

197. Peyton, S. R. and Putnam, A. J. (2005) Extracellular matrix rigidity governs smooth muscle cell motility in a biphasic fasion. Journal of Cellular Physiology 204, 198-209.

198. Wang, Y. and Pelham, R. (1998) Preparation of a flexible, porous polyacrylamide substrate for mechanical studies of cultured cells. Methods in Enzymology 298, 489-496.

199. Jiang, G., Huang, A. H., Cai, Y., Tanase, M., Sheetz, M. P. (2006) Rigidity sensing at the leading edge through AlphavBeta3 integrins and RPTPalpha. Biophysical Journal 90, 1804-1809.

200. Lauffenburger, D. A. and Linderman, J. J. (1993) Receptors: Models for Binding, Trafficking, and Signaling. Oxford University Press, New York.

201. Chettibi, S., Lawrence, A. J., Young, J. D., Lawrence, P. D., Stevenson, R. D. (1994) Dispersive locomotion of human neutrophils in response to a steroid-induced factor from monocytes. J Cell Sci 107 (Pt 11), 3173-81.

202. Gruler, H. and Bultmann, B. D. (1984) Analysis of cell movement. Blood Cells 10, 61-77.

203. DiMilla, P. A., Stone, J. A., Quinn, J. A., Albelda, S. M., Lauffenburger, D. A. (1993) Maximal migration of human smooth muscle cells on fibronectin and type IV collagen occurs at an intermediate attachment strength. J Cell Biol 122, 729-37.

204. Harley, B. A. C., Kim, H.-D., Zaman, M. H., Yannas, I. V., Lauffenburger, D. A., Gibson, L. J. (2008) Micro-architecture of three-dimensional scaffolds influences cell migration behavior via junctions interactions. Biophysical Journal 95, 4013-4024.

205. Gupton, S. L. and Waterman-Storer, C. M. (2006) Spatiotemporal feedback between actomyosin and focal-adhesion systems optimizes rapid cell migration. Cell 125, 1361-74.

206. Smith, L. A., Aranda-Espinoza, H., Haun, J. B., Dembo, M., Hammer, D. A. (2007) Neutrophil traction stresses are concentrated in the uropod during migration. Biophys J 92, L58-60.

207. Palecek, S. P., Huttenlocher, A., Horwitz, A. F., Lauffenburger, D. A. (1998) Physical and biochemical regulation of integrin release during rear detachment of migrating cells. J Cell Sci 111 (Pt 7), 929-40.

208. Huang, A. J., Manning, J. E., Bandak, T. M., Ratau, M. C., Hanser, K. R., Silverstein, S. C. (1993) Endothelial-Cell Cytosolic Free Calcium Regulates Neutrophil Migration across Monolayers of Endothelial-Cells. J Cell Biol 120, 1371-1380.

209. Saito, H., Minamiya, Y., Kitamura, M., Saito, S., Enomoto, K., Terada, K., Ogawa, J. (1998) Endothelial myosin light chain kinase regulates neutrophil migration across human umbilical vein endothelial cell monolayer. J Immunol 161, 1533-1540.

210. Garcia, J. G. N., Verin, A. D., Herenyiova, M., English, D. (1998) Adherent neutrophils activate endothelial myosin light chain kinase: role in transendothelial migration. J Appl Physiol 84, 1817-1821.

211. Hsu, J., Serrano, D., Bhowmick, T., Kumar, K., Shen, Y., Kuo, Y. C., Garnacho, C., Muro, S. (2011) Enhanced endothelial delivery and biochemical effects of alpha-galactosidase by ICAM-1-targeted nanocarriers for Fabry disease. J Control Release 149, 323-31.

212. Sumagin, R. and Sarelius, I. H. (2010) Intercellular adhesion molecule-1 enrichment near tricellular endothelial junctions is preferentially associated with leukocyte transmigration and signals for reorganization of these junctions to accommodate leukocyte passage. J Immunol 184, 5242-52.

213. Burns, A. R., Walker, D. C., Brown, E. S., Thurmon, L. T., Bowden, R. A., Keese, C. R., Simon, S. I., Entman, M. L., Smith, C. W. (1997) Neutrophil Transendothelial Migration Is Independent of Tight Junctions and Occurs Preferentially at Tricellular Corners. J Immunol 159, 2893-2903.

214. Saitoh, M., Ishikawa, T., Matsushima, S., Naka, M., Hidaka, H. (1987) Selective-Inhibition of Catalytic Activity of Smooth-Muscle Myosin Light Chain Kinase. J Biol Chem 262, 7796-7801.

215. Levental, I., Georges, P. C., Janmey, P. A. (2007) Soft biological materials and their impact on cell function. Soft Matter 3, 299-306.

216. Sans, E., Delachanal, E., Duperray, A. (2001) Analysis of the roles of ICAM-1 in neutrophil transmigration using a reconstituted mammalian cell expression model: Implication of ICAM-1 cytoplasmic domain and Rho-dependent signaling pathway. J Immunol 166, 544-551.

217. Sen, S., Tewari, M., Zajac, A., Barton, E., LeeSweeney, H., Discher, D. E. (2010) Upregulation of paxillin and focal adhesion signaling follows Dystroglycan

Complex deletions and promotes a hypertensive state of differentiation. European Journal of Cell Biology 90, 249-260.

218. Koukouritaki, S. B., Vardaki, E. A., Papakonstanti, E. A., Lianos, E., Stournaras, C., Emmanouel, D. S. (1999) TNF-alpha induces actin cytoskeleton reorganization in glomerular epithelial cells involving tyrosine phosphorylation of paxillin and focal adhesion kinase. Molecular Medicine 5, 382-392.

219. Li, Y. H. and Zhu, C. (1999) A modified Boyden chamber assay for tumor cell transendothelial migration in vitro. Clin Exp Metastasis 17, 423-9.

220. Harlan, J. M., Killen, P. D., Harker, L. A., Striker, G. E., Wright, D. G. (1981) Neutrophil-Mediated Endothelial Injury Invitro - Mechanisms of Cell Detachment. Journal of Clinical Investigation 68, 1394-1403.

221. Saito, H., Minamiya, Y., Saito, S., Ogawa, J. (2002) Endothelial Rho and Rho kinase regulate neutrophil migration via endothelial myosin light chain phosphorylation. J Leukocyte Biol 72, 829-836.

222. Levitan, I., Volkov, S., Subbaiah, P. V. (2010) Oxidized LDL: diversity, patterns of recognition, and pathophysiology. Antioxid Redox Signal 13, 39-75.

223. Berliner, J. A., Subbanagounder, G., Leitinger, N., Watson, A. D., Vora, D. (2001) Evidence for a role of phospholipid oxidation products in atherogenesis. Trends Cardiovasc Med 11, 142-7.

224. Diaz, M. N., Frei, B., Vita, J. A., Keaney, J. F., Jr. (1997) Antioxidants and atherosclerotic heart disease. N Engl J Med 337, 408-16.

225. Holvoet, P., Mertens, A., Verhamme, P., Bogaerts, K., Beyens, G., Verhaeghe, R., Collen, D., Muls, E., Van de Werf, F. (2001) Circulating oxidized LDL is a useful marker for identifying patients with coronary artery disease. Arterioscler Thromb Vasc Biol 21, 844-8.

226. Holvoet, P., Vanhaecke, J., Janssens, S., Van de Werf, F., Collen, D. (1998) Oxidized LDL and malondialdehyde-modified LDL in patients with acute coronary syndromes and stable coronary artery disease. Circulation 98, 1487-94.

227. Toshima, S., Hasegawa, A., Kurabayashi, M., Itabe, H., Takano, T., Sugano, J., Shimamura, K., Kimura, J., Michishita, I., Suzuki, T., Nagai, R. (2000) Circulating oxidized low density lipoprotein levels. A biochemical risk marker for coronary heart disease. Arterioscler Thromb Vasc Biol 20, 2243-7.

228. Gardner, G., Banka, C. L., Roberts, K. A., Mullick, A. E., Rutledge, J. C. (1999) Modified LDL-mediated increases in endothelial layer permeability are attenuated with 17 beta-estradiol. Arterioscler Thromb Vasc Biol 19, 854-61.

229. Liao, L. and Granger, D. N. (1995) Modulation of oxidized low-density lipoprotein-induced microvascular dysfunction by nitric oxide. Am J Physiol 268, H1643-50.

230. Blair, A., Shaul, P. W., Yuhanna, I. S., Conrad, P. A., Smart, E. J. (1999) Oxidized low density lipoprotein displaces endothelial nitric-oxide synthase (eNOS) from plasmalemmal caveolae and impairs eNOS activation. J Biol Chem 274, 32512-9.

231. Lehr, H. A., Frei, B., Olofsson, A. M., Carew, T. E., Arfors, K. E. (1995) Protection from oxidized LDL-induced leukocyte adhesion to microvascular and macrovascular endothelium in vivo by vitamin C but not by vitamin E. Circulation 91, 1525-32.

232. Lehr, H. A., Hubner, C., Nolte, D., Finckh, B., Beisiegel, U., Kohlschutter, A., Messmer, K. (1991) Oxidatively modified human low-density lipoprotein stimulates leukocyte adherence to the microvascular endothelium in vivo. Res Exp Med 191, 85-90.

233. Cominacini, L., Garbin, U., Pasini, A. F., Davoli, A., Campagnola, M., Contessi, G. B., Pastorino, A. M., Lo Cascio, V. (1997) Antioxidants inhibit the expression of intercellular cell adhesion molecule-1 and vascular cell adhesion molecule-1 induced by oxidized LDL on human umbilical vein endothelial cells. Free Radic Biol Med 22, 117-27.

234. Takei, A., Huang, Y., Lopes-Virella, M. F. (2001) Expression of adhesion molecules by human endothelial cells exposed to oxidized low density lipoprotein. Influences of degree of oxidation and location of oxidized LDL. Atherosclerosis 154, 79-86.

235. Shentu, T. P., Titushkin, I., Singh, D. K., Gooch, K. J., Subbaiah, P. V., Cho, M., Levitan, I. (2010) oxLDL-induced decrease in lipid order of membrane domains is inversely correlated with endothelial stiffness and network formation. Am J Physiol Cell Physiol 299, C218-29.

236. Kowalsky, G. B., Byfield, F. J., Levitan, I. (2008) oxLDL facilitates flow-induced realignment of aortic endothelial cells. Am J Physiol Cell Physiol 295, C332-40.

237. Mine, S., Tabata, T., Wada, Y., Fujisaki, T., Iida, T., Noguchi, N., Niki, E., Kodama, T., Tanaka, Y. (2002) Oxidized low density lipoprotein-induced LFA-1-

dependent adhesion and transendothelial migration of monocytes via the protein kinase C pathway. Atherosclerosis 160, 281-8.

238. Krishnan, R., Klumpers, D. D., Park, C. Y., Rajendran, K., Trepat, X., van Bezu, J., van Hinsbergh, V. W., Carman, C. V., Brain, J. D., Fredberg, J. J., Butler, J. P., van Nieuw Amerongen, G. P. (2011) Substrate stiffening promotes endothelial monolayer disruption through enhanced physical forces. Am J Physiol Cell Physiol 300, C146-54.

239. Xu, J., Wang, F., Van Keymeulen, A., Rentel, M., Bourne, H. R. (2005) Neutrophil microtubules suppress polarity and enhance directional migration. Proc Natl Acad Sci U S A 102, 6884-9.

240. Hashimoto, K., Kataoka, N., Nakamura, E., Hagihara, K., Hatano, M., Okamoto, T., Kanouchi, H., Minatogawa, Y., Mohri, S., Tsujioka, K., Kajiya, F. (2011) Monocyte trans-endothelial migration augments subsequent transmigratory activity with increased PECAM-1 and decreased VE-cadherin at endothelial junctions. Int J Cardiol 149, 232-9.